



THÈSE

En vue de l'obtention du

DOCTORAT DE L'UNIVERSITÉ DE TOULOUSE

Délivré par :

Université Toulouse 3 Paul Sabatier (UT3 Paul Sabatier)

Présentée et soutenue par :

Yandi LAN

le vendredi 11 décembre 2015

Titre :

Tertiary Treatment Combining Nanofiltration and Electrochemical Oxidation
for Elimination of Pharmaceuticals in Wastewater

École doctorale et discipline ou spécialité :

ED MEGEP : Génie des procédés et de l'Environnement

Unité de recherche :

Laboratoire de Génie Chimique UMR 5503, CNRS, Université de Toulouse

Directeur/trice(s) de Thèse :

Christel CAUSSERAND-ALEXANDROVITCH, Professeur, LGC, Université de Toulouse
(Directrice de thèse)

Karine GROENEN-SERRANO, Professeur, LGC, Université de Toulouse (co-Directrice de thèse)

Jury :

Murielle RABILLER-BAUDRY, Professeur, Université de Rennes, France (Président)

Marc CRETIN, Professeur, Université de Montpellier 2, France (Rapporteur)

Ane URTIAGA, Professeur, University of Cantabria, Spain (Rapporteur)

Matthieu JACOB, Ingénieur Recherche Total, France (Examinateur)

Clémence COETSIER, Maître de Conférences, LGC, Université de Toulouse (Invité)

Acknowledgement

I would like to thank the jury members Prof. Marc CRETIN and Prof. Anne URTIAGA for accepting to act as Reviewers for my thesis, Dr. Matthieu JACOB and Prof. Murielle RABILLER-BAUDRY for accepting to examine my Ph.D. study.

I would like to give my special appreciation to my supervisor Prof. Christel CAUSSERAND, first for accepting me in the team and second for her 'step-by-step' guidance. It is she that leads me into the area of membrane technology and chemical engineering. She introduces me not only how to prove a hypothesis and practice an idea theoretically and experimentally, but also how to improve the quality of scientific publications. I also would like to thank my co-supervisor Prof. Karine GROENEN-SERRANO for her endless guidance, patience, support and additionally for her enthusiastic interest in new results. I also would like to thank for their kindness and mother-like attitude beyond as supervisors. My special thanks to Clémence COETSIER who works like a supervisor and never stops helping and encouraging me, she makes every effort to help me and is always ready to spend time to introduce me.

Thank my lab-mates and friends Le HAN, Yingying GU, Jin WANG, Dancheng CHEN, Raluca CIUMAG, Izabella BOUHID, Yannis GERGIANAKIS, Lucia BENAVENTE, Mylene DETCHEBERRY, Johanne TEYCHENE, Waritha JANTAPORN, Arthur GAVEAU, Dmytro SNISARENKO, who always make me feel at home in France for their endless encouragement and motivation throughout my Ph.D. studies. It would be impossible to finish this challenging road without these valuable people. I appreciate their presence, friendship and amusement.

Many thanks also to Laure LATAPIE, Sandrine DESCLAUX, who help me to perform all the analysis and Jean Christophe ROUCH who help me for preparation and maintenance of experimental setups.

China Scholarship Council (CSC) are also acknowledged for financial support. Thanks to PANACEE ANR project conducted in LGC who provides the MBR effluents for my experiments.

All current and former members in LGC, we were lucky enough to host throughout the world. Thanks for your scientific discussions and also good friendship.

The last but not the least, my special appreciation and great thankfulness are dedicated to my mother Fangnong QIN, my father Wennian LAN, my boyfriend Guanghua JIN for their love, patience, unconditional support and motivation.

Contents

List of Abbreviations

General introduction 1

Chapter I 5

Background on the tertiary treatment of wastewater

Chapter II 43

Materials and methods

Chapter III 67

Nanofiltration for removal of pharmaceuticals from MBR effluent: Productivity and selectivity

Chapter IV 143

Elimination of pharmaceuticals by electrochemical oxidation

Chapter V 215

Treatment efficiency and toxicity removal of combining EO and NF process

Conclusions 225

Annex 229

LIST OF ABBREVIATIONS

Nanofiltration

A_m	Membrane active area (m^2)	L_t	Threshold permeability ($L\ h^{-1}\ m^{-2}\ bar^{-1}$)
A_{free}	Membrane area unoccupied by surface crystals (m^2)	m_s	Weight of the scaling on the membrane surface (mg)
A_{oc}	Membrane area occupied by surface crystals (m^2)	ΔP	Transmembrane pressure (bar)
C_m	Concentration on the membrane surface	R_f	Total fouling resistance (m^{-1})
C_b	Solute concentration in bulk	R_m	Intrinsic hydraulic membrane resistance (m^{-1})
C_p	Solute concentration in permeate	R_{rf}	Resistance due to reversible fouling (m^{-1})
CP	Concentration polarization degree	R_{if}	Resistance due to irreversible fouling (m^{-1})
D	Solute diffusivity ($m^2\ s^{-1}$)	R_{ir}	Residual irreversible fouling resistance after rinsing (m^{-1})
J	Permeate flux ($L\ h^{-1}\ m^{-2}$)	R_t	Threshold irreversible fouling resistance (m^{-1})
J_{lim}	Limiting flux ($L\ h^{-1}\ m^{-2}$)	R_{obs}	Observed ion rejection
$J_{critical}$	Critical flux ($L\ h^{-1}\ m^{-2}$)	S	Supersaturation ratio ($mol^2\ L^{-2}$)
k	Solute mass transfer coefficient ($m\ s^{-1}$)	S_m	Supersaturation ratio on membrane surface ($mol^2\ L^{-2}$)
K_{sp}	Thermodynamic solubility product ($mol^2\ L^{-2}$)	$S_{critical}$	Critical supersaturation ratio ($mol^2\ L^{-2}$)
L_p	Pure permeability ($L\ h^{-1}\ m^{-2}\ bar^{-1}$)	μ_p	Viscosity of permeate ($Pa\cdot s$)
L_{pf}	Pure water permeability after filtration ($L\ h^{-1}\ m^{-2}\ bar^{-1}$)	δ	Boundary layer thickness ($m\ s^{-1}$)
L_b	Permeability combining colloidal silica and organics fouling and scaling ($L\ h^{-1}\ m^{-2}\ bar^{-1}$)	β	Area occupied per unit mass ($m^2\ mg^{-1}$)

LIST OF ABBREVIATIONS

Electrochemical oxidation

C_0	Initial concentration
A	E electrode surface (m^2)
F	Faraday constant ($C\ mol^{-1}$)
i_{lim}	Limiting current density ($A\ m^{-2}$)
I_{lim}	Limiting current intensity (A)
$i_{lim,ne-}$	Limiting current density of directly electron transfer ($A\ m^{-2}$),
$i_{lim,\cdot OH}$ ($A\ m^{-2}$)	Limiting current density corresponding to the total mineralization of the organics
$i_{\cdot OH}$	Part of current density used to generate $\cdot OH$
k_d	Mass transfer coefficient ($m\ s^{-1}$)
k_m	Constant rate of mineralization ($m\ s^{-1}$)
r	Specific electrochemical reaction rate ($mol\ m^{-2}\ s^{-1}$)
V	Volume of solution (m^3)
Φ	Flow rate ($m^3\ s^{-1}$)
α	Ratio of applied current density and the initial limiting current density
γ	Equivalent number of exchanged electrons
Γ	Reaction rate of organic on the electrode ($mol\ m^{-2}\ s^{-1}$)
Γ_e	Electrochemical reaction rate by electrons transfer ($mol\ m^{-2}\ s^{-1}$)
Γ_R	Rate of electron transfer and the rate of reaction with $\cdot OH$ ($mol\ m^{-2}\ s^{-1}$)

General introduction

General introduction

It has been reported that micropollutants such as pharmaceuticals are widespread in the aquatic environment. Because of their limited biodegradability, micropollutants are incompletely eliminated in wastewater treatment plants, whatever the process used: activated sludge treatment or even membrane bioreactor (MBR) process which exhibits good purification performances. As a consequence, refractory pharmaceuticals remain in treated wastewater and are continuously discharged into aquatic systems. Considering their persistence and potential long-term toxicity, even at low concentrations, additional treatments are required to prevent their occurrence in aquatic ecosystems and limit the risk for exposed organisms. The difficulty in removing these contaminants from waters comes from their resistance to biological degradation, their small size or their extreme dilution. Within the framework of the conservation of the environment and the water resource, it seems necessary besides limiting the discharges of micropollutants, developing new technologies allowing the purification of waters.

In recent works, nanofiltration (NF) and reverse osmosis (RO) have been investigated for the rejection of pharmaceuticals in synthetic solution and surface water. Both techniques are considered really efficient to provide pharmaceutical-free treated water. However, they are only separation techniques, and their major drawback is to produce a concentrate stream which contains the pollutants in higher concentration and could be as consequence more toxic than the influent. In this case, concentrate stream cannot be discharged into the environment and its further treatment is necessary.

Electrochemical oxidation (EO) is a promising process for pollutants elimination in particular using a boron doped diamond (BDD) anode. The use of BDD anode allows the production of electrogenerated hydroxyl radicals from water discharge. Because the action of hydroxyl radicals is located close to the anode, there are transfer limitations in dilute solution. The coupling of electrochemical oxidation with the preconcentration step by nanofiltration renders it economically viable.

The objective of this project was to evaluate the performances of the coupling of nanofiltration and electrochemical oxidation as tertiary treatment of wastewater after membrane bioreactor treatment. Considering that the hospital wastewater is one of the main sources of micropollutants, especially pharmaceuticals, the study focused on the tertiary treatment of the secondary effluent of a MBR system which was fed directly from a hospital's

sanitary collection system (Toulouse, France).

More precisely, this Thesis focused on the effect of this complex water matrix containing a mixture of organics, inorganics, pharmaceuticals and numerous other components on the behavior of both processes, nanofiltration and electrochemical oxidation, during the treatment in operating conditions as comparable as possible to real ones.

In nanofiltration process, the monitoring of permeate flux is a particularly important way to control fouling and as a consequence process productivity. Numerous studies have been dedicated in one hand to develop procedures to identify and/or predict critical flux and limiting flux in synthetic solutions; in another hand to observe flux behaviors in a complex matrix. The key point is to implement the procedures developed in synthetic solutions to the case of a real complex matrix in order to be able to predict and possibly control fouling from the flux behaviors as a function of the water matrix properties such as pH, organics and salt concentrations.

Concerning the process selectivity, pharmaceuticals rejection by a nanofiltration membrane results from the complex combination of numerous mechanisms (steric exclusion, electrostatic and hydrophobic interactions...) which is not well understood mainly due to the specific properties of pharmaceutical molecules. Superimposed to that difficulty in predicting pharmaceuticals rejection by a certain membrane, it should be taken into account again the complexity of real water matrixes and its impact on pharmaceuticals rejection not only directly by modifying solute-membrane interactions, but also indirectly through the type of fouling generated during the filtration.

Hospital wastewater as well as numerous wastewater contain a lots of inorganic ions, the main part being retained in the membrane concentrate. Thanks to the presence of these salts, the concentrate is sufficiently conductive and no addition of electrolyte is required for further treatment by electrochemical process. However, the presence of chloride ions raises questions: numerous studies indicate the oxidation of organics in presence of chlorides may cause halogenated organic compounds. Moreover, the use of an anode at high oxygen overvoltage, such as BDD, can lead to the formation of perchlorate. Both types of compounds are very toxic for the environment. Nevertheless, very few information are given on the ability of the electrochemical process to control the production of such compounds. A specific study will be devoted to propose conditions allowing limiting the formation of such undesired species.

The manuscript is outlined as follows:

A literature review will be the subject of the first chapter of this manuscript. It will report the general principles of membrane filtration and electrochemical oxidation process and the

current state of knowledge on the elimination of pharmaceuticals by using these technologies.

The second chapter will be devoted to the description of the experimental techniques and methods. It will present the solutions used as well as analytical methods. It will describe in detail the experimental set-up used in this study.

Chapter III will present the investigations on the fouling mechanisms during the nanofiltration step and their association with the process productivity (critical and limiting fluxes) and selectivity (pharmaceuticals rejection). A method allowing to control the productivity will be proposed considering the fouling mechanism expected as a function of the water matrix properties.

The electrochemical oxidation of pharmaceuticals will be reported in chapter IV. The impact of the simultaneous presence of organics and inorganics on pharmaceuticals degradation will be investigated with a specific focus on the formation of by-products in presence of chlorine ions in synthetic solution. A numerical model giving the temporal concentration of pharmaceutical compounds during the electrolysis will be proposed. Finally the application of electrochemical oxidation to the nanofiltration concentrate will be demonstrated.

Chapter V will describe the efficiency of the coupling process and the main associated impact parameters through the monitoring of the toxicity.

Finally, chapter VI will give general conclusions and recommendations for a future work.

Chapter I

Background on the tertiary treatment of wastewater

Contents

I.1 Occurrence of pharmaceuticals in wastewater: Towards a new tertiary treatment	5
I.1.1 Threats of pharmaceuticals in aquatic systems.....	5
I.1.2 Source of pharmaceuticals and their pass-through from conventional wastewater treatment plants.....	6
I.1.3 Tertiary treatment for the elimination of pharmaceuticals in wastewater	7
I.1.3.1 Membrane process for production of high quality water	8
I.1.3.2 Electrochemical oxidation for elimination of pharmaceuticals.....	9
I.1.3.3 Combining NF and electrochemical oxidation as tertiary treatment of MBR effluent	11
I.2 Nanofiltration.....	12
I.2.1 General Presentation of the process.....	12
I.2.1.1 Cross-flow filtration	12
I.2.1.2 Continuous mode and batch filtration process	13
I.2.2 Fouling mechanisms in nanofiltration	14
I.2.2.1 Concentration polarization	14
I.2.2.2 Colloidal organics fouling	16
I.2.2.3 Inorganic fouling or scaling.....	17
I.2.3 Critical flux and Limiting flux.....	21
I.2.4 Factors affecting the rejection of pharmaceuticals during NF treatment	23
I.3 Electrochemical oxidation	25
I.3.1 BDD anode	26
I.3.2 Hydroxyl radicals	26
I.3.3 Theoretical model for oxidation of organic compounds on BDD	28
I.3.4 Long-term sustainability of electrochemical oxidation treatment.....	31
I.4 Main problem need to be addressed during the research.....	32
References.....	34

I.1 Occurrence of pharmaceuticals in wastewater: Towards a new tertiary treatment

I.1.1 Threats of pharmaceuticals in aquatic systems

It has been reported that micropollutants such as pharmaceuticals are widespread in the aquatic environment. Numbers of reports about the occurrence of pharmaceuticals in aquatic systems have been accumulated these decades [1–6]. By the early 2000s, pharmaceuticals and hormones have been detected in rivers [1], seawater [2], wastewater [3] in Europe, China [2], United States [3]. The concentrations of them were in the range of ng L^{-1} to even $\mu\text{g L}^{-1}$. To give precise and recent examples, micrograms per liter of ofloxacin, norfloxacin, ciprofloxacin and trimethoprim were commonly detected in water samples from three gorge reservoirs in Chongqing region in China [4]. Antibiotics were detected quite frequently in ng L^{-1} range, up to $\mu\text{g L}^{-1}$ in surface waters of six investigated rivers including freshwater, estuarine and marine samples [5,7]. Corre et al. reported that around 3000 pharmaceuticals were available in the aquatic system in the United States and Europe [6].

Even if pharmaceuticals occur at trace level in aquatic system they still pose severe threats not only to drinking water, but also long-term toxicity to eco-system in which pharmaceuticals could have detrimental interaction to aquatic organisms and humans being through water cycle.

Accumulation of pharmaceuticals in the aquatic system increases the risk of the appearance of them into drinking water. Heberer [8] began to track some persistent pharmaceutical compounds from municipal sewage to drinking water and sub- ng L^{-1} of pharmaceuticals have been found in drinking water. Fifty eight pharmaceutically active compounds were analyzed in 10 bottled of mineral drinking water brands produced in Spain. Nicotine was detected in concentrations in the ng L^{-1} range in half of them [9]. Bruce et al. [10] reported that 15 active pharmaceutical ingredients and four metabolites were detected in 19 drinking water treatment plants across the United States; these authors mentioned that safe long-term exposure to mixtures of compounds, particularly for sensitive population groups, had to be clarified, even if the adverse health effects from targeted pharmaceuticals were not expected at these concentrations. Johnson et al. [11] showed that cytotoxic drugs

such as 5-fluorouracil posed a risk to aquatic organisms and to humans through water cycle. The exposure of the pregnant woman, or more specifically her fetus, to these drugs via drinking water should be minimized. Kümmerer and Al-Ahmad [12] reported the additional risk of cancer due to the presence of cyclophosphamide and ifosfamide into the aquatic environment cannot be fully excluded, especially with respect to children.

Presence of pharmaceuticals in the environment could be mixed with other organic compounds and microorganisms. Some researches cared about the mixture effect which could be even worse [11,13]. It is generally accepted that mixtures with components exhibiting the same mode of action act according to the model of concentration addition [13]. Some other researches believed the pharmaceuticals exposure promotes the evolution of antibiotic-resistant bacteria [14].

Long-term effect on aquatic environment should also be taken into account as shown in the review paper of Ankley et al. [13]. For example, Ethinyl estradiol (EE) was present at extremely low environmental concentrations in sea, but this level was high enough to cause biological responses in fishes.

Special attentions should be taken to the exposure of pharmaceuticals in aquatic ecosystems even at low concentrations, considering their persistence, long-term toxicity as well as the potential endangerment through drinking water of certain people groups such as pregnant women and children. The elimination of pharmaceuticals from the source is required to prevent the escape of them into aquatic system and limit the risks previously mentioned.

I.1.2 Source of pharmaceuticals and their pass-through from conventional wastewater treatment plants

It was reported that one of the sources of pharmaceuticals is domestic sewerage network: excreted by people taking them, or disposed as unused drugs [15]. Another important source is hospital wastewater in which the concentration of target pharmaceuticals is higher than in the municipal wastewater [16]. For example, ciprofloxacin was detected at concentrations ranging from $0.8 \mu\text{g L}^{-1}$ in municipal wastewater to $13.7 \mu\text{g L}^{-1}$ in hospital effluent. As a consequence, pharmaceuticals in hospital wastewater are likely to pose the highest environmental risk compared to the influent and effluent of wastewater treatment plants [17]. Chang et al. [4] believed that hospitals, nurseries and slaughter houses are the main sources of antibiotics in rivers.

The removal of pharmaceuticals in conventional wastewater treatment plants (WWTP) is applied with activated sludge process. Although WWTP is effective in removing several pharmaceuticals, some refractory pharmaceuticals were still detected in WWTP effluents and discharged into aquatic system through the treatment plants [3,5,14,16,18]. Clara et al. investigated that antiepileptic pharmaceuticals like carbamazepine were not affected during the treatment [18]. Ciprofloxacin, sulfamethoxazole, trimethoprim, tetracycline, and clindamycin were detected in the treatment effluents at concentrations in the $\mu\text{g L}^{-1}$ range [19]. Buerge et al. found that there is no difference in concentrations of cyclophosphamide and ifosfamide between influent and effluent in two Swiss sewage treatment plants indicating the absence of any elimination [20]. Ciprofloxacin, sulfamethoxazole, and clindamycin were found as far as 100 meters in the receiving stream from the discharge point of WWTP, which indicates the spread of these drugs in aquatic system through the WWTP [19]. Moreover, the pharmaceuticals spreading into the aquatic environment could persist for a long time due to their low environmental degradability. Kümmerer et al. [21] reported only a few of pharmaceutical compounds were partially biodegraded under test conditions in aquatic systems. Most of them were persistent. Johnson et al. [11] raised that many pharmaceuticals could be extremely persistent in river water.

As a consequence, the refractory pharmaceuticals pass through the WWTP and accumulate in the aquatic system. They continue to pose significant threats to sustainability of the eco-system and safety of drinking water.

I.1.3 Tertiary treatment for the elimination of pharmaceuticals in wastewater

The incomplete removal of pharmaceuticals was observed from activated sludge process in the conventional wastewater treatment plants. Considering the threat they represent, a specific treatment of pharmaceuticals at source point has to be developed [16,17]. Escher et al. [17] suggested that separated treatment of hospital wastewater would reduce the pharmaceutical load of wastewater treatment plants, and the risk from the identified priority pharmaceuticals according to the EU Water Framework Directive.

In this context, membrane bioreactor (MBR) treatment shows an higher efficiency for removal of trace organics than the conventional activated sludge process in the wastewater treatment plants [22]. MBR is a process that integrates biological treatment and sludge

separation by microfiltration (MF) or ultrafiltration (UF) membranes which are placed either outside (outer loop) or inside the bioreactor (immersed membranes). MBR system can operate at a much higher mixed liquor suspended solids (MLSS) concentration which means higher biomass concentration than that of conventional activated sludge treatment [22].

Some studies propose to use MBR for hospital wastewater treatment [23–25], and they demonstrated that MBR system exhibited a higher efficiency and effluent quality than the conventional activated sludge system [23]. Kovalova et al. [24] operated the MBR treatment by directly feeding it from the hospital's sanitary collection system at a Swiss hospital. The elimination of pharmaceuticals vary from 0 to 99% and depends on the species. Quesada et al [25] applied MBR system for the direct treatment of hospital wastewater at the outlet of a French hospital and observed the decrease of the eco-toxicity of wastewater but pass-through of some pharmaceuticals into the MBR effluent was still observed.

Despite the high efficiency of MBR treatment, its remaining weakness comes from the fact that it is a process based on the biodegradation. Pharmaceuticals which exhibit poor biodegradability can persist in the MBR effluent. Tertiary treatment process is then necessary to ensure the purification.

I.1.3.1 Membrane process for production of high quality water

Pressure-driven membrane processes such as nanofiltration (NF) and reverse osmosis (RO) are recommended as powerful options which can be applied not only into wastewater treatment but also drinking water production for the removal of organic pollutants [26–29]. Several researches have shown that residues of pesticides, pharmaceuticals, endocrine disrupters and other trace organics can be effectively removed from contaminated waters by RO and also by NF. Bruggen et al. [30] concluded that NF can be a valuable alternative for the removal of micropollutants after having tested four NF membranes. Kiso et al. [31] demonstrated that NF membranes can reject effectively non phenolic pesticides and alkyl phthalates. Kimura et al. [27] showed that the polyamide membrane exhibited a better performance in terms of the rejection of selected pharmaceuticals and endocrine disrupters compared to cellulose acetate membrane. The rejections of them range from 57% to 91%. Verliefde et al. [28] reported NF can be a very powerful technique to remove not only large pollutants but also the smaller hydrophilic and/or charged organic micro-pollutants.

Radjenovic et al. [29] studied the removal of several pharmaceuticals such as ketoprofen, diclofenac, sulfamethoxazole and gemfibrozil by NF and RO processes. Even if the rejection of pharmaceuticals was related to their molecular charge, the authors recommended these processes for drinking water production due to their high efficiency of removal.

NF and RO are increasingly applied as tertiary treatment to obtain high quality water for water reuse from a secondary treated effluent such as MBR effluent [32–37]. Benefiting from MBR process, especially excellent solids separation and turbidity was achieved by the UF membrane of MBR and acceptable and stable flux (productivity) of RO and NF can be achieved during wastewater treatment [32–34]. Dialynas and Diamadopoulou [32] have obtained high quality effluent, devoid of heavy metals and with very low organic matters concentration (DOC level below 4 mg L^{-1}), after MBR-RO treatment of municipal wastewater. MBR-RO coupling also shows excellent capability for the removal of TOC, NH_4^+ and NO_3^- in domestic sewage and high productivity for RO with a good stability of the process over 5 months [33]. Finally, Alturki et al. [37] applied the combining MBR and NF/RO for the removal of 40 trace pharmaceuticals and organic micropollutants. These authors observed the MBR system shows effective removal of hydrophobic and biodegradable compounds, while remaining ones are mostly hydrophilic and can be almost completely removed by NF/RO. As a consequence, RO permeate complied with individual drinking water limits for organic contaminants and micro-organisms, and met water reuse regulations for several non-potable applications [34].

NF and RO applied as tertiary treatment of MBR effluent can then produce a treated water of excellent quality, free of pharmaceuticals. However, as a consequence, the retentate of NF/RO process which contains high concentrations of pharmaceuticals and other organic micropollutants could be more toxic than the influent. In this case, concentrate streams cannot be discharged into the environment and their further treatment is necessary. Also, the electrochemical oxidation can be a prospective process to eliminate the pharmaceuticals and organics of the NF/RO retentate.

1.1.3.2 Electrochemical oxidation for elimination of pharmaceuticals

The most important method well established and relatively cheap to decrease the chemical oxygen demand of wastewaters is based on biological treatment. But, unfortunately, certain substances responsible for chemical oxygen demand (COD) are not

easily biodegradable. In particular, toxic substances can inactivate microorganisms which slow down biological processes. Other methods for COD removal are hence required in the presence of refractory and/or toxic compounds. Physicochemical methods like wet chemical oxidation by O₂ (high pressure, high temperature) [38] or hydrogen peroxide (in the presence of catalyst) [39] have given rise to efficient processes. However, these technologies are quite expensive.

Electrochemistry is an alternative technique which has important advantage that degradation of organics into carbon dioxide, water and nontoxic substance can be achieved under particular conditions. Polcaro et al. [40] studied the EO of phenol and chlorophenols on porous carbon felt electrodes. Their results shows that this anode material allows to oxidize partially organic compounds and the total mineralization is not reached. This selective oxidation can serve as a pretreatment before biological treatment. Advanced oxidation process, electro-Fenton can be for degradation of persistent pollutant. In this process, •OH are produced through electrochemically assisted Fenton's reaction in which the Fenton's reagent (H₂O₂ + Fe²⁺) is electrochemical generated or regenerated [41]. Yahya et al. demonstrated that electro-Fenton process can be an efficient method for removal of pharmaceuticals through the study of degradation of ciprofloxacin [41].

Electrochemical oxidation with specific anode materials which allows electrogenerated •OH from water discharge were studied in order to achieve mineralization without chemical doping. Electrochemical oxidation of 2-chlorophenol was carried out using the Ti/PbO₂ and Ti/SnO₂ anodes. The greater electrochemical treatment efficiency was obtained on Ti/SnO₂ anode for its better ability to oxidize toxic compounds [42]. Currently, boron doped diamond (BDD) anode could be an efficient electrode for the mineralization of organic pollutants [43], because the use of BDD anode allows the production of electro-generated hydroxyl radicals which is a strong oxidant from water discharge. The BDD anode showed a better performance to degrade oxalic acid comparing to PbO₂. BDD provided not only higher oxidation rate, higher current efficiency but also lower energy consumption than using the PbO₂ electrode to reach mineralization [44]. The oxidation of cresol was studied using PbO₂ and BDD [45]. BDD is proved more efficient for the removal of cresol and its intermediates than PbO₂ at the same current density and electrolyte. Panizza et al. demonstrated that 2-naphthol and the intermediates can be oxidized using synthetic BDD thin film electrodes [46]. Weiss et al. [47] reported that a complete degradation of a phenol solution (20 mM) using a BDD anode obtained 99% removal of aromatics in 5 h under 47 mA cm⁻². A completely degradation of the chlorpyrifos

pesticide solution can be observed after 6 h electro oxidation (20 mA cm^{-2}) using BDD anode [48].

BDD electrochemical oxidation is a process of choice for the mineralization of pharmaceuticals. However, because the action of hydroxyl radicals is located close to the anode, there are transfer limitations in dilute solution. Thus, the coupling of electrochemical oxidation with a pre-concentration step by filtration process renders it economically viable.

I.1.3.3 Combining NF and electrochemical oxidation as tertiary treatment of MBR effluent

From sections I.1.3.1 and I.1.3.2, it can be concluded that tertiary treatment of secondary effluent could be a solution for point source treatment. Considering the combination of membrane separation technique and electrochemical oxidation, concentrated pharmaceuticals in the NF or RO retentate can be mineralized by electrochemical oxidation using a BDD anode to prevent the spread of them and reduce the environmental risk of concentrate stream.

Pérez et al. [49] investigated electrochemical oxidation of reverse osmosis concentrates using BDD anode. In this study the concentrates were generated from a UF (ultrafiltration) / RO pilot plant which treated the secondary effluent of a wastewater treatment plant. The authors presented the removals of COD, ammonium and ten emerging pollutants (including Caffeine, Naproxen and Gemfibrozil) from the RO concentrate using different applied current density, ranging from 2 to 20 mA cm^{-2} . More than 90 % of the regular emerging pollutants were removed after 2 h of electrolysis.

Urtiaga et al. [50] have studied a pilot system that integrated ultrafiltration (UF), reverse osmosis (RO), and electrochemical oxidation. The objective was to retain pharmaceuticals and other organic contaminants using UF-RO and mineralized the RO concentrate with BDD electrodes to avoid discharge of the compounds from municipal wastewater treatment plants. The coupling process shows great efficiency, not only the removal of the emerging contaminants but also their mineralization. UF pilot plant was applied to remove suspended solids and provide a disinfection barrier by retaining bacteria and viruses. Benefiting from the UF process, RO was subjected to a low pressure gradient ($\Delta P = 11 \text{ bar}$) and rejected more than 99% of all target compounds. The following EO treatment with boron-doped diamond electrodes removed more than 95% of most of the studied compounds from the

RO effluent. This study verifies the feasibility of the coupling of membrane separation and electrochemical oxidation for the complete removal of pharmaceuticals from wastewater after biological treatment.

Considering the tertiary treatment of MBR effluent, which benefits of the separation and removal of the sludge and suspended solids due to integrated membrane process (microfiltration in most cases), an acceptable and stable flux (productivity) can be achieved using nanofiltration instead of RO. Moreover, it is evident that NF requires lower pressure and obtains higher permeate flux in comparison with RO for tertiary treatment of MBR effluent [36]. NF membrane can reject organics with molecular weight (MW) much lower than 200 Da and therefore it could remove pharmaceuticals and organic micro-pollutants by molecular exclusion, electrostatic repulsion or hydrophobic interaction between the membrane and the solute [51]. Also, the rejection of pharmaceuticals can be enhanced due to fouling mechanisms and presence of natural organic matters in wastewater [52–54]. NF which can satisfy simultaneously high removal of pharmaceuticals and high productivity (by comparison with RO) could be a great choice in the coupling process.

I.2 Nanofiltration

In on-site applications, nanofiltration unit should operate in a cross-flow continuous mode. We propose in the following section to present this operating mode and to describe fouling mechanisms that are expected to impact productivity and selectivity over operation time.

I.2.1 General Presentation of the process

I.2.1.1 Cross-flow filtration

Fig.I-1 illustrates the difference between the dead-end and cross-flow configurations during filtration. In the dead-end configuration, the feed flows normal to membrane while in cross-flow it flows parallel or “tangential” to the membrane [55]. NF and RO are normally operated in cross-flow mode as in this mode the cake formation and concentration polarization are limited and the steady state operation is possible. In contrast, cake continues to accumulate until the capacity of the filter is reached in dead-end filtration [55].

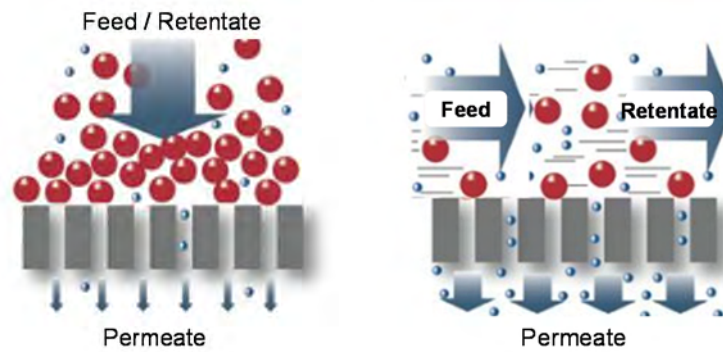


Fig.I-1 Dead-end and cross-flow modes of operation

I.2.1.2 Continuous mode and batch filtration process

A continuous membrane system is often operated as a feed-and-bleed mode. This operation mode is chosen for large-scale application. Fig.I-2 shows the single pass and feed-and-bleed continuous membrane filtration. In the feed-and-bleed mode, a portion of the retentate is recirculated, this requiring an additional pump. The presence of the recirculation loop increases the pressure of the fluid entering the module as well as the volumetric flow rate through the module.

The batch system is schematized by a closed loop in which the retentate is returned to the feed tank and the permeate is removed continuously until the desired volume reduction factor is reached [56]. Batch mode used is generally well adapted for small-scale applications. Recirculation can also be used in batch system as shown in Fig.I-3.

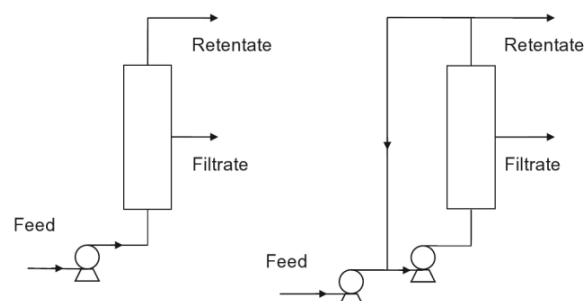


Fig.I-2 Process configurations for single pass and feed-and-bleed continuous membrane filtration [55]

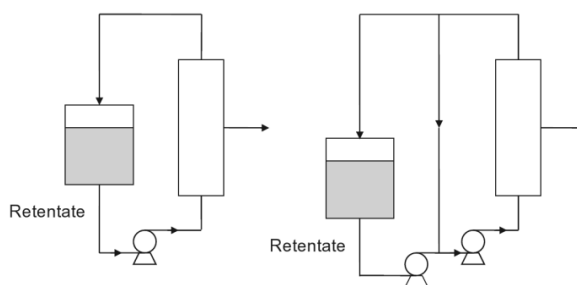


Fig.I-3 Process configurations for batch membrane filtration process showing simple and recirculation options [55].

The limitation of the membrane process is the membrane fouling [51]. In constant flux mode, when the membrane gets fouled, the system pressure increases to maintain constant permeate and retentate flow. The system will continue operating until reaching a certain pressure and then, the system is stopped [57]. Membrane cleaning is necessary before the system restarts. In constant pressure mode, the flux could be maximized at high operating pressure, while rapid fouling of membrane resulting from the high flux would reduce severely the flux immediately. As a consequence, the fouling increases the cost due to the increase of energy demand, additional labor for maintenance and chemical costs for cleaning. It also induces the shorter lifetime of the membrane. The control of the flux is then important for the application of membrane process in an economically viable and sustainable way.

I.2.2 Fouling mechanisms in nanofiltration

Fouling is “*the process resulting in loss of performance of a membrane due to the deposition of suspended or dissolved substances on its external surfaces, at its pore openings, or within its pores* [58].” It can reduce the permeate flux in relation to both the productivity and selectivity of membrane process. The fouling declines the flux by increasing the osmotic pressure and reducing the membrane permeability by pore blocking, gel layer or cake formation. The selectivity of membrane could be also modified due to fouling [52,59,60]. Serious fouling types: concentration polarization, fouling by colloidal organics, and scaling, related to the nanofiltration process, are described as follow.

I.2.2.1 Concentration polarization

Concentration polarization (CP) is known as the process of accumulation of retained

solutes in the membrane boundary layer [61] due to the different membrane permeability for various compounds. It occurs when the solutes and particles in the feed are convected towards the membrane with the solvent in pressure-driven liquid-phase membrane processes, such as NF. The back diffusion of solutes from the membrane is assumed to be in equilibrium with the convective transport [51]. Concentration polarization is normally considered to form rapidly at the beginning of the filtration [62]. Although the concentration polarization is reversible, one attributes to this mechanism the more problematic fouling's such as the adsorption and precipitation of solutes as well as the gel layer formation [63].

I.2.2.1.1 Film Theory

Based on the boundary layer mass balance, the permeate flux in presence of polarization concentration can be described by the Film Theory [64].

$$J = \frac{D}{\delta} \ln \left(\frac{C_m - C_p}{C_b - C_p} \right) = k \ln \left(\frac{C_m - C_p}{C_b - C_p} \right) \quad (\text{Eq.I-1})$$

where D ($\text{m}^2 \text{s}^{-1}$) and δ (m) are the solute diffusivity and the boundary layer thickness, respectively, k is the solute mass transfer coefficient in m s^{-1} , C_m , C_b and C_p are the solute concentration at the membrane surface, bulk solute concentration and permeate solute concentration, respectively.

I.2.2.1.2 Effect of concentration polarization on the membrane rejection

The concentration polarization introduces complexity into the membrane retention. It should be noticed that the observed rejection (R_{Obs}) and the real rejection (R_0) are conceptually distinct. The observed rejection can be measured in membrane application from permeate solute concentration (C_p) and bulk concentration (C_b) which is often approximated with either the feed concentration or the average of feed and retentate concentrations as Eq.I-2.

$$R_{Obs} = \left(1 - \frac{C_p}{C_b} \right) \cdot 100\% \quad (\text{Eq.I-2})$$

The real rejection (R_0) reflecting intrinsic membrane characteristics is determined by the

membrane solute concentration (C_m) and permeate concentration as Eq.I-3.

$$R_0 = \left(1 - \frac{C_p}{C_m}\right) \cdot 100\% \quad (\text{Eq.I-3})$$

R_0 cannot be determined from C_p and C_m measurements, because the solute concentration on the membrane surface cannot be directly measured.

The observed rejection which is calculated by the bulk solute concentration underestimates the rejection of the membrane due to the difference between C_m and C_b .

The effect of polarization concentration can be traduced through the use of CP the concentration polarization degree which is defined by Eq.I-4 deduced from a combination of equations I-1, I-2 and I-3 [65,66]

$$CP = \frac{C_m}{C_b} = (1 - R_{obs}) + R_{obs} \exp\left\{\frac{J}{k}\right\} \quad (\text{Eq.I-4})$$

Theoretically, the concentration polarization and, thus, CP increase with the flux. Higher is C_m , higher will be the solute diffusion from retentate to permeate compartments due to the difference between C_m and C_p . The observed rejection then decreases.

In addition, some authors [67] describe the mechanism of “concentration polarization enhancement by cake layer”. They explain that cake (fouling layer) can hinder the back-diffusion of solutes in the boundary layer and lead to enhancement of salt concentration polarization. This behavior also can lead to the decrease of the observed rejection of solute.

1.2.2.2 Colloidal organics fouling

Wastewater is usually rich in natural organic matters. The adsorption or deposition of them on the membrane surface decline flux irreversibly. The origin of organics fouling is complex. It can be related to the physicochemical characteristics of organic foulants, such as the charge and molecular conformation. The organics can also exhibit electrostatic interactions with membrane surface and ions in the matrix [68]. Organics fouling is normally related to a colloidal fouling due to the fact that organics in wastewater may be adsorbed onto colloids [69,70]. It was reported that foulants of greatest concern for nanofiltration are colloidal sized substances consisting of organics, silica, metal oxides, and microorganisms [51]. The organics fouling on the membrane not only induces the decline of the flux, but also modifies membrane characteristics by pore blocking [71], charge

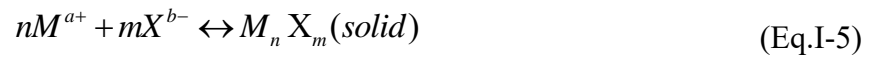
interaction [71,72] and hydrophobic interaction [73].

I.2.2.3 Inorganic fouling or scaling

The membrane scaling is a serious problem in applications of NF process. It leads to physical damage of the membrane due to the difficulty of scaling removal and to irreversible membrane pore blocking [51,74]. The scaling (or inorganic fouling) results from the concentration of one or more species beyond their solubility limits and their precipitation onto the membrane surface [75]. The precipitation or crystallization of inorganics on a membrane surface involves the nucleation and crystal growth. Both of them relate to the supersaturation rate which is the thermodynamic driving force for precipitation.

I.2.2.3.1 Driving force for inorganic precipitation- supersaturation ratio

The definition of the supersaturation rate is explained as follow [51]. An ionic substance M_nX_m crystallizes according to the reaction:



The thermodynamic driving force for the precipitation either in the bulk or at the membrane surface is defined as the change of the Gibbs free energy of transfer from the supersaturated state to equilibrium:

$$\Delta G = RT \ln \left[\frac{(M^{a+})(X^{b-})}{K_{sp}} \right]^{\frac{1}{n+m}} = RT \ln \left[\frac{IAP}{K_{sp}} \right]^{\frac{1}{n+m}} \quad (\text{Eq.I-6})$$

where, K_{sp} is the thermodynamic solubility product of the phase forming compounds in $\text{mol}^2 \text{L}^{-2}$; IAP is the ion activity product.

The supersaturation ratio in the bulk can be defined by:

$$S = \left[\frac{(M^{a+})(X^{b-})}{K_{sp}} \right]^{\frac{1}{n+m}} = \left[\frac{IAP}{K_{sp}} \right]^{\frac{1}{n+m}} \quad (\text{Eq.I-7})$$

Often in the literature S is written without the exponent. Activity coefficients can be estimated by the concentration of ions in dilute solution (or evaluated using various

equations applicable to low or high ionic strength). Thus, the supersaturation ratio can be simplified using following equation:

$$S = \left[\frac{[M^{a+}][X^{b-}]}{K_{sp}} \right] \quad (\text{Eq.I-8})$$

$[M^{a+}]$ and $[X^{b-}]$ are the ionic concentrations. For $S > 1$, $\Delta G < 0$, the transition to solid is spontaneous.

Indeed, precipitation of inorganics on membrane surface is actually related to the supersaturation ratio on membrane surface (S_m) which can be described by Eq.I-9:

$$S_m = \frac{[M^{a+}]_m [X^{b-}]_m}{K_{SP}} \quad (\text{Eq.I-9})$$

where $[M^{a+}]_m$ and $[X^{b-}]_m$ are the ionic concentrations on the membrane surface. They are related to the bulk concentrations $[M^{a+}]_b$ and $[X^{b-}]_b$, according to the concentration polarization degree CP as Eq.I-4. So, the supersaturation ratio of inorganic scalants on membrane surface S_m can be written as

$$S_m = \frac{[M^{a+}]_b [X^{b-}]_b \cdot CP(M^{a+}) \cdot CP(X^{b-})}{K_{SP}} \quad (\text{Eq.I-10})$$

CP is the concentration polarization degree which can be expressed by the flux and observed rejection as described in Eq.I-4.

From a theoretical point of view, the supersaturation ratio higher than 1 ($S_m > 1$) can be considered as the criterion for the crystal precipitation, but the precipitation of crystal is a complex process and relates to many factors such as the matrix, surface type and even the shape of droplet [76–78]. Thus, in real conditions, a critical supersaturation ratio ($S_{critical}$, most of case higher than 1) exist for the given salt [51]. When S_m exceeds $S_{critical}$ ($S_m > S_{critical}$), the precipitation of salt occurs. Otherwise, the system stays in a steady state without precipitation of crystal.

I. 2.2.3.2 Common scalants

Most common constituents of scaling are $\text{CaSO}_4 \cdot \text{H}_2\text{O}$, CaCO_3 and calcium phosphate in pressure-driving membrane processes [79–82]. The precipitation of inorganics relates to

their speciation and solubility in the matrix.

Calcium sulfate

The most common form of calcium sulfate that precipitates at room temperature is gypsum ($\text{CaSO}_4 \cdot \text{H}_2\text{O}$) [75]. The gypsum is relatively more soluble than calcium carbonate and calcium phosphate. The solubility of gypsum is $3.14 \times 10^{-5} \text{ mol}^2 \text{ L}^{-2}$ [83]. The effect of pH on gypsum solubility is marginal, while the effect of temperature is significant. The maximum solubility is observed around 25°C [84].

Calcium carbonate

Calcium carbonate is a most common alkaline scale formed [75]. Almost all naturally occurring waters contain bicarbonate and are rich in calcium. It is well known that the precipitation of calcium carbonate depends on water temperature and chemistry (e.g. pH, ionic strength) [51]. Nevertheless, for membrane processes operating at room temperature, water pH can be the most important factor. The breakdown of bicarbonate to carbonate occurs at alkaline pH. In these pH conditions, calcium carbonate precipitates owing to that its solubility ($3.3 \times 10^{-9} \text{ mol}^2 \text{ L}^{-2}$ [85]) is much lower than the one of calcium bicarbonate. As shown in Fig. I-1, in the range of pH 6 to 8, the carbonate concentration is negligible in water, while for pH above 8, the concentration of carbonate species becomes significant.

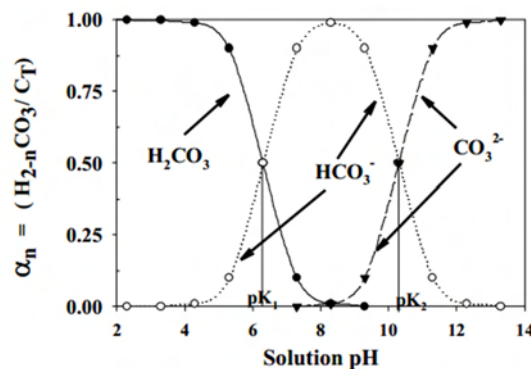


Fig. I-1 Distribution of carbonate species in relation to solution pH [86].

Calcium phosphate

Calcium phosphate scale has become more common in membrane processes due to the tendency to treat wastewaters which are rich in phosphates [87–90]. The solubility of the calcium phosphate highly depends on protonated species of phosphate. The solubility of common phases of calcium phosphate is shown in table I-1. It can be observed that the

phases of calcium hydrogen phosphate and calcium phosphate are the less soluble ones.

Table I-1 Solubility of calcium phosphate at 25°C [91,92]

Phase	Formula	Solubility -log (K _{sp})
Monocalcium phosphate monohydrate	Ca(H ₂ PO ₄) ₂ •H ₂ O	1.14
Monocalcium phosphate anhydrate	Ca(H ₂ PO ₄) ₂	1.14
Dicalcium phosphate dihydrate	CaHPO ₄ •2H ₂ O	6.59
Dicalcium phosphate anhydrate	CaHPO ₄	6.90
Octacalcium phosphate	Ca ₈ (HPO ₄) ₂ (PO ₄) ₄ • 5H ₂ O	96.6
Calcium-deficient	Ca _{10-x} (HPO ₄) _x (PO ₄) _{6-x} (OH) _{2-x}	≈85.1
Hydroxyapatite	Ca ₁₀ (PO ₄) ₆ (OH) ₂	116
α-Tricalcium phosphate	α-Ca ₃ (PO ₄) ₂	25.5
β-Tricalcium phosphate	β-Ca ₃ (PO ₄) ₂	28.9
Amorphous phosphate	Ca _x (PO ₄) _y • nH ₂ O	28.9

The protonated species of phosphate relates to the pH of water. The fraction of phosphate at different pH is presented on Fig. I-2.

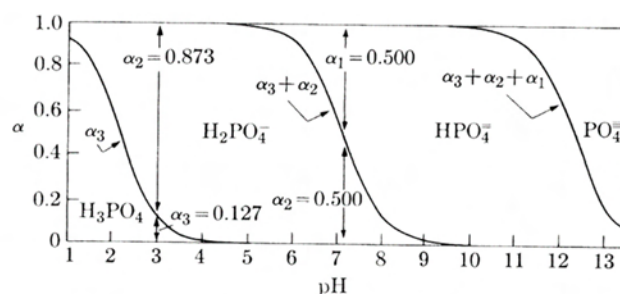


Fig. I-2 Distribution diagram of phosphate species as a function of pH [93].

From the figure, it is clear that H₂PO₄⁻ is the main specie for pH below 7 while HPO₄²⁻ specie prevails for pH between 7 and 10. For pH higher than 12.5, the concentration of PO₄³⁻ specie becomes significant. Consequently, the precipitation of calcium phosphate significantly relates to the water pH due to its solubility strongly dependent on the solution pH.

In conclusion, various types of fouling can occur during NF process and the presence of them declines the permeate flux severely but also shortens the lifetime of membrane. Fouling is influenced by not only the feed water characteristics (such as types of foulants,

pH and ionic composition), but also by the operating conditions (such as the flux, crossflow velocity, and temperature). For certain feed waters, the definition of the appropriate operating conditions to mitigate the effects of fouling is extremely important.

1.2.3 Critical flux and Limiting flux

During NF operation, various types of fouling could occur depending on the feed water characteristics and operating conditions. In a certain feed, the permeate flux is a particularly interesting parameter to control fouling. Increasing flux enhances both the concentration polarization and the rate of foulants deposition due to the increase of hydrodynamic drag force on foulants towards the membrane surface [94]. Foulants interact in a complex way with the membrane surface due to various phenomenon: electrostatic repulsion, van der Waals attraction or hydrophobic/hydrophilic interactions with different interaction lengths [95]. Interactions between foulants and membrane surface can be summarized to be the force (flux) which drags foulants to the membrane surface and interactions between foulants and membrane which repulse them from the surface.

Based on these, the critical flux (J_c) concept was proposed in 1994 [96,97]. Theoretically, the critical flux was defined as the *flux above which an irreversible deposit appears at the membrane surface* [95]. The critical flux is generally a balance between foulants–foulants or foulants–membrane repulsive forces and permeate flux drag forces. Above the critical flux, permeate drag forces overcome repulsive forces which induces the deposit of foulants on the membrane surface. At that time fouling occurs and the permeate flux declines. This can be described in filtration laws through an additional hydraulic resistance.

As an extension of the critical flux concept, the flux exceeding the critical flux tends to a limiting value which is defined as limiting flux (J_L) [98]. It is related to the concept that the higher the flux, the stronger the drag force towards the membrane (and hence deposition of foulants), thus, the concentration polarization will be stronger and the compaction of the deposit will be higher. At high flux, the drag force overcomes repulsive forces and the flux continues to decrease until the hydrodynamic drag force is lower or sufficiently close to the foulant-membrane and/or foulant deposited-foulant interaction forces [98].

The critical and limiting flux has been studied for modeling and experimental analysis with latex particles by Bacchin et al. [99]. Then, Tang and Leckie [100] developed the

conception of critical and limiting flux by studying the flux behaviors for RO and NF membranes fouled by humic acid. They proposed that the critical flux is membrane dependent while the limiting flux is membrane independent. The limiting flux is considered to be achieved at steady state in a certain feed water composition.

According to these authors [100], the critical flux J_C can be considered as the triggering flux for the initial deposition of foulants, and its value shall be governed by the foulant-membrane interaction, $F_{\text{barrier}}^{\text{f-m}}$; when the limiting flux is reached, further foulants deposition is determined by the foulants-deposited foulants interaction, $F_{\text{barrier}}^{\text{f-f}}$.

Based on relative magnitudes of $F_{\text{barrier}}^{\text{f-m}}$ and $F_{\text{barrier}}^{\text{f-f}}$, three types of conceptual behaviors of limiting and critical fluxes might be expected as described in Fig. I-3 [100].

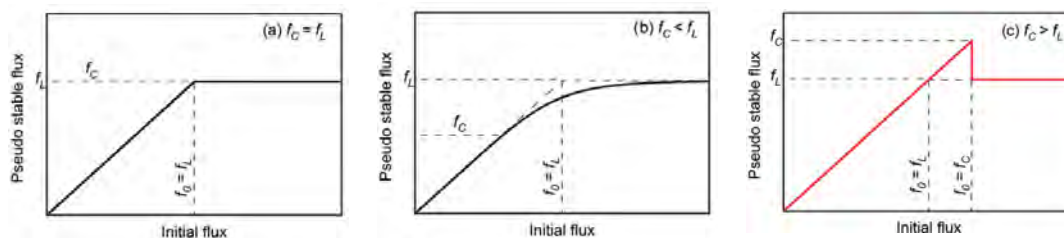


Fig. I-3 Conceptual flux behaviors when (a) the limiting flux is identical to the critical flux; (b) the limiting flux is greater than the theoretical flux; (c) the limiting flux is less than the critical flux [100].

(a) $J_C = J_L$, the pseudo stable flux versus initial flux plot completely corresponds to the magnitude of the limiting flux; when the initial flux J_0 is lower than the limiting and /or critical flux, there is no flux reduction;

(b) $J_C < J_L$ when $F_{\text{barrier}}^{\text{f-m}}$ is less repulsive than $F_{\text{barrier}}^{\text{f-f}}$, the foulants deposition and flux reduction start to occur once the critical flux is exceeded, as depicted by the transitional region between J_C and J_L ;

(c) $J_C > J_L$, this last behavior is a special case, no flux reduction will occur as long as the initial flux is below the critical flux, even if the limiting flux is exceeded. Such case is highly unstable. Soon after a small patch of foulants is deposited on the membrane surface, the interaction force is switched to foulants-deposited-foulants interaction locally, which enables the initial patch of foulants to serve as a “nuclei site” for further foulants deposition.

Series of NF and RO semi-aromatic and fully-aromatic polyamine membranes were tested [100] and belong to the type a and b. Type c has never been observed by these authors.

The knowledge of the critical flux is particularly important in membrane processes to mitigate the effect of fouling and even to avoid it. An experimental procedure to determine

critical flux: “the square wave filtration method” has been developed by Espinasse et al. [95,101]. The principle of this technique will be introduced in chapter II.

1.2.4 Factors affecting the rejection of pharmaceuticals during NF treatment

Several studies investigated the rejection capacities of nanofiltration membranes towards pharmaceuticals. The rejection of pharmaceuticals is greatly influenced by characteristics of compounds besides molecular structure, electrokinetic properties such as pKa, physicochemical properties (polarity and hydrophobicity) [51]. As a consequence, separation is considered to be accomplished via size exclusion, charge repulsion and hydrophobic interaction [51]. The mechanisms of pharmaceuticals rejection are then complex and not well understood.

Size exclusion

Sieving effect is mainly determined by the size of the solute relatively to the size of membranes pores: solutes larger than the pore size of the membrane are retained. However, in nanofiltration process, neither pores nor pharmaceuticals have a uniform size. Moreover, their size during filtration can be modified due to water matrix properties. Previous studies reported that pH, ionic strength of the matrix can impact the molecular weight cut-off (MWCO) of the membrane due to electrostatic interactions within membrane pores [72,102–105]. The relatively alkaline pH can promote the dissociation of functional groups; then increasing electrostatic repulsions in the pore enlarge their size [102–104]. Low ionic strength also leads to larger pore size [105]. On the other hand, pharmaceutical solutes are not easily represented by equivalent spheres. It seems that pharmaceuticals rejection correlates with different compound size parameters, such as the molecular weight, molecular volume, equivalent width or molecular length [52,53].

Charge interactions

Charge interactions can be related to pH directly. Some trace organics exhibit amphoteric properties, meaning that they can carry a negative or a positive charge depending on the pH. The pH value of the feed solution can also affect characteristics of the membrane [103]. Subsequently, electrostatic interactions between compounds and the membrane surface can vary according to characteristics of the solution and then affect

rejection. Some model studies about charge interactions are reported. Wang et al. have proposed a model to describe charge interactions named electrostatic and space-charge model by combining the space-charge and steric-hindrance pore physical phenomena [106].

Hydrophobic interactions

Organics can be adsorbed to the membrane surface due to high log P or hydrogen bonding capacity that contributes to the membrane rejection. Zhang et al. [107] showed high rejection (>90%) of BPA at the beginning of the filtration due to adsorption onto the membrane structure and a decrease of the observed rejection to around 50% when the adsorption sites on the membrane became saturated. The hydrophobic/hydrophilic attraction or repulsion also plays an important role in the pharmaceuticals rejection [73,108,109].

The effect of fouling

In the application of NF process, the impact of matrix and fouling is significant on the pharmaceuticals rejection. Some studies focused on the influence of NF membrane fouling on the pharmaceuticals rejection [52,54,59,60]. The influence of fouling can be various. The difference in rejections of pharmaceuticals by clean and fouled membrane is based on the modification of membrane surface properties by fouling layer such as charge, hydrophobicity or adsorption capacity of pharmaceuticals. Yangali-Quintanilla et al. [52] investigated rejections of endocrine disruptors by clean and fouled nanofiltration membranes. Fouling with sodium alginate affected the selectivity of the NF-200 membrane by decreasing the rejection of hydrophilic neutral compounds as well as hydrophilic and hydrophobic ionic compounds. In contrast, rejections of hydrophobic neutral compounds by the fouled membrane increased by 5 to 38% depending on compounds. Verliefe et al. [59] evaluated the influence of different membrane fouling types on the rejection of pharmaceuticals. Various rejections of pharmaceuticals with different types of fouled membranes were attributed to the change of membrane surface hydrophobicity due to fouling but also to the modification of size exclusion and charge effect. Botton et al. [60] demonstrated the biomass attachment and growth on the membrane surface lead to a slight modification of surface charge and hydrophobicity comparing to the clean membrane. As a consequence, the presence of the negatively charged biofilm induced accumulation of positively charged pharmaceuticals within the biomass layer, which probably also hindered back diffusion. These effects caused a reduction in the rejection efficiency of positively

charged solutes while no variation was observed for neutral and negatively charged pharmaceuticals.

In conclusion, the productivity/permeate flux and the selectivity/rejection of pharmaceuticals during NF operation in real matrix depend on numerous factors, the combined effect of which is not obvious to anticipate.

Thus, in the present work, specific interest is focus on the improvement of productivity (to reduce or avoid the effect of fouling) and pharmaceuticals rejection in an MBR effluent matrix.

I.3 Electrochemical oxidation

Electrochemical oxidation is a physico-chemical technique convenient for the treatment of industrial effluents containing organics. Electrochemical techniques which allow reducing the quantity of organic pollutants in solution are: i) separation by electroflocculation, ii) oxidation by the electrogenerated Fenton's reagent, iii) direct oxidation on a suitable anode material. Electrochemical oxidation of organic compounds can be fully achieved under conditions for which transfer of oxygen atoms is efficient. It is generally assumed that hydroxyl radicals resulting from the water discharge are particularly active to carry out oxygen atoms transfer, as described in the reaction Eq.IV-11, below:



The strong activity of these radicals in aqueous solution results from the high value of their standard potential $E_0 = 2.74 \text{ V / SHE}$ [110]. Organic molecules are degraded into smaller molecules by a succession of oxygen atom transfers until complete destruction of the carbon skeleton. A crucial point to operate mineralization is the choice of the anodic material; this one should have a high oxygen overvoltage to allow the production of $\cdot OH$ radicals by water discharge while preventing oxygen evolution. Some metal oxides such as SnO_2 , PbO_2 , WO_3 have electrocatalytic properties required for this application but since about twenty years the boron doped diamond (BDD) has been successfully used on the laboratory scale in reason of its electrochemical properties.

I.3.1 BDD anode

The first extensive study of the use of diamond electrodes in electrochemistry was performed by Pleskov et al. in 1987 [111]. Since then, synthetic BDD thin films have been applied in a number of applications due to their outstanding properties, which are remarkably different from those of other conventional electrodes, e.g., glassy carbon or platinum. In the 90's, Fujishima and his group began to study the photo-electrochemical properties of boron doped diamond electrodes [112]. In 1993, Tenne et al [110] studied the removal of nitrates with BDD electrode. After that the number of publications on BDD electrode increases exponentially from 1994 [43]. Indeed, BDD exhibits properties that distinguish it from conventional electrodes. Compared to graphite or glassy carbon electrodes, diamond electrodes have a good resistance towards corrosive conditions and resistance to fouling (deactivation). Furthermore, diamond thin films exhibit a very large potential window with respect to hydrogen / oxygen evolution, extending to almost 4 V, and a low background current. Compared to Pt electrodes, the potential window of BDD is about 2 V larger. High anodic stability of BDD in acid medium and high overpotential for oxygen evolution allow producing powerful oxidants of high redox potential.

Boron-doped diamond films, Diachem®, used in this study were synthesized by the hot filament chemical vapor deposition technique (HF CVD) on conducting p-Si substrate (0.1 Ωcm, Siltronix). The filament temperature ranged from 2440 to 2560°C and the substrate was kept at 830°C. The reactive gas used was methane in an excess of dihydrogen (1% CH₄ in H₂). The doping gas was trimethylboron at a concentration of 3 ppm. The gas mixture was supplied to the reaction chamber, providing a 0.24 μm h⁻¹ growth rate for the diamond layer. Diamond films were about 1 μm thick. This HF CVD process produces columnar, randomly textured, polycrystalline films.

I.3.2 Hydroxyl radicals

It is commonly assumed that electrogenerated hydroxyl radicals, the most powerful oxidants in water, are very active in the degradation of organic molecules. In the particular case of BDD, because of the weak interaction between its surface and hydroxyl radicals, •OH can be considered as quasi free [113]. Briefly, the main reaction pathways of •OH in the reaction with organic compounds occurs in C-C, C-N and C-S double bonds and H-abstraction [114]. Since most organic compounds reveal structural moieties which allow addition and H-abstraction, •OH react fast with a large variety of compounds (i.e., kinetic constant > 10⁹ M⁻¹ s⁻¹) [115].

Although kinetics of most $\bullet\text{OH}$ addition reactions are close to diffusion controlled [116], different kinetics were observed in the mixture solution containing two compounds which have different reactivity with $\bullet\text{OH}$ [117]. Groenen Serrano et al. [117] observed and modeled the phenomenon in the case of a solution containing maleic acid and formic acid, and showed that the formic acid oxidation only began when the maleic acid had completely disappeared.

Kapałka et al [118] investigated an oxidation mechanism between organics and electrogenerated hydroxyl radicals for the mineralization of acetic acid. It was reported that the reaction allows the formation of organic radicals via dehydrogenation reactions, and then the addition of molecular oxygen to an organic free radical results in the formation of an organic peroxy radical [119]. Peroxy radicals are very reactive and can initiate subsequent chain reactions which can lead and involve the degradation of other organics in the solution, via several possible intermediates, to completely mineralization. The proposed procedure is shown on Fig.I-4 [118].

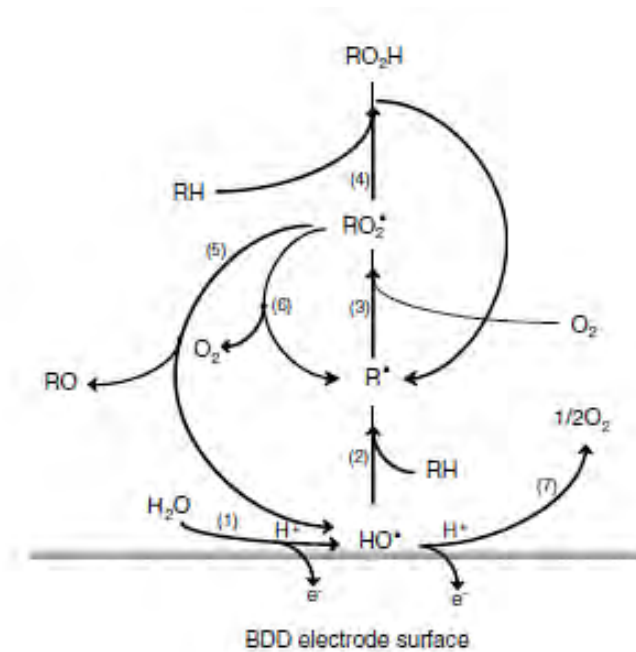


Fig.I-4 Simplified diagram for electrochemically induced oxidation of organic compounds via molecular oxygen dissolved in aerated solution on boron-doped diamond electrode; (1) water discharge to hydroxyl radical $\bullet\text{OH}$; (2) dehydrogenation of organic compound RH via $\bullet\text{OH}$ and formation of free organic radical $\text{R}\bullet$; (3) addition of molecular oxygen to R resulting in the formation of an organic peroxy radical $\text{RO}_2\bullet$; (4) dehydrogenation of RH via $\text{RO}_2\bullet$ resulting in the formation of hydroperoxide ROOH and regeneration of $\text{R}\bullet$; (5) decomposition of $\text{RO}_2\bullet$ leading to the regeneration of $\bullet\text{OH}$ and formation of RO ; (6) decomposition of $\text{RO}_2\bullet$ to $\text{R}\bullet$; (7) oxygen evolution, a side reaction [118].

Moreover, in the presence of salts, the $\bullet\text{OH}$ can react with these inorganic compounds (Cl^- , SO_4^{2-} , CO_3^{2-}) to electrogenerate strong oxidants such as peroxy, oxo compounds, ozone, and chlorine species [120,121]. The electrogeneration of strong oxidants including the inorganic oxidants has been summarized by Groenen Serrano [122]. The presence of these strong oxidants can influence the organic removal.

I.3.3 Theoretical model for oxidation of organic compounds on BDD

Thanks to the properties of BDD, the radicals $\bullet\text{OH}$, which are free at the surface, react very fast with organics. The general pathway can be written as follow:
the global rate of oxygen transfer depends on (i) the mass transfer rate to the electrode surface and (ii) intermediate compounds which are generated and their reactivity with hydroxyl radicals.

For electrochemical processes two different kinetic regimes can be defined depending on the value of the current density for a given reactant concentration.

- (i) If the applied current density is lower than the corresponding limiting current density: the electrolysis is under charge transfer control, the current efficiency is then 100%.
- (ii) If the applied current density is higher than its limiting value, the electrolysis is under mass transport control; secondary reactions (such as oxygen evolution) occur.

During electrolyses, concentrations of organics or intermediate species are unknown, so based on properties of BDD anode, a limiting current density can be defined by using a global parameter, the Chemical Oxygen Demand (COD) [123].

$$i_{\text{lim}} = 4Fk_d\text{COD} \quad (\text{Eq.I-12})$$

Where i_{lim} is the limiting current density for organics mineralization (A m^{-2}), F is the Faraday constant (C mol^{-1}) and COD is in $\text{molO}_2 \text{ m}^{-3}$.

The oxidation of organics can be considered to be carried out on the system presented in Figure I-5.

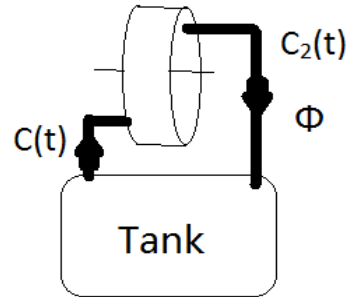


Fig.I-5 The diagram of recirculation electrochemical reactor system, $C(t)$ is the concentration into the reactor and $C_2(t)$ is the concentration out of the reactor, both of them in mol s^{-1}

The model which gives the COD variation during galvanostatic electrolysis is based on the following assumptions:

- volume of solution is constant during the electrolysis,
- reservoir volume (1L) is much greater than that of the electrochemical reactor (63 mL),
- flow is large enough to ensure that the concentration is the same in all the volume of the tank,
- adsorption of organics at the electrode surface is negligible.

The mass balance in the reactor can be written as Eq.I-13

$$rA = -\Phi(C_2(t) - C(t)) \quad (\text{Eq.I-13})$$

where, r is the specific electrochemical reaction rate in $\text{mol m}^{-2} \text{s}^{-1}$, Φ is the flow rate in $\text{m}^3 \text{s}^{-1}$. This reaction rate is simply associated to the applied current density and the current efficiency is 100%, but not all of the current is necessarily used to oxidize the organic compound. This rate depends on the kinetic regime; its expression will be developed further.

On the tank side, the mass balance can be written as:

$$V \frac{dC(t)}{dt} = \Phi(C_2(t) - C(t)) \quad (\text{Eq.I-14})$$

where, V is the volume of the solution in m^3 .

Combining Eq.I-13 and Eq.I-14,

$$V \frac{dC(t)}{dt} = -rA \quad (\text{Eq.I-15})$$

Then, Eq.I-15 can be expressed as a function of COD values to obtain Eq.I-16

$$V \frac{dC(t)}{dt} = \Phi (COD_2(t) - COD(t)) = -r_{COD}A \quad (\text{Eq.I-16})$$

where, r_{COD} is the reaction rate of COD.

The applied current density can be higher or lower than the limiting current and the oxidation of organics is in different kinetic regimes: charge or mass transfer controlled.

α is defined as the ratio of applied current density and the initial limiting current density. Under galvanostatic conditions, α is constant

$$\alpha = \frac{i}{i_{lim}^0} \quad (\text{Eq.I-17})$$

- $i < i_{lim}$

The oxidation is charge controlled and all the current is used to oxidize organics. The reaction rate of COD can be written as:

$$r_{COD} = \frac{i}{4F} \quad (\text{Eq.I-18})$$

Combining Eq.I-16 and Eq.I-18, the equation I-19 can be obtained:

$$V \frac{dCOD(t)}{dt} = -\frac{i}{4F} A \quad (\text{Eq.I-19})$$

Integrating this equation subject to the initial condition $COD = COD_0$ and $t = 0$ gives the evolution of COD with time in the operating regime $i < i_{lim}$.

$$COD(t) = COD^0 \left(1 - \alpha \frac{t}{\tau} \right) \quad (\text{Eq.I-20})$$

This behavior persists until a critical time (t_{cr}). At this time the applied current density is equal to the limiting current density, which corresponds to:

$$COD_{cr} = \alpha COD^0 \quad (\text{Eq.I-21})$$

Then the critical time can be obtained as Eq.I-22.

$$t_{cr} = \left(\frac{1-\alpha}{\alpha} \right) \frac{V}{Ak_d} \quad (\text{Eq.I-22})$$

- $i > i_{lim}$

The oxidation is controlled by mass transfer to the electrode surface; the oxidation rate of COD is not related to the current.

$$V \frac{dCOD(t)}{dt} = -k_d A \quad (\text{Eq.I-23})$$

Integrating this equation subject to the initial condition $COD = COD_0$ and $t = 0$ gives the evolution of COD with time in the operating regime $i > i_{lim}$.

$$COD(t) = COD^0 \exp\left(-\frac{Ak_d t}{V}\right) \quad (\text{Eq.I-24})$$

1.3.4 Long-term sustainability of electrochemical oxidation treatment

Considering the application of EO process for wastewater treatment, the long-term sustainability should be taken into account.

The minimization of toxic intermediates from the degradation of pharmaceuticals should be considered to select appropriate operating conditions. A typical example showed that phenol oxidation under appropriate conditions of current intensity can control the formation of aromatic intermediates and reach mineralization efficiently [124].

In the wastewater, more attentions should be taken for the effects of the presence of organic matters and inorganic ions on the pharmaceuticals degradation and formation of by-products. The production of organohalogenes were reported during the electrochemical oxidation of reverse osmosis concentrate from the study by Perez et al [49]. The concentration of organhalogenes seems to increase with the electrooxidation time [125] and electric charge [126]. Moreover the formation of undesired perchlorate (ClO_4^-) during electrochemical oxidation also has been linked to health risks [127,128].

The energy consumption has to be considered in parallel; the complete mineralization is not necessary for an economically viable tertiary treatment.

I.4 Main problem need to be addressed during the research

Considering that, in a membrane filtration process, the permeate flux is of particular interest to control fouling, thus, critical and limiting fluxes have been studied by numerous authors for conceptual and experimental analysis in synthetic solutions [95,100]. The key interest is to implement developed procedures, “the square wave filtration method” in the case of the filtration of a real wastewater and obtain information’s in this complex matrix considering the maximum process productivity and selectivity we can expect. This objective can be reached through prediction and possible control of fouling from the flux behaviors as a function of the water matrix properties such as pH, organic and salt concentrations. This question will be addressed in sections III-A and III-B.

The rejection of pharmaceuticals directly influences the quality of treated water. Pharmaceuticals rejections by NF membrane can be influenced by molecular exclusion, electrostatic repulsion or hydrophobic interaction between the membrane and solutes [51]. The combination of these mechanisms is complex and not well understood mainly due to the specific properties of pharmaceutical molecules. On the other hand, several studies focus on the impact of membrane fouling on the pharmaceuticals rejection [52,54,59,60] with membranes fouled by certain matrix such as lake water, which can lead to the question whether the fouling composition and water matrix can affect the pharmaceutical rejection. This part will be discussed in section III-C.

Electrochemical oxidation using BDD anode exhibits excellent performance for elimination of micro pollutants [43,46,47], even in wastewater matrix [49,50]. However, the risk of formation of toxic by-products is exposed and becomes a critical factor to apply electrochemical process. The challenge of electrochemical oxidation application is to consider both economic and environmental perspectives. To solve these questions, the strategy proposed is to study first the process using a synthetic solution to simplify the number of parameters and identify how operating conditions impact the mineralization efficiency. In a second step, it will be possible to study the influence of common organics, salts and other pharmaceuticals in a complex matrix on the degradation of specific pharmaceuticals; and go further in the identification of mechanisms and impacting factors on the formation of by-product, especially formation of organochlorine from chlorine ions.

These studies will be helpful to select appropriate operating conditions to improve the process efficiency and control the formation of toxic by-products, simultaneously.

Theoretical model allows an excellent prediction of COD decay in synthetic solution [123] and wastewater matrix [129]. Considering the target of the study to propose an economically viable process for wastewater treatment, more focus should be taken on the degradation of pharmaceuticals with electrooxidation time. Due to the properties of BDD which allows the electrogeneration of oxygen species, electroactive pharmaceuticals can be oxidized both by direct electron exchange and via \bullet OH oxidation. The theoretical model for oxidation of organics by electron exchange could be limited to predict the variation of pharmaceuticals concentration in the electrooxidation process using BDD. Existing model will be then changed in this direction in chapter IV.

Regarding to previous studies, the evaluation of the efficiency of a treatment process mainly focused on the concentration of pharmaceuticals in effluent and influent, while a study which determines the removal of pharmaceuticals and related toxicity could be more appropriate to address the process efficiency in term of removal with environmental perspective.

Moreover, nanofiltration and electrochemical oxidation are usually studied as two processes, even if they are applied in coupling. How to select appropriate operating conditions in each process to obtain the mutual promotion in the coupling process could be an interesting question and is addressed in chapter V.

References

- [1] E. Zuccato, D. Calamari, M. Natangelo, R. Fanelli, Presence of therapeutic drugs in the environment, *The Lancet*. 355 (2000) 1789–1790.
- [2] J. Zhou, H. Hong, Z. Zhang, K. Maskaoui, W. Chen, Multi-phase distribution of organic micropollutants in Xiamen Harbour, China, *Water Res.* 34 (2000) 2132–2150.
- [3] D.W. Kolpin, E.T. Furlong, M.T. Meyer, E.M. Thurman, S.D. Zaugg, L.B. Barber, et al., Pharmaceuticals, Hormones, and Other Organic Wastewater Contaminants in U.S. Streams, 1999–2000: A National Reconnaissance, *Environ. Sci. Technol.* 36 (2002) 1202–1211.
- [4] X. Chang, M.T. Meyer, X. Liu, Q. Zhao, H. Chen, J. Chen, et al., Determination of antibiotics in sewage from hospitals, nursery and slaughter house, wastewater treatment plant and source water in Chongqing region of Three Gorge Reservoir in China, *Environ. Pollut.* 158 (2010) 1444–1450.
- [5] A.J. Watkinson, E.J. Murby, D.W. Kolpin, S.D. Costanzo, The occurrence of antibiotics in an urban watershed: From wastewater to drinking water, *Sci. Total Environ.* 407 (2009) 2711–2723.
- [6] K.S. Le Corre, C. Ort, D. Kateley, B. Allen, B.I. Escher, J. Keller, Consumption-based approach for assessing the contribution of hospitals towards the load of pharmaceutical residues in municipal wastewater, *Environ. Int.* 45 (2012) 99–111.
- [7] S. Mompelat, O. Thomas, B.L. Bot, Contamination levels of human pharmaceutical compounds in French surface and drinking water, *J. Environ. Monit.* 13 (2011) 2929–2939.
- [8] T. Heberer, Tracking persistent pharmaceutical residues from municipal sewage to drinking water, *J. Hydrol.* 266 (2002) 175–189.
- [9] S. González Alonso, Y. Valcárcel, J.C. Montero, M. Catalá, Nicotine occurrence in bottled mineral water: Analysis of 10 brands of water in Spain, *Sci. Total Environ.* 416 (2012) 527–531.
- [10] G.M. Bruce, R.C. Pleus, S.A. Snyder, Toxicological Relevance of Pharmaceuticals in Drinking Water, *Environ. Sci. Technol.* 44 (2010) 5619–5626.
- [11] A.C. Johnson, M.D. Jürgens, R.J. Williams, K. Kümmerer, A. Kortenkamp, J.P. Sumpter, Do cytotoxic chemotherapy drugs discharged into rivers pose a risk to the environment and human health? An overview and UK case study, *J. Hydrol.* 348 (2008) 167–175.
- [12] K. Kümmerer, A. Al-Ahmad, Estimation of the cancer risk to humans resulting from the presence of cyclophosphamide and ifosfamide in surface water, *Environ. Sci. Pollut. Res.* 17 (2010) 486–496.
- [13] G.T. Ankley, B.W. Brooks, D.B. Huggett, and J.P. Sumpter, Repeating History: Pharmaceuticals in the Environment, *Environ. Sci. Technol.* 41 (2007) 8211–8217.
- [14] K. Kümmerer, Significance of antibiotics in the environment, *J. Antimicrob.*

- Chemother. 52 (2003) 5–7.
- [15] T.J. Runnalls, L. Margiotta-Casaluci, S. Kugathas, J.P. Sumpter, Pharmaceuticals in the Aquatic Environment: Steroids and Anti-Steroids as High Priorities for Research, *Hum. Ecol. Risk Assess. Int. J.* 16 (2010) 1318–1338.
- [16] S. Rodriguez-Mozaz, S. Chamorro, E. Marti, B. Huerta, M. Gros, A. Sánchez-Melsió, et al., Occurrence of antibiotics and antibiotic resistance genes in hospital and urban wastewaters and their impact on the receiving river, *Water Res.* 69 (2015) 234–242.
- [17] B.I. Escher, R. Baumgartner, M. Koller, K. Treyer, J. Lienert, C.S. McArdell, Environmental toxicology and risk assessment of pharmaceuticals from hospital wastewater, *Water Res.* 45 (2011) 75–92.
- [18] M. Clara, N. Kreuzinger, B. Strenn, O. Gans, H. Kroiss, The solids retention time—a suitable design parameter to evaluate the capacity of wastewater treatment plants to remove micropollutants, *Water Res.* 39 (2005) 97–106.
- [19] A.L. Batt, I.B. Bruce, D.S. Aga, Evaluating the vulnerability of surface waters to antibiotic contamination from varying wastewater treatment plant discharges, *Environ. Pollut.* 142 (2006) 295–302.
- [20] I.J. Buerge, H.-R. Buser, T. Poiger, M.D. Müller, Occurrence and Fate of the Cytostatic Drugs Cyclophosphamide and Ifosfamide in Wastewater and Surface Waters†, *Environ. Sci. Technol.* 40 (2006) 7242–7250.
- [21] K. Kümmerer, A. Al-Ahmad, V. Mersch-Sundermann, Biodegradability of some antibiotics, elimination of the genotoxicity and affection of wastewater bacteria in a simple test, *Chemosphere.* 40 (2000) 701–710.
- [22] S. Judd, The status of membrane bioreactor technology, *Trends Biotechnol.* 26 (2008) 109–116.
- [23] B. Pauwels, F.F. Ngwa, S. Deconinck, W. Verstraete, Effluent Quality of a Conventional Activated Sludge and a Membrane Bioreactor System Treating Hospital Wastewater, *Environ. Technol.* 27 (2006) 395–402.
- [24] L. Kovalova, H. Siegrist, H. Singer, A. Wittmer, C.S. McArdell, Hospital Wastewater Treatment by Membrane Bioreactor: Performance and Efficiency for Organic Micropollutant Elimination, *Environ. Sci. Technol.* 46 (2012) 1536–1545.
- [25] I. Quesada, Y. Gonzalez, S. Schetrite, H. Budzinski, K. Le Menach, O. Lorain, et al., PANACÉE : évaluation du fonctionnement d’un bioréacteur à membranes immergées traitant des effluents hospitaliers d’oncologie, *Rev. Sci. Eau.* 28 (2015) 1.
- [26] J.E. Drewes, C. Bellona, M. Oedekoven, P. Xu, T.-U. Kim, G. Amy, Rejection of wastewater-derived micropollutants in high-pressure membrane applications leading to indirect potable reuse, *Environ. Prog.* 24 (2005) 400–409. doi:10.1002/ep.10110.
- [27] K. Kimura, S. Toshima, G. Amy, Y. Watanabe, Rejection of neutral endocrine disrupting compounds (EDCs) and pharmaceutical active compounds (PhACs) by RO membranes, *J. Membr. Sci.* 245 (2004) 71–78.
- [28] A. Verliefde, E. Cornelissen, G. Amy, B. Van der Bruggen, H. van Dijk, Priority organic micropollutants in water sources in Flanders and the Netherlands and

- assessment of removal possibilities with nanofiltration, *Environ. Pollut.* 146 (2007) 281–289.
- [29] J. Radjenovic, M. Petrovic, F. Ventura, D. Barcelo, Rejection of pharmaceuticals in nanofiltration and reverse osmosis membrane drinking water treatment, *Water Res.* 42 (2008) 3601–3610.
- [30] B. Van der Bruggen, J. Schaep, W. Maes, D. Wilms, C. Vandecasteele, Nanofiltration as a treatment method for the removal of pesticides from ground waters, *Desalination.* 117 (1998) 139–147.
- [31] Y. Kiso, Y. Sugiura, T. Kitao, K. Nishimura, Effects of hydrophobicity and molecular size on rejection of aromatic pesticides with nanofiltration membranes, *J. Membr. Sci.* 192 (2001) 1–10.
- [32] E. Dialynas, E. Diamadopoulou, Integration of a membrane bioreactor coupled with reverse osmosis for advanced treatment of municipal wastewater, *Desalination.* 238 (2009) 302–311.
- [33] J.-J. Qin, K.A. Kekre, G. Tao, M.H. Oo, M.N. Wai, T.C. Lee, et al., New option of MBR-RO process for production of NEWater from domestic sewage, *J. Membr. Sci.* 272 (2006) 70–77.
- [34] L.S. Tam, T.W. Tang, G.N. Lau, K.R. Sharma, G.H. Chen, A pilot study for wastewater reclamation and reuse with MBR/RO and MF/RO systems, *Desalination.* 202 (2007) 106–113.
- [35] A.M. Comerton, R.C. Andrews, D.M. Bagley, Evaluation of an MBR–RO system to produce high quality reuse water: Microbial control, DBP formation and nitrate, *Water Res.* 39 (2005) 3982–3990.
- [36] M. Jacob, C. Guigui, C. Cabassud, H. Darras, G. Lavison, L. Moulin, Performances of RO and NF processes for wastewater reuse: Tertiary treatment after a conventional activated sludge or a membrane bioreactor, *Desalination.* 250 (2010) 833–839.
- [37] A.A. Alturki, N. Tadkaew, J.A. McDonald, S.J. Khan, W.E. Price, L.D. Nghiem, Combining MBR and NF/RO membrane filtration for the removal of trace organics in indirect potable water reuse applications, *J. Membr. Sci.* 365 (2010) 206–215.
- [38] G. Mezohegyi, B. Erjavec, R. Kaplan, A. Pintar, Removal of Bisphenol A and its Oxidation Products from Aqueous Solutions by Sequential Catalytic Wet Air Oxidation and Biodegradation, *Ind. Eng. Chem. Res.* 52 (2013) 9301–9307.
- [39] J. Choi, H. Lee, Y. Choi, S. Kim, S. Lee, S. Lee, et al., Heterogeneous photocatalytic treatment of pharmaceutical micropollutants: Effects of wastewater effluent matrix and catalyst modifications, *Appl. Catal. B Environ.* 147 (2014) 8–16.
- [40] A.M. Polcaro, S. Palmas, Electrochemical Oxidation of Chlorophenols, *Ind. Eng. Chem. Res.* 36 (1997) 1791–1798.
- [41] M.S. Yahya, N. Oturan, K. El Kacemi, M. El Karbane, C.T. Aravindakumar, M.A. Oturan, Oxidative degradation study on antimicrobial agent ciprofloxacin by electro-fenton process: Kinetics and oxidation products, *Chemosphere.* 117 (2014) 447–454.
- [42] A.M. Polcaro, S. Palmas, F. Renoldi, M. Mascia, On the performance of Ti/SnO₂ and Ti/PbO₂ anodes in electrochemical degradation of 2-chlorophenol for wastewater

- treatment, *J. Appl. Electrochem.* 29 (1999) 147–151.
- [43] A. Kraft, Doped diamond: A compact review on a new, versatile electrode material, *Int. J. Electrochem. Sci.* 2 (2007) 355–385.
- [44] E. Hmani, Y. Samet, R. Abdelhedi, Electrochemical degradation of auramine-O dye at boron-doped diamond and lead dioxide electrodes, *Diam. Relat. Mater.* 30 (2012) 1–8.
- [45] C. Flox, C. Arias, E. Brillas, A. Savall, K. Groenen-Serrano, Electrochemical incineration of cresols: A comparative study between PbO₂ and boron-doped diamond anodes, *Chemosphere.* 74 (2009) 1340–1347.
- [46] M. Panizza, P.A. Michaud, G. Cerisola, C. Comninellis, Anodic oxidation of 2-naphthol at boron-doped diamond electrodes, *J. Electroanal. Chem.* 507 (2001) 206–214.
- [47] E. Weiss, K. Groenen-Serrano, A. Savall, A comparison of electrochemical degradation of phenol on boron doped diamond and lead dioxide anodes, *J. Appl. Electrochem.* 38 (2007) 329–337.
- [48] Y. Samet, L. Agengui, R. Abdelhedi, Electrochemical degradation of chlorpyrifos pesticide in aqueous solutions by anodic oxidation at boron-doped diamond electrodes, *Chem. Eng. J.* 161 (2010) 167–172.
- [49] G. Perez, A.R. Fernandez-Alba, A.M. Urriaga, I. Ortiz, Electro-oxidation of reverse osmosis concentrates generated in tertiary water treatment, *Water Res.* 44 (2010) 2763–2772.
- [50] A.M. Urriaga, G. Pérez, R. Ibáñez, I. Ortiz, Removal of pharmaceuticals from a WWTP secondary effluent by ultrafiltration/reverse osmosis followed by electrochemical oxidation of the RO concentrate, *Desalination.* 331 (2013) 26–34.
- [51] A.I. Schafer, A.G. Fane, T.D. Waite, *Nanofiltration-Principles and Application*, Elsevier Advance Technology, 2005.
- [52] V. Yangali-Quintanilla, A. Sadmani, M. McConville, M. Kennedy, G. Amy, Rejection of pharmaceutically active compounds and endocrine disrupting compounds by clean and fouled nanofiltration membranes, *Water Res.* 43 (2009) 2349–2362.
- [53] A.M. Comerton, R.C. Andrews, D.M. Bagley, C. Hao, The rejection of endocrine disrupting and pharmaceutically active compounds by NF and RO membranes as a function of compound a water matrix properties, *J. Membr. Sci.* 313 (2008) 323–335.
- [54] A.M. Comerton, R.C. Andyews, D.M. Bagley, The influence of natural organic matter and cations on the rejection of endocrine disrupting and pharmaceutically active compounds by nanofiltration, *Water Res.* 43 (2009) 613–622.
- [55] G. Foley, *Membrane Filtration: A Problem Solving Approach with MATLAB*, Cambridge University Press, 2013.
- [56] Y. Pouliot, V. Conway, P.-L. Leclerc, Separation and Concentration Technologies in Food Processing, in: S. Clark, S. Jung, B. Lamsal (Eds.), *Food Process.*, John Wiley & Sons, Ltd, 2014: pp. 33–60.

- [57] Z.F. Cui, H.S. Muralidhara, *Membrane Technology: A Practical Guide to Membrane Technology and Applications in Food and Bioprocessing*, Elsevier, 2010.
- [58] W.J. Koros, Y.H. Ma, T. Shimidzu, Terminology for membranes and membrane processes (IUPAC Recommendations 1996), *Pure Appl. Chem.* 68 (2009) 1479–1489.
- [59] A.R.D. Verliefde, E.R. Cornelissen, S.G.J. Heijman, I. Petrinic, T. Luxbacher, G.L. Amy, et al., Influence of membrane fouling by (pretreated) surface water on rejection of pharmaceutically active compounds (PhACs) by nanofiltration membranes, *J. Membr. Sci.* 330 (2009) 90–103.
- [60] S. Botton, A.R.D. Verliefde, N.T. Quach, E.R. Cornelissen, Influence of biofouling on pharmaceuticals rejection in NF membrane filtration, *Water Res.* 46 (2012) 5848–5860.
- [61] T.K. Sherwood, P.L.T. Brian, R.E. Fisher, L. Dresner, Salt Concentration at Phase Boundaries in Desalination by Reverse Osmosis, *Ind. Eng. Chem. Fundam.* 4 (1965) 113–118.
- [62] M. Mänttari, M. Nyström, Critical flux in NF of high molar mass polysaccharides and effluents from the paper industry, *J. Membr. Sci.* 170 (2000) 257–273.
- [63] S. Sablani, M. Goosen, R. Al-Belushi, M. Wilf, Concentration polarization in ultrafiltration and reverse osmosis: a critical review, *Desalination.* 141 (2001) 269–289.
- [64] A. Staff, *Microfiltration and Ultrafiltration Membranes for Drinking Water (M53)*, American Water Works Association, 2011.
- [65] X. Wei, Z. Wang, F. Fan, J. Wang, S. Wang, Advanced treatment of a complex pharmaceutical wastewater by nanofiltration: Membrane foulant identification and cleaning, *Desalination.* 251 (2010) 167–175.
- [66] A.L. Zydney, Stagnant film model for concentration polarization in membrane systems, *J. Membr. Sci.* 130 (1997) 275–281.
- [67] E.M.V. Hoek, M. Elimelech, Cake-Enhanced Concentration Polarization: A New Fouling Mechanism for Salt-Rejecting Membranes, *Environ. Sci. Technol.* 37 (2003) 5581–5588.
- [68] Q. Li, M. Elimelech, Organic Fouling and Chemical Cleaning of Nanofiltration Membranes: Measurements and Mechanisms, *Environ. Sci. Technol.* 38 (2004) 4683–4693.
- [69] C.L. Tiller, C.R. O’Melia, Natural organic matter and colloidal stability: Models and measurements, *Colloids Surf. Physicochem. Eng. Asp.* 73 (1993) 89–102.
- [70] R. Beckett, N.P. Le, The role of organic matter and ionic composition in determining the surface charge of suspended particles in natural waters, *Colloids Surf.* 44 (1990) 35–49.
- [71] P. Xu, J.E. Drewes, T.-U. Kim, C. Bellona, G. Amy, Effect of membrane fouling on transport of organic contaminants in NF/RO membrane applications, *J. Membr. Sci.* 279 (2006) 165–175.
- [72] J. Kaewsuk, G.T. Seo, Verification of NOM removal in MIEX-NF system for

- advanced water treatment, *Sep. Purif. Technol.* 80 (2011) 11–19.
- [73] A.H.M.A. Sadmani, R.C. Andrews, D.M. Bagley, Impact of natural water colloids and cations on the rejection of pharmaceutically active and endocrine disrupting compounds by nanofiltration, *J. Membr. Sci.* 450 (2014) 272–281.
- [74] A.S. Al-Amoudi, Factors affecting natural organic matter (NOM) and scaling fouling in NF membranes: A review, *Desalination*. 259 (2010) 1–10.
- [75] A. Antony, J.H. Low, S. Gray, A.E. Childress, P. Le-Clech, G. Leslie, Scale formation and control in high pressure membrane water treatment systems: A review, *J. Membr. Sci.* 383 (2011) 1–16.
- [76] J.A. Dirksen, T.A. Ring, Fundamentals of crystallization: Kinetic effects on particle size distributions and morphology, *Chem. Eng. Sci.* 46 (1991) 2389–2427.
- [77] D. Kashchiev, G.M. van Rosmalen, Review: Nucleation in solutions revisited, *Cryst. Res. Technol.* 38 (2003) 555–574.
- [78] R.P. Sear, Estimation of the Scaling of the Nucleation Time with Volume When the Nucleation Rate Does Not Exist, *Cryst. Growth Des.* 13 (2013) 1329–1333.
- [79] T. Darton, U. Annunziata, F. del Vigo Pisano, S. Gallego, Membrane autopsy helps to provide solutions to operational problems, *Desalination*. 167 (2004) 239–245.
- [80] M.R. Wiesner, J.G. Jacangelo, B.J. Marinas, Committee Report -- Membrane Processes in Potable Water Treatment, *J. - Am. Water Works Assoc.* 84 (1992) 59–67.
- [81] F.H. Butt, F. Rahman, U. Baduruthamal, Identification of scale deposits through membrane autopsy, *Desalination*. 101 (1995) 219–230.
- [82] M. Karime, S. Bouguecha, B. Hamrouni, RO membrane autopsy of Zarzis brackish water desalination plant, *Desalination*. 220 (2008) 258–266.
- [83] D.R. Lide, *CRC Handbook of Chemistry and Physics*, 85th Edition, CRC Press, 2004.
- [84] P. Dydo, M. Turek, J. Ciba, K. Wandachowicz, J. Miształ, The nucleation kinetic aspects of gypsum nanofiltration membrane scaling, *Desalination*. 164 (2004) 41–52.
- [85] M.M. Benjamin, *Water Chemistry*, Waveland Press, Incorporated, 2002.
- [86] <http://lawr.ucdavis.edu/classes/ssc102/Section5.pdf>, (n.d.).
- [87] F.H. Butt, F. Rahman, U. Baduruthamal, Characterization of foulants by autopsy of RO desalination membranes, *Desalination*. 114 (1997) 51–64.
- [88] G. Greenberg, D. Hasson, R. Semiat, Limits of RO recovery imposed by calcium phosphate precipitation, *Desalination*. 183 (2005) 273–288.
- [89] A. Zach-Maor, R. Semiat, A. Rahardianto, Y. Cohen, S. Wilson, S.R. Gray, Diagnostic analysis of RO desalting treated wastewater, *Desalination*. 230 (2008) 239–247.
- [90] S.P. Chesters, Innovations in the inhibition and cleaning of reverse osmosis membrane scaling and fouling, *Desalination*. 238 (2009) 22–29.
- [91] M. Asadi-Eydivand, M. Solati-Hashjin, A. Farzadi, N.A.A. Osman, Artificial neural network approach to estimate the composition of chemically synthesized biphasic calcium phosphate powders, *Ceram. Int.* 40 (2014) 12439–12448.

- [92] S.V. Dorozhkin, M. Epple, Biological and medical significance of calcium phosphates, *Angew. Chem. Int. Ed Engl.* 41 (2002) 3130–3146.
- [93] K. Karageorgiou, M. Paschalis, G.N. Anastassakis, Removal of phosphate species from solution by adsorption onto calcite used as natural adsorbent, *J. Hazard. Mater.* 139 (2007) 447–452.
- [94] L. Song, M. Elimelech, Particle Deposition onto a Permeable Surface in Laminar Flow, *J. Colloid Interface Sci.* 173 (1995) 165–180.
- [95] B. Espinasse, P. Bacchin, P. Aimar, Filtration method characterizing the reversibility of colloidal fouling layers at a membrane surface: Analysis through critical flux and osmotic pressure, *J. Colloid Interface Sci.* 320 (2008) 483–490.
- [96] P. Bacchin, Formation et résistance au transfert d'un dépôt de colloïdes sur une membrane d'ultrafiltration, Université Paul Sabatier - Toulouse III, 1994.
- [97] R.W. Field, D. Wu, J.A. Howell, B.B. Gupta, Critical flux concept for microfiltration fouling, *J. Membr. Sci.* 100 (1995) 259–272.
- [98] P. Bacchin, P. Aimar, R.W. Field, Critical and sustainable fluxes: Theory, experiments and applications, *J. Membr. Sci.* 281 (2006) 42–69.
- [99] P. Bacchin, B. Espinasse, P. Aimar, Distributions of critical flux: modelling, experimental analysis and consequences for cross-flow membrane filtration, *J. Membr. Sci.* 250 (2005) 223–234.
- [100] C.Y. Tang, J.O. Leckie, Membrane Independent Limiting Flux for RO and NF Membranes Fouled by Humic Acid, *Environ. Sci. Technol.* 41 (2007) 4767–4773.
- [101] B. Espinasse, P. Bacchin, P. Aimar, On an experimental method to measure critical flux in ultrafiltration, *Desalination.* 146 (2002) 91–96.
- [102] A.E. Childress, M. Elimelech, Effect of solution chemistry on the surface charge of polymeric reverse osmosis and nanofiltration membranes, *J. Membr. Sci.* 119 (1996) 253–268.
- [103] A.E. Childress, M. Elimelech, Relating Nanofiltration Membrane Performance to Membrane Charge (Electrokinetic) Characteristics, *Environ. Sci. Technol.* 34 (2000) 3710–3716.
- [104] M. Mänttari, A. Pihlajamäki, M. Nyström, Effect of pH on hydrophilicity and charge and their effect on the filtration efficiency of NF membranes at different pH, *J. Membr. Sci.* 280 (2006) 311–320..
- [105] A. Braghetta, F.A. DiGiano, W.P. Ball, Nanofiltration of natural organic matter: pH and ionic strength effects (vol 123, pg 637, 1997), *J. Environ. Eng.-Asce.* 124 (1998) 79–79.
- [106] X. Wang, T. Tsuru, M. Togoh, S. Nakao, S. Kimura, Transport of Organic Electrolytes with Electrostatic and Steric-Hindrance Effects Through Nanofiltration Membranes, *J. Chem. Eng. Jpn.* 28 (1995) 372–380.
- [107] Y. Zhang, C. Causserand, P. Aimar, J.P. Cravedi, Removal of bisphenol A by a nanofiltration membrane in view of drinking water production, *Water Res.* 40 (2006) 3793–3799.
- [108] Y. Kiso, Y. Sugiura, T. Kitao, K. Nishimura, Effects of hydrophobicity and molecular

- size on rejection of aromatic pesticides with nanofiltration membranes, *J. Membr. Sci.* 192 (2001) 1–10.
- [109] A.R.D. Verliefde, E.R. Cornelissen, S.G.J. Heijman, I. Petrinic, T. Luxbacher, G.L. Amy, et al., Influence of membrane fouling by (pretreated) surface water on rejection of pharmaceutically active compounds (PhACs) by nanofiltration membranes, *J. Membr. Sci.* 330 (2009) 90–103.
- [110] R. Tenne, K. Patel, K. Hashimoto, A. Fujishima, *An International Journal Devoted to all Aspects of Electrode Kinetics, Interfacial Structure, Properties of Electrolytes, Colloid and Biological Electrochemistry* Efficient electrochemical reduction of nitrate to ammonia using conductive diamond film electrodes, *J. Electroanal. Chem.* 347 (1993) 409–415.
- [111] Y.V. Pelskov, A.Y. Sakharova, M.D. Krotova, L.L. Bouilov, B.V. Spitsyn, Photoelectrochemical properties of semiconductor diamond, *J. Electroanal. Chem. Interfacial Electrochem.* 228 (1987) 19–27.
- [112] K. Patel, K. Hashimoto, A. Fujishima, Photoelectrochemical investigations on boron-doped chemically vapour-deposited diamond electrodes, *J. Photochem. Photobiol. Chem.* 65 (1992) 419–429.
- [113] A. Kapałka, G. Fóti, C. Comninellis, Kinetic modelling of the electrochemical mineralization of organic pollutants for wastewater treatment, *J. Appl. Electrochem.* 38 (2007) 7–16.
- [114] *The Hydroxyl Radical, in: Free-Radic.-Induc. DNA Damage Its Repair*, Springer Berlin Heidelberg, 2006: pp. 47–75.
- [115] G.V. Buxton, C.L. Greenstock, W.P. Helman, A.B. Ross, Critical Review of rate constants for reactions of hydrated electrons, hydrogen atoms and hydroxyl radicals ($\cdot\text{OH}/\cdot\text{O}^-$ in Aqueous Solution, *J. Phys. Chem. Ref. Data.* 17 (1988) 513–886.
- [116] H. Lutze, *Sulfate radical based oxidation in water treatment*, Universität Duisburg-Essen, 2013.
- [117] K. Groenen-Serrano, E. Weiss-Hortala, A. Savall, P. Spiteri, Role of Hydroxyl Radicals During the Competitive Electrooxidation of Organic Compounds on a Boron-Doped Diamond Anode, *Electrocatalysis.* 4 (2013) 346–352.
- [118] A. Kapałka, B. Lanova, H. Baltruschat, G. Fóti, C. Comninellis, Electrochemically induced mineralization of organics by molecular oxygen on boron-doped diamond electrode, *Electrochem. Commun.* 10 (2008) 1215–1218.
- [119] G. Scholes, J. Weiss, Oxygen Effects and Formation of Peroxides in Aqueous Solutions, *Radiat. Res. Suppl.* 1 (1959) 177–189.
- [120] M. Panizza, G. Cerisola, Direct And Mediated Anodic Oxidation of Organic Pollutants, *Chem. Rev.* 109 (2009) 6541–6569.
- [121] M. Panizza, G. Cerisola, Application of diamond electrodes to electrochemical processes, *Electrochimica Acta.* 51 (2005) 191–199.
- [122] K.G. Serrano, Wastewater Treatment by Electrogeneration of Strong Oxidants Using Borondoped Diamond (BDD), in: G. Kreysa, K. Ota, R.F. Savinell (Eds.), *Encycl. Appl. Electrochem.*, Springer New York, 2014: pp. 2126–2132.

- [123] M. Panizza, P.A. Michaud, G. Cerisola, C. Comninellis, Anodic oxidation of 2-naphthol at boron-doped diamond electrodes, *J. Electroanal. Chem.* 507 (2001) 206–
- [124] A. Kapałka, G. Fóti, C. Comninellis, Basic Principles of the Electrochemical Mineralization of Organic Pollutants for Wastewater Treatment, in: C. Comninellis, G. Chen (Eds.), *Electrochem. Environ.*, Springer New York, 2010: pp. 1–23.
- [125] V. Díaz, R. Ibáñez, P. Gómez, A.M. Urriaga, I. Ortiz, Kinetics of electro-oxidation of ammonia-N, nitrites and COD from a recirculating aquaculture saline water system using BDD anodes, *Water Res.* 45 (2011) 125–134.
- [126] V. Schmalz, T. Dittmar, D. Haaken, E. Worch, Electrochemical disinfection of biologically treated wastewater from small treatment systems by using boron-doped diamond (BDD) electrodes – Contribution for direct reuse of domestic wastewater, *Water Res.* 43 (2009) 5260–5266.
- [127] E.T. Urbansky, M.R. Schock, Issues in managing the risks associated with perchlorate in drinking water, *J. Environ. Manage.* 56 (1999) 79–95.
- [128] B.P. Chaplin, Critical review of electrochemical advanced oxidation processes for water treatment applications, *Environ. Sci. Process. Impacts.* 16 (2014) 1182–1203.
- [129] A. Anglada, A. Urriaga, I. Ortiz, Pilot Scale Performance of the Electro-Oxidation of Landfill Leachate at Boron-Doped Diamond Anodes, *Environ. Sci. Technol.* 43 (2009) 2035–2040.

Chapter II

Materials and methods

Contents

II.1 Solutions.....	43
II.1.1 Water matrix.....	43
II.1.2 Chemicals	44
II.2 Nanofiltration equipment and membrane.....	46
II.2.1 Nanofiltration set-up and filtration procedure	46
II.2.1.1 Flux and rejection measurement under the concentration mode.....	46
II.2.1.2 Flux and rejection measurement at constant feed concentration.....	47
II.2.1.3 Rejection of ciprofloxacin in ultrapure water	47
II.2.2 Membrane characterization	48
II.2.2.1 Membrane characteristics.....	48
II.2.2.2 Membrane preservation and preparation.....	49
II.2.2.3 Pure water permeability	49
II.2.3 Square wave filtration method to determine the critical flux	51
II.2.4 Accumulation of salts and organic matters during nanofiltration process.....	54
II.3 Electrochemical oxidation equipment.....	55
II.3.1 Electrochemical oxidation set-up	55
II.3.2 Electrochemical oxidation of synthetic solutions and nanofiltration retentate.....	55
II.3.3 Cyclic Voltammetry Study.....	56
II.4 Analytical method	56
II.4.1 High-performance liquid chromatograph (HPLC)	56
III.4.1.1 HPLC-UV	56
III.4.1.2 HPLC-MS	58
II.4.2 Ionic chromatography (ICE).....	59
II.4.3 Total organic carbon (TOC).....	59
II.4.4 Chemical oxygen demand (COD)	60
II.4.5 Ultraviolet-visible spectrometry (UV).....	60

II.4.6 The concentration of urea	61
II.4.7 Adsorbable Organic Halogens (AOX).....	62
II.4.8 Quantification of “endocrine disruptor effects” by in-vitro bioassays	62
II.5 Membrane surface characterization methods	63
II.5.1 ATR-FTIR	63
II.5.2 SEM-EDX	64
II.5.3 Contact angles	64
References.....	65

II.1 Solutions

Two kinds of experimental solutions were used in the Nanofiltration (NF) and Electrochemical Oxidation (EO) processes. One was the hospital wastewater after membrane bioreactor treatment (MBR effluent). The other was synthetic solution which was prepared by doping pharmaceuticals in the ultrapure water.

II.1.1 Water matrix

MBR effluents of this study are supplied from PANACEE ANR project conducted in LGC. Characteristics of ultrapure water and MBR effluent from hospital are shown on table II-1.

Table II-1 Characteristics of ultrapure water and MBR effluent from hospital

Item	MBR effluent	Ultrapure water
pH	6.0-8.0	5.6-6.1
COD mg L ⁻¹	24.0-73.0	-
TOC mg L ⁻¹	10.0-23.0	0.3
HCO ₃ ⁻ /CO ₃ ²⁻	2.0-60.0	0.3
UV ₂₅₄	0.46-0.84	-
Na ⁺ mg L ⁻¹	35.0-135.0	1.5-2.5
K ⁺ mg L ⁻¹	15.0-25.0	-
Mg ²⁺ mg L ⁻¹	3.0-5.0	0.3
Ca ²⁺ mg L ⁻¹	30.0-60.0	1.6
Cl ⁻ mg L ⁻¹	37.0-65.0	0.9
NO ₃ ⁻ mg L ⁻¹	10.0-200.0	-
SO ₄ ²⁻ mg L ⁻¹	20.0-50.0	-
PO ₄ ³⁻ * mg L ⁻¹	5.0-20.0	0.2

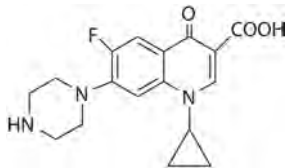
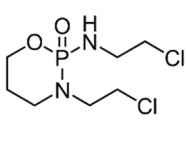
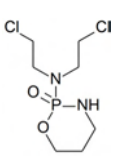
*Due to analysis method, all the H₃PO₄, H₂PO₄⁻, HPO₄²⁻ and PO₄³⁻ in the solution were measured as PO₄³⁻ form.

The range of some of parameters is quite important (HCO₃⁻/CO₃²⁻, Na⁺, NO₃⁻) due to high variability of water usage in the hospital during day time and the difference in the time of sampling. Also, specific additions of NaHCO₃ were done in the membrane bioreactor regularly to ensure good performances of the biomass, especially nitrification efficiency which explain the high variation of NO₃⁻.

Around 50 pharmaceuticals from 10 different therapeutic classes have been detected in

this MBR effluent from hospital [1]. Because of high concentrations in hospital wastewater and low to medium removal in the MBR, concentrations ranged from 10 ng L⁻¹ to 90 µg L⁻¹ in MBR effluent. Ciprofloxacin (CIP), ifosfamide (IFO) and cyclophosphamide (CYP) were selected to be analyzed in the MBR effluent for this study. They are always present in the MBR effluent from hospital at concentrations due to their poor biodegradability [2–4]. In addition, these pharmaceuticals (Table II-2) represent different physicochemical properties (molecular weight, hydrophobicity, polarity, and charge) that have been reported to influence membrane rejection [5].

Table II-2 Selected pharmaceuticals in MBR effluent and their physicochemical properties

	Ciprofloxacin	Ifosfamide	Cyclophosphamide
Formula	C ₁₇ H ₁₈ FN ₃ O ₃	C ₇ H ₁₅ C ₁₂ N ₂ O ₂ P	C ₇ H ₁₅ C ₁₂ N ₂ O ₂ P
Molecular weight (g mol ⁻¹)	331.3	261.1	261.1
log P (ALOGPS)	0.28	0.57	0.7
pK _a ^a	3.7, 6, 10.3	0.12, 13.24	-0.57, 12.78
Charge at neutral pH	Positively charge	neutral	neutral
Chemical structure ^b			

pK_a: Acid dissociation constant.

log P: Octanol – water partition coefficient

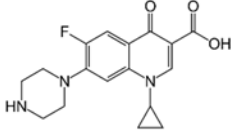
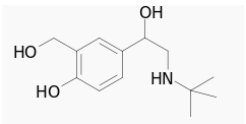
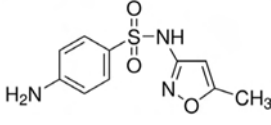
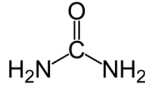
^a <http://www.drugbank.ca>; ^b <https://commons.wikimedia.org>

II.1.2 Chemicals

The electrochemical oxidation was first carried out with synthetic solution. The model molecules were three pharmaceuticals (ciprofloxacin, salbutamol and sulfamethoxazole) and one common organics (urea). The ciprofloxacin (CIP) (≥ 98 % purity) was purchased from Fluka Company. USA). The salbutamol (SALBU) (Salbutamol·sulfate ≥ 99 % purity) and sulfamethoxazole (SMX) (≥ 98 % purity) were obtained from Alfa Aesar and Fluka, respectively. Urea was laboratory reagent grade from Fisher chemical. All synthetic solutions were prepared with ultrapure water. The structures of these molecules were reported in Table II-3. Potassium sulfate (≥ 99 % purity) as

supporting electrolyte for electrochemical oxidation in synthetic solution was analytical grade and supplied by Fisher Science. Other chemicals, organics or solvents were HPLC or analytical grade.

Table II-3 Structure of pharmaceuticals for synthetic solution

	Ciprofloxacin (CIP)	Salbutamol (SALBU)	Sulfamethoxazole (SMX)	Urea
Formula	C ₁₇ H ₁₈ FN ₃ O ₃	C ₁₃ H ₂₁ NO ₃	C ₁₀ H ₁₁ N ₃ O ₃ S	CH ₄ N ₂ O
Molecular weight (g mol ⁻¹)	331.3	239.3	253.3	60.06
Log P (ALOGPS)	0.28	0.44	0.79	-1.8
Structure ^b				

* <http://pubchem.ncbi.nlm.nih.gov>

log P: Octanol – water partition coefficient

II.2 Nanofiltration equipment and membrane

II.2.1 Nanofiltration set-up and filtration procedure

Nanofiltration experiments were conducted in a cross-flow filtration unit (Fig.II-1). The volume of feed tank (1) was 10 L; the membrane was installed into a stainless cross-flow cell (Sepa CF II, Osmonics) (3) in which the effective membrane area was $1.4 \times 10^{-2} \text{ m}^2$. Permeate can be collected in a vessel and weighted on a balance (5) connected to a computer for automatic acquisition. There are two modes of filtration applied in this study: (i) the concentration mode for which the recirculation of retentate stream back to the feed vessel is done while the permeate is collected in the permeate vessel, (ii) the constant feed concentration mode for which both retentate and permeate streams are recycled back to the feed tank in order to maintain a constant feed concentration.

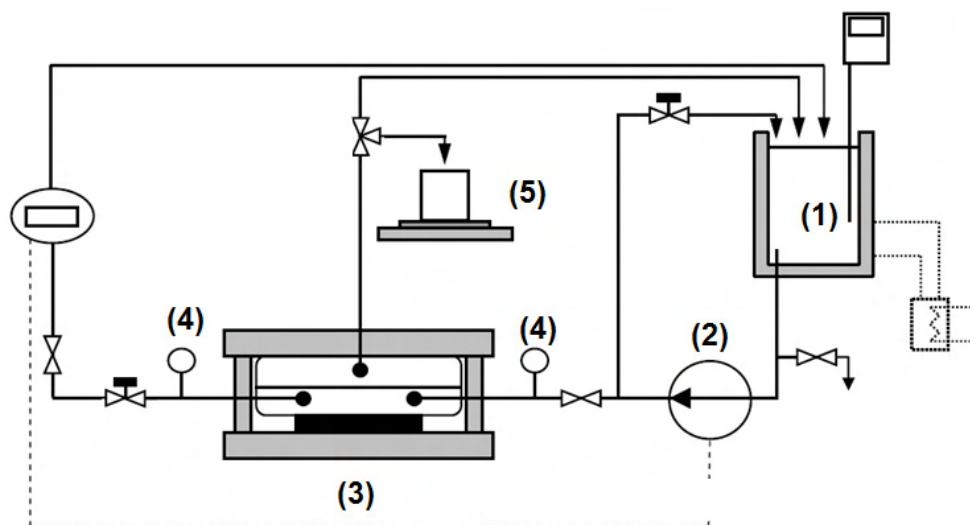


Fig. II-1 Nanofiltration set-up, (1) feed tank, (2) high pressure pump, (3) cross-flow filtrate cell, (4) pressure monitor, (5) permeate tank and balance

II.2.1.1 Flux and rejection measurement under the concentration mode

Filtrations of MBR effluent were firstly carried out in a concentration mode to reach volume reduction factor of 5 ($\text{VRF} = 5$). According to preliminary studies performed with the same equipment and same membrane NE 70 for the filtration of MBR effluent, $\text{VRF} = 5$ was found to be the best compromise between keeping favorable NF productivity and

reaching high pollutants concentration for electro chemical oxidation step (mitigate the transfer limitation). The initial volume of feed were 7 L. Filtrations were performed at cross-flow velocities of 0.2 or 0.35 m s⁻¹. The samples were collected from the feed tank (retentate) and permeate stream, when the volume reduction factor reached 1,2,3,4 and 5 respectively. Concentrations of salts and pharmaceuticals were measured in both retentate and permeate. The rejection of salts and pharmaceuticals by the NF unit was determined at each volume reduction step using Eq. II-1:

$$R = \frac{C_f - C_p}{C_f} \times 100\% \quad (\text{Eq. II-1})$$

Where C_p and C_f are the concentrations in the permeate and the feed tank, respectively.

During the filtration, the permeate streams were weighed to determine the permeate flux. Moreover, temperature and pH of retentate and permeate were measured over time.

II.2.1.2 Flux and rejection measurement at constant feed concentration

Constant feed filtrations were conducted with MBR effluent once a volume reduction factor of 5 was reached to determine the sustainable flux and productivity of the nanofiltration process. Both feed and permeate streams were recycled into the feed tank. In order to determine the flux, the permeate was weighed every 30 min and all the permeate was poured back into the feed tank after measurement. When the permeate flux stabilized (variation of flux less than 1% of initial flux), the recirculation for a certain pressure was terminated. Permeate and retentate samples were collected and the rejection of salts and pharmaceuticals were calculated by Eq. II-1. The temperature and pH are also measured during filtration. The final retentate was stored in the fridge for electrochemical oxidation.

II.2.1.3 Rejection of ciprofloxacin in ultrapure water

The rejection of CIP as a function of the permeate flux in ultrapure water was evaluated in order to be compared to the rejection of CIP in the MBR effluent and then identify the impacts MBR effluent on the pharmaceuticals rejection. The ultrapure water was spiked with CIP as a feed solution. The concentration of CIP was in the same range as in the MBR effluent (0.07 to 0.09 mg L⁻¹). In order to avoid the impact of adsorption

of CIP on the system and overestimate the rejection, the feed solution was recycled without pressure in the NF system for 8 hours prior to the filtration experiment itself. Then the feed solution was stored into the system for 16 hours with cooling at 4° C to reach equilibrium [6]. The filtration was then conducted at a transmembrane pressure ranging from 3 to 35 bar in order to apply different permeate fluxes. At a certain pressure, the permeate and retentate were first recycled into the feed tank until flux stabilization. Then the samples of retentate and permeate were collected and the rejection was computed according to the Equation II-1.

II.2.2 Membrane characterization

II.2.2.1 Membrane characteristics

All the nanofiltration experiments were performed using a NE 70 membrane (provided by Woongjin Chemical). Its characteristics are presented in Table II-4.

Table II-4 Characteristics of membrane NE 70*

Material	MWCO (Da)	Max. temperature (°C)	Max. pressure (bar)	pH range	Surface Charge	Rejection (%)
Thin film composite polyamide	250	45	41.4	3-10	Negative	40-70 (NaCl) 99.5 (MgSO ₄)

*Provided by manufacturer: Woongjin Chemical Co., Ltd., considering specific conditions: 2000 mg/l MgSO₄, 25°C, recovery 15%, pressure 0.5 MPa, pH 6.5-7.0; 1500 mg/l NaCl, 25°C, recovery 15%, pressure 1 MPa, pH 6.5-7.0

The NE70 is a thin film composite polyamide membrane which is constituted of polysulfone as a sub-layer and polyamide as active layers. Manufacturer doesn't provide any information about the coating layer. Tang et al. [7,8] indicated that polyvinyl alcohol was coated partially above the active polyamide layer of the NE70 membrane which was provided by Saehan Industries Inc© (South Korea). However, these authors did not mention the thickness and morphology of the coating layer. The possible structure of this kind of thin film composite membrane is shown on Fig II-2 (a) and the cross-section micrograph of NE 70 which was obtained from SEM in this study is presented

in Fig II-2 (b).

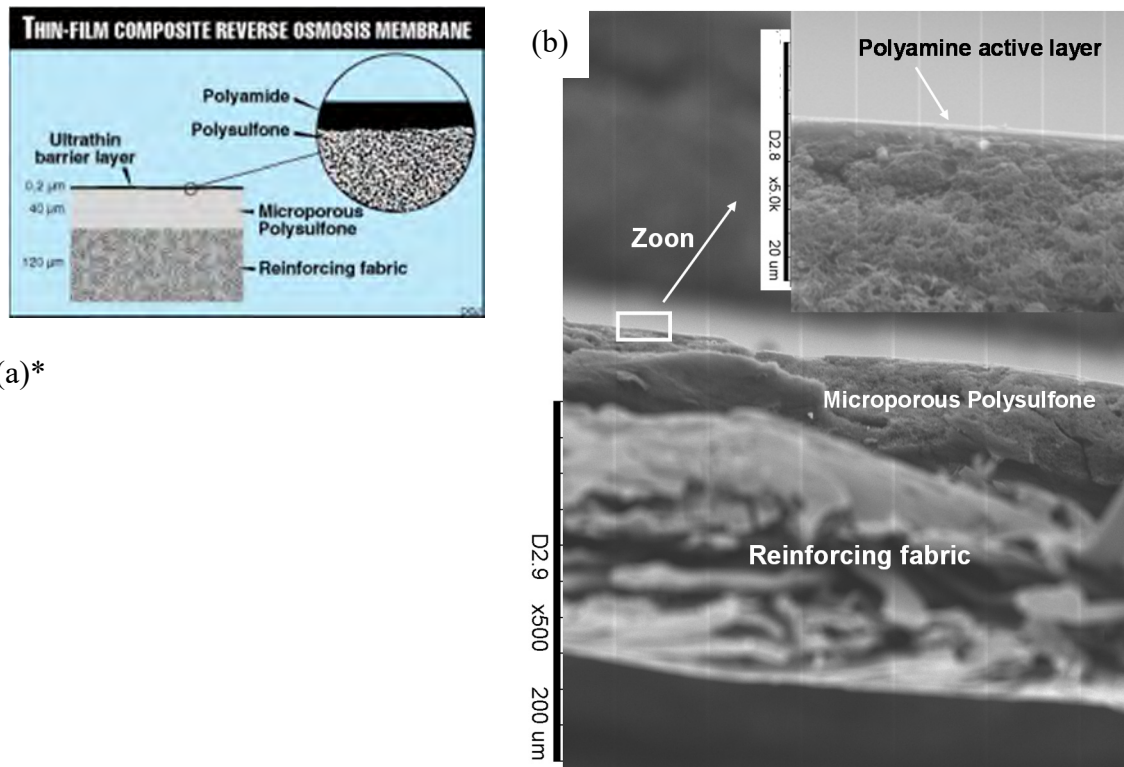


Fig.II-2 Structure of a thin film composite polyamide membrane (a) Schematic diagram* (b) SME picture of NE70

*<http://www.ogj.com/articles/print/volume-94/issue-48/in-this-issue/production/membranes-solve-north-sea-waterflood-sulfate-problems.html>

II.2.2.2 Membrane preservation and preparation

Membranes were stored in a preservative solution at 4 °C (NaHSO_3 0.1 g L⁻¹). They were rinsed and cleaned with ultrapure water before filtrations and then installed in the cross-flow cell. The membrane compaction was performed by filtration of ultrapure water at a transmembrane pressure (TMP) equal to 40 bar until a constant flow rate was obtained (around 3 h).

II.2.2.3 Pure water permeability

The pure water permeability was measured after compaction by circulating ultrapure water in order to check if the membrane sample was in good condition.

The water flux was measured at applied pressure such as 4, 10, 20, 30 and 40 bar at a cross-flow velocity of 0.35 m s⁻¹. Collected permeate samples were weighed in order to

determine the permeation flux. The mean permeability (L_p) was then calculated from the slope of the plot of flux versus pressure as Eq.II-2.

$$L_p = \frac{J}{\Delta P} \quad (\text{Eq.II-2})$$

where L_p is the permeability in $\text{L h}^{-1} \text{m}^{-2} \text{bar}^{-1}$, J and ΔP are the permeate flux in $\text{L h}^{-1} \text{m}^{-2}$ and transmembrane pressure, respectively.

Table II-5 shows the initial pure water permeability of each membrane used in this study. The pure water permeability varies from 12.9 to 17.4 $\text{L h}^{-1} \text{m}^{-2} \text{bar}^{-1}$ and has average value as 15.6 $\text{L h}^{-1} \text{m}^{-2} \text{bar}^{-1}$. In addition, the R^2 values obtained from the linear plots of the flux versus pressure were higher than 0.9889 and the average value was 0.9963. It can be stated that all membranes used for filtration experiments during this study were in good condition with a good reproducibility of their initial performances.

Table II-5 Initial pure water permeability of NF 70 in this study (20°C and 3 to 40 bar)

	Pure water permeability ($\text{L h}^{-1} \text{m}^{-2} \text{bar}^{-1}$)	R-square
1	15.3	0.9964
2	17.4	0.9909
3	13.9	0.9929
4	15.7	0.9971
5	17.2	0.9906
6	17.4	0.9889
7	14.6	0.9911
8	15.9	0.9962
9	17.5	0.9951
10	17.2	0.994
11	15.6	0.9967
12	14.3	0.9976
13	13.0	0.9992
14	12.9	0.9963
Average	15.6 ± 1.6	0.9945

In addition, the membrane resistance can be computed by the initial pure water permeability (L_{p0}) with Eq. II-3.

$$L_{p0} = \frac{1}{\mu_p R_m} \quad (\text{Eq. II-3})$$

where, R_m (m^{-1}) is the intrinsic hydraulic membrane resistance and μ_p is viscosity of permeate ($\text{Pa}\cdot\text{s}$).

After filtrations, the NF system was rinsed 3 times by reverse osmosis water and once by ultrapure water. Then the pure water permeability after filtration (L_{pf}) was measured in order to determine the difference before and after. The irreversible fouling resistance after rinsing (R_{ir}) can be calculated using Eq. II-3 and Eq. II-4.

$$L_{pf} = \frac{1}{\mu_p (R_m + R_{ir})} \quad (\text{Eq. II-4})$$

where, R_m and R_{ir} are the intrinsic hydraulic membrane resistance and the irreversible fouling resistance after rinsing, respectively.

II.2.3 Square wave filtration method to determine the critical flux

The square wave filtration technique developed by Espinasse et al. [9,10] can be applied to determine the critical flux and distinguish the reversible fouling due to osmotic pressure (R_{rf}) and irreversible fouling (R_{if}). The principle of it is to alternate stepwise the applied force (the pressure) with positive and negative variations, as presented in Fig. II-3, and to continuously measure the permeate flux.

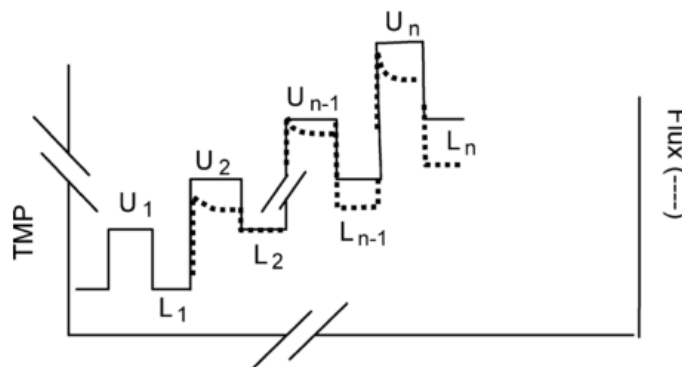


Fig.II-3 Principle of the square wave technique; pressure and flux vs time; upper and lower steps [9,10]

U steps correspond to upper steps and L steps to lower steps. At each step, a pseudo steady state flux is reached. The stabilization of the system (i.e., steady state) takes from a few minutes to several hours depending on the system evolution. By comparing the flux between steps L_n and U_{n-1} which have the same pressure, the decrease of flux is associated to the fouling phenomenon that took place at step U_n . If the flux is the same at steps U_{n-1} and L_n , the fouling is considered as totally reversible, the flux is below the critical value; if not, the fouling is partly irreversible, the flux is above the critical value.

Fig.II-4 shows the fouling resistance against the pseudo stable flux, which can indicate the reversible fouling and irreversible fouling according to the filtration procedure developed by Espinasse et al. [9,10]. At the beginning of filtration the fouling resistance increases with increasing pressure, while a decrease of pressure allows it to go back to the preceding resistance value; in this case, the increase in resistance is reversible. Otherwise, an increase of resistance can be observed between steps $n-1$ and n , such that resistance remains constant when the pressure decreases at L_n (the increase of resistance is consequently irreversible).

The significance of this pattern is the appearance of an irreversible deposit on the membrane surface. If the resistance at L_n is the same value as resistance at step U_n , the resistance is totally irreversible.

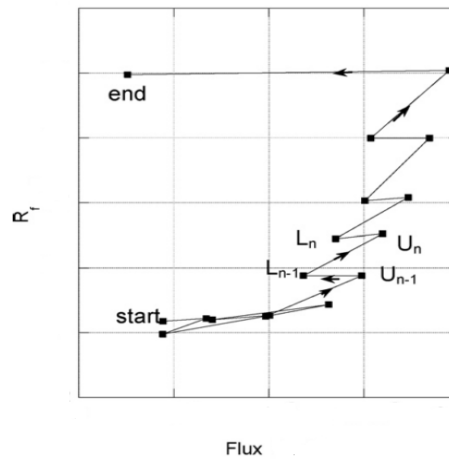


Fig.II-4 Evolution of the total fouling resistance vs flux obtained with the “square wave technique”: indication for reversible and irreversible components [9,10]

The flux can be described by osmotic pressure model, as follow:

$$J = \frac{\Delta P - \Delta \pi}{\mu_p (R_m + R_{if})} \quad (\text{Eq. II-5})$$

where J is the permeate flux, ΔP is the transmembrane pressure, $\Delta \pi$ is the osmotic pressure, μ_p is viscosity of permeate and R_m , R_{if} is the intrinsic hydraulic membrane resistance and resistance due to the irreversible fouling, respectively.

The osmotic pressure can also be incorporated into the reversible fouling resistance. In this case, the reversible resistance associated with the polarization concentration layer can be treated like a term of osmotic pressure:

$$J = \frac{\Delta P}{\mu_p (R_m + R_{if} + R_{rf})} = \frac{\Delta P}{\mu_p (R_m + R_f)} \quad (\text{Eq. II-6})$$

where R_f is the total fouling resistance and R_{rf} is the resistance due to the reversible fouling which is related to the polarization concentration.

According to the square wave filtration method, the fouling reversibility can be determined by comparing the fouling resistance at a same TMP before and after an upper pressure step. The irreversible resistance that appears for an upper pressure step U_n can be reached by comparing the fouling resistance at step L_n and U_{n-1} as follow:

$$r_{if,n} = R_f \Big|_{L_n} - R_f \Big|_{U_{n-1}} \tag{Eq. II-7}$$

where $r_{if,n}$ is the irreversible fouling resistance relative to the step. When R_f at step L_n equals R_f at step U_{n-1} the resistance observed at U_n step is totally reversible. To calculate the value of the total R_{if} , at a given pressure step, all step resistances r_{if} are summed. The fouling resistance at n is the sum of the resistance measured at the previous steps:

$$R_{if} = \sum_n r_{if,n} \tag{Eq. II-8}$$

The relationship between the intrinsic hydraulic membrane resistance and fouling resistances is shown on Fig.II-5.

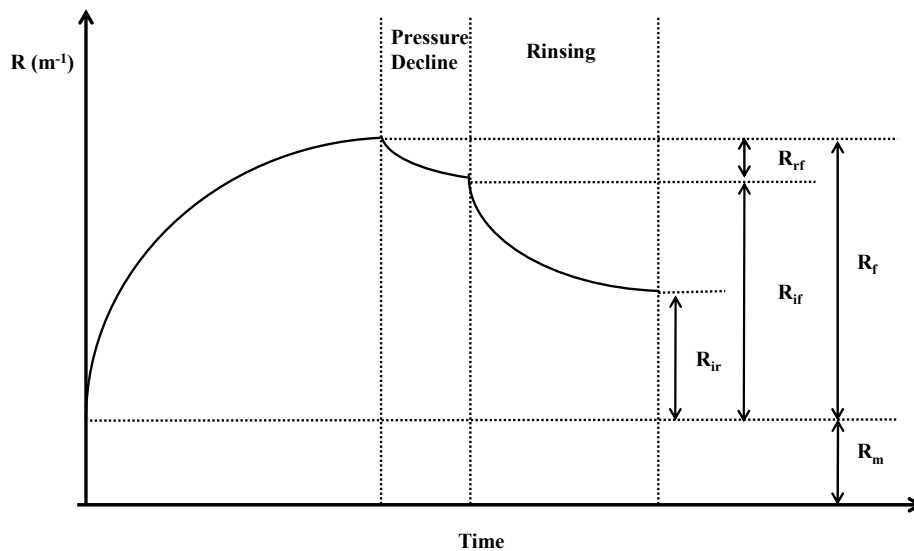


Fig.II-5 The relationship of the intrinsic hydraulic membrane resistance and fouling resistances

In the figure,

R_m is the intrinsic hydraulic membrane resistance (m^{-1});

R_f is the total fouling resistance (including R_{rf} , R_{if}) (m^{-1});

R_{rf} is the resistance due to reversible fouling which is relative to the polarization concentration (m^{-1});

R_{if} is resistance due to irreversible fouling (m^{-1}) (unable to be removed by declining the pressure);

R_{ir} is the residual irreversible fouling resistance after rinsing (unable to be removed by declining pressure and rinsing) (m^{-1});

II.2.4 Accumulation of salts and organic matters during nanofiltration process

The accumulation of organics and salts on the membrane surface and in the structure was calculated by the mass balance between initial mass (total mass on the feed) and the mass after NF (the sum of mass on the permeate and the retentate). The concentration of salts was measured by ionic chromatography. The adsorption of organic matters was characterized by UV₂₅₄ absorbance (see II.4.5).

The accumulation of salts and organics on membrane are calculated for the two filtration modes: concentration mode and constant feed concentration mode.

In the concentration mode, the permeate was collected while the retentate was recycled into the feed tank. The accumulated mass was computed by quantification of the concentration in the feed, concentration in the retentate and concentration in the mixed permeate (total permeate collected from the beginning to the end of the concentration step) as Eq. II-9.

$$Q_{ads} = C_f \cdot V_f - C_R \cdot V_R - C_{p_{mix}} \cdot V_p \quad (\text{Eq. II-9})$$

where, Q_{ads} is the accumulated mass; C_f , C_R and $C_{p_{mix}}$ are concentrations in the feed, retentate and mixed permeate in $g L^{-1}$, respectively, and V_f , V_R and V_p are corresponding volumes.

At constant feed concentration, both permeate and retentate were recycled into the feed tank. The sample of collected permeate was less than 4% of the total volume in the tank. The accumulated mass was calculated by the concentration in the tank before and after circulation using Eq. II-10

$$Q_{ads} = C_{be} \cdot V - C_{end} \cdot V \quad (\text{Eq. II-10})$$

where C_{be} and C_{end} are concentrations before and after recirculation and V is the volume in the retentate loop and is assumed to be constant.

II.3 Electrochemical oxidation equipment

II.3.1 Electrochemical oxidation set-up

The experimental solution was stored in 1 liter thermoregulated glass reservoir (1) and circulated through the electrolytic cell using a centrifugal pump (2) (Fig. 2). The flow rate was 366 L h^{-1} . Electrolyses were conducted at $30 \text{ }^\circ\text{C}$ in a one-compartment flow filterpress reactor under galvanostatic conditions (3). Electrodes were two discs of 69 cm^2 of active surface separated 10 mm . The BDD anode from Adamant (Switzerland) was elaborated by chemical vapour deposition on a conductive substrate of silicium. The cathode was a 1 mm thick disc of zirconium. The current was supplied by an ELC AL 924 power supply.

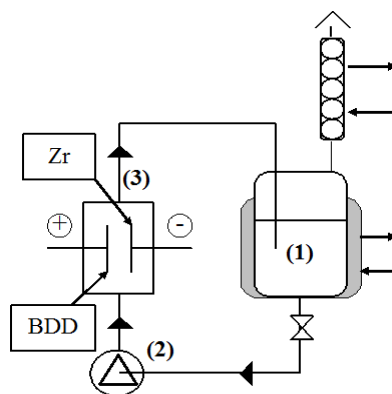


Fig.II-5 Discontinuous process with a single compartment electrochemical reactor, (1) tank, (2) pump, (3) electrochemical cell.

The value of mass transfer coefficient (k_m) varies is correctly represented by a linear relation with flow rate (Φ) in the operating range of flow rate ($120 - 300 \text{ L h}^{-1}$) at $30 \text{ }^\circ\text{C}$ [11], as shown in Eq. II-11. In the present study, the flow rate was 360 L h^{-1} , the mass transfer coefficient can be calculated to be $2.30 \times 10^{-5} \text{ m s}^{-1}$.

$$k \times 10^5 = 0.0051\Phi + 0.4367 \quad (\text{Eq. II-11})$$

where, k is the mass transfer coefficient (m s^{-1}), Φ is the flow rate in L h^{-1}

II.3.2 Electrochemical oxidation of synthetic solutions and nanofiltration retentate

The system was first washed by ultrapure water, then cleaned electrochemically with an electrolysis of a solution of K_2SO_4 at a current intensity of 1.5 A during 3 hours and

finally was rinsed by ultrapure water. TOC of the rinsing solution was measured in order to ensure the system was perfectly cleaned before next electrolysis. Electrolysis of synthetic solutions (electrolyte spiked with CIP) and NF retentate were carried out after polarization. The solution to be treated was filled (1L) into the tank and the electrolysis was carried out. K_2SO_4 (0.1M) as electrolyte was added in the synthetic solution for the sufficient conductivity but not in NF retentate. Samples were taken at regular intervals in the tank to measure the concentration of CIP, TOC and COD. The global volume of samples was less than 10 % of the total volume. After electrolysis, the treated solution was collected for further analysis of halogenates (AOX) and the evaluation of the remaining toxicity using bioassays was performed.

II.3.3 Cyclic Voltammetry Study

Cyclic voltammograms were carried out in a conventional three-electrode cell of 100 mL capacity using a computer controlled Autolab potentiostat Model 30. A BDD thin film of 0.196 cm^2 from Adamant was used as working electrode, a Pt wire as counter electrode and a $Hg/Hg_2Cl_2, Cl^-$ (sat) electrode (SME) as the reference electrode. Before each experiment, the electrode was pre-treated using anodic polarization at 2.84 V/SHE during 40 s into a 1 M H_2SO_4 solution.

II.4 Analytical method

II.4.1 High-performance liquid chromatograph (HPLC)

High performance liquid chromatography is a chromatographic technique used to separate a mixture of compounds with the purpose of individually identifying, quantifying or purifying components of a mixture. In this study HPLC connected with ultraviolet-visible spectrometry detector (HPLC-UV) or mass spectrometry (HPLC-MS) was applied to determine the concentration of pharmaceuticals in synthetic solutions, MBR effluents, nanofiltration and electro-oxidation treated samples.

III.4.1.1 HPLC-UV

HPLC-UV analyses were conducted on Agilent 1200 Series HPLC systems (Agilent

Technologies, USA). Two HPLC columns: Vydac reverse phase C18 column and Agilent ZORBAX Eclipse Plus C18 column are used for analysis the concentration of pharmaceuticals.

Vydac reverse phase C18 column (5 μm , 4.6 mm \times 250 mm) manufactured by Chrom Tech (USA) was applied for the quantification of CIP concentrations in pure synthetic solutions. The detection UV wavelength was set at 278 nm. The mobile phase of HPLC consisted of a mixture of water: acetonitrile: triethylamine (80: 20: 0.3 v/v/v) and the pH was adjusted to 3.3 with phosphoric acid. The flow rate was 1.0 mL min⁻¹ and volume of injection was 20 μL as described in literature [12]. With this analytical method, the detection limit of CIP is 0.1 mg L⁻¹ and the analytical error is 1%.

Agilent ZORBAX Eclipse Plus C18 column (3.5 μm , 3 mm \times 100 mm) from Agilent Technologies was used for the analysis of the concentration of SAL and SMX in pure synthetic solutions, the concentration of CIP, SAL and SMX in the mixture solution as well as the concentration of CIP in the MBR effluents (for EO). The detection UV wavelength was set at 278 nm. The mobile phase of HPLC consisted of a gradient of ultrapure water (with 0.1 % of formic acid) and acetonitrile (with 0.1 % of formic acid) and the column temperature was set at 30°C. The flow rate was 0.4 mL min⁻¹ and volume of injection was 10 μL .

The gradient for the mobile phase is reported in the table II-5 for the analysis of the concentration of SAL, SMX and CIP in synthetic solution.

Table II-5 Gradient of the mobile phase for analysis of pharmaceuticals in synthetic solutions with ZORBAX

Eclipse Plus C18 column	
Time (min)	acetonitrile % (with 0.1 % formic acid)
0	5
3	5
18	95
21	5
30	5

Retention times, detection limits and analytical error for the measurement of pharmaceuticals are listed on Table II-6.

Table II-6 The retention times detection limits and the analytical error for each pharmaceuticals with

ZORBAX Eclipse Plus C18 column			
Compounds	Retention time (min)	Detection limits ($\mu\text{g L}^{-1}$)	Analytical error
Salbutamol	5.1	100	1 %
Ciprofloxacin	9.9	10	0.18 %
sulfamethoxazole	12.1	10	0.3%

The concentration of CIP in MBR effluents can also be measured using ZORBAX Eclipse Plus C18 column and the gradient to the mobile phase (mixture of ultrapure water with 0.1 % of formic acid and acetonitrile with 0.1 % of formic acid) is presented on table II-7. The detection limit of CIP is $10 \mu\text{g L}^{-1}$ and the analytical error is 0.8%.

Table II-7 Gradient of the mobile phase for analysis of CIP in MBR effluent with ZORBAX Eclipse Plus C18 column

Time (min)	acetonitrile % (with 0.1 % formic acid)
0	5
15	95
18	5
20	5

For quantification, calibration curves were established in pure water and MBR effluents spiked with known concentrations. They served as identification points during analysis of samples.

III.4.1.2 HPLC-MS

Concentrations of ciprofloxacin, ifosfamide and cyclophosphamide in MBR effluent samples, retentates and permeates from NF, as well as final effluents of electrochemical oxidation were measured by UPLC-MS/MS (Waters Acquity™ Ultrapformance LC - QuattroPremier XE Micromass MS Technologies) by LPTC in Bordeaux (Université de Bordeaux 1, EPOC, LPTC, UMR 5805, Laboratoire de Physico et Toxico Chimie de l'Environnement) after addition of specific internal standards and purification by solid phase extraction (SPE, Oasis HLB™, 200mg, 6cc, Waters®). The quantification limits are shown in table II-8. Residual standard deviation is about 10%.

Table II-8 Quantification limits of ciprofloxacin, ifosfamide and cyclophosphamide in MBR matrix with UPLC-MS/MS analysis from LPTC (Bordeaux)

Compounds	Quantification limits (ng L^{-1})
Ciprofloxacin	22.3
Ifosfamide	22.7
Cyclophosphamide	50.5

II.4.2 Ionic chromatography (ICE)

Ionic chromatography (ICE) is a process that allows the separation of ions and polar molecules based on their affinity to the ion exchanger. In this study, the concentrations of salts in both synthetic solution and MBR matrix were measured by ionic chromatography with an ICS 3000 system (Dionex, France). The injection volume is 25 μL and the column temperature was set at 30 $^{\circ}\text{C}$. The concentrations of anions and cations were analyzed with two columns (Thermo Scientific, Dionex) as shown on table II-9.

Table II-9 Analysis conditions for anions and cations using ionic chromatography

	Colume	Mobile phase	Suppressor
Anions	IonPac TM AS11	NaOH: 5 mM (95%) and 100 mM (5%)	ASRS_4mm (137mA)
Cation	IonPac TM CS12	CH ₄ O ₃ SO ₃ 20 mM	CSRS_4mm (59 mA)

The ionic chromatography can detect the concentration of anions and cations in a range of 1 mg L⁻¹ to 100 mg L⁻¹. Analytical errors of each ion are listed on table II-10.

Table II-10 Analytical errors for anions and cations

Anions	Analytical error	Cations	Analytical error
Cl ⁻	2.1 %	Na ⁺	1.8 %
NO ₃ ⁻	1.5 %	K ⁺	1.5 %
SO ₄ ²⁻	6.0 %	Mg ²⁺	1.5 %
PO ₄ ^{3-*}	3.1 %	Ca ²⁺	1.4 %

*Due to the analytical method, all forms of the phosphate (H₃PO₄, H₂PO₄⁻, HPO₄²⁻ and PO₄³⁻) were measured as PO₄³⁻

Calibration curves were obtained using a mixture of pure standard solutions and used for quantification.

II.4.3 Total organic carbon (TOC)

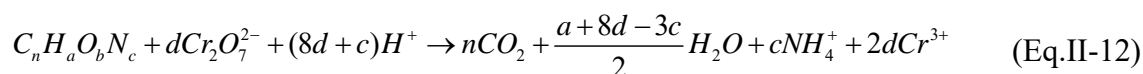
Total Organic Carbon (TOC) was measured during both NF and EO experiments as a global pollution parameter to evaluate the efficiency of both processes. TOC was measured with TOC-VCSN instrument (Shimadzu). From this measurement, the total carbon (TC) is obtained after complete combustion of the organic or inorganic carbon fractions at 680 $^{\circ}\text{C}$ with a cobalt / platinum catalyst. The concentration of inorganic carbon is measured after acidification and degassing, performed automatically. Finally, total organic carbon can be

calculated from the difference between the total carbon and inorganic carbon (IC). The TC of all samples was measure three times and the coefficient of variation is less than 2 %. The detection limit is 50 ppb and the analytical error is 5%. Calibration curves were established using commercially available standard solutions (Shimadzu).

II.4.4 Chemical oxygen demand (COD)

Chemical oxygen demand actually indicates the mass of oxygen consumed per liter of solution, which is commonly used to indirectly measure the amount of organic compounds in water and widely used to analyze the efficiency of the organic pollutants removal in water. COD is also measured as a global parameter during NF and EO processes. COD was determined by photometry using disposable test tubes (HI93754H-25 LR from HANNA Instruments) and a HACH DR/2400 photometer. After sample addition, test tubes were heated at 150°C for 2 hours and cool down at room temperature before measurement.

The organics can be oxidized by dichromate, as follow:



The amount of Cr^{3+} was determined after oxidization is completed with HACH DR/2400 photometer. The detection limit is 3 ppm and the analytical error is 5%. Specifications from the manufacturer are shown on Table II-11.

Table II-11 Specifications of COD measurement from the manufacturer

Standard value (mg L ⁻¹)	Target value (mg L ⁻¹)	Mean value (mg L ⁻¹)
0	0 ± 5	0
140	140 ± 7	142

II.4.5 Ultraviolet-visible spectrometry (UV)

Ultraviolet-visible spectrometry refers to absorption spectroscopy or reflectance spectroscopy in the ultraviolet-visible spectral region using light in the visible and adjacent (near-UV and near-infrared, NIR) ranges. The absorption or reflectance in the

visible range directly affects the perceived color of chemicals involved. It can be used for quantitative determination of different analytes according to Beer-Lambert law.

In this study, UV spectrometry is applied for the determination of urea concentration (see II.4.6).

Previous researches [13] proved good correlation between TOC and UV_{254} , as well as between COD and UV_{254} . Thus, UV_{254} can be successfully applied to determine natural organic matter concentrations using the relationship below:

$$UV_{254} = \alpha [\text{Organic matters}] \quad (\text{Eq.II-13})$$

Where, α is the correlation slop between the UV_{254} and concentration of organic matters.

Using this equation, an estimation of the adsorption of organic matters on the membrane during NF has been calculated as described in the table II-12. As shown in the example, the concentration of organic matters in feed, permeate and retentate were estimated by UV_{254} . Comparing the mass in the feed and in retentate as well as in permeate, the adsorption of organic matters can be computed as 0.85α mg which represents 26 % of the initial mass for the present example.

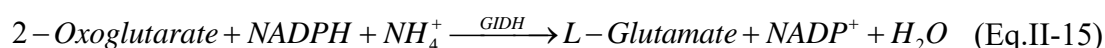
Table II-12 Example of calculation to estimate organic matters adsorption on the membrane

	Feed	Retentate	Permeate (Average)
UV254 absorbance	0.46	1.37	0.08
[organic matters] (mg L^{-1})	0.46α	1.37α	0.08α
Volume (L)	7	1.4	5.6
Mass (mg)	3.22α	1.92α	0.45α
Q_{ads} (mg)		0.85α	
Percentage of Q_{ads} to the initial mass		26%	

II.4.6 The concentration of urea

Concentrations of urea were determined by a L-Arginine/Urea/Ammonia kit from Nzytech (Portugal). The principle of the measure is shown as follow, according to the Eq.II-14 and Eq.II-15. The amount of nicotinamide adenine dinucleotide phosphate (NADP^+ , measured at UV 340 nm) formed through the combined action of urease (URE) and glutamate dehydrogenase (GIDH), is stoichiometric with the amount of urea.





The sensitivity of the assay is based on 0.005 absorbance units and a sample volume of 2.00 ml. The detection limit of urea is 0.13 mg L⁻¹. The relative standard deviation of urea test is 3%.

II.4.7 Adsorbable Organic Halogens (AOX)

The Adsorbable organic halogens in the synthetic solution, MBR effluent, NF retentate and solution after EO treatment were analyzed by the Laboratoire Départemental 31: Eau - Vétérinaire - Air in Toulouse, according to the ISO 9562 Method [14]. ISO 9562 usually specifies the methodology for the direct determination of a concentration of 10 µg L⁻¹ in water for organic chlorine, bromine and iodine (expressed as chloride) adsorbable on activated carbon. This method is applicable to test samples with concentrations of inorganic chloride ions of less than 1 g L⁻¹. Samples with higher concentrations are diluted prior to analysis.

II.4.8 Quantification of “endocrine disruptor effects” by in-vitro bioassays

A set of in-vitro bioassays allowing the quantification of receptor-mediated activities, namely estrogen (ER), androgen (AR), and pregnane X (PXR) receptors was performed by INERIS according to previous studies [15,16].

Briefly, 250 to 500 mL of samples were filtered on GF/C glass fiber filters (1.2 µm, Whatman) and extracted by SPE on Oasis HLBTM (200mg, 6cc, Waters®) prior bioassays testing.

In both assays, results are expressed as percent of maximal luciferase activity induced by the positive controls, Estradiol E2 10 nM in MELN cell line for estrogenic activity, Dihydrotestosterone (DHT) or Dexamethasone (Dex) 1 nM in MDA-kb2 cell line for androgenic and glucocorticoid activities, and the cholesterol lowering drug, SR12813 (SR) 3 µM in HG5LN-hPXR cell line for PXR-like activity. The last one corresponds to the detoxication activity induced by xenobiotic compounds. Limits of detection for the different bioassays are reported in the table II-13.

Table II-13 Limits of detection for the different bioassays for quantification of “endocrine disruptor effects”

bioassays and receptor-mediated activities	Limits of detection in the culture medium*
<u>MELN</u> , Estrogenic (ER)	0,8 ng L ⁻¹
<u>MDA-kb2</u> Androgenic (AR) and glucocorticoid (GR)	DHT : 23 ng L ⁻¹ Dex : 0,15 µg L ⁻¹
<u>HG5LN-hPXR</u> PXR-like (PXR)	4,5 µg L ⁻¹

*estimated from EC5 value (concentration inducing 5% of the total effect)

Dose–response curves were modelled by using Hill equation with the Excel™ macro RegTox (http://www.normalesup.org/~vindimian/fr_index.html) which allows obtaining EC20 (concentrations of test chemical or sample extract that induce 20% of the maximal response). Biological activities of samples were quantified as biological toxic equivalents (BioT-EQ), E2-equivalents (E2-EQ), DHT-EQ and SR-EQ and were determined by dividing the EC20 of reference chemicals (expressed in ng L⁻¹) by the EC20 value of the sample.

II.5 Membrane surface characterization methods

Virgin and fouled membrane surfaces were characterized after drying at 60 °C with a vacuum degree fixed at -0.8 bar (C3000 – XF020 France Etuves).

II.5.1 ATR-FTIR

ATR-FTIR spectra (Attenuated total reflection-Fourier transform infrared spectroscopy) were obtained with Thermo-Nicolet Nexus 670 (USA). It was applied for identification of some functional groups which are present on the surface of materials. The sample was supported on diamond crystal substrates and the analytical depth is around 2 µm. Virgin and fouled membranes were examined using ATR-FTIR to identify the property of membrane and the fouling composition.

II.5.2 SEM-EDX

Surface morphology of membranes was examined with a Scanning Electron microscope (SEM, Hitachi Tabletop Microscope TM-1000) interfaced with Energy Dispersive X-ray (EDX) spectroscopy system (Thermo-Fisher). SEM-EDX analysis is a non-destructive approach for surface analysis, by which some qualitative elemental information on the membrane surface can be obtained.

Membrane samples were sputtered with a thin layer of gold before SEM analysis for better contrast. The EDX analyses were carried out at the same time. Elemental analysis begins from sodium. EDX measurements were taken place at different locations of membrane surface in order to obtain the comprehensive elemental composition.

Cross-sections of samples are prepared by cryo-fracture: membranes were first immersed in ethanol and fractured in liquid nitrogen.

II.5.3 Contact angles

The hydrophilicity of the membrane samples was characterized by membrane contact angle measurements which were performed using GBX Digidrop goniometer (model DGD/Fast 60, France). The water droplet (0.5 μL) was deposited on the membrane surface and the contact angle can be measured as shown on Fig.II-6. Measurements were carried out several times at different locations on the dried membrane surface using $\sim 2 \mu\text{L}$ liquid droplet in ambient conditions. The measurement of contact angles was reproducible in the range $\pm 5^\circ$ and an average valued was determined.

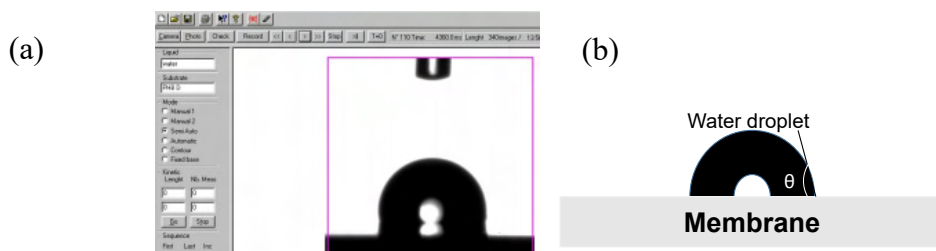


Fig.II-6 The measurement of contact angles by GBX Digidrop contact angle meter: (a) picture during measurement, (b) Schematic diagram, θ is the contact angles.

References

- [1] I. Quesada, Y. Gonzalez, S. Schetrite, H. Budzinski, K. Le Menach, O. Lorain, et al., PANACÉE : évaluation du fonctionnement d'un bioréacteur à membranes immergées traitant des effluents hospitaliers d'oncologie, *Rev. Sci. Eau.* 28 (2015) 1.
- [2] A. Al-Ahmad, F.D. Daschner, K. Kümmerer, Biodegradability of Cefotiam, Ciprofloxacin, Meropenem, Penicillin G, and Sulfamethoxazole and Inhibition of Waste Water Bacteria, *Arch. Environ. Contam. Toxicol.* 37 (1999) 158–163.
- [3] K. Kümmerer, T. Steger-Hartmann, M. Meyer, Biodegradability of the anti-tumour agent ifosfamide and its occurrence in hospital effluents and communal sewage, *Water Res.* 31 (1997) 2705–2710.
- [4] T. Steger-Hartmann, K. Kümmerer, A. Hartmann, Biological Degradation of Cyclophosphamide and Its Occurrence in Sewage Water, *Ecotoxicol. Environ. Saf.* 36 (1997) 174–179.
- [5] V. Yangali-Quintanilla, A. Sadmani, M. McConville, M. Kennedy, G. Amy, Rejection of pharmaceutically active compounds and endocrine disrupting compounds by clean and fouled nanofiltration membranes, *Water Res.* 43 (2009) 2349–2362.
- [6] A.M. Comerton, R.C. Andrews, D.M. Bagley, P. Yang, Membrane adsorption of endocrine disrupting compounds and pharmaceutically active compounds, *J. Membr. Sci.* 303 (2007) 267–277.
- [7] C.Y. Tang, Y.-N. Kwon, J.O. Leckie, Effect of membrane chemistry and coating layer on physiochemical properties of thin film composite polyamide RO and NF membranes: I. FTIR and XPS characterization of polyamide and coating layer chemistry, *Desalination.* 242 (2009) 149–167.
- [8] C.Y. Tang, Y.-N. Kwon, J.O. Leckie, Effect of membrane chemistry and coating layer on physiochemical properties of thin film composite polyamide RO and NF membranes: II. Membrane physiochemical properties and their dependence on polyamide and coating layers, *Desalination.* 242 (2009) 168–182.
- [9] B. Espinasse, P. Bacchin, P. Aimar, Filtration method characterizing the reversibility of colloidal fouling layers at a membrane surface: Analysis through critical flux and osmotic pressure, *J. Colloid Interface Sci.* 320 (2008) 483–490.
- [10] B. Espinasse, P. Bacchin, P. Aimar, On an experimental method to measure critical flux in ultrafiltration, *Desalination.* 146 (2002) 91–96.
- [11] C. Rcaud, A. Savall, P. Rondet, N. Bertrand, K. Groenen Serrano, New electrodes for silver(II) electrogeneration: Comparison between Ti/Pt, Nb/Pt, and Nb/BDD, *Chem. Eng. J.* 211–212 (2012) 53–59.
- [12] N.M. Kassab, A.K. Singh, E.R.M. Kedor-Hackmam, M.I.R.M. Santoro, Quantitative determination of ciprofloxacin and norfloxacin in pharmaceutical preparations by high performance liquid chromatography, *Rev. Bras. Ciênc. Farm.* 41 (2005) 507–513.
- [13] R. Albrektienė, M. Rimeika, E. Zalieckienė, V. Šaulys, A. Zagorskis, Determination of Organic Matter by UV Absorption in the Ground Water, *J. Environ. Eng. Landsc. Manag.* 20 (2012) 163–167.

- [14] ISO 9562:2004(en) Water quality — Determination of adsorbable organically bound halogens (AOX), (n.d.).
- [15] S. Kinani, S. Bouchonnet, N. Creusot, S. Bourcier, P. Balaguer, J.-M. Porcher, et al., Bioanalytical characterisation of multiple endocrine- and dioxin-like activities in sediments from reference and impacted small rivers, *Environ. Pollut.* 158 (2010) 74–83.
- [16] N. Creusot, S. Kinani, P. Balaguer, N. Tapie, K. LeMenach, E. Maillot-Maréchal, et al., Evaluation of an hPXR reporter gene assay for the detection of aquatic emerging pollutants: screening of chemicals and application to water samples, *Anal. Bioanal. Chem.* 396 (2009) 569–583.

Chapter III

**Nanofiltration for removal of
pharmaceuticals from MBR effluent:**

Productivity and selectivity

Contents

III.A Limiting flux and foulant identification during nanofiltration of MBR effluent following a square wave filtration method	67
III.A.1 Experimental procedure.....	67
III.A.2 Flux behavior.....	69
III.A.2.1 Variation of permeate flux with time during concentration and recirculation steps.....	69
III.A.2.2 Pseudo stable flux against applied pressure.....	70
III.A.2.3 Limiting and critical flux	71
III.A.3 Reversible and irreversible fouling resistances – determination of critical flux.....	73
III.A.4 Fouling layer characterization	75
III.A.4.1 Composition of NF feed and of the retentate after recirculation step....	75
III.A.4.2 Roles of ions during concentration step.....	75
III.A.4.3 Roles of ions during recirculation step	77
III.A.4.3 ATR-FTIR analysis	80
III.A.4.4 SEM-EDX analysis.....	81
III.A.5 Effects of fouling phenomena on flux behavior	83
III.A.5.1 Role of colloidal silica and organics fouling layer in the initiation of scaling	83
III.A.5.2 Development of scaling and limiting flux.....	84
III.A.6 A method predicting scaling - threshold permeability before scaling	87
III.A.7 Conclusions	92
III.B Flux behavior during independent nanofiltration experiments - limiting flux and influence of the water matrix	94
III.B.1 Experimental procedure.....	94
III.B.2 Flux behavior.....	95

III.B.2.1 Variation of permeate flux with time.....	95
III.B.2.2 Influence of cross-flow velocity on pseudo-stable fluxes and existence of limiting flux	96
III.B.3 Fouling resistances.....	98
III.B.4 Fouling layer characterization	100
III.B.4.1 SEM-EDX analysis	100
III.B.4.2 ATR-FTIR analysis.....	111
III.B.5 Influence of the feed matrix composition on fouling mechanisms and flux behavior.....	114
III.B.5.1 Influence of the concentration of organic matters.....	114
III.B.5.2 Influence of salts concentration and solution pH.....	116
III.B.5.3 Conclusions	118
III.B.6 Filtration with adjusted pH	118
III.B.6.1 Experimental procedure	118
III.B.6.2 Variation of permeate flux with time in different matrix pH	119
III.B.6.3 Characteristics of fouling layer in different matrix pH	120
III.B.7 Productivity control	123
III.B.8 Conclusion	126
III.C Process selectivity - Influence of fouling types (water matrix) and operating conditions on the rejection.....	128
III.C.1 Salts rejection.....	128
III.C.2 Pharmaceuticals rejection	131
III.C.2.1 Effect of fouling types and pharmaceuticals properties - hydrophobic interaction and size exclusion	131
III.C.2.2 Effects of water matrix.....	134
III.C.2 Conclusion	135
III. Conclusion	136
Reference	137

The objective of this chapter is to investigate the main parameters which influence the productivity and the selectivity of nanofiltration for the removal of pharmaceuticals in the primary step of tertiary treatment. Thanks to the knowledge acquired, we aim at optimizing operating conditions in order to improve permeate flux and pharmaceuticals rejection.

Considering that the limitation of nanofiltration is membrane fouling, part of the study is dedicated to the identification of fouling mechanisms during filtration of the complex MBR effluent matrix. The critical flux (before the occurrence of irreversible fouling) and the limiting flux are determined and linked to the different fouling mechanisms. Based on the results obtained, a diagram showing the permeate flux behavior versus the applied pressure will give us information's about the necessary conditions to reach a high process productivity as a function of the treated water matrix.

Simultaneously, the pharmaceuticals rejection is evaluated. The influences of the water matrix and of the fouling types during the filtration on pharmaceuticals removal are studied.

III.A Limiting flux and foulant identification during nanofiltration of MBR effluent following a square wave filtration method

This section investigates the critical and limiting fluxes during the filtration of MBR effluent following the square wave filtration method (see section II.2.3). This method consists in one unique filtration using the same water matrix during which we increase and decrease alternatively transmembrane pressure. After the calculation of the reversible and irreversible fouling resistances at each applied pressure, we will focus on the identification of fouling phenomena involved in the irreversible part of the fouling. These results will allow us to define a threshold permeability below which scaling occurs, decreasing drastically the flux.

III.A.1 Experimental procedure

The pilot batch experiments simulate a feed-and-bleed continuous mode (see chapter I). The cross flow velocity is fixed to 0.2 m s^{-1} . As presented in chapter 2 (see section II.2.1.1

and II.2.1.2 experimental procedure is divided in two steps as shown in Fig III-1. The feed solution (MBR effluent) is firstly filtrated in a concentration mode. The retentate stream is recycled into feed tank while the permeate is collected until a VRF of 5 is reached; this step corresponds to a transient state as retentate concentration increases over filtration time. The second step is a recirculation step at constant retentate composition: both retentate and permeate streams are recycled into the feed tank. The permeate flux is monitored during both filtration steps. The square wave filtration method developed by Espinasse et al. [1,2] (see chapter II.2.3) is applied during the recirculation step. The pseudo stable flux is considered to be obtained when the change of flux over a 30 min period is less than 2% of the initial flux for typical runs. Beginning from 3 bar, when the flux becomes pseudo stable at a certain applied pressure, the pressure is altered positively and negatively to a new value (see Fig.III-1). For example, 5 bar is a positive variation (from 3 to 5) of pressure and 5 bar* is the negative variation (from 10 to 5).

As the square wave filtration method allows the identification of fouling type (reversible or irreversible), the critical flux can be identified. For instance, the fouling type at 10 bar can be identified by comparison of fluxes at 5 bar and 5 bar *. If the fluxes are equal, the fouling produced at 10 bar is totally reversible; if the flux at 5 bar * is lower than the one at 5 bar, it means that irreversible fouling occurs and the initial flux exceeds the critical flux.

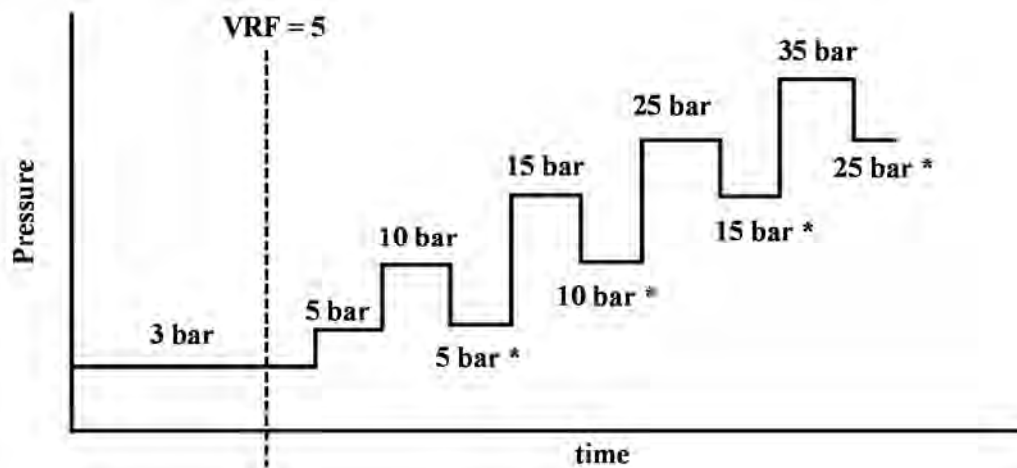


Fig.III-1 Experimental procedure

III.A.2 Flux behavior

III.A.2.1 Variation of permeate flux with time during concentration and recirculation steps

Fig III-2 presents the flux evolution over the experimental procedure (Fig.III-1). During the concentration step (at 3 bar), the flux slightly increases at the beginning and then reaches an almost stabilized value at around $62 \text{ L h}^{-1} \text{ m}^{-2}$ when $\text{VRF} = 5$ is reached. Following recirculation step, the applied pressures range from 3 to 35 bar. Clearly, when the applied pressure is maintained at 3 bar, the flux stabilizes at around $62 \text{ L h}^{-1} \text{ m}^{-2}$. As expected, when the pressure is switched to 5 bar, the flux immediately increases. After that a decline of the flux during recirculation time is observed until it reaches a stable value again at $67 \text{ L h}^{-1} \text{ m}^{-2}$. The similar increase of flux with pressure increase is observed with an applied pressure of 10 bar. However, the pseudo stable flux reaches a new value of $33 \text{ L h}^{-1} \text{ m}^{-2}$. The procedure continues with an increase of applied pressure step by step until 35 bar. With the applied pressures of 15, 25, 35 bar, the fluxes also stabilize at about $33 \text{ L h}^{-1} \text{ m}^{-2}$ (first reach), after an increase of flux at the beginning of positive variation of pressure.

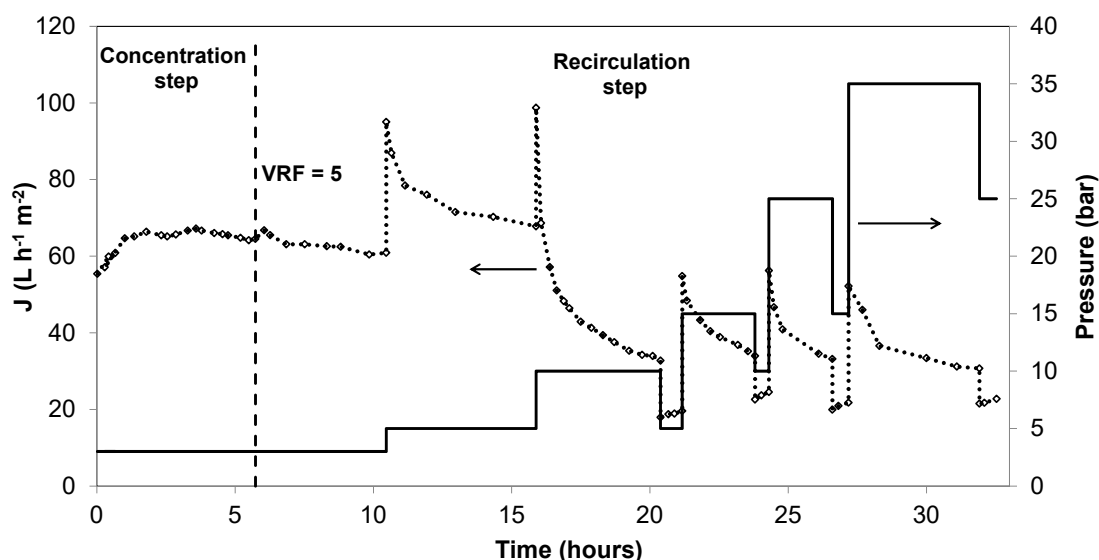


Fig. III-2 Flux evolution following the experimental procedure over time: — the continuous line represents the applied pressure; ··· the dotted line denotes the permeate flux.

III.A.2.2 Pseudo stable flux against applied pressure

Fig.III-3 plots the membrane pseudo stable flux against applied pressure following the procedure shown in Fig.III-1.

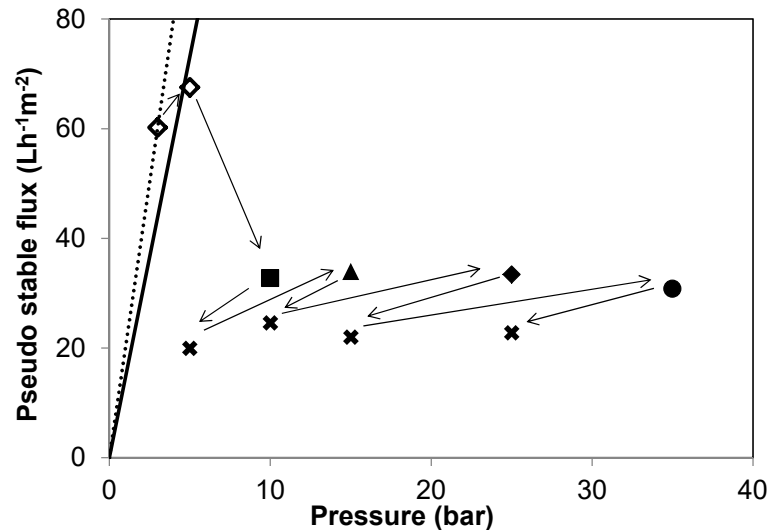


Fig.III-3 Pseudo stable flux vs applied pressure following the procedure shown on Fig.III-1; — the continuous line is the pure water permeability of membrane; ··· the dotted line is the initial MBR effluent permeability; hollow and bold points are the first pseudo stable flux reached at a certain pressure; the crosses are the stable flux reached after negative variation of pressure (5 bar*, 10 bar*, 15bar*, 25 bar* in Fig.III-1). Arrows represent the positive or negative variations of pressure.

At low pressure 3 bar, the pseudo stable flux is slightly higher above the line of pure water permeability. First, it can be assumed that this increase of flux is due to the presence of some components such as surfactants in the MBR effluent. These components can adsorb on the membrane surface and structure, enhancing membrane's wettability. However this explanation is contradictory with results presented later in the manuscript (contact angle measurements which reveal an increase of hydrophobicity and decrease of pharmaceuticals rejection which could deal with higher hydrophobic surface). Secondly, this increase in flux could be attributed to effects of the matrix pH. Previous studies [3–5] observed that the permeability of polyamide membranes increased with pH and that this phenomenon was more significant when the pH tended to alkaline. The authors [3,4] explained this behavior from the chemical nature of the polymer chains in the membrane skin layer: dissociating groups in the polymer made the surface looser when charges of the polymer chains started to repel each other at elevated pH. Braghetta et al. [3] observed 15 %

of permeate flux increase when the solution pH increased from 4 to 10 in an organic-free solution. In the present study, the new membrane was prepared in ultrapure water, the pH of which was around 6 and then the filtration carried out in MBR effluent matrix at a pH of 8. The flux increases then from $55 \text{ L h}^{-1}\text{m}^{-2}$ to $65 \text{ L h}^{-1}\text{m}^{-2}$ which represents 18 %. As a consequence, the increase of flux at the beginning of filtration could be attributed to a slight enlargement of pore size. However, considering the complex water matrix, the accumulation of ions and organics could also play a role by modifying membrane charge and pore size [6,7]. If we consider now the evolution of flux with time, we observe that under 3 bar the flux does not decrease, which means that no fouling occurs at this pressure. Then the permeability at the end of 3 bar (described as dotted line in Fig.III-3) is considered as initial permeability for filtration of MBR effluent in further calculations of fouling resistances.

When the applied pressure switches to 5 bar, the pseudo stable flux is obtained at a lower value than the one expected from initial permeability. It can be suggested that fouling occurred at 5 bar, since a flux decline with time is observed at this pressure (FigIII-2). With the increase of pressure from 5 to 10 bar (positive variation), the pseudo stable flux considerably drops.

Crosses in the Fig.III-3 represent the flux values from decreasing pressure (negative variations: 5 bar*, 10 bar*, 15bar*, 25 bar* in Fig III-1). It can be observed that two different fluxes are obtained at 5 bar and 5 bar*, the latter being well lower, which indicates that an irreversible fouling occurs during the recirculation step at 10 bar. As a consequence, the initial flux under 10 bar is above the critical flux.

III.A.2.3 Limiting and critical flux

Fig.III-4 presents the pseudo stable flux of each applied pressures. For an applied pressure of 3 bar, the pseudo stable flux is on the line of initial permeability, which means no fouling occurs. The pseudo stable flux starts to deviate from the initial permeability with an applied pressure of 5 bar due to fouling. It can be expected that the flux then obtained is not far away from the possible critical flux. When the applied pressure varies positively to 10 bar, the pseudo stable flux reduces sharply and reaches a value around $33 \text{ L h}^{-1} \text{ m}^{-2}$ that is much lower than the flux obtained when the pressure increases to 5 bar and even lower than the flux at 3 bar. It can be inferred that the possible critical flux exists in between the stable fluxes at 3 and 5 bar (between $62 \text{ L h}^{-1} \text{ m}^{-2}$ and $67 \text{ L h}^{-1} \text{ m}^{-2}$). Moreover the fact that

the positive variation of pressure from 10 to 35 bar cannot lead to an increase in pseudo stable flux indicates that the limiting flux is reached.

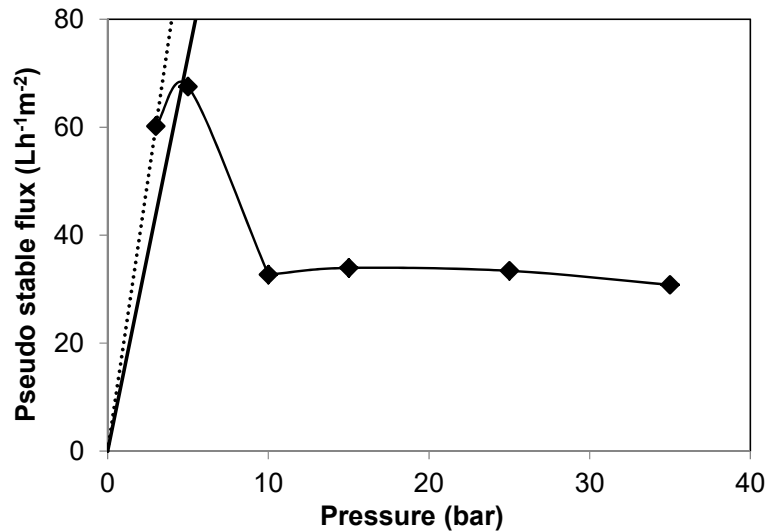


Fig.III-4 Pseudo stable flux versus pressure during filtration of MBR effluent (positive variation only); — the pure water permeability of membrane; ···· the initial MBR effluent permeability.

According to the study of Tang and Leckie [8], the critical flux depends on the membrane types, while the limiting flux is membrane independent. Based on that, three types of conceptual behaviors of critical flux and limiting flux were developed (section I.2.3). Regarding type (a) and type (b), the limiting flux is higher or equal to the critical flux. For type (c), the limiting flux is lower than the critical flux. Several types of semi-aromatic and fully aromatic membranes were tested in the study of Tang and Leckie [8] to measure the limiting flux, including the same type of membrane as the one used in the present study: NE70. The membranes were fouled by humic acid in different ionic strengths with or without calcium. All of the tested membranes including NE 70 were described as type (a) and type (b). Type (c) was not observable during humic acid filtration in the conditions tested by the authors. In the present study, the critical flux is probably exceeded with an applied pressure of 5 bar and the behavior of flux seems to correspond to type (a) or type (b) in accordance with the results of Tang and Leckie [8]. However, a further increase of the pressure (10 to 35 bar) leads to a drastic decrease of flux until a limiting value which is rather low by comparison to probable critical flux. This limiting flux behavior is similar to type (c), observation which has never been reported before.

The origin of this flux behavior will be discussed in next sections based on: i) the calculation of reversible and irreversible fouling resistances, ii) the characterization of

fouling layer at each step of the filtration procedure.

III.A.3 Reversible and irreversible fouling resistances – determination of critical flux

Thanks to the application of the square wave filtration method (alternating positive and negative variations of applied pressure), reversible and irreversible part of the fouling can be deduced [1,2] (see II.2.3).

The total fouling resistance corresponding to each pseudo stable flux can be calculated from Eq. II-5 (section II.2.3). Fig.III-5 illustrates the evolution of total fouling resistance against pseudo stable flux obtained at each pressure according to the square wave method (section II.2.3).

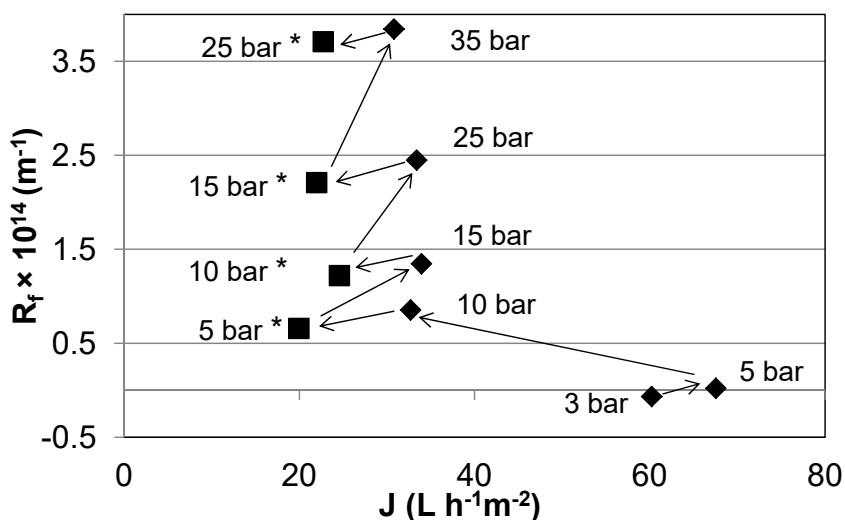


Fig III-5 Evolution of the total fouling resistance (R_f) v.s. pseudo stable flux obtained at each pressure according to the square wave method procedure (see Fig.II.4,section II.2.3)

From Fig.III-5, it can be indicated that the total fouling resistance formed at 10 bar includes both reversible and irreversible parts. First, the total fouling resistance at 5 bar* (as L_n step in Fig.II.4, section II.2.3) is larger than the total fouling resistance at 5 bar (as U_{n-1} step in Fig.II.4). It means that after an up pressure (10 bar as U_n step in Fig.II.4) the resistance cannot recover the preceding value, and this remaining resistance is the irreversible part (the difference of fouling resistance at 5 bar and 5 bar*). On the other hand, the total resistance declines from 10 bar (as U_n step in Fig.II.4) to 5 bar* (as L_n step in Fig.II.4), which refers to the reversible fouling. Similarly, the total fouling resistance formed at 15 bar, 25 bar, 35 bar includes reversible and irreversible components. Following

Eq.II-6 and Eq.II-7 (section II.2.3), the resistances due to reversible and irreversible fouling can be calculated respectively from Fig.III-5.

Fig.III-6 plots the evolution of pseudo stable flux, reversible and irreversible fouling resistances against transmembrane pressure. As we can see in Fig.II-6, both resistances due to irreversible and reversible fouling increase with the transmembrane pressure, the irreversible fouling being the dominate part of total fouling resistance. In particular, from the figure we can define a critical pressure (between 3 and 5 bar) below which irreversible fouling is not observed. In contrast, when the pressure exceeds this critical value, the irreversible fouling occurs. From the linear relationship between irreversible fouling resistance and transmembrane pressure, this critical value can be estimated to be 3.4 bar. The corresponding critical flux is evaluated to be around $69 \text{ L h}^{-1}\text{m}^{-2}$. These results verify the inference drawn in section III.A.2.3 according which critical flux is reached for an applied pressure between the 3 and 5 bar.

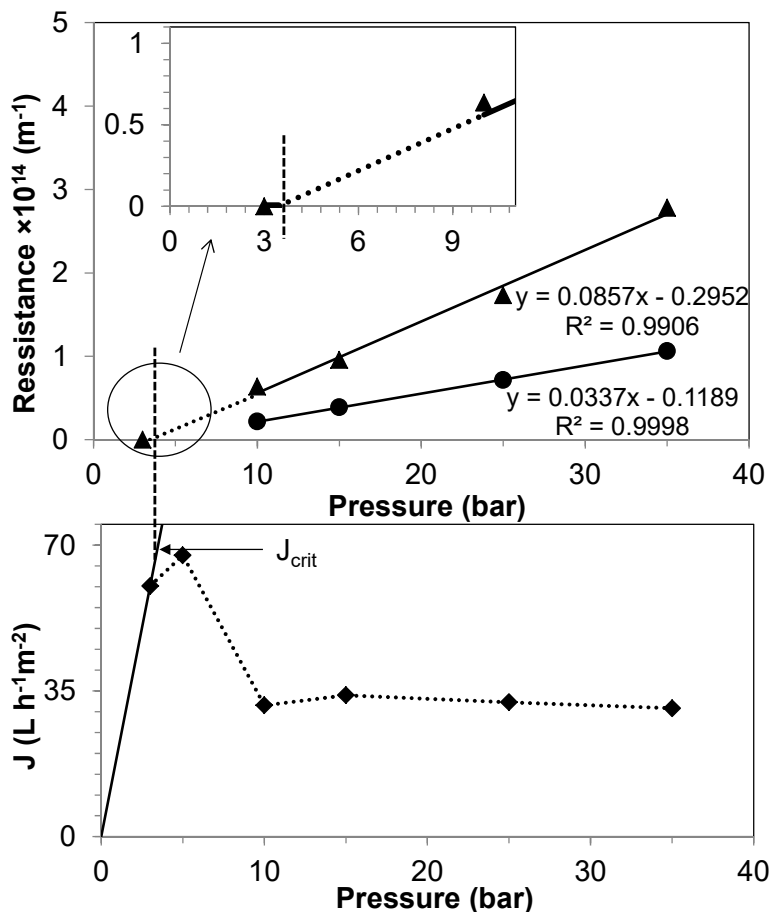


Fig.III-6 Evolution of pseudo stable flux \blacklozenge , irreversible fouling resistance \blacktriangle and reversible fouling resistance \bullet as function of pressure.

III.A.4 Fouling layer characterization

In order to explain the flux behaviors presented previously, the chemical composition of foulant layer will be identified in this section. First, the accumulation of salts can be quantified from a mass balance calculation. Then, two analytical methods are applied to identify the fouling layer components: ATR-FTIR (Fourier transform infrared spectroscopy) and SEM-EDX (scanning electron microscope with energy dispersive X-ray spectroscopy).

III.A.4.1 Composition of NF feed and of the retentate after recirculation step

As mentioned previously, the feed solution of the nanofiltration system is the MBR effluent from hospital. It is firstly concentrated 5 times in a concentration mode and then the concentrated MBR effluent (recirculation solution) is filtrated at constant retentate concentration (recirculation mode). The characteristics of the feed and the recirculation solution are presented in Table III-1.

Table III-1 Characteristics of MBR effluent and of the recirculation solution after concentration step

Item	MBR effluent (NF feed)	Recirculation solution (after concentration step VRF = 5)
pH	7.9 ± 0.2	7.6 ± 0.2
COD (mg L ⁻¹)	48 ± 3	112 ± 3
TOC (mg L ⁻¹)	19.6 ± 0.1	55.1 ± 0.1
UV ₂₅₄	0.46	1.37
Na ⁺ (mg L ⁻¹)	62.4 ± 1.1	77.9 ± 1.4
K ⁺ (mg L ⁻¹)	19.6 ± 0.3	25.4 ± 0.4
Mg ²⁺ (mg L ⁻¹)	3.3 ± 0.1	4.9 ± 0.1
Ca ²⁺ (mg L ⁻¹)	29.3 ± 0.9	43.2 ± 0.6
Cl ⁻ (mg L ⁻¹)	44.9 ± 0.9	41.6 ± 0.9
NO ₃ ⁻ (mg L ⁻¹)	7.1 ± 0.1	5.6 ± 0.1
SO ₄ ²⁻ (mg L ⁻¹)	26.8 ± 1.6	76.5 ± 4.6
PO ₄ ³⁻ * (mg L ⁻¹)	8.0 ± 0.2	18.6 ± 0.6

*Due to the analytical method, all the H₃PO₄, H₂PO₄⁻, HPO₄²⁻ and PO₄³⁻ in the solution were measured as PO₄³⁻.

III.A.4.2 Roles of ions during concentration step

During the concentration step, even if the permeate flux does not decrease and the fouling does not occur according to the flux behavior as discussed above, the accumulation

of salts on the membrane and system is observed. The accumulation of Na^+ , Ca^{2+} is the most important when the one of Cl^- is weaker as shown in table II-2 (calculation, see section II.2.4)

Table III-2 Accumulation of ions during concentration step

Mass (mg)	Na^+	K^+	Mg^{2+}	Ca^{2+}	Cl^-	NO_3^-	SO_4^{2-}	PO_4^{3-}
Feed	436.2	137.3	23.0	205.0	314.1	5.0	18.8	56.3
Retentate +Permeate								
VRF = 5	405.5	136.3	21.4	187.0	299.7	5.7	18.0	55.3
Q_{ads}	30.7	1.0	1.6	18.0	14.4	-0.7	0.8	1.0
Error \pm mg	10.7	2.9	0.4	3.6	9.1	0.1	1.6	2.6

The accumulation of Na^+ and Ca^{2+} is probably due to the electrostatic attraction between the negative charge of the virgin membrane and the positive charge of Na^+ and Ca^{2+} . Li and Elimelech [6] observed the reduction of the negative charges on the membrane surface in Na^+ and Ca^{2+} solution, Ca^{2+} being more effective than Na^+ in reducing the negative charges on the membrane surface. The authors explained these phenomena from the complexation of Ca^{2+} with the COO^- groups on the NF270 membrane (polyamine) surface. Moreover, Yoon et al. [9] found that calcium can act as a bridge between negatively charged functional groups of humic acid and membrane as shown on Fig.III-7. Li and Elimelech [10] reported that in consequence the presence of Ca^{2+} was able to induce specific membrane-NOM (natural organic matters) and NOM-NOM interactions.

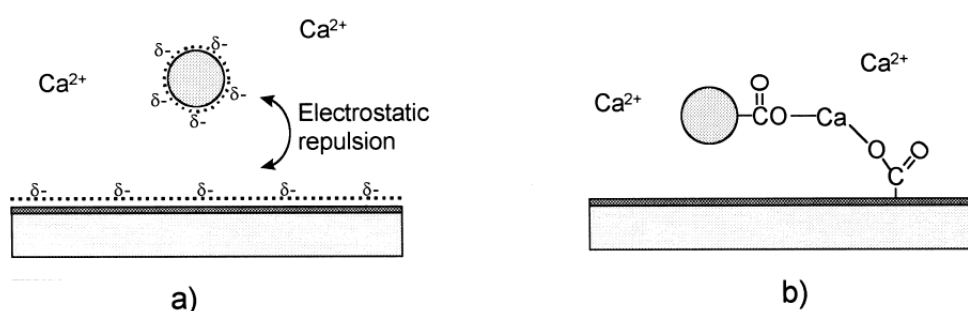


Fig.III-7 'Bridge' affection of Ca^{2+} to humic acid adsorption (a) Van der Waals force and electrostatic repulsion to the negative groups of humic acid and (b) bridging of calcium ion between negatively charged functional groups[9].

Considering the specific interactions between Ca^{2+} and negatively charged functional groups of organics, the accumulation of organic matters is deduced from the measurement of UV_{254} during the concentration step (table II-12, section II.4.5). During this step, 26% of

organic matters from the feed are accumulated on the membrane and system, which implies that the combined accumulation of Ca^{2+} and organic matters occurs. However, according to the flux behavior during the concentration step, it appears this accumulation of organics and ions does not lead to a decrease of flux. The combined accumulation could be loose and relax on the membrane surface/structure and system in the pressure conditions used during this step: 3 bar, which is quite soft.

III.A.4.3 Roles of ions during recirculation step

The concentrations of ions in the tank are monitored during recirculation step by samples collection when a stable flux is reached at each applied pressure (the volume of samples collected is less than 4% of the total volume of recirculation solution).

As we can see, in the Fig.III-8, the concentrations of Na^+ , K^+ , Mg^{2+} , Cl^- , SO_4^{2-} and HCO_3^- keep almost stable and equal to the initial concentration. The variation of Na^+ is specific, it increases and then decreases, when the concentrations of Ca^{2+} , PO_4^{3-} exhibit a slight decrease during filtration.

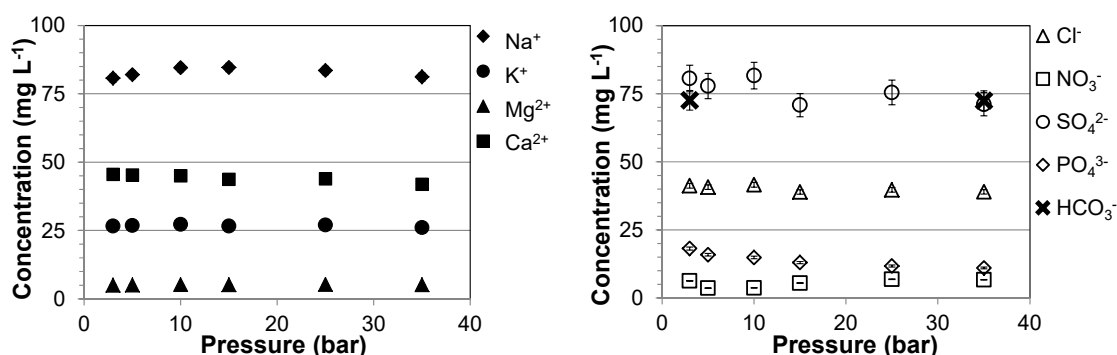


Fig.III-8 Concentrations of ions in the tank during recirculation step when stable flux is reached at each applied pressure

During the recirculation step, both retentate and permeate were recycled into the feed tank. The lost mass of ions is supposed to be accumulated on the membrane surface and structure. The accumulated mass is calculated from the concentration difference between the beginning of recirculation and the time at which the pseudo stable flux is reached at each pressure (see II.2.4).

Considering the fact that the accumulation of ions could contribute to the increase of irreversible fouling resistance, Fig.III-9 plots the evolution of both irreversible fouling

resistance and ions accumulation on the membrane surface versus the applied pressure. Three different tendencies of ions accumulation are observed. First, the accumulation of Na^+ exhibits a negative value, which implies the release of Na^+ accumulated during the concentration step (see III.A.4.2) from the membrane surface and structure to the retentate when at the same time irreversible fouling increases. Second, the accumulation of Cl^- is fluctuant around a mean value whatever the applied pressure and the irreversible fouling resistance. Third, Ca^{2+} which is slightly accumulated during concentration step is released from the membrane surface and structure to the retentate during the recirculation at 3 bar, while its accumulation increases at higher pressure (when fouling occurs). Similarly, the accumulation of PO_4^{3-} also enhances with the aggravation of fouling.

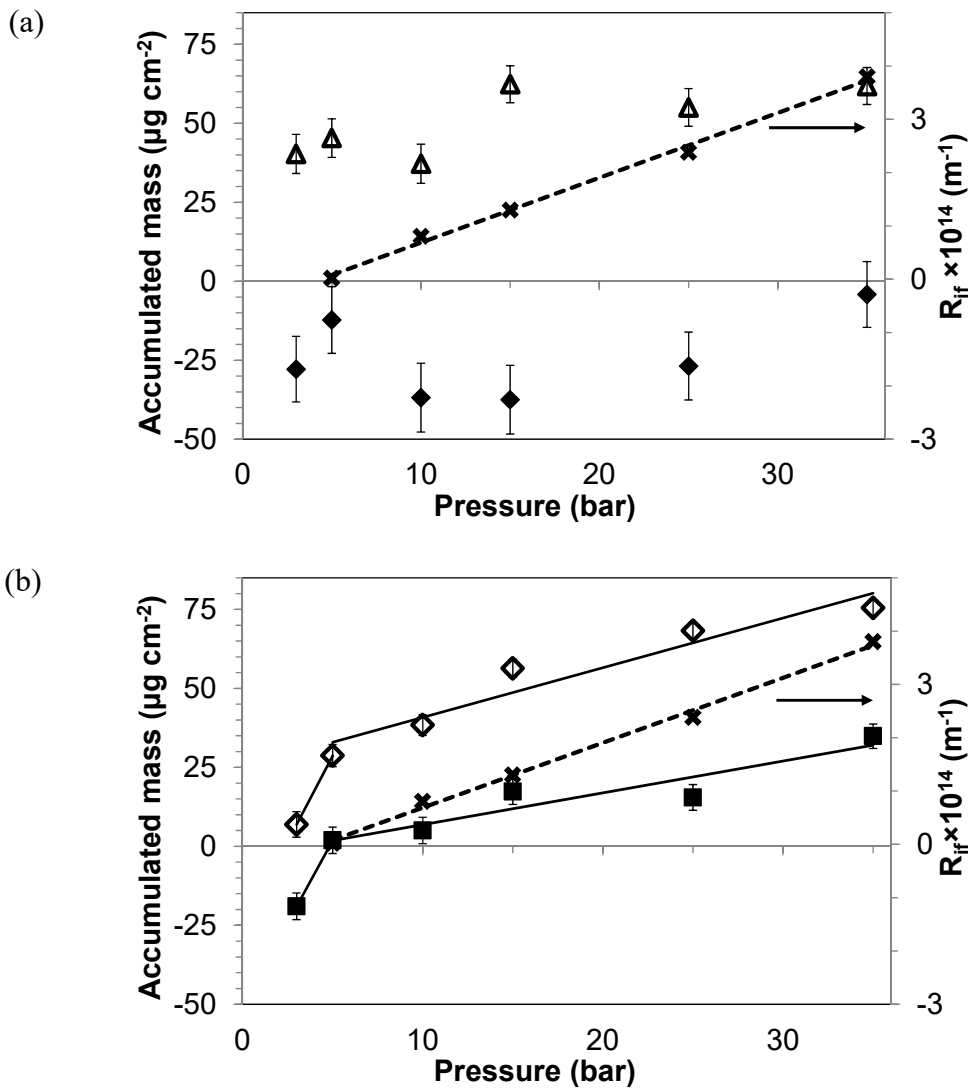


Fig. III-9 Evolution of irreversible fouling resistance \times and ions accumulated mass: (a) Na^+ \blacklozenge , Cl^- \blacktriangle , (b) Ca^{2+} \blacksquare , PO_4^{3-} \blacklozenge on the membrane with increasing applied pressure during recirculation step.

Considering these tendencies, the accumulation of Na^+ and Cl^- seems to be not related to the increase of the membrane fouling resistance. On the contrary, the accumulation of Ca^{2+} and PO_4^{3-} on the membrane surface and structure is probably correlated to the occurrence of irreversible fouling. Fig.III-9 (b) shows that the accumulation of PO_4^{3-} and Ca^{2+} exhibits good linear relationships with applied pressure during recirculation from 5 to 35 bar, while other tendency is observed during recirculation at 3 and 5 bar. This change of slope in Fig.III-9 (b) occurs for the same pressure range (between 5 and 10 bar) as the change in flux behavior in Fig III.4 (drastic drop), but we don't have at this stage all data to properly correlate both.

The accumulations of Ca^{2+} and PO_4^{3-} can induce different modifications on membrane surface characteristics. As discussed on section III.A.4.2, the accumulation of Ca^{2+} on the membrane surface acts like a bridge between membrane surface and negatively charged functional groups of organic matters. However, here the increasing accumulation of Ca^{2+} does not lead to more adsorption of organic matters. Only 2 % of organic matters from the feed (calculation, see II.2.4) is accumulated on the membrane surface and structure during the recirculation step, which is quite lower than adsorbed amount during concentration step (26% of organic matters from the feed). We can then assume in our conditions that during the recirculation step the increase of irreversible fouling resistance versus pressure is not related to organics adsorption but to salt deposit on membrane surface and structure. On the other hand, the accumulation of calcium is also referred to inverse-solubility of salts (CaCO_3 , $\text{CaSO}_4 \cdot x\text{H}_2\text{O}$, calcium phosphate etc.) which can precipitate and form a hard fouling layer on the membrane named scaling [11]. Consequently, the accumulation of Ca^{2+} during recirculation step is probably relative to the membrane scaling. For PO_4^{3-} , it has been found in previous studies [12] that the presence of phosphates can cause the formation of a viscous gel with silica and other metals at a higher hydration number resulting in a hard cement-like layer irreversibly bonded to the membrane surface. In addition, phosphates can precipitate with calcium and induce the common calcium phosphate scaling as some autopsies on membrane elements shown [11,13].

Consequently during recirculation step, the accumulation of PO_4^{3-} and Ca^{2+} contribute strongly to irreversible fouling resistance, while Cl^- and Na^+ accumulation certainly plays a negligible role on it.

III.A.4.3 ATR-FTIR analysis

ATR-FTIR spectra of virgin and fouled membrane over a wave lengths range of $4000\text{-}750\text{ cm}^{-1}$ are presented on Fig.III-10. The relative penetration depth during analysis is $2\text{ }\mu\text{m}$.

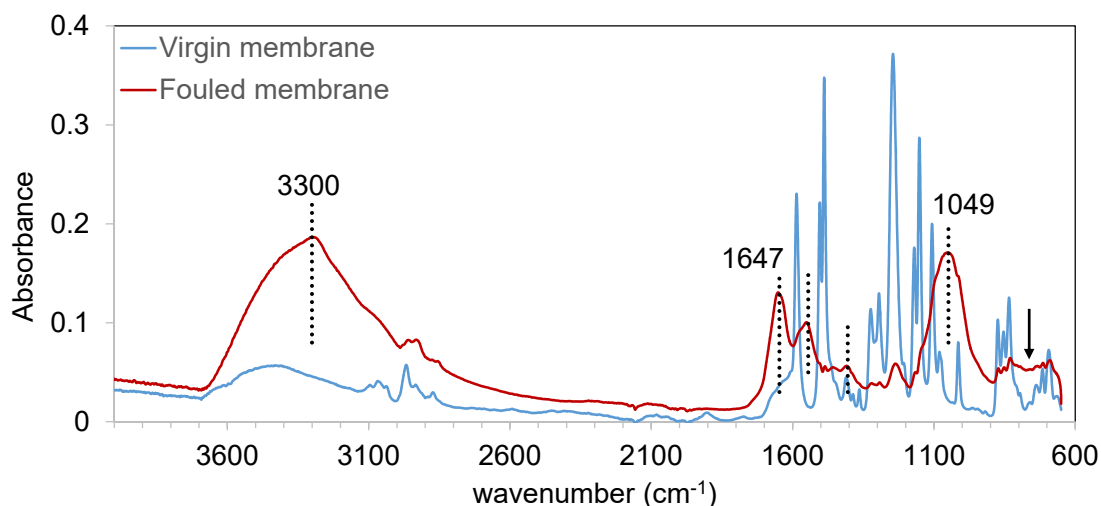


Fig.III-10 ATR-FTIR spectra of fouled and clean membrane

For virgin NE70 membrane, the characteristic absorbance of active polyamide layer, polysulfone as sub-layer, in addition to coating layer (top of the active polyamide layer) are detected. Concerning the polyamide top-layer, the peak at 1631 cm^{-1} corresponding to the amide band [14] is observed. According to the study of Tang et al. [14], polysulfone groups are detected at 1587, 1504, 1488, 1365, 1350-1280, 1245, 1180-1145, and 830 cm^{-1} . These peaks are clearly observed on the spectra of virgin membrane. The peaks observed in high wave number region ($3700\text{ - }2700\text{ cm}^{-1}$) are associated to the coating layer [14]. The strong peak around 3000 cm^{-1} suggests that the coating layer probably has rich aliphatic carbon and the peak around 3440 cm^{-1} is probably due to the additional O-H groups from the coating.

For the fouled membrane after filtration, almost all the characteristic peaks of sub-layer of polysulfone and polyamide layer cannot be observed and are replaced by the ones of foulants; even the peaks related to the coating layer (top of the active polyamide layer) are weak and difficult to be recognized. It seems that in the thickness analyzed by the equipment ($2\text{ }\mu\text{m}$) signal can be mainly attributed to fouling layer. It can be then assumed that the fouling layer thickness is close to $2\text{ }\mu\text{m}$. The absorbance at 1545, 1647 and 1040 cm^{-1} indicates the presence of colloidal organics on the fouling layer [15]: the peaks at 1545

and 1647 cm^{-1} are related to the colloidal reflected functional groups of primary and secondary amides; the absorbance at 1040 cm^{-1} is indicative of proteins and N-acetyl amino sugars, possibly present in bacterial cell [16]. OH stretching and Si-OH group vibration are observed in the regions $830\text{-}1110\text{ cm}^{-1}$ and $3700\text{-}3200\text{ cm}^{-1}$ [17], the vibration of Si-O bond appears at 791 and 754 cm^{-1} [18]. In particular, the absorbance around 820 cm^{-1} associates with the symmetric bond stretching vibration of network Si-O-Si [19]. These signals imply the presence of colloidal silica fouling. The wide and intensive peak at 1049 cm^{-1} is proposed to be characteristic of phosphate (including PO_4^{3-} , HPO_4^{2-} , $\text{H}_2\text{PO}_4^{-}$) and crystallized calcium phosphate [20–22]. The presence of the absorbance of calcium phosphate is in accordance with the accumulation of Ca^{2+} and PO_4^{3-} on membrane surface/structure which was highlighted previously (Fig III-9).

III.A.4.4 SEM-EDX analysis

SEM analysis was performed on membrane surface and cross-section before and after filtration to observe fouling layer and characterize its structure and morphology (Fig.III-11). Comparing the micrographs of virgin and fouled membrane, a variety of foulants is observed evenly distributed over the entire membrane surface. As shown on images (b) and (d), the homogenous “bright” points superpose on the dark foulant layer. According to the FTIR analysis and the morphology of the foulant, the “bright” points could be the surface crystallization of calcium phosphate and dark layer is possibly the colloidal silica and organics foulant. The image (c) presents the cross-section of fouled membrane. By comparing with the cross-section of virgin membrane (shown in Fig.II.2, chapter II), the bottom and porous part is the polysulfone sub-layer. Above it, the thin and bright layer (around $0.2\text{ }\mu\text{m}$) is the active polyamine layer. The fouling layer which is around $2\text{ }\mu\text{m}$ is on the top and its thickness is quite uniform.

Combined with SEM, EDX was used to analyze the element compositions on the surface of virgin membrane and fouling layer. EDX sampled different locations on the virgin and fouled membrane surface. The virgin membrane surface is composed by 100 % of sulphate, while the elements on the fouled membrane surface are various. The weight percentages of main elements are shown in table III-3. The major elements on the fouling layer (analyzed by the instrument) are phosphorus and calcium, which is in good agreement with the calculation of accumulated ions on the membrane and FTIR analysis. Moreover these analysis also confirm the occurrence of scaling during NF and that the

main salts responsible for scaling are calcium and phosphate. The distribution of calcium and phosphate is quite uniform, which confirms that the scaling is homogeneous on the membrane surface and structure.

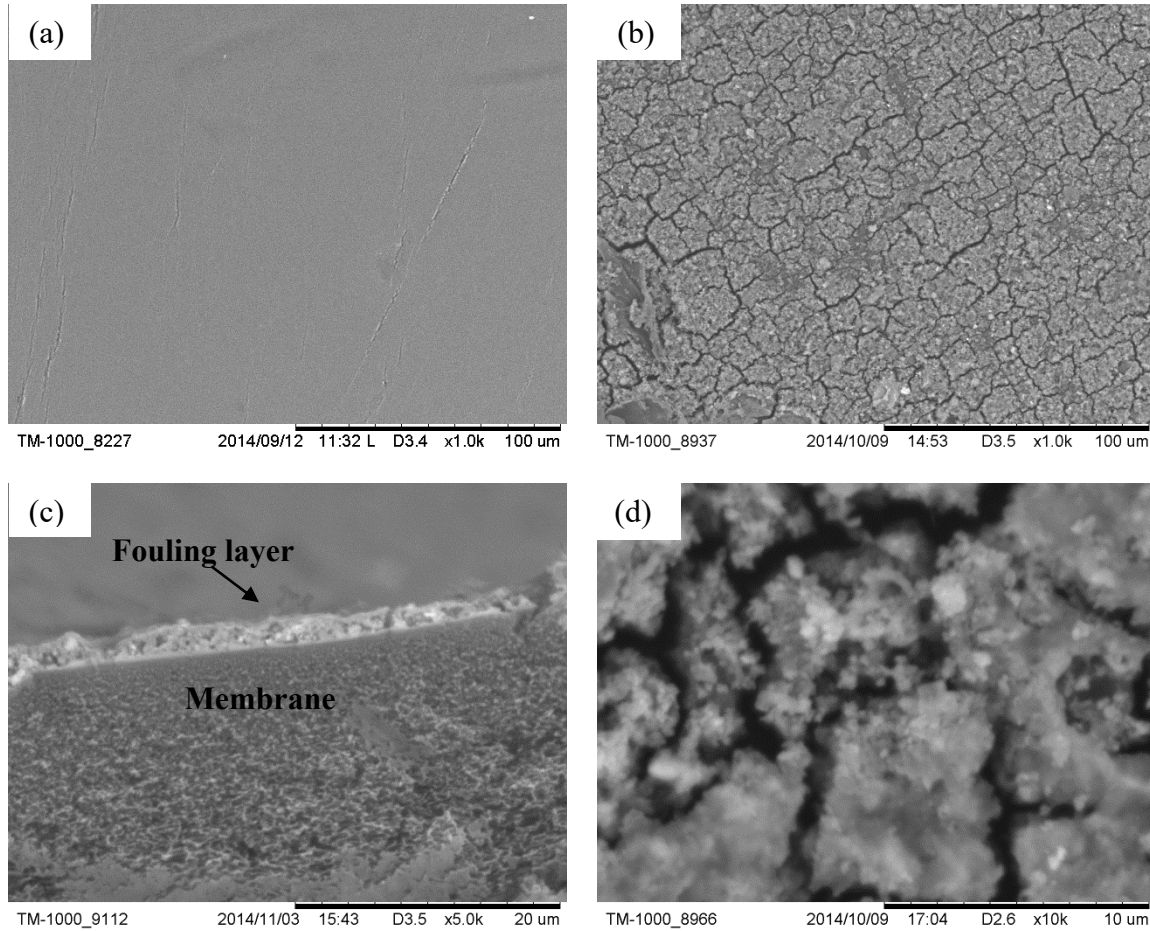


Fig. III-11 SEM images of virgin and fouled membrane: (a) Clean membrane surface 1000 ×; (b) fouled membrane 1000 ×; (c) Section of fouled membrane 5000 ×; (d) Fouled membrane surface 10000 ×.

Table III-3 EDX elements analysis at different locations on fouled membrane surface*

Samples	1	2	3	4	Average
Main element	Weight % from different locations				
Silicon	0	2.4	0	0	0.6
Phosphorus	24.6	26.6	23.2	28.8	25.8
Calcium	50.3	53.7	57.4	54.6	54
Chromium	4.8	5.0	0	7.6	4.3
Iron	4.7	4.9	0	0	2.4
Sulfur	0	0	19.3	9.8	14.6

*This instrument cannot detect C, N, O.

Based on FTIR and SEM analysis, the composition of fouling layer indicates the combined presence of colloidal silica and organics fouling and calcium phosphate inorganic fouling during filtration of MBR effluent.

III.A.5 Effects of fouling phenomena on flux behavior

The flux behaviors during filtration of MBR effluent with square wave filtration method are shown in section III.A.2. During recirculation at 3 bar, the flux keeps stable and the pseudo stable flux follows the initial permeability. The critical flux is detected around $69 \text{ L h}^{-1}\text{m}^{-2}$ (corresponding to a transmembrane pressure of 3.4 bar) from the study of fouling resistances on section III.A.3. At 5 bar, the pseudo stable flux ($67 \text{ L h}^{-1}\text{m}^{-2}$) begins to slightly deviate from the initial permeability. Its value of $67 \text{ L h}^{-1}\text{m}^{-2}$ is quite close to the value of critical flux ($69 \text{ L h}^{-1}\text{m}^{-2}$). With the applied pressure increasing to 10 bar, the pseudo stable flux decreases sharply to $33 \text{ L h}^{-1} \text{ m}^{-2}$. During the filtration with a continuing increase of applied pressure to 15, 25, 35 bar, pseudo stable fluxes keep this value identified to be the limiting flux which is well below the critical flux.

According to the characterization of fouling layer on section III.4, the fouling mechanism during filtration of MBR effluent is proposed to be the combination of colloidal silica and organics and calcium phosphate inorganic fouling. Based on this ensemble of results, it can be considered that the first deviation of stable flux from the initial permeability at 5 bar is probably due to the colloidal silica and organics fouling, the flux behavior is then in accordance with the results of Tang and Leckie [8] who fouled the membrane with humic acid. Then the sharp decline of pseudo stable flux from 5 bar to 10 bar can be attributed to the occurrence of scaling which could reduce the flux more severely than colloidal silica and organics. The following section is devoted to the identification of the phenomenon responsible for the initiation of scaling in the water matrix used in the present study.

III.A.5.1 Role of colloidal silica and organics fouling layer in the initiation of scaling

As discussed above, the sharp decrease of flux from 67 to $33 \text{ L h}^{-1} \text{ m}^{-2}$ is due to the occurrence of scaling. According to previous studies, there are two pathways of scaling in membrane systems: bulk (homogeneous) and surface (heterogeneous) crystallizations [23,24]. In the present study, the bulk crystallization is not observed (scaling does not occur at pressures 3 and 5 bar). Scaling in our system is then considered to be mainly linked to

surface crystallization [25]. Moreover, the experimental velocity 0.2 m s^{-1} is in the range of low velocity, which is in favor of surface crystallization according to the study of Lee and Lee [26].

There are two prerequisites for the occurrence of scaling at a surface: the presence of crystallization nuclei or the large enough supersaturation ratio on the membrane surface to exceed the critical supersaturation ratio for nucleation [27]. In our experiments both of them can be associated with colloidal silica and organics fouling layer built at 5 bar.

The colloidal silica and organics fouling layer possibly serves as “nuclei site” for scaling. It can be assumed that the probably electrostatic attractive interactions between the negatively charged functional groups of organic foulants adsorbed (or deposited) on membrane surface and calcium [9,10] help the formation of crystallization nuclei. Specially, it was reported that polysilicon which acts as a substrate can promote the nucleation of calcium phosphate crystal (hydroxyapatite) from the solution [28].

On the other hand, colloidal silica and organics fouling layer can increase the supersaturation ratio on the membrane surface (S_m) by means of concentration polarization. According to the study of Heok and Elimelech [29], the colloidal silica and organics cake layer hinders the back-diffusion of salt ions, which results in an enhancement of salt concentration polarization on the membrane surface.

Moreover, based on the theory of nucleation, the nucleation barrier is extremely sensitive to details (such as roughness) of the surface [25]. The colloidal silica and organics fouling layer can modify the surface state of the membrane and then the contact of liquid and membrane surface can be changed.

For all these reasons, we can believe that the colloidal silica and organics fouling layer plays a major role in the initiation of scaling formation.

III.A.5.2 Development of scaling and limiting flux

We remember that the supersaturation ratio on the membrane surface (S_m) is the driving force for the development of scaling and that S_m is associated with salts concentration on the membrane surface, in other words is linked to concentration polarization. We then propose in the following to describe the link between the permeate flux (responsible for the polarization concentration) and scaling development.

In the present study, at each positive pressure increment the flux increases at least

temporarily (just after the pressure increase) leading to a more serious polarization concentration. Consequently, the increase of salts concentration on the membrane surface leads to a S_m value higher than the critical supersaturation ratio ($S_{critical}$) on the membrane surface (chapter I), which results in the precipitation of scalants, as shown in Fig.III-12 (b). The development of scaling causes the decline of flux due to a more important surface area occupied by the scalants. At the same time, both the precipitation and decrease of flux can reduce the salts concentration on the membrane surface and then decrease S_m . The further development of scaling continues until the value of S_m reduces to $S_{critical}$. Then flux reaches a pseudo stable value again as shown in Fig.III-12 (c). Thus, it can be assumed that in the steady state conditions, the supersaturation ratio on the membrane surface reaches the critical value and the permeate flux reaches the limiting flux.

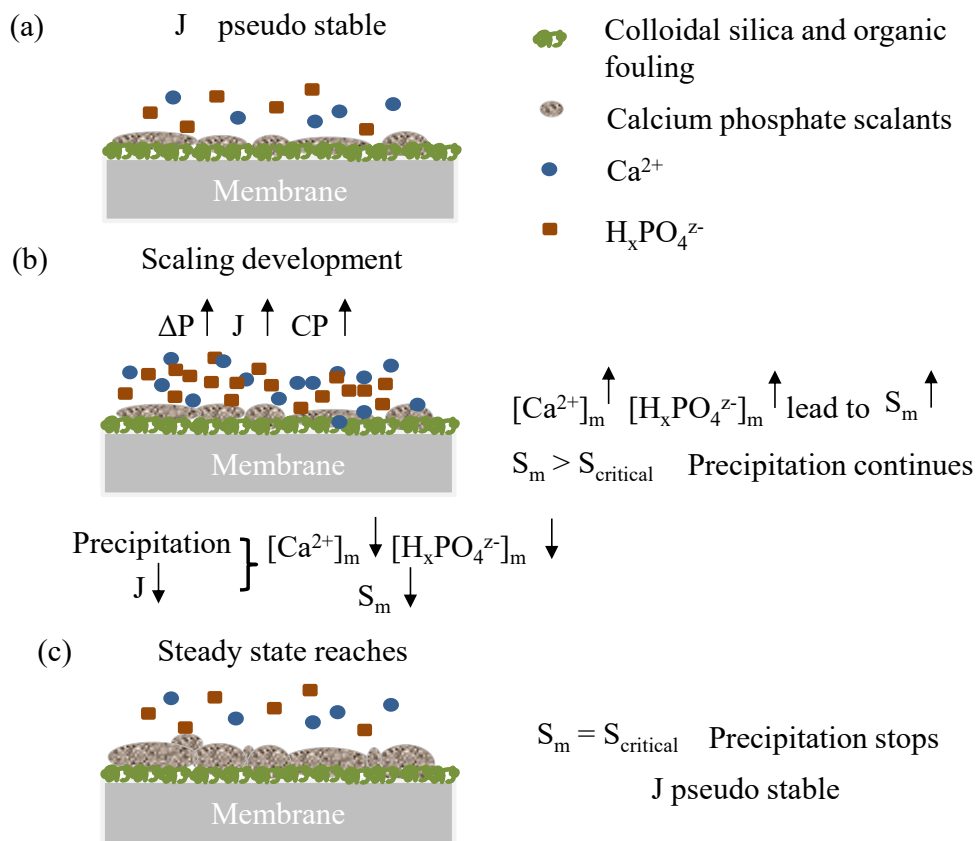


Fig.III-12 Relationship between the permeate flux (responsible for the polarization concentration) and scaling development. $[Ca^{2+}]_m$ and $[H_xPO_4^{z-}]_m$ are the concentration of calcium and phosphate on membrane surface, respectively.

As discussed on chapter I, the supersaturation ratio on membrane surface can be expressed as Eq.III-1.

$$S_m = \frac{[Ca^{2+}]_b [H_x PO_4^{z-}]_b \cdot CP(Ca^{2+}) \cdot CP(H_x PO_4^{z-})}{K_{sp}} \quad (\text{Eq.III-1})$$

where, $[Ca^{2+}]_b$ and $[H_x PO_4^{z-}]_b$ are the concentration of calcium and phosphate in the bulk, CP is the concentration polarization degree; K_{sp} is the thermodynamic solubility product of the scalant compound;

The concentration polarization degree for each ion is written as Eq.III-2 [30,31].

$$CP(H_x PO_4^{z-}) = \frac{[H_x PO_4^{z-}]_m}{[H_x PO_4^{z-}]_b} = (1 - R_{Obs(H_x PO_4^{z-})}) + R_{Obs(H_x PO_4^{z-})} \exp\left\{\frac{J}{k_{H_x PO_4^{z-}}}\right\} \quad (\text{Eq.III-2})$$

$$CP(Ca^{2+}) = \frac{[Ca^{2+}]_m}{[Ca^{2+}]_b} = (1 - R_{Obs(Ca^{2+})}) + R_{Obs(Ca^{2+})} \exp\left\{\frac{J}{k_{Ca^{2+}}}\right\} \quad (\text{Eq.III-3})$$

where $[Ca^{2+}]_m$, $[Ca^{2+}]_b$ and $[HPO_4^{2-}]_m$, $[HPO_4^{2-}]_b$ are the ion concentrations on the membrane surface and in the bulk of calcium and phosphate, respectively; J is the permeate flux; $R_{Obs(Ca^{2+})}$ and $R_{Obs(H_x PO_4^{z-})}$ are the observed ion rejections; $k_{H_x PO_4^{z-}}$ and $k_{Ca^{2+}}$ are the mass transfer coefficients of phosphate and calcium, respectively. Considering the observed salt rejections of Ca^{2+} and PO_4^{3-} approximate 1 in presence of scaling (results shown in section III.C.1), Eq.III-2 and III-3 can be simplified to Eq.III-4 and III-5 as follow. Both of them relate to the flux.

$$CP(H_x PO_4^{z-}) = \exp\left\{\frac{J}{k_{H_x PO_4^{z-}}}\right\} \quad (\text{Eq.III-4})$$

$$CP(Ca^{2+}) = \exp\left\{\frac{J}{k_{Ca^{2+}}}\right\} \quad (\text{Eq.III-5})$$

Combining the Eq.III.1, Eq.III-4 and Eq.III-5, the supersaturation ratio on the membrane surface can be expressed as Eq.III-6

$$S_m = \frac{[Ca^{2+}]_b [H_x PO_4^{z-}]_b \cdot \exp\left\{\frac{J}{k_{H_x PO_4^{z-}}}\right\} \cdot \exp\left\{\frac{J}{k_{Ca^{2+}}}\right\}}{K_{sp}} \quad (\text{Eq.III-6})$$

In steady state conditions described at the beginning of the paragraph, this equation can be rewritten as:

$$S_{critical} = \frac{[Ca^{2+}]_b [H_x PO_4^{z-}]_b \cdot \exp\left\{\frac{J_{lim}}{k_{H_x PO_4^{z-}}}\right\} \cdot \exp\left\{\frac{J_{lim}}{k_{Ca^{2+}}}\right\}}{K_{sp}} \quad (\text{Eq.III-7})$$

where, $S_{critical}$ is the critical supersaturation ratio and J_{lim} is the limiting flux.

We then assume through the mechanisms proposed in this section that, at each increment of pressure, the obtention of a pseudo stable flux corresponding to the limiting flux comes from the stabilization of supersaturation ratio on the membrane surface at its critical value $S_{critical}$, all other parameters in Eq.III-7 being constant at a certain applied pressure and tangential velocity.

III.A.6 A method predicting scaling - threshold permeability before scaling

Based on the discussion in section III.A.5, the colloidal silica and organics fouling is found at 5 bar. This fouling layer built at 5 bar plays a critical role to induce scaling. One assumption here is that there is a threshold colloidal silica and organics fouling layer which can be characterized by a threshold irreversible fouling resistance above which scaling occurs. Corresponding to this threshold resistance, we propose in this section to estimate the threshold permeability L_t , below which scaling starts to form.

As developed before, we consider in our system that the main scaling mechanism is surface crystallization. Scaling due to the surface crystallization follows the surface blockage mechanism. The membrane surface would be blocked by the lateral growth of crystals and the permeate flux only can pass through the membrane surface which is not

occupied by the crystals [26,32], as shown in Fig.III-13[26].

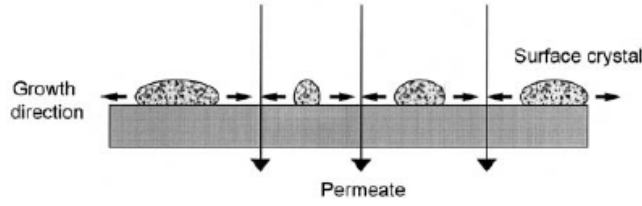


Fig.III-13 surface blockage fouling mechanism by surface crystallization in NF [26]

If fouling does not occur, the initial permeate flux can be expressed as Eq.III-8.

$$J = \frac{\Delta P}{\mu_p R_m} \quad (\text{Eq.III-8})$$

In which μ_p and R_m are the viscosity of permeate (Pa·s) and the membrane resistance (m^{-1}), respectively.

When the scaling layer is formed following a surface blockage mechanism, assuming the area occupied by crystals is completely impermeable, the flux could be expressed as follow:

$$J_a = \frac{\Delta P}{\mu_p R_m} \cdot \frac{A_{free}}{A_m} = \frac{\Delta P}{\mu_p R_m} \cdot \frac{A_m - A_{oc}}{A_m} \quad (\text{Eq.III-9})$$

where J_a is the permeate flux estimated from the surface blockage model, A_m is the membrane active area, A_{free} and A_{oc} are the membrane area unoccupied and occupied by surface crystals respectively. With the assumption that the thickness of the crystal formed on the membrane surface is constant [33], the A_{oc} could be defined as Eq.III-10:

$$A_{oc} = \beta m_s \quad (\text{Eq.III-10})$$

where β ($\text{m}^2 \text{mg}^{-1}$) is the area occupied per unit mass and m_s (mg) is the weight of the scaling layer formed directly on the membrane surface.

J_t is defined as flux decline due to colloidal silica and organics fouling, and it can be described as:

$$J_t = \frac{L_t}{\mu_p} \Delta P = \frac{\Delta P}{\mu_p (R_m + R_t + R_{tf})} \quad (\text{Eq.III-11})$$

where R_t is the threshold irreversible fouling resistance which include colloidal silica and organics fouling ; R_{rf} is reversible fouling resistance corresponding to the concentration polarization.

When scaling occurs (from 10 to 35 bar), the flux declines due to colloidal fouling layer, relative concentration polarization and surface crystals hindering. This flux can be represented by combining eq. (Eq.III-9) and (Eq.III-11):

$$J_b = \frac{L_b}{\mu_p} \Delta P = \frac{\Delta P}{\mu_p (R_m + R_t + R_{rf})} \cdot \frac{A_m - A_{oc}}{A_m} \quad (\text{Eq.III-12})$$

where J_b is the decline of flux combining two fouling mechanisms (colloidal silica and organics as well as scaling).

The reduction of permeability by surface crystallization superposed on the colloidal silica and organics layer can be expressed as follow:

$$\frac{L_b}{L_t} = \frac{J_b}{J_t} = \frac{A_m - A_{OC}}{A_m} \quad (\text{Eq.III-13})$$

where L_b is the permeability combining two mechanisms (colloidal silica and organics fouling and scaling); L_t is the permeability before scaling (corresponding to R_t). When the permeability is lower than L_t , scaling occurs.

Combining Eq.III-10 and Eq.III-13, L_b can be written as:

$$L_b = -\frac{L_t}{A_m} \beta \cdot m_s + L_t \quad (\text{Eq.III-14})$$

This function provides the relationship between the threshold permeability before scaling, the permeability combining two fouling mechanisms, and the weight of the scaling layer formed directly on the membrane surface. m_s can be estimated from the mass balance during the filtration. L_b can be obtained from the filtration with square wave filtration method. Thus, from this relationship, the threshold permeability L_t can be evaluated.

Considering that the organic and scaling combined fouling occurs from 10 to 35 bar, the permeability combining two mechanisms (L_b) at 10, 15, 25 and 35 bar is the observed permeability during filtration. This permeability can be estimated from pseudo stable flux

at a certain pressure and stable flux after negative variation of applied pressure according to the experimental procedure (Fig.III-14). For example, L_b at 10 bar can be evaluated from the pseudo stable fluxes at 10 bar and 5 bar*. Moreover, due to this procedure, the value of L_b then determined is not impacted by the concentration polarization and the reversible fouling. Consequently, L_t which is evaluated from L_b doesn't include the reversible fouling. The relationship between the threshold permeability (L_t) and the threshold fouling resistance (R_t) can be then written as Eq.III-15.

$$L_t = \frac{1}{\mu_p (R_m + R_t)} \tag{Eq.III-15}$$

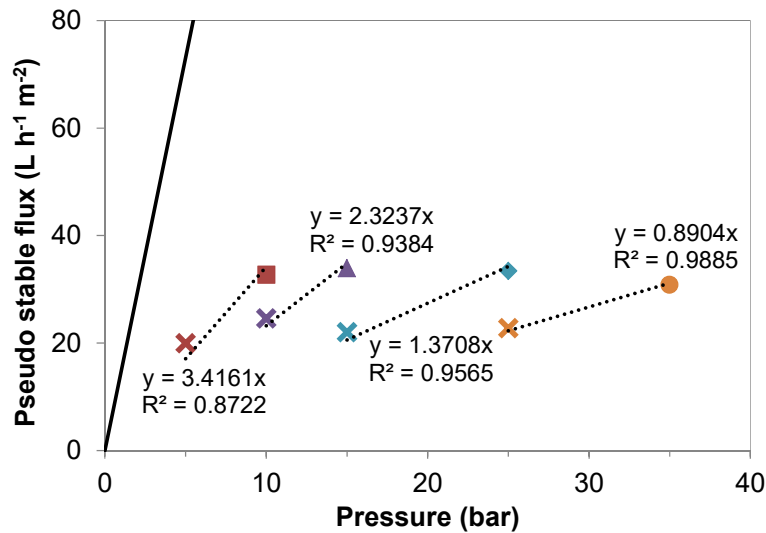


Fig.III-14 Experimental permeability measurement — the continuous line is the pure water flux of membrane; bold points are the first pseudo stable fluxes reached at a certain pressure; the crosses are the stable fluxes reached after negative variation of pressure (5 bar*, 10 bar*, 15bar*, 25 bar* in Fig.III-1).

As shown on Fig.III-14, the first permeability of 3.42 L h⁻¹ m⁻² bar⁻¹ (begin from left) is L_b after reaching pseudo stable flux at 10 bar. The following values are the permeability reached at 15, 25 and 35 bar.

In sections III.A.4.2 and III.A.4.3, we have shown that the increase in irreversible fouling resistance (from 10-35 bar) is directly linked to the accumulation of calcium and phosphate on the membrane surface. As a consequence to estimate the weight of the scaling layer on the membrane surface (m_s), the accumulated masses of Ca^{2+} and PO_4^{3-} are

calculated in the pressure range 10 to 35 bars and reported on table III-4.

Table III-4 Experimental permeability and accumulated mass of ions on the membrane

Pressure (bar)	L_b ($L h^{-1} m^{-2} bar^{-1}$)	$m_s = m_s(Ca^{2+}) + m_s(PO_4^{3-})$ (mg)
10	3.42	1.79
15	2.33	6.01
25	1.37	7.43
35	0.89	11.16

Fig.III-15 illustrates a great linear relationship between accumulated mass of Ca^{2+} and PO_4^{3-} and L_b permeability combining two fouling mechanisms. From this linear relationship, the threshold permeability L_t is calculated as $3.85 L h^{-1} m^{-2} bar^{-1}$ and the corresponding R_t as $6.83 \times 10^{13} m^{-1}$. Using this relationship the area occupied per unit mass (β) can also be deduced as $1.02 \times 10^{-3} m^2 mg^{-1}$, considering the membrane surface is $1.4 \times 10^{-2} m^2$.

The threshold fouling resistance (R_t) value is between resistance when pseudo stable flux was reached at 5 bar ($2.02 \times 10^{12} m^{-1}$) and 10 bar ($8.07 \times 10^{13} m^{-1}$). L_t predicts scaling occurs between the pressure 5 and 10 bar, which is accordance with the experimental flux behavior. The actual value of threshold pressure before scaling is not experimentally measured in this study and more filtrations are necessary to identify this pressure. It should be noticed that this threshold permeability is obtained for a given feed water composition, effects of water matrix will be discussed in next section III-B.

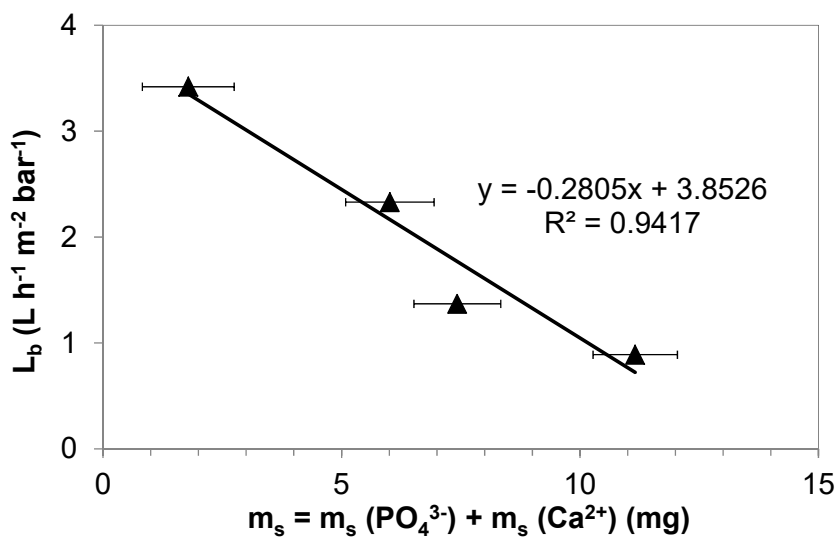


Fig.III-15 Relationship between Ca^{2+} and PO_4^{3-} accumulated mass on membrane and L_b permeability combining two fouling mechanisms.

Based on these results, if during the filtration of a certain water matrix in a certain pressure range, a great linear relationship is obtained between L_b and accumulated mass of ions, we can conclude that scaling controls fouling. If not, the process productivity is probably not affected by the problem of scaling.

The value of L_t estimated here will be verified in section III-B during independent filtrations.

III.A.7 Conclusions

The critical flux is determined with the square wave filtration method during nanofiltration of MBR effluent. For permeate fluxes exceeding the critical flux, two pseudo stable flux behaviors are observed due to different fouling mechanisms in the complex matrix used in this study.

In the first case, flux approximates to the value of critical flux, which is probably due to colloidal silica and organics fouling. This flux behavior is in accordance with the results of Tang and Leckie [8] who fouled the membrane with humic acid.

In the second case, flux is well below the critical flux and reaches the limiting flux. The analysis by ATR-FTIR and SEM-EDX of the fouling layer confirms that this limiting flux is dominantly induced by membrane scaling. Calcium and phosphate are proved to be the scaling salts. The FTIR analysis also verifies that colloidal silica and organics fouling and scaling are simultaneously present on fouled membrane surface.

The colloidal silica and organics layer plays a critical role in the inducement of the calcium and phosphate scaling. The applied pressure has also a certain effect on the development of scaling by means of flux. When the permeate flux increases, salts supersaturation ratio on membrane surface increases suddenly (concentration polarization) and gives the driving-force to continue the development of scaling until reaching the equilibrium between increase of the supersaturation ratio with flux and the decrease of flux due to the development of scaling. This equilibrium flux is the limiting flux of scaling.

Based on the critical role of colloidal silica and organics fouling in initiation of scaling, threshold permeability before scaling is defined and estimated from the observed permeability (combining colloidal fouling and scaling) and the accumulation weight of scalants. L_t predicts that scaling occurs between the pressure 5 and 10 bar in this system, which is in accordance with the experimental flux behavior.

The verification of the relevance and accuracy of L_t value is carried out in section III-B with independent filtrations.

Conclusion Figure

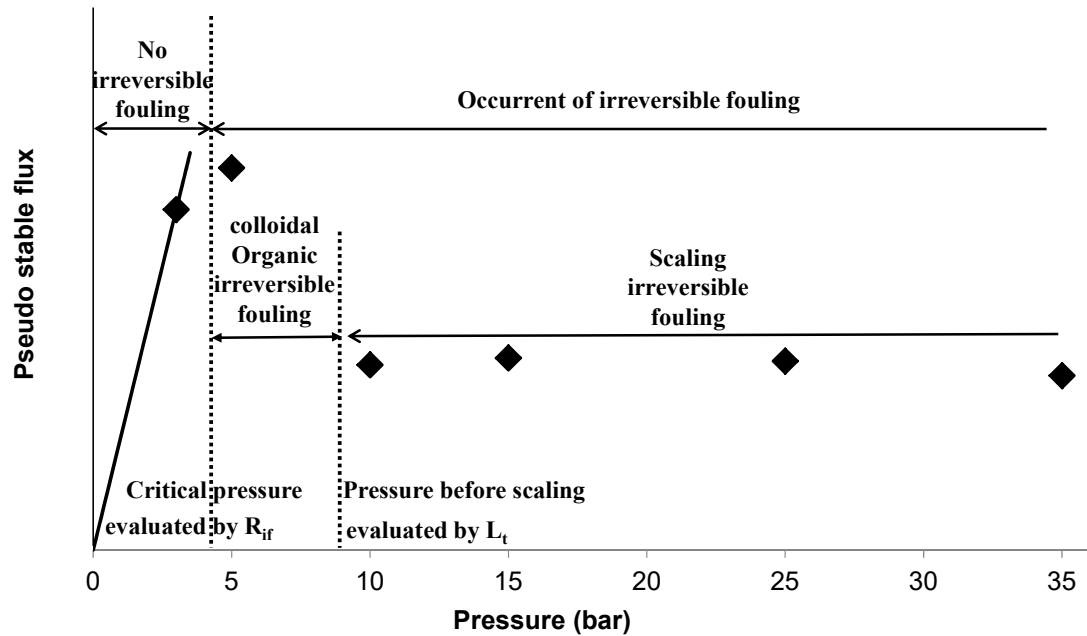


Fig.III-16 Relation between flux behaviors versus applied pressure and fouling mechanisms. The continuous line — is the initial MBR effluent permeability; bold points ◆ are the pseudo stable flux at the applied pressure.

III.B Flux behavior during independent nanofiltration experiments - limiting flux and influence of the water matrix

This section investigates flux behaviors, fouling mechanisms and productivity control during independent filtrations of MBR effluents with variabilities of water matrix. Similarly to calculations in the previous section, a critical flux can be determined by the study of fouling resistances. The association between limiting flux and the fouling mechanisms is probed from the characterization of fouling layer on the membrane surface after filtrations. The effects of effluent matrix and pH on fouling and as a consequence on flux are then discussed. Finally, these results are used to propose some actions to control nanofiltration productivity.

III.B.1 Experimental procedure

Separate filtrations were conducted at various constant applied pressures (5 to 35 bar) and two cross-flow velocities (0.2 m s^{-1} and 0.35 m s^{-1}). The operating pressures and velocities used during the filtrations are presented on Table III-5

Table III-5 Operating pressures and velocities used during independent filtrations

Pressure (bar)	Velocity = $0.2 \text{ (m s}^{-1}\text{)}$	Velocity = $0.35 \text{ (m s}^{-1}\text{)}$
3	M	
5	I	H
10	K	
15	E,G	F, L*
25	B	A,P,Q
35	D	C

A, B, C, D, E, F, G, H, I, K, L, M, P and Q are the serial name for the filtrations.

*Filtration L follows slightly different procedure, see section III.B.6

For each experiment, a new membrane sample and a new MBR effluent were used. After compaction of the membrane with ultrapure water for 3 hours, the feed (7 L of MBR effluent) was poured into the feed tank. The filtration was firstly conducted in a concentration mode (concentration step) at the selected pressure with the collection of permeate until a volume reduction factor (VRF) of 5 was reached. Then both permeate and retentate were recycled in the tank in order to keep a constant feed concentration during the recirculation step. The recirculation was stopped when the flux reached a pseudo stable

value (change of the flux over 1 hour was less than 1% of the initial flux). After the collection of the retentate, the system was rinsed with ultrapure water and then the pure water permeability was measured again.

III.B.2 Flux behavior

III.B.2.1 Variation of permeate flux with time

Fig.III-17 presents the evolution of permeate flux during nanofiltration of MBR effluent with cross-flow velocity of 0.2 and 0.35 m s⁻¹. The applied pressure ranges from 3 to 35 bar.

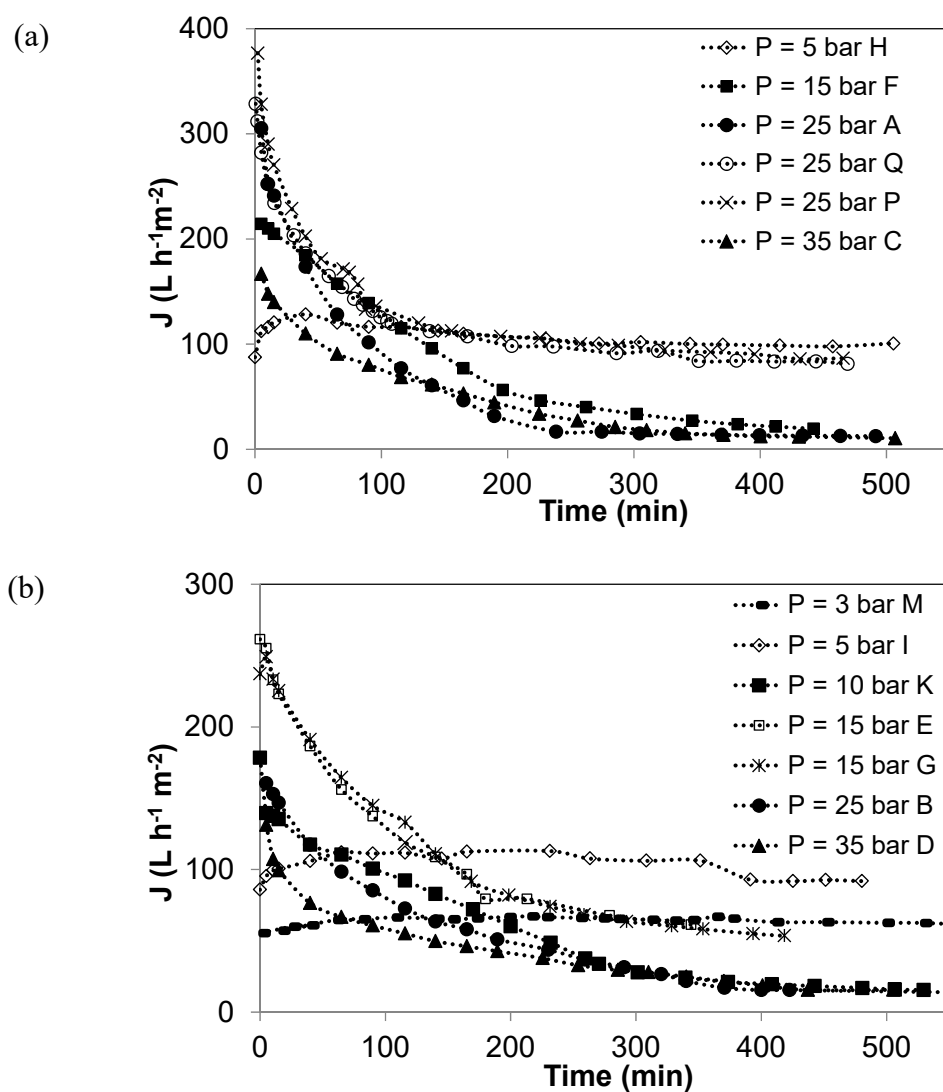


Fig.III-17 Evolution of permeate flux during NF at various pressures and two cross-flow velocities: (a) 0.35 m s⁻¹ and (b) 0.2 m s⁻¹

At low pressure (5 bar at 0.35 m s^{-1} , 3 and 5 bar at 0.2 m s^{-1}), the flux increases at the beginning of filtrations. The same rise of flux has been observed in section III.A and explained by an increase of permeability with the change of water matrix (from pure water to MBR effluent with different pH, salt composition...). When the cross-flow velocity is 0.35 m s^{-1} and the pressure 5 bar, the flux keeps stable at $100 \text{ L h}^{-1}\text{m}^{-2}$ after the increase, which indicates that fouling does not occur. The same tendency is observed at 3 bar and 0.2 m s^{-1} with a stable flux at $61 \text{ L h}^{-1}\text{m}^{-2}$. During the filtration at 5 bar and 0.2 m s^{-1} , the initial flux and steady state flux are greater than the ones at 3 bar, but the flux seems to decrease slightly from 400 min and stabilizes at $84 \text{ L h}^{-1}\text{m}^{-2}$, these conditions certainly approximate critical flux.

We can then assume that for both velocities the possible critical flux is not so far from the initial flux at 5 bar, around $100 \text{ L h}^{-1}\text{m}^{-2}$ at 0.35 m s^{-1} and $86 \text{ L h}^{-1}\text{m}^{-2}$ at 0.2 m s^{-1} . Thus, the filtration at higher velocity (0.35 m s^{-1}) can tolerate higher applied pressure and reach greater flux before fouling. The relationship between critical flux and velocity is in accordance with previous study which showed that cross-flow velocity increased the critical flux [11]. The critical pressure and flux before irreversible fouling occurs will be evaluated on section III.B.2.2 at each cross-flow velocity by means of fouling resistances calculation.

In presence of fouling, in most of the cases, filtrations at low applied pressure (corresponding to low theoretical initial flux) exhibit less flux decline to reach pseudo stable flux. In contrast, the higher the applied pressure, the greater is the flux decline whatever the velocity. These results are generally similar with the results reported by Tang and Leckie [8], Hong and Elimelech [34]. The authors suggest that the greater flux reduction at higher initial flux is probably due to the increased hydrodynamic drag force on foulant in addition to the concentration polarization.

At high applied pressure (e.g. at 35 bar), the low flux value observed at the very beginning of filtration owing to the immediate occurrence of severe fouling. Then the flux continuously decreases until it reaches pseudo stable value around $10 \text{ L h}^{-1}\text{m}^{-2}$ which is well below stable flux at 5 bar.

III.B.2.2 Influence of cross-flow velocity on pseudo-stable fluxes and existence of limiting flux

Fig.III-18 plots pseudo-stable fluxes against applied pressure for both studied

velocities. In this figure, the stable fluxes of most filtrations at 10 bar to 35 bar reach a quite similar value around 16 to 10 $\text{L h}^{-1}\text{m}^{-2}$. However, it can be noticed that filtrations P, Q, E and G reach greater pseudo stable flux than the others conducted at the same velocity and applied pressure. Due to the different flux behavior of these 4 filtrations, they are separated from the other ones and named “superior filtration”, in the following study.

At low applied pressures, the results are in good agreement with previous studies: higher is the cross-flow velocity during filtration, higher is the pseudo-stable flux [35–37]. This beneficial effect of high cross-flow velocity on the flux is attributed to the reduction of concentration polarization and to the greater shear force along the membrane surface which might help to sweep foulant away from the membrane [37,38]. Nevertheless, it seems that the benefits of high cross-flow velocity are not so significant at high applied pressures. For pressures 25 and 35 bar, the stable fluxes at 0.35 m s^{-1} and 0.2 m s^{-1} are close to each other. Especially at 35 bar, the stable fluxes reach the same value of around $10 \text{ L h}^{-1}\text{m}^{-2}$ for both velocities.

As mentioned on section III.B.2.1, figure III-18 shows that no fouling occurs for pressures lower or equal to 5 bar.

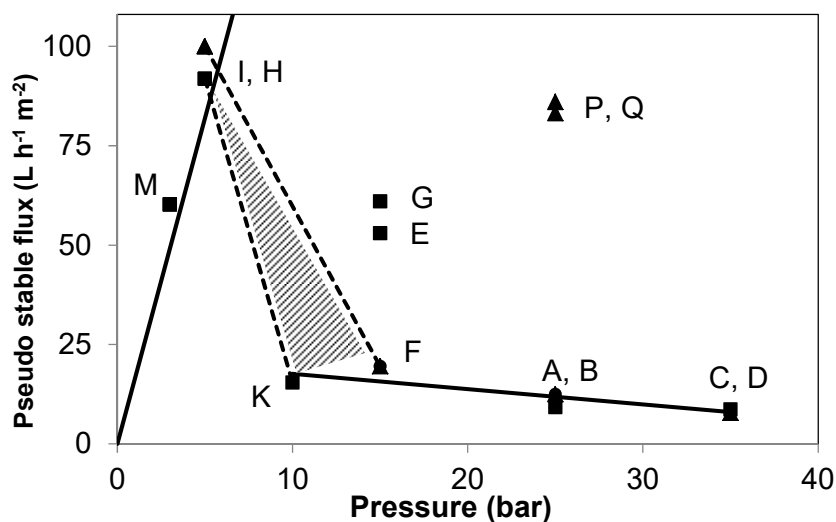


Fig.III-18 Pseudo stable flux against applied pressure with different velocities: \blacktriangle 0.35 m s^{-1} , \blacksquare 0.2 m s^{-1} during independent filtrations. The continuous line corresponds to the average pure water permeability of membranes. A, B...Q is the serial name of filtrations (see table III-5)

The pseudo stable flux deteriorates sharply for filtrations conducted at 10 bar or 15 bar for both velocities. A further increase of pressure to 35 bar does not lead to an

increase of pseudo stable flux which indicates the limiting flux is reached. The limiting value is rather low (around $10 \text{ L h}^{-1}\text{m}^{-2}$) by comparison to the probable critical flux: $100 \text{ L h}^{-1}\text{m}^{-2}$ at 0.35 m s^{-1} and $86 \text{ L h}^{-1}\text{m}^{-2}$ at 0.2 m s^{-1} . This location of limiting flux by comparison to critical flux is described as type (c) by Tang and Leckie [8] and is similar to the behavior observed in section III.A during a unique filtration using the square wave filtration method.

The four “superior filtrations” lead to higher stable flux than the others at the same applied pressure, even if the flux of them also deviates from the pure water permeability. In particular, the pseudo stable flux reaches at the end of P and Q experiments approximates the possible critical flux obtained at 5 bar ($100 \text{ L h}^{-1}\text{m}^{-2}$). Tang and Leckie [8] tested the same membrane (NE70) fouled by humic acid and obtained identical results. They described this relationship between limiting flux and critical flux as type (a) or type (b) as developed in chapter I.

Interestingly, it seems to exist two types of limiting fluxes during nanofiltration of MBR effluent with different water matrixes: one approximates the possible critical flux; the other is surprisingly well below the critical flux. As mentioned by Tang and Leckie [8], the limiting flux is membrane independent and relates to the feed matrix and the physicochemical properties of the foulants. To explain the flux behaviors observed in the present study and identify the effective parameters which influence them, further studies are carried out to characterize the foulants and to seek the relation between these characteristics and the observed limiting flux.

III.B.3 Fouling resistances

The total fouling resistance (R_f) includes the effect of concentration polarization, reversible fouling which can be removed by rinsing and the irreversible fouling remaining after rinsing (R_{ir}) (as described in Fig.II-5, chapter II). For each filtration, R_f can be calculated using the pseudo stable flux from Eq.II-7 (chapter II) and R_{ir} can be deduced from pure water permeability after filtration and rinsing using Eq.II-8 (chapter II). Considering the different flux behaviors of the four “superior filtrations” (E, G: 15 bar and 0.2 m s^{-1} and P, Q: 25 bar and 0.35 m s^{-1}), they will be discussed separately.

Fig.III-19 (a) illustrates the evolution of total and irreversible fouling resistance against the applied pressure.

The variation of R_{ir} with pressure is presented on Fig.III-19 (b). Irreversible resistance

after rinsing follows the same tendency for both velocities in the range 5-25 bar. The higher cross-flow velocity seems to slightly reduce the irreversible fouling remaining after rinsing but the lack of experimental points in the range 5-25 bar doesn't allow us to precisely locate the critical pressure for each velocity. We can only mention that we expect a critical pressure between a minimum value of 4.7 at $0.2 \text{ m}\cdot\text{s}^{-1}$ and a maximum value of 13 bar at $0.35 \text{ m}\cdot\text{s}^{-1}$.

The variation of R_f with pressure (Fig.III-19 (a)) follows a linear relationship for both cross-flow velocities with almost the same slope excepted for one point at 35 bar and $0.35 \text{ m}\cdot\text{s}^{-1}$, for which R_f increases drastically. For all the other experiments, as expected, total fouling resistance at velocity $0.2 \text{ m}\cdot\text{s}^{-1}$ is higher than the one at $0.35 \text{ m}\cdot\text{s}^{-1}$.

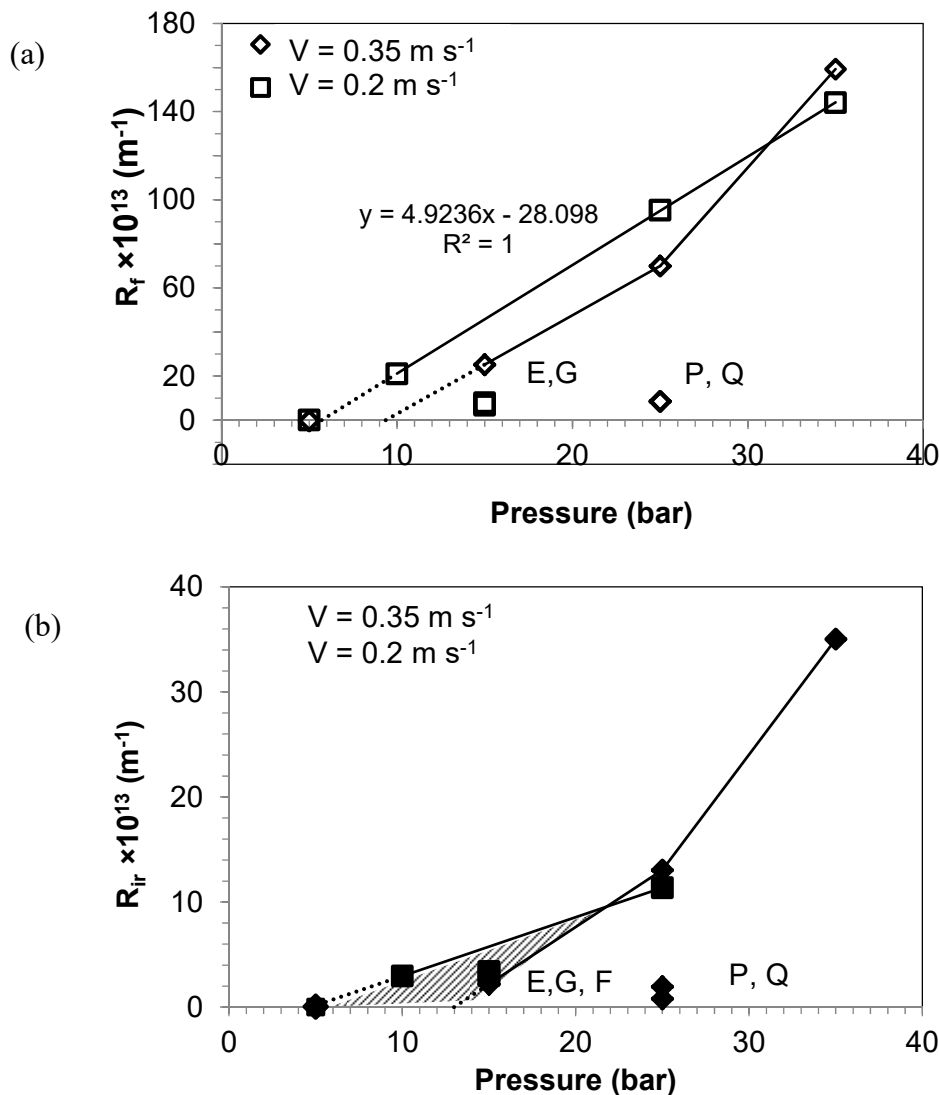


Fig.III-19 Fouling resistances: (a) total fouling resistance, (b) irreversible fouling resistance (remaining after rinsing) during each nanofiltration at various pressure and two velocities.

For the “superior filtrations”, they exhibit as expected low total fouling resistance (R_f). R_{ir} of filtrations P and Q at 25 bar and 0.35 m s^{-1} are also well below the ones of other filtrations. It can be assumed that the fouling mechanism during these 2 experiments is distinct from the other filtrations. In contrast, R_{ir} values for filtrations E and G at 15 bar and 0.2 m s^{-1} seem to follow the same relationship with the pressure as the one of the other filtrations, which indicates the mechanism leading to irreversible fouling in these 2 specific experiments is similar to the one in others filtration at the same pressure.

In next section we propose to investigate the fouling mechanisms during the various filtrations performed thanks to characterization of fouling layer.

III.B.4 Fouling layer characterization

To understand the flux behaviors, the physico-chemical properties of the foulants were analyzed by SEM-EDX and FTIR.

III.B.4.1 SEM-EDX analysis

Fig.III.20 shows the SEM images and the EDX surface element analysis of the membrane after nanofiltration in various conditions. As already mentioned, the instrument cannot detect the elements: carbon, nitrogen and oxygen.

Picture (a) is the image by SEM of the clean membrane surface. It shows a clean and homogenous surface. Sulfur is the only element detected by EDX analysis.

Picture (b) shows the membrane surface after filtration at 5 bar, 0.2 m s^{-1} . It can be observed that few spots on the surface are covered by some foulants which seem to be loose on the membrane surface. The element analysis shows the corresponding results. Only sulfur which corresponds to the membrane structure is detected on most of locations and few sample points exhibit silicon and calcium which belong to the fouling layer. Considering the flux behaviors, it can be inferred that this loose and partial fouling layer on the membrane surface does not impact on the membrane permeability.

Picture (c) presents the micrograph of membrane surface after filtration at 25 bar; 0.35 m s^{-1} (P). This filtration is one of “superior filtrations” which leads to high stable flux. The surface seems to be fouled homogeneously, which is confirmed by the EDX analysis: all the sample points show around 12 % of silicon coming from foulants and 87 % of sulfur related to membrane structure.

Picture (d) is the micrographs of fouled membrane after “superior filtration” at 15 bar, 0.2 m s^{-1} and the Picture (e) is the microscopy images of fouled membrane exhibiting a low pseudo stable flux at 15 bar, 0.35 m s^{-1} . The pictures show a dark layer with some “gel-like” particle and bright white “points” above it (especially on picture e). The distribution of these “points” is inhomogeneous on the surface. The elements correlated with fouling are disparate: silicon, calcium, phosphorus, iron, aluminum et al. The percentages of them are also various.

Pictures (f) and (g) show the fouled membrane surface after filtrations at 25 and 35 bar. During these filtrations, the stable fluxes were significantly inferior to the possible critical flux. The surfaces of these fouled membranes seem to present an homogeneous distribution of ‘bright’ particles. The shape of these “bright” particles is sharper and the size of them (varying from $0.5 \mu\text{m}$ to $2 \mu\text{m}$) is larger in the case of 35 bar on picture (g) than the ones at 25 bar on picture (f). From the cross-section image, it can be observed that the thickness of the foulant layer containing the dark and bright parts is homogenous around $2\mu\text{m}$. The species and the percentage of elements are uniform on both fouled membranes, mainly Ca and P. The percentage of Ca increases from 56% to 73% for the membrane after filtration at 25 and 35 bar, respectively. In both cases the detection of sulfur related to membrane structure is scarce. Especially at 35 bar, most of measurements do not contain sulfur.

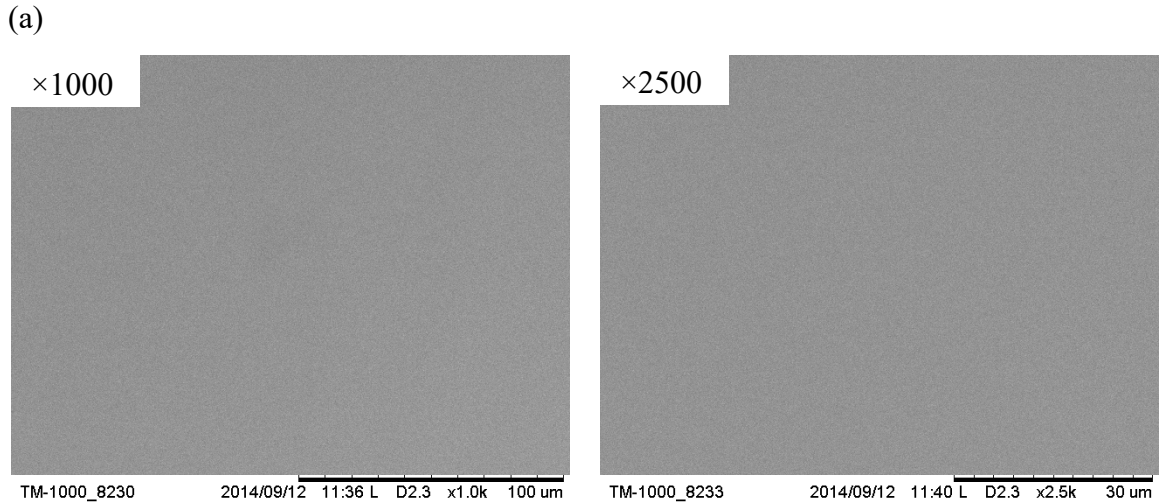


Fig.III-20 (a) SEM pictures of the virgin membrane surface

Table III-6 (a) EDX surface element analysis of the virgin membrane

Element	Weight %
Sulfur	100.0

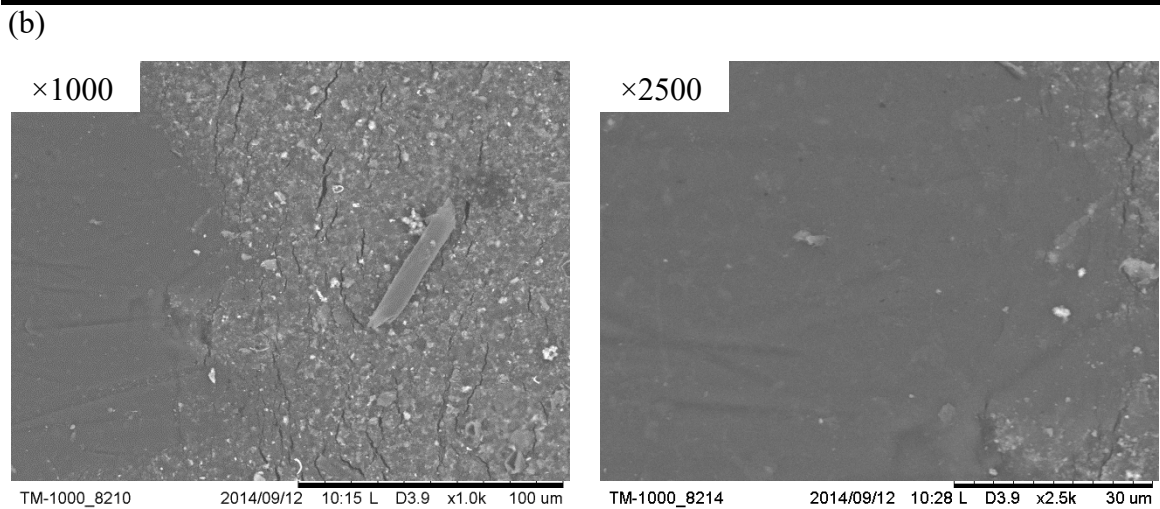


Fig.III-20 (b) SEM pictures of the membrane surface after nanofiltration at 5 bar, $V = 0.2 \text{ m s}^{-1}$ (filtration I)

Table III-6 (b) EDX surface element analysis of different locations on the membrane after filtration H

Samples	Point 1	Point 2	Point 3	Point 4	Average
Element	weight % from the different locations				
Silicon	0	9.8	14.4	0	12.1
Sulfur	100	90.2	60.3	100	87.6
Calcium	0	0	25.3	0	25.3

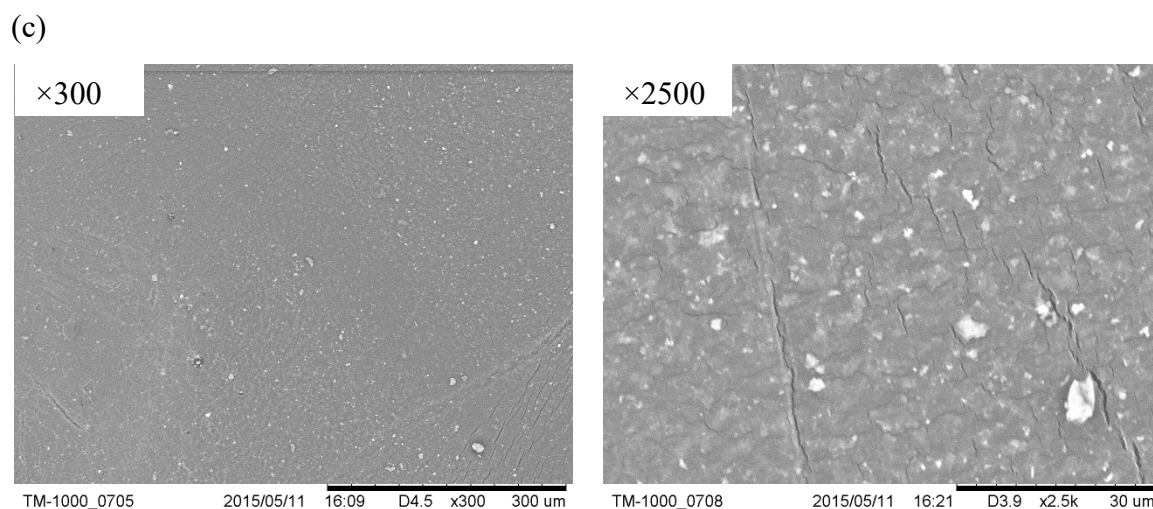


Fig.III-20 (c) SEM pictures of the membrane surface after nanofiltration at 25 bar, $V = 0.35 \text{ m s}^{-1}$ (filtration P)

Table III-6 (c) EDX surface element analysis of different locations on the membrane after filtration P

Samples	Point 1	Point 2	Point 3	Point 4	Point 5	Average
Element	weight % from the different locations					
Silicon	9.1	14.2	16.7	12.6	9.2	12.4
Sulfur	90.9	85.8	83.3	87.4	90.8	87.6

(d)

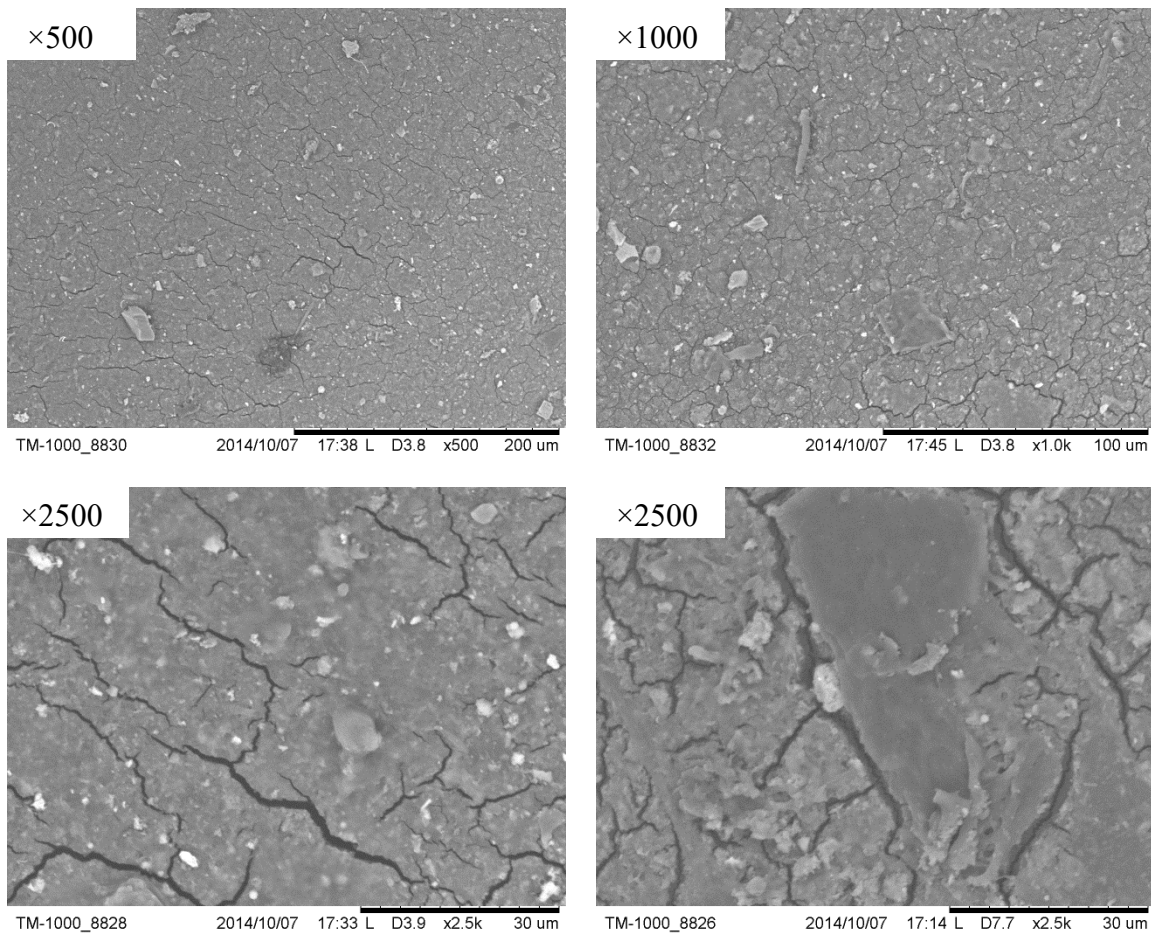


Fig.III-20 (d) SEM pictures of the membrane surface after nanofiltration at 15 bar, $V = 0.2 \text{ m s}^{-1}$ (filtration G)

Table III-6 (d) EDX surface element analysis of different locations on the membrane after filtration G

Samples	Point 1	Point 2	Point 3	Point 4	average
Element	weight % from the different locations				
Silicon	16.9	10.5	0	7.5	8.7
Sulfur	70.9	89.5	24.5	25.9	52.7
Calcium	12.2	0	45.4	33.5	22.8
phosphorus	0	0	14.7	33.1	12.0
Iron	0	0	15.4	0	3.7

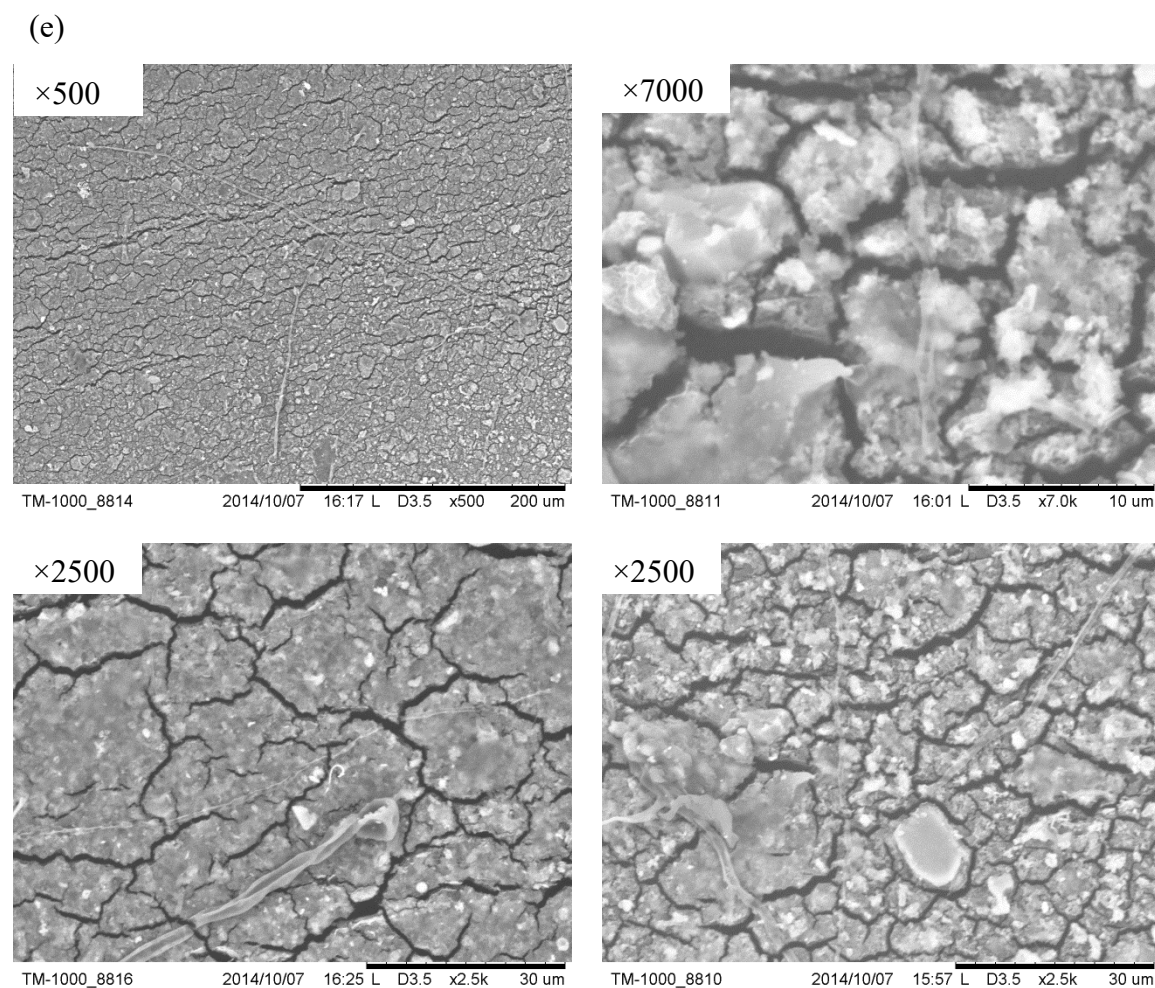


Fig.III-20 (e) SEM pictures of the membrane surface after nanofiltration at 15 bar, $V = 0.35 \text{ m s}^{-1}$ (filtration F)

Table III-6 (e) EDX surface element analysis of different locations on the membrane after filtration F

Samples	Point 1	Point 2	Point 3	Point 4	Point 5	Average
Element	weight % from the different locations					
Silicon	28.6	0	0	0	0	4.8
Sulfur	71.4	41.2	41.3	26.5	34.8	43.0
Calcium	0	47.9	45	55.3	46.2	38.9
phosphorus	0	0	13.7	18.2	19	10.2
Aluminum	0	10.8	0	0	0	1.8

(f)

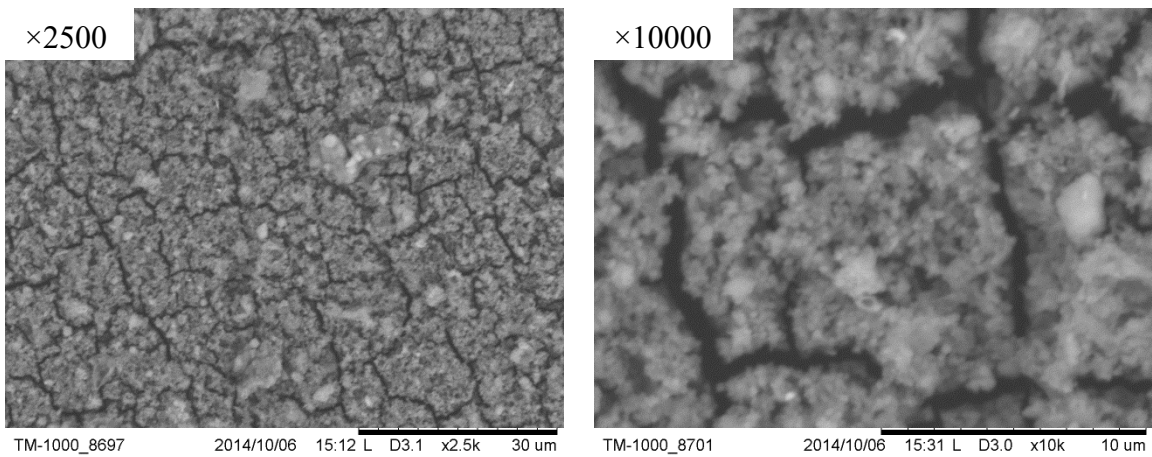


Fig.III-20(f) SEM pictures of the membrane surface after nanofiltration at 25 bar, $V=0.35 \text{ m s}^{-1}$ (filtration A)

(g)

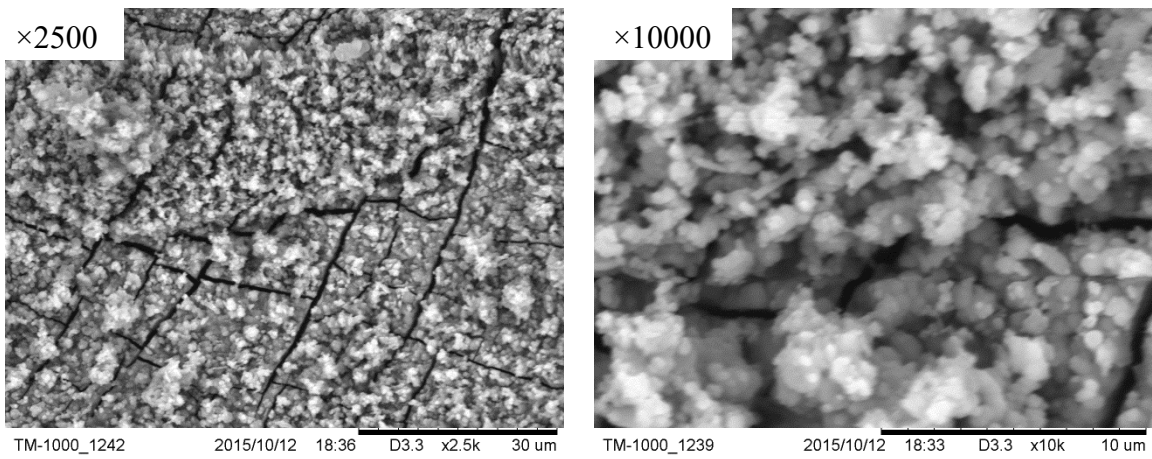


Fig.III-29 (g) SEM pictures of the membrane surface after nanofiltration at 35 bar, $V=0.2 \text{ m s}^{-1}$ (filtration D)

(h)

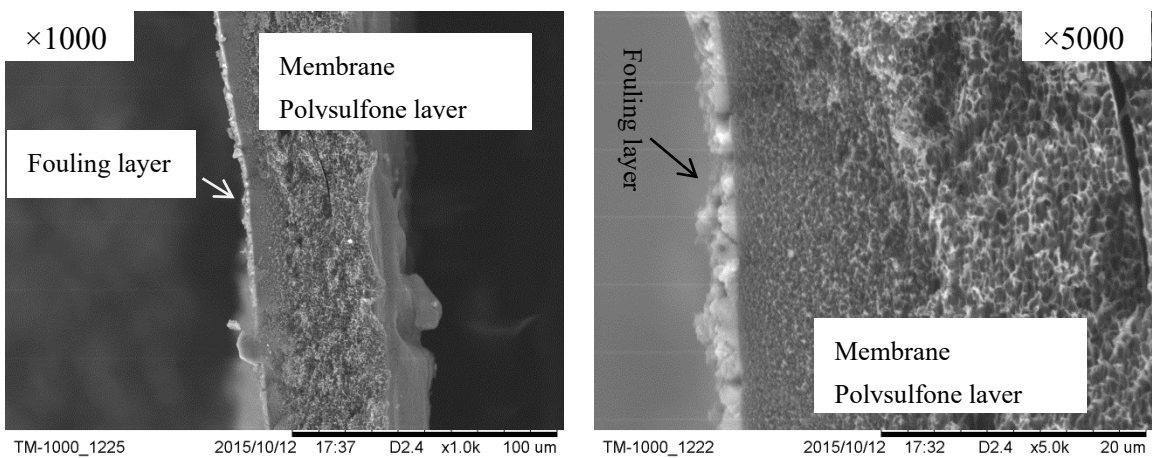


Fig.III-20 (h) SEM pictures of the cross-section of membrane surface after nanofiltration at 35 bar, $V = 0.2 \text{ m s}^{-1}$ (filtration D)

Table III-6 (f) EDX surface element analysis of different locations on the membrane after filtration at 25 bar, $V = 0.35 \text{ m s}^{-1}$ (filtration A)

Samples	Point 1	Point 2	Point 3	Average
Element	weight % from the different locations			
Silicon	2.7	3.6	2	2.8
Sulfur	11.8	7.7	7.2	8.9
Calcium	57.4	62.7	47.2	55.8
phosphorus	28.1	24.1	21.2	24.5
Magnesium	0	1.9	0	0.63
Antimony	0	0	16.3	0
Iodine	0	0	6.1	0

Table III-6 (g) EDX surface element analysis of different locations on the membrane after filtration at 35 bar, $V = 0.2 \text{ m s}^{-1}$ (filtration D)

Samples	Point 1	Point 2	Point 3	Point 4	Point 5	Point 6	Average
Element	weight % from the different locations						
Sulfur	0	0	19.3	0	0	0	3.2
Calcium	80.5	80.1	57.9	72.8	71.6	78.7	73.6
phosphorus	19.5	19.9	22.7	27.2	28.4	21.3	23.2

According to the EDX element analysis, sulfur is related to the membrane structure when calcium and phosphorus are the main elements detected in foulant layer. In order to understand the impact of these elements on fouling mechanisms, Fig.III-21 plots the relation between the percentage of calcium and sulfur, phosphorus and sulfur of sample spots on the virgin and fouled membrane surfaces.

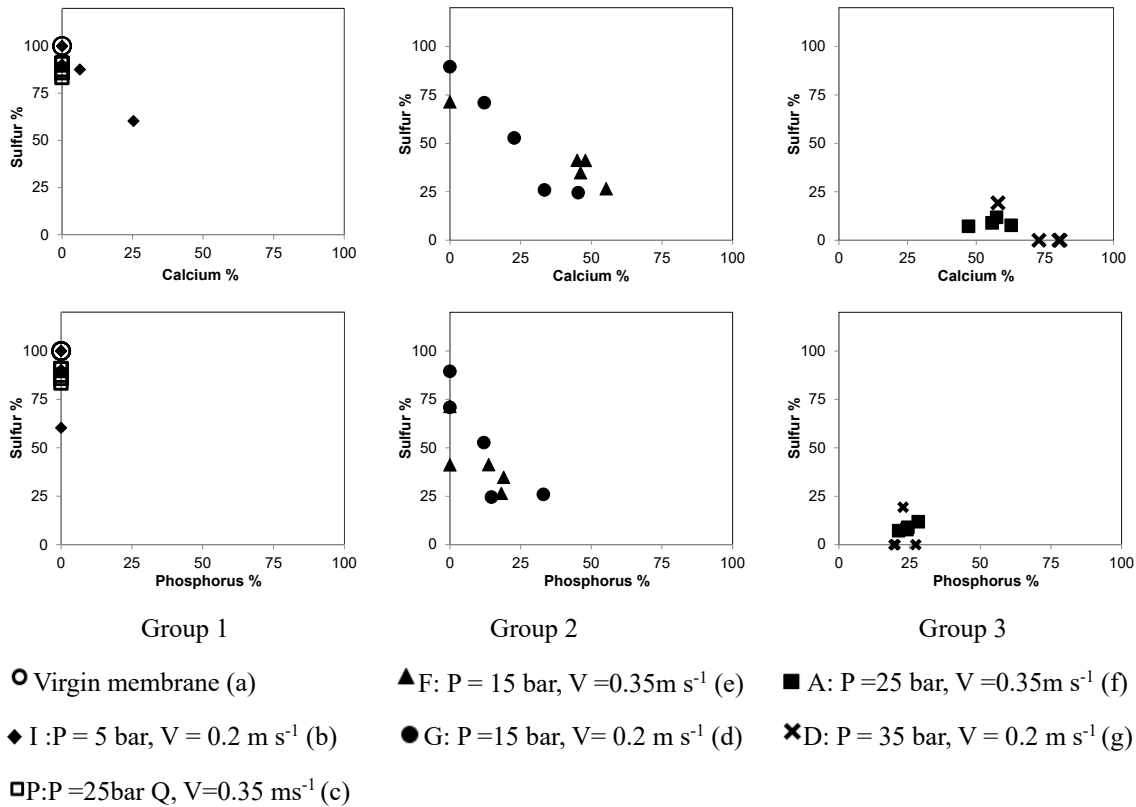


Fig.III-21 Relation between the percentages of calcium and sulfur, phosphorus and sulfur on different spots on clean and various fouled membrane samples from EDX analysis (Table III-6 (a-g)). A, D, F, I, G and P are the serial names of filtrations.

The Y-axis is the percentage of sulfur which related to the membrane structure on the virgin and fouled membrane surfaces from the EDX analysis (Table III-6(a-g)). The X-axis is the percentage of calcium or phosphorus which related to foulants on the membrane surface (Table III-6(a-g)). The virgin membrane corresponds to a coordinate point (0,100) which means 100% of sulfur for both comparisons Sulfur/Calcium and Sulfur/Phosphorus. The other coordinate points on the Y-axis indicate that the foulants on the membrane surface are not related to the X-axis element (calcium or phosphorus). The coordinate points on the X-axis correspond to samples on which the sulfur from the membrane structure cannot be detected due to severe fouling. The distribution of

coordinate points gives us information on homogenous or inhomogeneous distribution of analyzed elements on the membrane surface. For example, in group 3, all the coordinate points distribute in the same region approaching to X-axis, which means that the elements on the membrane surface is quite homogenous with less percentage of sulfur and higher percentage of calcium and phosphorus. In contrast, in group 2, the coordinate points correspond to large range of percentages of sulfur and calcium/ phosphorus, which means these percentages are different from points to points. This observation characterizes an inhomogeneous distribution of the elements on the membrane surface.

Based on the distribution of coordinate points which relates to the percentages of calcium, phosphorus and sulfur on the membrane surface, the fouling layers characterize after filtrations have been separated into three groups on Fig.III-21.

Moreover, Fig.III-22 illustrates the relationship between element ratio (Ca/S, P/S) on the fouled membrane surface and pseudo stable flux for all conditions tested. The higher the ratio Ca/S and P/S are, the more the membrane surface area is occupied by calcium and phosphate. It can be observed that the stable fluxes decrease with the increase of ratio of Ca/S and P/S. The presence of calcium and phosphorus reduces the flux seriously, in particular phosphorus which can lead to rather inferior flux even if presents at low percentage.

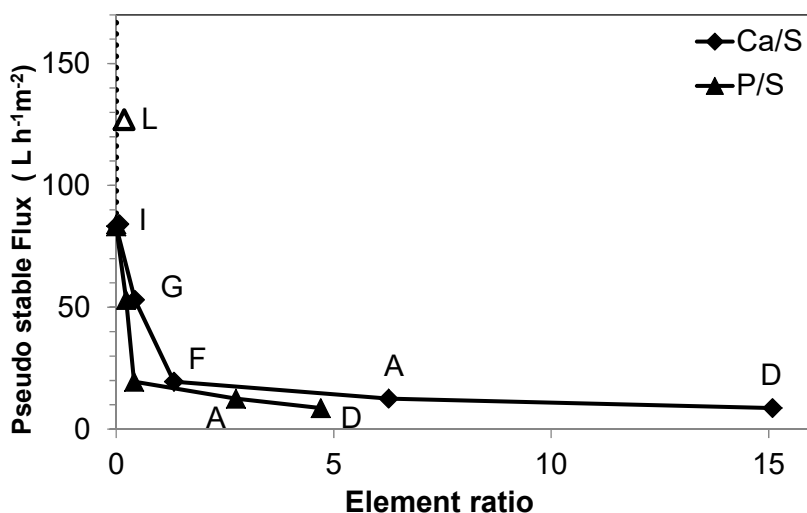


Fig.III-22 Relationship between element ratio (Ca/S, P/S) on the membrane surface and pseudo stable flux. A, D, F, H, G, and I are the serial names of filtrations.

Finally, according to Fig.III-20 to Fig.III-22, the various pseudo stable fluxes can be associated with different fouling characteristics.

Group 1, most of sample points in Fig III-21 are in the high percentage of sulfur with

seldom calcium and phosphorus. This group includes two cases in the present study: membrane after filtration at 5 bar and fouled membrane after filtration at 25 bar (one of the “superior filtrations”), the coordinate points of which is on the Y-axis. For the filtration at 5 bar, no fouling occurs (stable flux $86 \text{ L h}^{-1}\text{m}^{-2}$). For the “superior filtration” at 25 bar (stable flux $85 \text{ L h}^{-1}\text{m}^{-2}$), fouling is not related to calcium and phosphorus deposit but associated with silicon presence (EDX analysis) and probably organics.

Group 2, the coordinate points in Fig.III-21 are distributed in large region. The percentages of sulfur, calcium and phosphorus are different from sample points. The distribution of elements on the membrane surface is then inhomogeneous. This group includes two filtrations at 15 bar which lead to different stable fluxes: $19.5 \text{ L h}^{-1}\text{m}^{-2}$ for the “normal” filtration (picture (e) and table III-6(e)) and $53 \text{ L h}^{-1}\text{m}^{-2}$ for the “superior filtration” (picture (d) and table III-6(d)). As shown thanks to SEM-EDX analysis, membrane sample with more calcium and phosphorus on the surface (both observation and percentage) reaches lower pseudo stable flux. Then, the higher stable flux obtains at the “superior filtrations” (E, G) is due to less membrane surface area occupied by calcium and phosphorus.

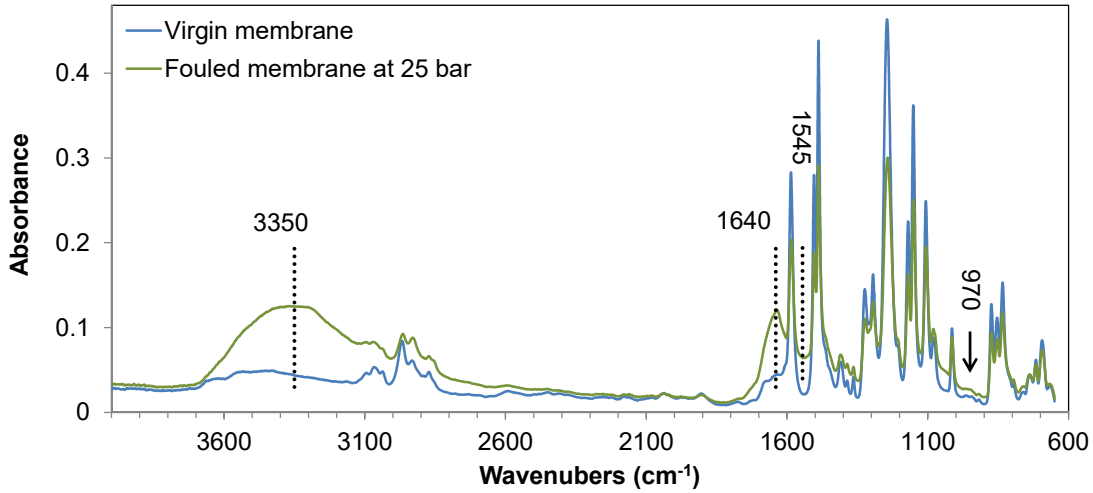
Group 3, the coordinate points in Fig.III-21 are in the same region close to the X-axis (or even on it). In this group, membrane surface is almost completely covered by the foulant layer and the distributions of calcium and phosphate are homogeneous on the membrane surface. Filtrations at 25 and 35 bar, for which lower stable fluxes in the range of $10 \text{ L h}^{-1}\text{m}^{-2}$ are observed, belong to this group. When distribution of calcium and phosphorus is homogeneous (Fig.III-21) and the ratios of Ca/S and P/S are above 1.3 and 0.4 (Fig.III-22), the increasing percentage of Ca and P seems to not affect the pseudo stable flux severely: the percentages of Ca and P are higher on the membrane after filtration at 35 bar (D) than the ones at 25 bar (A), while the stable fluxes are quite similar ($12 \text{ L h}^{-1}\text{m}^{-2}$ at 25 bar and $9 \text{ L h}^{-1}\text{m}^{-2}$ at 35 bar).

It is then evidenced that calcium and phosphorus are the most important components in the fouling layer. Calcium probably comes from Ca^{2+} , while the identification of the form of phosphorus needs further studies to be confirmed. Silicon has been confirmed to be related to colloidal fouling during NF and RO processes [39,40]. It is detected on the fouled membrane surface exhibiting the higher stable flux and its percentage decreases when the pseudo stable flux is low. The absence of sulfur and silicon in the case of severe fouling is probably due to the fact that they are beneath calcium and phosphorus layer and out of the range of detection depth of EDX analysis.

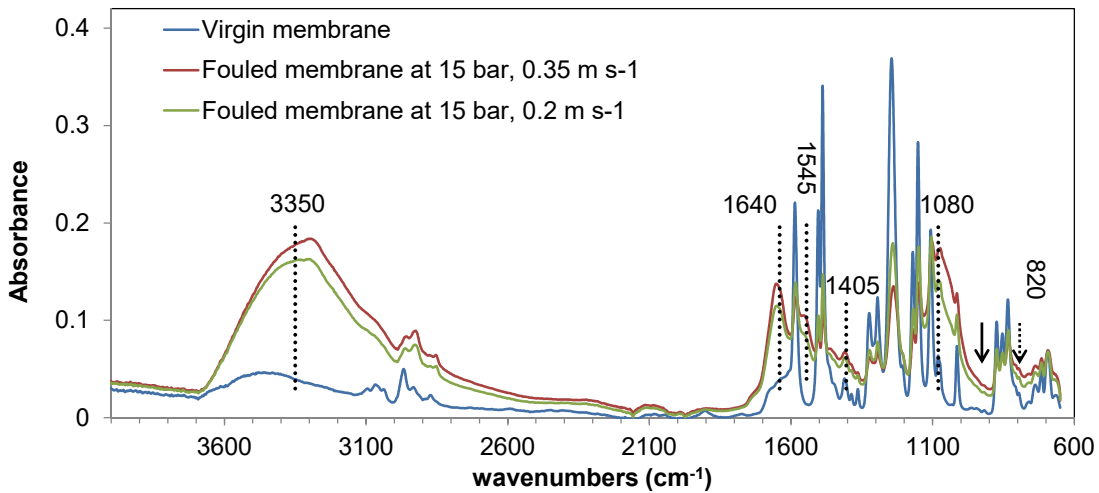
II.B.4.2 ATR-FTIR analysis

The chemical composition of the foulants was qualitatively analyzed by FTIR. Fig III-23 presents the ATR-FTIR spectra of virgin and fouled membranes. On the spectrum of the virgin membrane, peaks at 1587, 1504, and 1488 cm^{-1} are attributed to the polysulfone support; peaks at 1630 cm^{-1} to the polyamide active layer, and peaks over (3000-2900 cm^{-1}) corresponds to the absorbance of the coating layer. The spectra of fouled membranes are separated in three groups according to the different fouling characteristics discussed above.

Group 1:



Group 2:



Group 3:

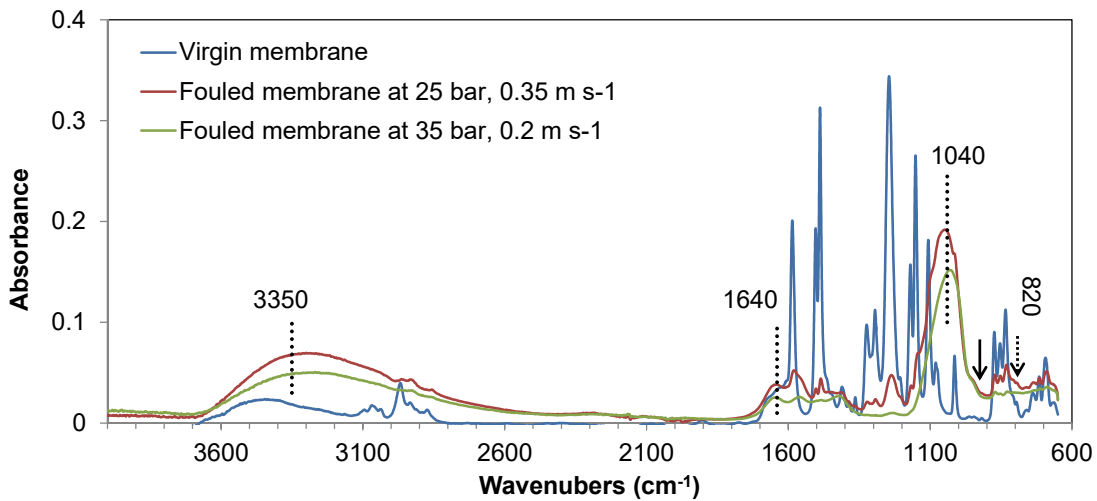


Fig III-23 FTIR spectra of virgin and fouled membranes after filtration at various pressures

Group 1: The absorbance at the wave numbers of 1545, 1647 and 1040 cm^{-1} relates to the colloidal organics fouling on NF membrane [15]. The OH stretching vibrations of the Si-OH group are observed in the regions of 900-1110 cm^{-1} and 3700-3200 cm^{-1} [17]. These absorbances specially associate with the Si-O vibrations of silanol [19]. The perpendicular vibration of Si-O appear at 754 cm^{-1} [18], which confirms the presence of silica. The absence of the absorbance of Si-O-Si indicates that the form of silica in the fouling layer is mainly monosilicic acid. The foulant layer is then proposed to be composed of colloidal organics and monosilicic acid.

Group 2: The absorbance of the membrane structure (polysulfone and polyamide) is weaker. The absorbance of the colloidal organics fouling is observed as in group 1. The absorbance in the regions of 830-1110 cm^{-1} , 3700-3200 cm^{-1} and 754 cm^{-1} correlates with the monosilicic acid presence. The absorbance at the wave numbers of 820 cm^{-1} associated to the symmetric bond stretching vibrations of network Si-O-Si [19] indicates the presence of polysilicic acid or colloidal silica on the fouling layer. In addition, an absorbance peak at 1080 cm^{-1} is observed corresponding to phosphate and calcium phosphate presence [21,22,41]. It can be confirmed that the form of calcium and phosphorus on the fouling layer is calcium phosphate. These results infer that the combined fouling of colloidal silica, organics and scaling (calcium phosphate) occurs, while the scaling part (calcium phosphate) distributes on the membrane surface and structure heterogeneously according to SEM-EDX analysis.

Group 3: The absorbance of the membrane structure is scarcely observed, we can then assume that the fouling layer thickness is around 2 μm above the membrane surface, considering the analyzed depth. The absorbance relating to colloidal silica and organics fouling becomes weaker, while the peak corresponding to calcium phosphate is intense and wide in the range of 1000-1100 cm^{-1} [21,22,41]. The scaling layer becomes thicker and homogenous (according to the discussion on SEM-EDX results).

From the SEM-EDX and ATR-FTIR analysis, it is confirmed that the two ranges of limiting fluxes during nanofiltration with NE70 is due to distinct fouling mechanisms.

The limiting flux with the value approaching to the possible critical flux (86 $\text{L h}^{-1}\text{m}^{-2}$) is induced by an homogeneous colloidal silica and organics fouling (group 1).

The limiting flux is well below the possible critical flux when the membrane is fouled simultaneously by colloidal silica and organics and homogenous calcium and phosphate scaling. The fluxes reduce severely in this case. The limiting flux is in the range of 10 $\text{L h}^{-1}\text{m}^{-2}$ (1% - 2% of theoretical initial flux). In this case the increasing percentage of Ca

and P on the membrane surface seems not to affect the pseudo stable flux, because the membrane surface is almost completely occupied by an homogenous calcium phosphate layer. The filtrations at 25 (A) and 35 bar (D) associated with this type of fouling mechanisms belong to the group 3 according SEM-EDX and ATR-FTIR analysis.

There is an “intermediate” case for which the fouling layer exhibits the characteristics of both colloidal silica and organics fouling and calcium phosphate scaling, but in this case calcium and phosphate distribute inhomogeneously on partial membrane surface. The pseudo stable flux can be in a wide range between the limiting flux due to silica organic fouling and the one due to combined effects of silica organic fouling and homogenous scaling. The pseudo stable flux then greatly depends on the surface area occupied by calcium phosphate scaling. The two filtrations at 15 bar correspond to this situation. The pseudo stable fluxes obtained can be 53 or 19 L h⁻¹m⁻² depending on the distribution and the percentage of calcium and phosphate on membrane surface. These results are in accordance with the discussion of R_{ir} development with pressure: “superior filtrations” at 15 bar follows almost the same tendency with the other filtrations in section III.B.3 (Fig.III-19).

Thus, three types of fouling mechanisms related to the different ranges of pseudo stable and limiting fluxes have been proposed in the present section. The next paragraphs are dedicated to the study of the effects of feed matrix composition and pH on the extent of these mechanisms.

III.B.5 Influence of the feed matrix composition on fouling mechanisms and flux behavior

This section is devoted to investigate the influence of matrix composition on the pseudo-stable fluxes obtained during filtration, based on the fouling mechanisms discussed on section III.B.4. Especially we will focus on the influence of concentrations of organics, calcium and phosphate but also of the pH of the feed.

III.B.5.1 Influence of the concentration of organic matters

According to the film theory, when the concentration of the solute in the permeate is negligible and the tangential velocity kept constant, Eq.III-9 links pseudo-stable flux (J_{stab}),

solute concentration in the retentate (C_R) and at the membrane surface (C_m) (see Chapter I)

$$J_{stab} = k \ln C_m - k \ln C_R \quad (\text{Eq.III-9})$$

From Eq.III-9, J_{stab} exhibits a linear relationship with $\ln C_R$ which allows the calculation of mass transfer coefficient of the solute in the boundary layer (k). In our experiments, filtrations for which fouling and related fluxes are controlled by organics are the ones belonging to group 1 (H, P and Q). In these experiments organics concentration in the recirculation solution (C_R) was determined by the UV absorbance of the solution at the wavelength of 254 nm when the pseudo stable flux was reached.

Fig.III-24 exhibits the relationship between pseudo-stable flux and $\ln UV_{254}$ for filtrations of group 1 and velocity 0.35 m s^{-1} (filtrations H, P, Q). For these experiments, it has been verified that organics rejection is higher than 90%.

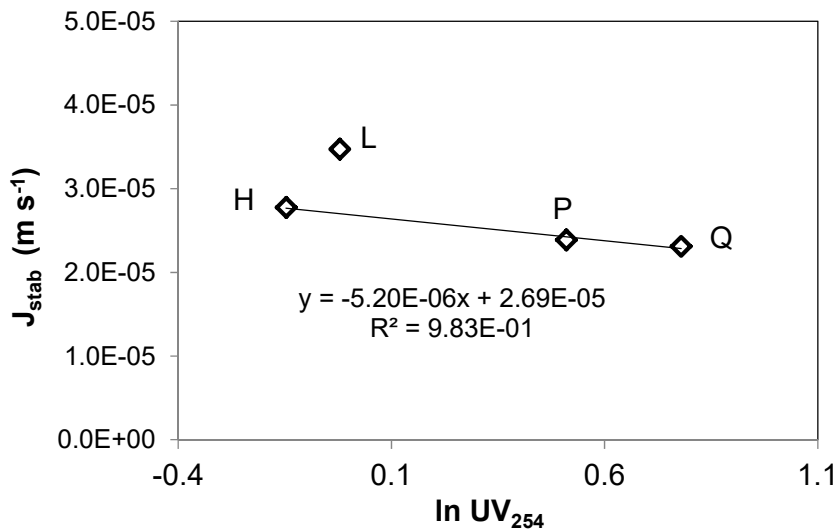


Fig. III-24 Relationship between pseudo-stable flux and $\ln UV_{254}$ (absorbance of the retentate) obtained during independent filtrations at a velocity of 0.35 m s^{-1} and belonging to group 1 (homogeneous colloidal silica and organics fouling).

The linear relationship obtained between $\ln UV_{254}$ and J_{stat} confirms the role of the organics concentration in the value of the steady-stable flux obtained during filtrations belonging to group 1. The mass transfer coefficient for organics deduced from this figure is $5.2 \times 10^{-6} \text{ m s}^{-1}$ (for the velocity 0.35 m s^{-1}).

III.B.5.2 Influence of salts concentration and solution pH

It was illustrated on section III.B.4 that the serious fouling and low limiting flux are induced by the scaling from precipitation of calcium phosphate. The precipitation of these components depends on the supersaturation ratio on membrane surface (S_m) as Eq III-I (in section III.A.5.2) as consequence on $[Ca^{2+}]$ and $[H_xPO_4^{z-}]$ the concentration of calcium and phosphate in the solution.

Fig III-25 plots the pseudo stable flux against $[Ca^{2+}] \cdot [H_xPO_4^{z-}]$ for all the filtrations performed. Salt concentrations and pH are measured in the recirculation solution once the flux is stabilized.

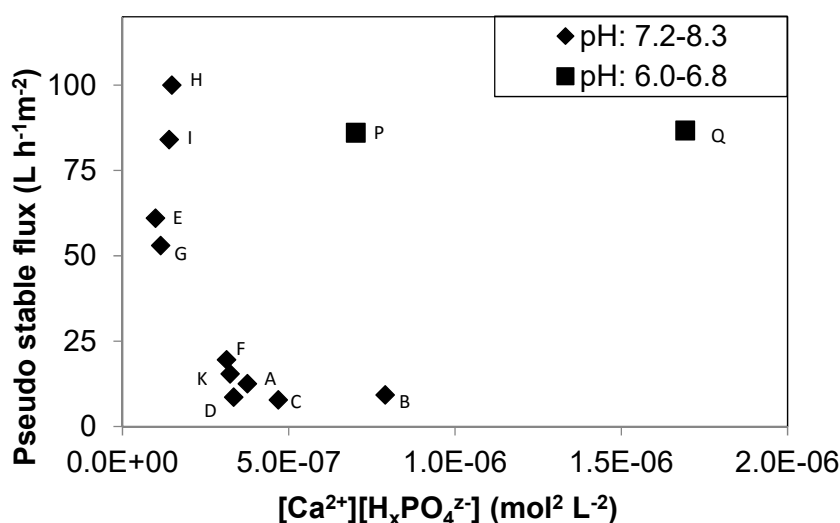


Fig III-25 Pseudo stable flux of independent filtrations against $[Ca^{2+}] \cdot [H_xPO_4^{z-}]$ at various applied pressures (10 to 35 bar) and velocities (0.2 and 0.35 m s⁻¹), the letter around the points indicates the serial name of the filtration (see Table III-5 for operating conditions). *all H₃PO₄, H₂PO₄⁻, HPO₄⁻, and PO₄³⁻ are analyzed as PO₄³⁻ by the ionic chromatography.

Two different behaviors can be observed on the figure. First, when the pH is in the range 7.2 to 8.3, the pseudo stable flux decreases with the increase of $[Ca^{2+}] \cdot [H_xPO_4^{z-}]$ until the stable flux reduces to around 10 L h⁻¹m⁻². Second, pH in the range 6.0 to 6.8, the pseudo stable flux keeps a high value which is not influenced by the concentration of Ca²⁺ and H_xPO₄^{z-}.

Scaling by Ca²⁺ and H_xPO₄^{z-} is not observed on the fouled membrane after filtration of a solution the pH of which is lower than 7 (see section III.B.4).

It is worth noting that the pH of MBR effluents is in the range 6.08 to 8, the phosphate is then in the form of dihydrogen phosphate ion (H₂PO₄⁻) or hydrogen phosphate ion

(HPO_4^-) depending on the pH. The acidic dissociation constant of them is equals to 7.21 as Eq. III-17.



According to previous studies [42,43], the solubility of calcium phosphate depends on the form of phosphate. Table III-7 presents the relative forms of calcium phosphate and their solubility. It can be observed that all calcium and hydrogen phosphate (HPO_4^-) compounds have rather lower solubility than calcium and dihydrogen phosphate (H_2PO_4^-) compounds. For example, the solubility of CaHPO_4 is 10^5 times lower than the one of $\text{Ca}(\text{H}_2\text{PO}_4)_2$. According to Eq. III-16, the supersaturation ratio of CaHPO_4 is then 10^5 times the one of $\text{Ca}(\text{H}_2\text{PO}_4)_2$ at the same concentrations of calcium and phosphate. Thus, the hydrogen phosphate (HPO_4^-) present in the solution with higher pH has much more risk to precipitate with calcium due to the low solubility.

Table III-7 Solubility product of calcium phosphate (in form of H_2PO_4 and HPO_4) [42,43]

Compound	Formula	K_{sp} at 25°C ($\text{mol}^2\text{L}^{-2}$)
Monocalcium phosphate monohydrate	$\text{Ca}(\text{H}_2\text{PO}_4)_2 \cdot \text{H}_2\text{O}$	7.24×10^{-2}
Monocalcium phosphate anhydrate	$\text{Ca}(\text{H}_2\text{PO}_4)_2$	7.24×10^{-2}
Dicalcium phosphate dihydrate	$\text{CaHPO}_4 \cdot 2\text{H}_2\text{O}$	2.57×10^{-7}
Dicalcium phosphate anhydrate	CaHPO_4	1.26×10^{-7}
Octacalcium phosphate	$\text{Ca}_8(\text{HPO}_4)_2(\text{PO}_4)_4 \cdot 5\text{H}_2\text{O}$	5.51×10^{-97}
Calcium-deficient	$\text{Ca}_{10-x}(\text{HPO}_4)_x(\text{PO}_4)_{6-x}(\text{OH})_{2-x}$	$\approx 7.94 \times 10^{-86}$
Hydroxyapatite	$\text{Ca}_{10}(\text{PO}_4)_6(\text{OH})_2$	1×10^{-116}

Thus, the two kinds of impact of $[\text{Ca}^{2+}] \cdot [\text{H}_x\text{PO}_4^{z-}]$ on the pseudo stable flux shown on Fig III-25 can be explain as follow.

When the pH of the filtration feed is higher than 7.2, the main form of phosphate in the filtrated solution is HPO_4^{2-} . Considering its lower solubility, the supersaturation ratio of it and calcium is extremely higher than the one of a feed the pH of which ranges between 6 and 6.8 (phosphate in the form of H_2PO_4^-). The precipitation of calcium phosphate (scaling) has much more risk to occur on the membrane. The pseudo stable flux then depends on the concentrations of calcium and phosphate in solution. These concentrations being link to the extent of scaling at the membrane surface, higher are the concentrations in solution, more important is the membrane surface area occupied by the calcium phosphate, lower is the

pseudo stable flux until the entire surface is covered by the scaling. This meets the discussion in section III.B.4 on the relationship between element analysis of fouling layer and pseudo-stable flux (Fig.III-22).

When the pH of the filtration feed is in the range 6 - 6.8, the main form of phosphate is H_2PO_4^- . The system can tolerate higher concentration of calcium and phosphate before scaling occurs on the membrane surface.

In this study, the fouling types (see section II.B.4) highly relate to the feed pH and the concentration of calcium and phosphate. For pH lower than 7, scaling doesn't occur at the given concentration of calcium and phosphate and the foulant layer composition is colloidal silica and organic (fouling type 1). In contrast, for $\text{pH} \geq 7.2$, scaling can occur. The fouling types can then belong to groups 2 or 3: inhomogeneous or homogeneous scaling, depending on supersaturation ratio of CaHPO_4 .

III.B.5.3 Conclusions

The fouling types highly relate to the pH of the filtrated solution and in a second step to the concentration of calcium and phosphate in water matrix. Higher stable flux (productivity) can be obtained when the pH of the feed solution is lower than 7, scaling of calcium and phosphate being avoided at this pH. The pseudo stable and limiting fluxes depend in this case on the concentration of organic matters. For a feed pH equals or higher than 7.2, the risk of scaling is much higher. The value of the pseudo-stable flux then decreases with the increase of membrane surface area occupied by the calcium phosphate until an almost homogeneous scaling occurs corresponding to a low limiting flux.

III.B.6 Filtration with adjusted pH

Considering the study of flux behaviors and fouling mechanisms, the higher productivity is proposed to be obtained at pH around 6. This section is devoted to verify the influence of pH on the fouling mechanism and the associated variation of flux.

III.B.6.1 Experimental procedure

All the steps of the filtration are conducted with a transmembrane pressure of 15 bar and a cross-flow velocity of 0.35 m s^{-1} . The pH is adjusted with H_2SO_4 1M.

After installing and preparing the membrane, a MBR effluent (solution (a)) is

introduced in the tank after adjusting its pH to 6. The filtration is first conducted in a concentration mode until the volume reduction factor reaches 5. Then the filtration follows the procedure corresponding to the recirculation mode during which the retentate (solution (b)) and permeate are both recycled into the feed tank. After 1 hour of recirculation, the pH is adjusted to 6 again and the recirculation continues for 2 hours with a continuous regulation of pH at 6. Then the recirculation solution (solution (c)) is collected for a new recirculation step with a virgin membrane. In this step, both retentate and permeate are normally recycled into feed tank and again the pH is adjusted to keep it constant at 6. The serial name of this filtration is “L”. The characteristics of solutions (a), (b) and (c) are reported in Table III-8.

Table III-8 Characteristics of filtrated solutions during experiment with adjusted pH

Item	MBR effluent solution (a)	Retentate (VRF = 5) solution (b)	Retentate (VRF = 5) solution (c)
pH	6.06± 0.2	7.06 ± 0.2	5.9± 0.2
COD (mg L ⁻¹)	38 ± 3	67 ± 3	67 ± 3
UV ₂₅₄	0.527	1.21	0.979
Na ⁺ (mg L ⁻¹)	222.4 ± 4.0	390.2 ± 7.0	339.6 ± 6.1
K ⁺ (mg L ⁻¹)	20.6 ± 0.3	42.3 ± 0.6	36.6 ± 0.5
Mg ²⁺ (mg L ⁻¹)	4.2 ± 0.1	11.1 ± 0.2	10.4 ± 0.1
Ca ²⁺ (mg L ⁻¹)	63.5 ± 0.8	152.9 ± 2.0	147.0 ± 1.9
Cl ⁻ (mg L ⁻¹)	60.6 ± 1.3	54.1 ± 1.1	41.9 ± 0.9
NO ₃ ⁻ (mg L ⁻¹)	199.4 ± 3.0	167.9 ± 2.5	130.1 ± 2.0
SO ₄ ²⁻ (mg L ⁻¹)	209.6 ± 12.6	888.0 ± 53.3	893.6 ± 53.6
PO ₄ ³⁻ * (mg L ⁻¹)	29.4 ± 0.9	49.7 ± 1.5	39.2 ± 1.2

*Due to the analytical method, all the H₃PO₄, H₂PO₄⁻, HPO₄²⁻ and PO₄³⁻ were measured as PO₄³⁻.

III.B.6.2 Variation of permeate flux with time in different matrix pH

Fig.III-26 exhibits the variation of flux with time during the different filtration steps. During the concentration step of solution (a), pH increases from the initial value of 6 to 6.9. Simultaneously, the flux significantly decreases from 185 to 35 L h⁻¹m⁻². During the recirculation of concentrate (b), the pH slightly rises to 7.06. The reduction of flux continues in this pH condition until 32 L h⁻¹m⁻². As soon as pH is controlled to 6, the permeate flux stabilizes at 32 L h⁻¹ m⁻² over the 2 hours of recirculation. Then the recirculation solution (c) is collected and the filtration is restarted with a new membrane. The pH is maintained at 6 during this step. The initial flux (166 L h⁻¹m⁻²) is almost the

same than the one obtained with solution (a). However, it can be observed that the reduction of flux is less than during the filtration of solution (a) even if the concentrations of organics and ions in solution (c) are higher. The pseudo stable flux is obtained at $127 \text{ L h}^{-1} \text{ m}^{-2}$.

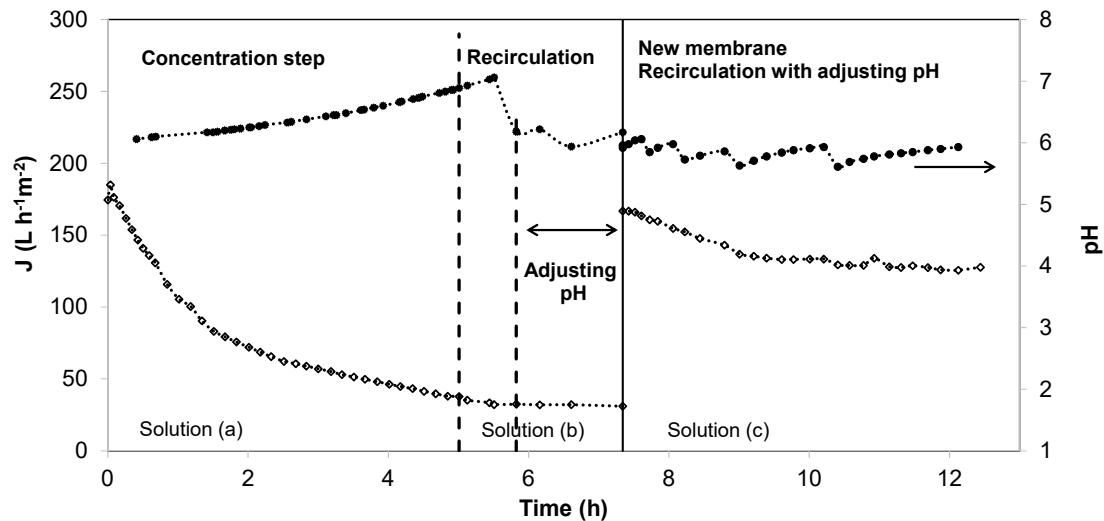


Fig. III-26 Variation of flux during filtrations in different pH conditions. The hollow points represent the flux and the solid points represent the pH of the filtrated solution at the same time.

A high correlation between the permeate flux and the feed pH is observed during these filtrations. In the concentration and the first recirculation steps, the flux continuously decreases, when the value of pH rises from 6 to 7. The reduction of flux is stopped when the pH of the matrix is adjusted again to 6. We have previously demonstrated that this last pH value is inappropriate to form scaling. However, the permeate flux cannot recover its initial value from the shift of pH, which verifies the irreversibility of the fouling layer formed. The slight decrease of flux during recirculation using a new membrane maintaining the pH at 6 confirms that the fouling can be controlled by adjusting pH.

Based on the discussion in sections III.B.4 and III.B.5, it can be confirmed that the severe reduction of flux during the filtration at elevated feed pH is due to the occurrence of scaling. The characterization of fouling layer on membrane samples is carried out in next section to verify the effect of pH on the fouling mechanisms.

III.B.6.3 Characteristics of fouling layer in different matrix pH

The SEM-EDX analysis was conducted to determine the characteristics of fouling layer.

Fig. III-27 shows the micrographs of the membranes after filtrations.

The first membrane is the one that reached rather low flux after concentration and recirculation steps with elevated pH of the filtrated solution. The second membrane is the one that obtained greater pseudo stable flux with pH of the filtrated solution maintained at 6. From the images, it can be observed that the morphology of the two membranes surface is different after dehydration in the same conditions (see section II.5). For the first membrane, serious surface cracking is observed. The surface cracking after dehydration is probably due to the different compositions and characteristics of the fouling layer. The top flat-board-like fouling seems to be compact. The surface cracking is not significant in the micrograph of second fouled membrane. The fouling layer is looser than the one on the other membrane.

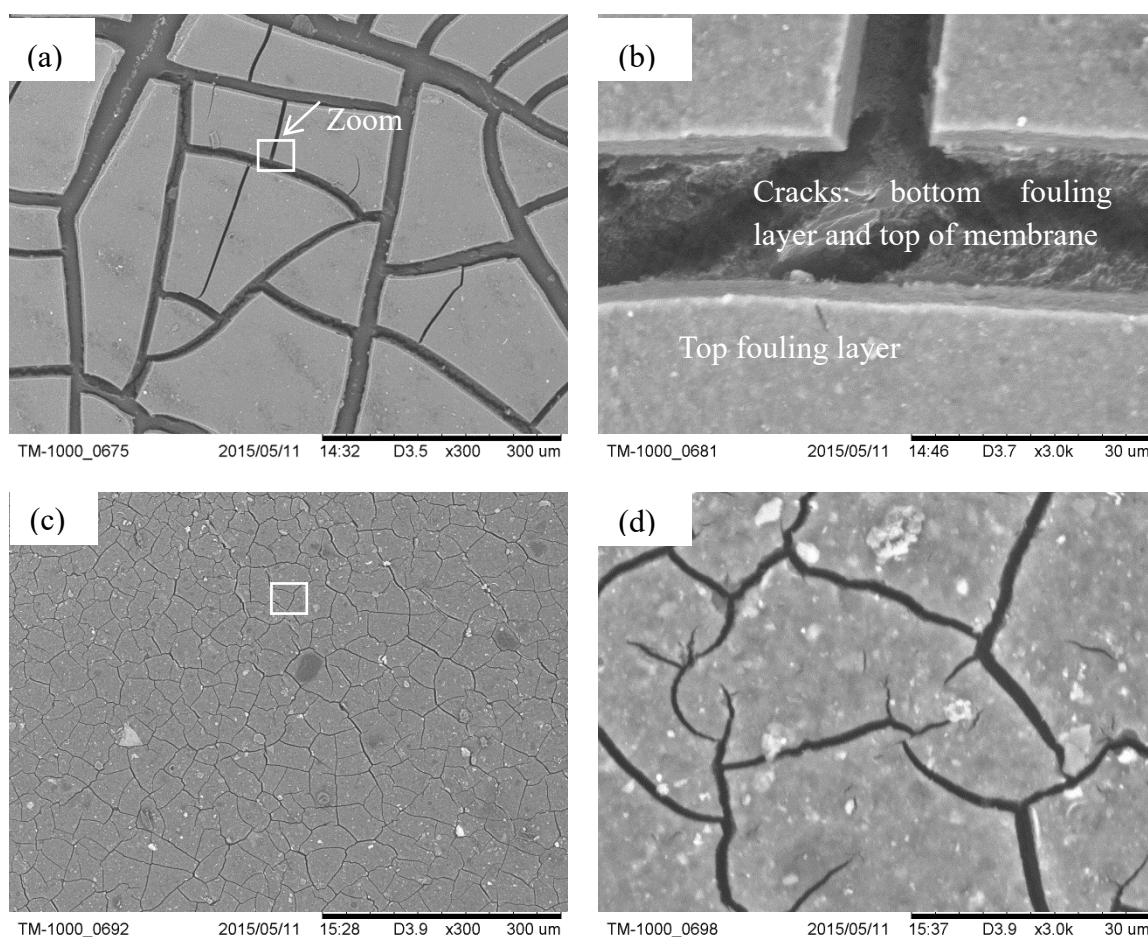


Fig. III-27 SEM images of membranes after filtrations: (a) first fouled membrane 300 \times , (b) first membrane fouled 3000 \times , (c) second fouled membrane 300 \times , (d) second fouled membrane 3000 \times

The EDX analysis was conducted to measure the elements composition at different

locations on the membrane surface. Tables III-9 and III-10 present the elements composition for the first and the second membrane, respectively.

Table III-9 Elements composition on different locations on the first fouled membrane surface

Top fouling layer								
Samples	1	2	3	4	5	6	7	Average
Elements	Weight % from the different locations							
Silicon	7.3	8.8	8.3	9	5.2	8.2	12.2	8.4
Sulfur	0	3.9	0	0	4.1	0	0	1.1
Calcium	45.6	47.9	40.4	38.1	51.6	39.6	38	43.0
phosphorus	29.6	24.5	27.8	29.3	23.6	31.4	30.1	28.0
Magnesium	0	0	0	3.5	0	0	2.9	0.9
Aluminum	8.4	7.3	6.8	8.9	5.8	9.8	9.1	8.0
Iron	9.1	0	11.1	0	9.6	10.9	7.7	6.9
Bottom dark layer: fouling layer below and top of membrane surface								
Samples	1	2	3	Average				
Elements	Weight % from the different locations							
Silicon	0	12.5	13.3	8.6				
Sulfur	100	87.5	86.7	91.4				

Table III-10 Elements composition on different locations on the second fouled membrane surface

Samples	1	2	3	4	5	Average
Element	Weight % from the different locations					
Silicon	9.3	13.2	7.9	0	12.6	8.6
Sulfur	35.6	30.4	26.7	0	71.1	32.8
Calcium	19.5	23	18	39.4	16.3	23.2
phosphorus	11.9	0	17.8	0	0	5.9
Magnesium	0	0	5.2	0	0	1.0
Aluminum	6.6	10.2	9.7	0	0	5.3
Iron	17.2		14.7	0	0	8.0
Chlorine	0	0	0	28.8	0	5.8
Potassium	0	0	0	39.1	0	7.8

From the analysis, the major elements on the flat-board-like top fouling layer of the first membrane are calcium and phosphate, which confirms that the scaling occurs during the concentration and the first recirculation steps. The distributions of calcium and phosphate are quite uniform, which indicates that the scaling is homogenous on the membrane surface. The sulfur that correlates with the membrane structure is present in low

percentage and even cannot be detected on most of locations. It means that the flat-board-like top fouling layer is thicker than the analyzed depth by EDX. The Ca/S and P/S ratio are equal to 39 and 25, respectively. The main elements detected on the bottom dark layer (cracks) are silicon and sulfur which correlates with colloidal silica fouling and the membrane structure, respectively. The cracks between flat-board-like pieces could be the bottom fouling layer and top of membrane.

For the second membrane, the main elements detected in the fouling layer are silicon and calcium. The phosphate can be detected rarely on some locations of the membrane surface. Sulfur is detected on almost all locations with a high percentage. The average P/S ratio which is related to scaling is calculated to be 0.18 much less than in the first membrane. The P/S is of great accordance with the relationship between elements ratio and pseudo stable flux presented in Fig.III-22 (point L, section III.B.4.1). Moreover, it was studied on section III.B.5 that in absence of scaling, pseudo-stable flux is correlated to organics concentration according the film theory. The pseudo stable flux obtained during this last filtration (L) at pH 6 is not so far from the linear relationship with concentration of organics (UV_{254}) (point L, Fig.III-24, section III.B.5.1). These results confirm that the main fouling type during the recirculation at pH = 6 is colloidal silica and organics fouling even if some other elements can be detected on the membrane surface.

Thus, the first membrane after filtration at elevated pH (6-7) is fouled by a combination of colloidal silica fouling and homogenous calcium phosphate scaling. The fouling type for the second membrane after filtration at a pH maintained at 6 is colloidal silica and organics fouling in absence of scaling. These results are in accordance with the study on section III.B.5.2 showing that the fouling types (with or without scaling) are greatly influenced by the pH of filtrated solution. It is confirmed that the severe calcium and phosphate scaling can be avoided by controlling the pH of feed at 6 (or lower) increasing considerably the productivity of the process.

III.B.7 Productivity control

This section is devoted to investigate the productivity control during nanofiltration process, according to the studies of critical flux and limiting flux, fouling mechanisms and parameters influencing them.

According to previous sections, three types of flux behaviors associated with fouling mechanism are described as follow.

Type 1: the limiting flux approximates to the critical flux, membrane is fouled by an homogenous colloidal silica and organics layer.

Type 2: the limiting flux is lower than the estimated critical flux. Membrane is fouled by colloidal silica and organics and an inhomogeneous scaling. The value of limiting flux depends on the membrane surface area occupied by scaling.

Type 3: the limiting flux is well below the possible critical flux. The coupling of colloidal silica and organics fouling and homogenous scaling is observed.

Scaling that is the most important fouling mechanisms can lead to severe reduction of stable flux. Base on the study above, it can be controlled by the pH, the concentration of calcium and phosphate.

It was assumed on section III-A-5 that there is a colloidal silica and organics fouling layer which can be characterized by a threshold fouling resistance above which scaling occurred. This threshold resistance (R_t) and the corresponding threshold permeability (L_t) before scaling were defined. L_t was estimated on the section III-A-5, as $3.86 \text{ L h m}^{-2} \text{ bar}^{-1}$.

In Fig.III-28, we can separate the variations of pseudo stable flux as a function of applied pressure into three regions through the pure water permeability and the threshold permeability before scaling (L_t): non-fouling region, fouling by colloidal organics and fouling by scaling. The non-fouling region is enclosed on the left by the average pure water permeability (full line). The region in between pure water permeability and threshold permeability before scaling (L_t) (dashed line) corresponds to conditions for which colloidal silica and organics fouling is observed (fouling type 2). Finally flux in the region on the right side of L_t (region of scaling) indicates scaling occurs (fouling type 2 and 3).

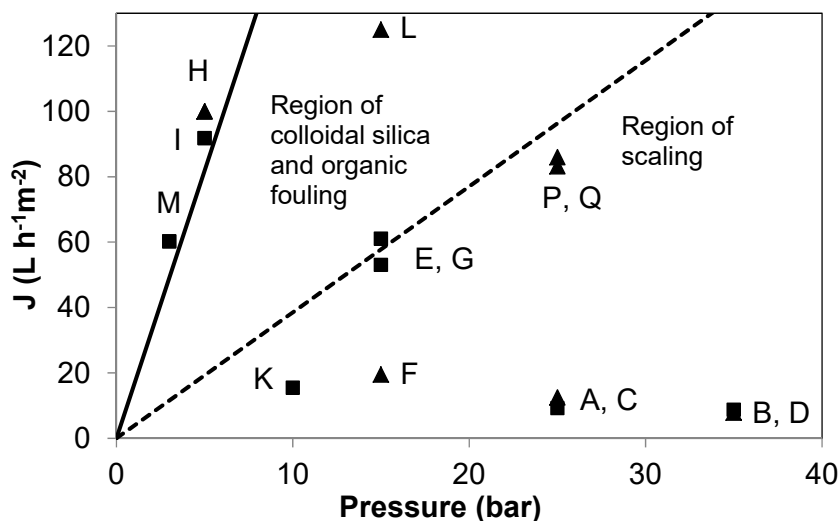


Fig III-28 Experimental pseudo stable flux as a function of applied pressure with various cross flow velocities: ▲ 0.35 m s^{-1} , ■ 0.2 m s^{-1} . The full line is the average pure water permeability of all pieces of membrane

used. The dashed line is the threshold permeability (L_t).

The experimental fluxes obtained during the whole study are also shown on Fig.III-28. A great accordance between the experimental results and the predictive regions is obtained.

-The filtration at the pressure (3 and 5 bar) lower than the critical pressure, the corresponding flux is on the line of pure water permeability.

-The fluxes of filtrations L, P, Q (15, 25, 35 bar) are in the region of colloidal organic fouling and close to L_t . The fouling type of them is confirmed to be colloidal silica and organics fouling by ATR-FTIR and SEM-EDX analysis on section III.B.4 and III.B.6.

-The fluxes of filtrations E, G, F (15 bar) are included in fouling type 2: combination of inhomogeneous scaling and colloidal silica and organics fouling. From the SEM-EDX analysis, for the filtrations E and G, less surface area of membrane is occupied by calcium phosphate scalant, the stable flux of them is then close to L_t ; in contrast, the stable flux of filtration F deviates more from L_t due to higher membrane surface coverage by calcium phosphate scalant.

-The flux of filtrations A, B, C, D (25 and 35 bar) with a pseudo stable flux around $10 \text{ L h}^{-1}\text{m}^{-2}$ are in the region of scaling (type 3). The fouling analysis evidences an homogenous scaling on the fouled membrane surface after filtration.

It can be observed a slight shift of fluxes for filtrations P and Q beyond L_t line, noting that no scaling occurs during these experiments. This is due to the fact that L_t is evaluated experimentally with a certain feed from the filtration experiment following the square wave method. The exact value of this threshold permeability can “shift” depending on the water matrix due to different organics concentrations.

In this study, UV_{254} absorbance (related to the concentration of organic matters) of the various feeds used (MBR effluents) is in the range of 0.78 to 2.18. Table III-10 compares UV_{254} absorbance of feeds used in filtrations L, P, Q to the one used for the evaluation of L_t (UV_{254} 1.38).

Table III-10 Absorbance of UV_{254} for various filtrations

	Exp. for evaluation of L_t	L	P	Q
UV_{254}	1.38	0.97	2.09	2.18

-In the case of a feed with lower concentration of organics, the pseudo stable flux is above L_t in the region of colloidal silica and organics fouling (like point L in Fig III.28)

-In the case of a feed with higher concentration of organics, the pseudo stable flux can

exhibit a shift as points P and Q in Fig.III.28. However, this shift is slight, even if the UV_{254} absorbance of these feeds is almost twice the one of the water matrix used to evaluate L_t .

Thus, in the context of the water matrix variability identified in the MBR effluent used in this project, L_t quantification for a certain matrix composition from the method presented in section III.A can give a satisfactory evaluation of the threshold permeability below which scaling is expected.

To conclude, the productivity is ideal in the un-fouling region, acceptable in the region of colloidal organics fouling, while low in the region of scaling. During the continuous nanofiltration process, if the flux approaches the scaling region, some actions such as adjusting feed pH and even cleaning membrane could be considered to avoid the scaling.

III.B.8 Conclusion

For independent nanofiltration of MBR effluent, the pseudo stable flux increases with the transmembrane pressure and does not decrease with filtration time until the initial flux above the critical flux. Greater critical flux is obtained with higher cross-flow velocity.

Two limiting fluxes are observed: one approximates possible critical flux, the other is well below the critical flux. Considering that the limiting flux may relate to the fouling types, the fouling compositions are determined by FTIR and SEM-EDX. It is evidenced that the two limiting fluxes relate to different fouling mechanisms. The one approximating possible critical flux is induced by an homogeneous colloidal silica and organics fouling; the other one with rather low flux is due to the presence of homogenous calcium phosphate scaling and colloidal silica and organics fouling simultaneously on the membrane surface. In this last situation, membrane surface is almost completely occupied by an homogenous calcium phosphate layer. Even if the percentage of Ca and P on the membrane surface increases, no further decrease of flux is observed. There is an “intermediate” case for which calcium and phosphate distribute inhomogeneously on partial membrane surface. The pseudo stable flux can be in a wide range between the two extreme limiting fluxes mentioned before. Its value then greatly depends on the surface area occupied by calcium and phosphate scaling.

The fouling types highly relate to the pH of the filtrated solution and in a second step to the concentration of calcium and phosphate in solution. When the pH of the feed solution is lower than 7, scaling of calcium and phosphate is avoided. The pseudo-stable

flux depends in this case on the concentration of organic matters in solution. For a feed pH equal or higher than 7.2, the risk of scaling is much higher.

The effect of pH on fouling types and related flux is verified by an additional filtration with adjusted pH. The combined fouling by colloidal silica and homogenous calcium phosphate scaling occurs at elevated pH (6-7) and the pseudo stable flux is rather low in this case. In contrast, at a pH maintained at 6 only colloidal silica and organics fouling is observed leading to greater flux. It is then confirmed that the severe calcium and phosphate scaling can be avoided by controlling the feed pH at 6 (or lower), increasing considerably the productivity of the process.

Finally, the relevance of threshold permeability before scaling (L_t) which is estimated in section III-A is verified from fluxes obtained in a series of independent filtrations. Thus, it can be recommended to estimate L_t for certain filtration system and matrix (from the method presented in section III.A) before application of nanofiltration process. If the flux approximates to the scaling region, some actions such as adjusting feed pH and even cleaning membrane could be considered to avoid the scaling.

III.C Process selectivity - Influence of fouling types (water matrix) and operating conditions on the rejection

This section investigates the selectivity of the nanofiltration process with regard to components (pharmaceuticals and salts) of the MBR effluent. Rejection of salts and pharmaceuticals is studied to determine the influence of the water matrix and the fouling types on the selectivity, beside other significant factors such as membrane material and structure and pharmaceuticals properties.

III.C.1 Salts rejection

Rejections of salts were calculated according to the equation Eq.II-1 as stable flux was reached at the end of different filtration experiments. Results are reported in Fig.III-29. Variations of the rejection of salts are presented considering the different fouling types described in previous section.

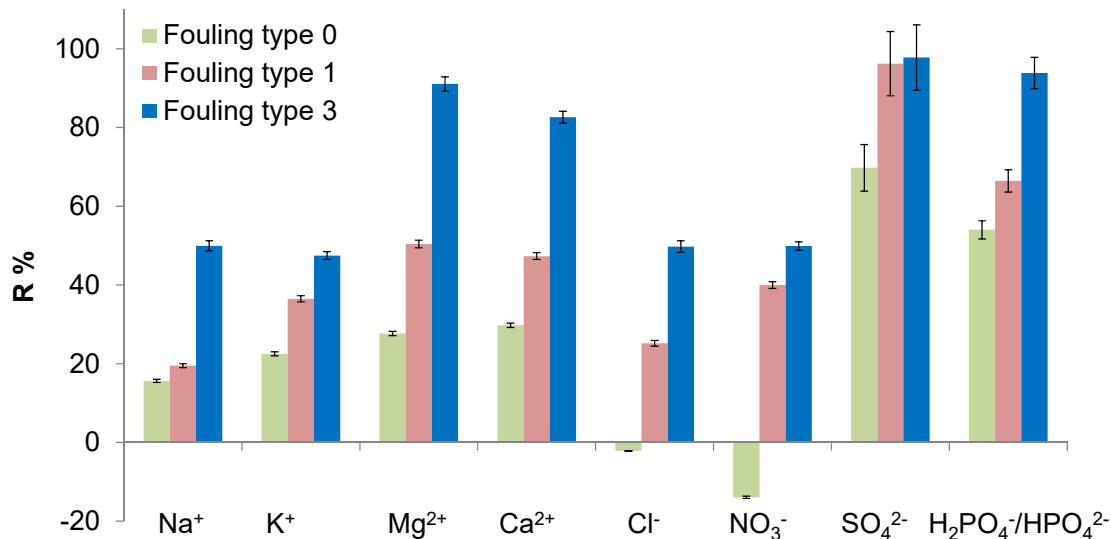


Fig.III-29 Salts rejections according to different fouling types: unfouled membrane (type 0), membrane fouled by homogenous colloidal silica and organics (Fouling type1), membrane fouled by colloidal silica and organics fouling and homogenous scaling (Fouling type 3)

For the unfouled membrane, the salts rejection is mainly influenced by size exclusion and electrostatic repulsions [11]. The pore size (r_p) of NE 70 which is estimated

from filtration of organic tracers and model fitting [44] and the hydrated radius of ions of interest for us [45,46] are presented in the table III-11.

Table III-11 Estimated membrane pore radius and hydrated radius of ions

NE 70 Membrane pore (r_p): 0.34 - 0.36 [44]									
Hydrated ionic radius (r_h) (nm)									
	Na ⁺	K ⁺	Mg ²⁺	Ca ²⁺	Cl ⁻	NO ₃ ⁻	SO ₄ ²⁻	HPO ₄ ²⁻	H ₂ PO ₄ ⁻
Kiriukhin and Collins [45]	0.178	0.201	0.300	0.253	0.195	-	0.300	0.327	0.302
Marcus [46]					0.181	0.179			

By taking into account hydrated ionic radius; big ions should exhibit higher rejection. Fig III-29 shows that the rejection of SO₄²⁻ is higher than the rejection of Mg²⁺, even if hydrated ionic radiuses (table III-11) of them are approximately the same. These rejection behaviors can be explained by electrostatic interactions between ions and the membrane surface [47]. Considering the negative charge of the membrane surface, the higher rejection of SO₄²⁻ can be explained by the electrostatic repulsions between SO₄²⁻ and membrane surface. The positive charge of Mg²⁺ could lead to electrostatic attractions with the membrane surface, which can enhance the concentration of Mg²⁺ on membrane surface and the diffusion of Mg²⁺ to the permeate side. HPO₄²⁻/ H₂PO₄⁻ and SO₄²⁻ have similar hydrated ionic radiuses; however rejections of them are difficult to be compared. The filtrated solution pH being 7.4 the ratio of HPO₄²⁻ and H₂PO₄⁻ is 2.3:1. HPO₄²⁻ is a divalent ion as SO₄²⁻, while H₂PO₄⁻ is a monovalent ion.

Considering electrostatic repulsions, negative rejections of Cl⁻ and NO₃⁻ are observed. Previous studies demonstrated that co-ions (ions with the same sign of charge as the membrane) rejection decreases dramatically with the ion charge and may even become negative [48–50]. The authors explained the co-ions behavior by the Donnan exclusion. In the present study, the negative rejection of Cl⁻ and NO₃⁻ can be understood by the Donnan effect and steric exclusion. A more significant negative rejection of NO₃⁻ than Cl⁻ probably attributed to the smaller hydrated ionic radius of NO₃⁻, which is commonly reported in NF process [51–53]. On the other hand, rejections of cations are low because of electrostatic attractive interactions with the membrane surface. This also contributes to the transfer of smaller anions Cl⁻, NO₃⁻, respect of electroneutrality in the permeate side being in this case the driving-force.

For the membrane fouled by homogenous colloidal organics and silica layer (Fouling type 1), rejection of SO_4^{2-} and Mg^{2+} follows the same tendency as unfouled membrane ($R(\text{SO}_4^{2-}) > R(\text{Mg}^{2+})$) which indicates the dominant effect of electrostatic repulsions on ions rejection.

When the membrane is fouled by colloidal silica and organics layer and homogenous scaling (type 3), the rejection of ions seems not being significantly related to the electrostatic effects. Rejections of SO_4^{2-} and Mg^{2+} reach the same high value. The ions rejection follows the order:

$$R(\text{SO}_4^{2-}) \approx R(\text{Mg}^{2+}) \approx R(\text{HPO}_4^{2-}/\text{H}_2\text{PO}_4^-) > R(\text{Ca}^{2+})$$

This order is in excellent accordance with the size of hydrated ionic radius.

$$r_h(\text{SO}_4^{2-}) \approx r_h(\text{Mg}^{2+}) \approx r_h(\text{HPO}_4^{2-}/\text{H}_2\text{PO}_4^-) > r_h(\text{Ca}^{2+})$$

These results indicate that ions rejections by fouled type 3 membrane are governed by the size exclusion. Indeed, it can be assumed that the scaling layer on the membrane surface attenuates (or even cancels) the effect of the negative charge of the membrane surface on the rejection of solutes. Previous studies [47,54,55] reported the positive shift of zeta potential on membrane surface after fouling. The electrostatic repulsions between solutes and membrane surface being attenuated we can assume that size exclusion mechanism becomes predominant. The membrane active pore size can be changed by pore blocking which can increase the sieving effect. The rejection of SO_4^{2-} , Mg^{2+} , $\text{HPO}_4^{2-}/\text{H}_2\text{PO}_4^-$ and Ca^{2+} is greater than 85 % by means of size exclusion even if their hydrated ionic radius is less than the estimated virgin membrane pore radius.

It can be noticed that the membrane manufacturer specifications for rejections of NaCl (40~70 %) and MgSO_4 (99.5 %) which are obtained in specific conditions seem to not relate well to the salts rejection in MBR effluent, excepted for SO_4^{2-} .

In conclusion, the rejection of ions by the unfouled membrane and the membrane fouled by an homogenous colloidal organics and silica layer (fouling type1), is dominantly governed by electrostatic repulsions; while the ions rejection by a membrane fouled by colloidal silica and organics and homogenous scaling (fouling type 3) is

governed by size exclusion. Concerning the ions rejection by the membrane fouled with inhomogeneous scaling (fouling type 2) it is expected to be an intermediate situation between fouling type 1 and type 3 depending on the membrane surface area occupied by scalants.

III.C.2 Pharmaceuticals rejection

III.C.2.1 Effect of fouling types and pharmaceuticals properties - hydrophobic interaction and size exclusion

This section is devoted to quantify pharmaceuticals rejection in MBR effluent and identify key factors affecting it. The rejection of three selected pharmaceuticals in MBR effluent is studied in consideration with the different fouling types previously defined. These three pharmaceuticals: ciprofloxacin (CIP), ifosfamide (IFO) and cyclophosphamide (CYP) present different physico-chemical properties reported in table II-2 (section II.1.1). Based on these properties and on the literature [47,56,57], factors affecting these pharmaceuticals rejection by a nanofiltration membrane are expected to be not only size exclusion and electrostatic interactions but also hydrophobic-hydrophilic interactions. In order to be able to discuss this point, the contact angle of the membrane surface was measured at the end of each filtration (corresponding to the different fouling types) and was reported as a function of the weight percentage of calcium and phosphate on the membrane surface after filtrations (Ca+ P%), considering that calcium and phosphate are the most important components contributing to scaling (section III.B).

Fig.III-30 shows the variation of membrane contact angle after filtration of MBR effluent as a function of the percentage of Ca and P detected on the membrane surface (from EDX analysis, table III-6 in section III.B.4.1). Contact angle indicates the hydrophobicity level of the membrane surface. The larger the contact angle, the more hydrophobic the membrane surface is. The contact angle of the virgin membrane (before compaction) is 40 (on Y-axis). This value seems to increase considerably to around 80 after compaction and filtration at 5 bar (point I), even if there is no evidence of the presence of a fouling layer. Verliefde et al. [58] found that after compaction in ultrapure water, contact angles of some polyamide membranes increase from 48 to 80. Higher is the initial

hydrophilicity of the membrane, the more significant the increase in contact angle due to compaction is. Then, similarly to Verliefe et al. work, contact angle increase after filtration at 5 bar can be mainly attributed to the effect of membrane compaction.

From Fig.III-30, it can be observed that the contact angle decreases with the percentage of calcium and phosphate on membrane surface, in particular when the scaling is homogeneous (fouling type 3). It seems that scaling modifies the hydrophobicity of the membrane to a more hydrophilic surface.

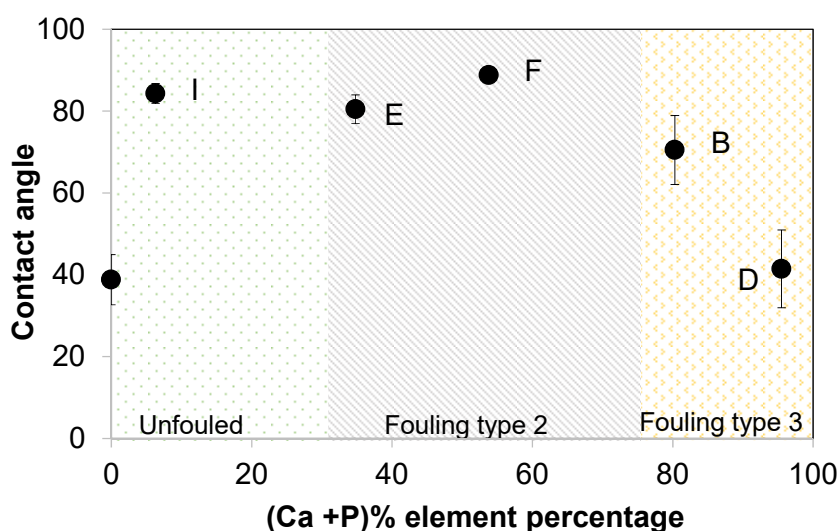


Fig.III-30 Contact angles of the membrane surface after filtration of MBR effluent as a function of the percentage of Ca and P detected on fouled membrane surface (from EDX analysis, table III-6 in section III.B.4.1). 3 regions can be defined corresponding to: Unfouled membrane; fouling type 2: membrane fouled by inhomogeneous scaling and colloidal silica and organics layer; fouling type 3: membrane fouled with homogenous scaling and colloidal silica and organics fouling. B, D...I is the serial name of filtrations.

Fig.III-31 exhibits rejections of ciprofloxacin, ifosfamide and cyclophosphamide for each filtration according to different fouling types and the corresponding contact angle. Generally, the rejection of pharmaceuticals decreases with the increase of hydrophobicity (contact angle). The relatively less hydrophilic pharmaceutical (cyclophosphamide, $\log P = 0.76$) shows a more significant reduction in rejection when the contact angle increases. In contrast, the rejection of CIP, which is more hydrophilic, decreases less ($\log P = 0.28$).

Considering the influence of fouling types, when the membrane is unfouled or suffers from an inhomogeneous scaling and fouling by colloidal organic matters, the pseudo stable flux is greater. The rejection of pharmaceuticals is lower and differs according to pharmaceuticals properties. More precisely, the rejection of pharmaceuticals seems to be

correlated with their hydrophobicity. The pharmaceuticals rejection follows the order:

$$R(\text{CIP}) > R(\text{IFO}) > R(\text{CYP})$$

The higher value of $\log P$ indicates that the molecule is more hydrophobic:

$$\log P (\text{CIP}) < \log P (\text{IFO}) < \log P (\text{CYP})$$

The low rejection of cyclophosphamide can be due to hydrophobic interactions between membrane surface and compounds.

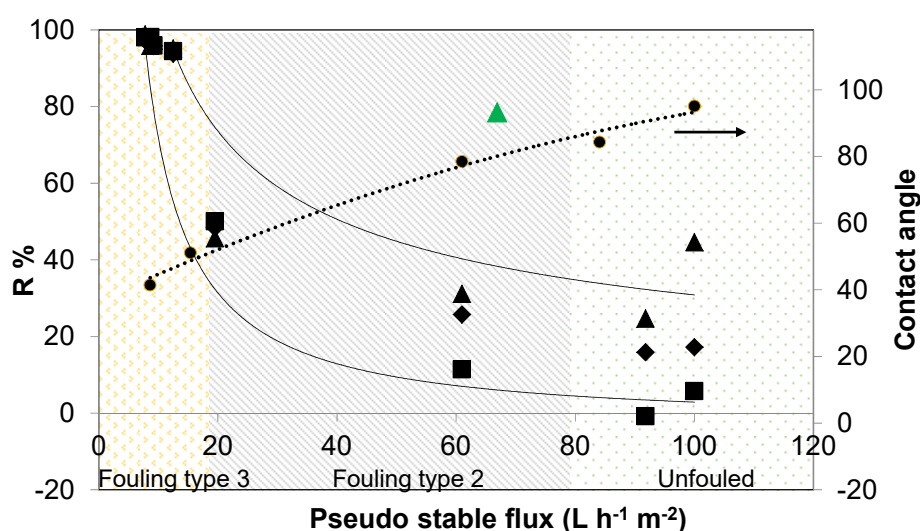


Fig.III-31 Rejection values of pharmaceuticals: ▲ and ▲ ciprofloxacin rejection in MBR effluent and ultrapure water, ◆ ifosfamide, ■ cyclophosphamide; ● the tendency of contact angle as a function of the pseudo stable flux for different fouling conditions: Unfouled membrane; fouling type 2: membrane fouled with inhomogeneous scaling and colloidal silica and organics fouling; fouling type 3: membrane fouled with homogenous scaling and colloidal silica and organics fouling.

These interactions decrease when the membrane surface is less hydrophobic (smaller contact angle), resulting in a significant increase of the rejection of hydrophobic pharmaceuticals in fouling type 2 region.

When a homogeneous scaling occurs on the membrane surface (fouling type 3), a low pseudo stable flux is observed. In this case, rejections of pharmaceuticals are around 100% independently of pharmaceuticals or matrix properties. Previous studies show that the fouling layer can reduce the membrane pore size [47,55] by pore blocking which can

increase the pharmaceutical rejection by size exclusion. This is also in accordance with the increase of ions rejection (both cations and anions) for this type of fouling (section III.C.1). As a consequence with fouling type 3, the contribution of hydrophobic interactions is totally screened, size exclusion becoming the principal rejection phenomenon.

III.C.2.2 Effects of water matrix

When the membrane is unfouled, the rejection of pharmaceuticals in MBR effluent is not only related to the interactions with the virgin membrane but is also influenced by water matrix characteristics. Previous studies reported that pH, ionic strength and the hardness of the water matrix can impact MWCO of membrane by modifying the electrostatic interactions within the membrane pores [9,34,59–62]. Relatively alkaline pH of MBR effluent (MBR effluent, pH 7-8, conductivity 600-700 $\mu\text{s cm}^{-1}$; ultrapure water, pH 5-6, conductivity 0.18 $\mu\text{s cm}^{-1}$) can increase the electrostatic repulsions within the membrane pores and enlarge the pore size, while the higher ionic strength can reduce the electrostatic repulsions in membrane pores and induce a decrease in apparent pore radius. Due to these competitive effects, the membrane MWCO following contact with MBR effluent can be different from the one of the virgin membrane (in ultrapure water). The increase of flux at the beginning of the MBR effluent filtration by comparison to pure water filtration (Chapter III.B) seems to confirm an enlargement of membrane pore. A rather lower rejection of pharmaceuticals is then expected when the membrane is unfouled during filtration of MBR effluent compared to results obtained in pure water. As shown on Fig.III-31, the rejection of CIP in MBR effluent is considerably lower than the one in ultrapure water, when the membrane is unfouled.

When severe fouling is established, there is a predominant effect of pore blocking on the pharmaceuticals rejection which is higher than in pure water. This last case is observed for fouling type 3.

For moderate fouling, combined impact of MBR matrix which reduces pharmaceuticals rejection and of fouling layer which increases it can contribute to intermediate rejection behavior.

III.C.2 Conclusion

With the unfouled membrane and membrane fouled with homogenous colloidal organics and silica the rejection of ions and pharmaceuticals is predominantly governed by electrostatic repulsions and hydrophobic interactions respectively. The rejection of both ions and pharmaceuticals with membrane fouled by colloidal silica and organics and homogenous scaling is governed by size exclusion. When the fouling layer is not settled, the apparent MWCO of the membrane is enlarged in MBR effluent compared to ultrapure water; then pharmaceuticals, usually retained by NE70, can pass through. In contrast, when fouling is established, this effect of water matrix is screened by pore blocking.

The combined effect of the matrix and fouling layer on the pharmaceuticals rejection results in various rejection behaviors of pharmaceuticals depending on the type and extent of the fouling.

III. Conclusion

The aim of this chapter was to investigate the main parameters which can influence the productivity and the selectivity of nanofiltration as primary step of tertiary treatment.

It has been possible to estimate a critical flux in the case of the filtration of the MBR effluent complex matrix from the square wave method. The ideal productivity could be obtained with an initial flux lower than the critical flux to avoid the fouling. Two limiting fluxes are observed. One of them is around the estimated critical flux while the other is well below due to the presence of scaling. A working diagram reporting permeate flux versus applied pressure has been divided in three regions: un-fouling region, region of colloidal silica and organics fouling and region of scaling. The productivity is ideal in the un-fouling region, acceptable in the region of organics fouling while low in the region of scaling. Maintaining the pH of filtrated solution at 6 is verified to be a solution to avoid the scaling.

Rejection of pharmaceutical are various due to the combined effect of water matrix, membrane properties and fouling mechanisms. The presence of homogeneous scaling on membrane surface can induce the rather low flux while lead to the excellent rejection of pharmaceuticals.

Regarding association of productivity and selectivity with fouling types, in a continuous process, the filtration retentate characteristics can differ over time, impacting the performance of electrochemical oxidation considered as second step of the tertiary treatment. The efficiency of EO to eliminate pharmaceuticals in the nanofiltration retentate will be studied in section IV and V with the concentrates collected after the various filtrations. Then the operating conditions offering the best compromise for the coupling process will be discussed to improve the global efficiency of the treatment.

Reference

- [1] B. Espinasse, P. Bacchin, P. Aimar, Filtration method characterizing the reversibility of colloidal fouling layers at a membrane surface: Analysis through critical flux and osmotic pressure, *J. Colloid Interface Sci.* 320 (2008) 483–490.
- [2] B. Espinasse, P. Bacchin, P. Aimar, On an experimental method to measure critical flux in ultrafiltration, *Desalination.* 146 (2002) 91–96.
- [3] A. Braghetta, F.A. DiGiano, W.P. Ball, Nanofiltration of natural organic matter: pH and ionic strength effects (vol 123, pg 637, 1997), *J. Environ. Eng.-Asce.* 124 (1998) 79–79.
- [4] M. Mänttari, A. Pihlajamäki, M. Nyström, Effect of pH on hydrophilicity and charge and their effect on the filtration efficiency of NF membranes at different pH, *J. Membr. Sci.* 280 (2006) 311–320.
- [5] M. Dalwani, N.E. Benes, G. Bargeman, D. Stamatialis, M. Wessling, A method for characterizing membranes during nanofiltration at extreme pH, *J. Membr. Sci.* 363 (2010) 188–194.
- [6] Q. Li, M. Elimelech, Synergistic effects in combined fouling of a loose nanofiltration membrane by colloidal materials and natural organic matter, *J. Membr. Sci.* 278 (2006) 72–82.
- [7] J. Kaewsuk, G.T. Seo, Verification of NOM removal in MIEX-NF system for advanced water treatment, *Sep. Purif. Technol.* 80 (2011) 11–19.
- [8] C.Y. Tang, J.O. Leckie, Membrane Independent Limiting Flux for RO and NF Membranes Fouled by Humic Acid, *Environ. Sci. Technol.* 41 (2007) 4767–4773.
- [9] S.-H. Yoon, C.-H. Lee, K.-J. Kim, A.G. Fane, Effect of calcium ion on the fouling of nanofilter by humic acid in drinking water production, *Water Res.* 32 (1998) 2180–2186.
- [10] Q. Li, M. Elimelech, Organic Fouling and Chemical Cleaning of Nanofiltration Membranes: Measurements and Mechanisms, *Environ. Sci. Technol.* 38 (2004) 4683–4693.
- [11] A.I. Schafer, A.G. Fane, T.D. T.D. Waite, *Nanofiltration-Principles and Application*, Elsevier Advance Technology, 2005.
- [12] D.L. Kronmiller, What every reverse osmosis water system manager should know, *Desalination.* 98 (1994) 401–411.
- [13] F.H. Butt, F. Rahman, U. Baduruthamal, Characterization of foulants by autopsy of RO desalination membranes, *Desalination.* 114 (1997) 51–64.
- [14] C.Y. Tang, Y.-N. Kwon, J.O. Leckie, Effect of membrane chemistry and coating layer on physiochemical properties of thin film composite polyamide RO and NF membranes: I. FTIR and XPS characterization of polyamide and coating layer chemistry, *Desalination.* 242 (2009) 149–167.

- [15] C. Jarusutthirak, G. Amy, J.-P. Croué, Fouling characteristics of wastewater effluent organic matter (EfOM) isolates on NF and UF membranes, *Desalination*. 145 (2002) 247–255.
- [16] J.A. Leenheer, J.P. Croue, M. Benjamin, G.V. Korshin, C.J. Hwang, A. Bruchet, et al., Comprehensive isolation of natural organic matter from water for spectral characterizations and reactivity testing., *Abstr. Pap. Am. Chem. Soc.* 217 (1999) U725–U725.
- [17] N. Lee, G. Amy, J.-P. Croué, H. Buisson, Identification and understanding of fouling in low-pressure membrane (MF/UF) filtration by natural organic matter (NOM), *Water Res.* 38 (2004) 4511–4523.
- [18] L. Vaculikova, E. Plevova, S. Vallova, I. Koutnik, Characterization and Differentiation of Kaolinites from Selected Czech Deposits Using Infrared Spectroscopy and Differential Thermal Analysis, *Acta Geodyn. Geomater.* 8 (2011) 59–67.
- [19] M. Muroya, Correlation between the formation of silica skeleton structure and Fourier transform reflection infrared absorption spectroscopy spectra, *Colloids Surf. Physicochem. Eng. Asp.* 157 (1999) 147–155.
- [20] E.J. Elzinga, D.L. Sparks, Phosphate adsorption onto hematite: An in situ ATR-FTIR investigation of the effects of pH and loading level on the mode of phosphate surface complexation, *J. Colloid Interface Sci.* 308 (2007) 53–70.
- [21] A. Ślósarczyk, C. Paluszkiwicz, M. Gawlicki, Z. Paszkiewicz, The FTIR spectroscopy and QXRD studies of calcium phosphate based materials produced from the powder precursors with different CaP ratios, *Ceram. Int.* 23 (1997) 297–304.
- [22] T. Theophile, ed., *Infrared Spectroscopy - Materials Science, Engineering and Technology*, InTech, 2012.
- [23] S. Lee, J. Kim, C.-H. Lee, Analysis of CaSO₄ scale formation mechanism in various nanofiltration modules, *J. Membr. Sci.* 163 (1999) 63–74.
- [24] A.G. Pervov, Scale formation prognosis and cleaning procedure schedules in reverse osmosis systems operation, *Desalination*. 83 (1991) 77–118.
- [25] R.P. Sear, Estimation of the Scaling of the Nucleation Time with Volume When the Nucleation Rate Does Not Exist, *Cryst. Growth Des.* 13 (2013) 1329–1333.
- [26] S. Lee, C.-H. Lee, Effect of operating conditions on CaSO₄ scale formation mechanism in nanofiltration for water softening, *Water Res.* 34 (2000) 3854–3866.
- [27] D. Kashchiev, G.M. van Rosmalen, Review: Nucleation in solutions revisited, *Cryst. Res. Technol.* 38 (2003) 555–574.
- [28] J.J.M. Damen, J.M.T. Cate, The Effect of Silicic Acid on Calcium Phosphate Precipitation, *J. Dent. Res.* 68 (1989) 1355–1359.
- [29] E.M.V. Hoek, M. Elimelech, Cake-Enhanced Concentration Polarization: A New Fouling Mechanism for Salt-Rejecting Membranes, *Environ. Sci. Technol.* 37 (2003) 5581–5588.

- [30] X. Wei, Z. Wang, F. Fan, J. Wang, S. Wang, Advanced treatment of a complex pharmaceutical wastewater by nanofiltration: Membrane foulant identification and cleaning, *Desalination*. 251 (2010) 167–175.
- [31] A.L. Zydney, Stagnant film model for concentration polarization in membrane systems, *J. Membr. Sci.* 130 (1997) 275–281.
- [32] J. Borden, J. Gilron, D. Hasson, Analysis of RO flux decline due to membrane surface blockage, *Desalination*. 66 (1987) 257–269.
- [33] J. Gilron, D. Hasson, Calcium sulphate fouling of reverse osmosis membranes: Flux decline mechanism, *Chem. Eng. Sci.* 42 (1987) 2351–2360.
- [34] S.K. Hong, M. Elimelech, Chemical and physical aspects of natural organic matter (NOM) fouling of nanofiltration membranes, *J. Membr. Sci.* 132 (1997) 159–181.
- [35] A. Seidel, M. Elimelech, Coupling between chemical and physical interactions in natural organic matter (NOM) fouling of nanofiltration membranes: implications for fouling control, *J. Membr. Sci.* 203 (2002) 245–255.
- [36] C.Y. Tang, Y.-N. Kwon, J.O. Leckie, Fouling of reverse osmosis and nanofiltration membranes by humic acid—Effects of solution composition and hydrodynamic conditions, *J. Membr. Sci.* 290 (2007) 86–94.
- [37] Q. She, C.Y. Tang, Y.-N. Wang, Z. Zhang, The role of hydrodynamic conditions and solution chemistry on protein fouling during ultrafiltration, *Desalination*. 249 (2009) 1079–1087.
- [38] M.F.A. Goosen, S.S. Sablani, H. Al-Hinai, S. Al-Obeidani, R. Al-Belushi, D. Jackson, Fouling of Reverse Osmosis and Ultrafiltration Membranes: A Critical Review, *Sep. Sci. Technol.* 39 (2005) 2261–2297.
- [39] X. Zhu, M. Elimelech, Colloidal Fouling of Reverse Osmosis Membranes: Measurements and Fouling Mechanisms, *Environ. Sci. Technol.* 31 (1997) 3654–3662.
- [40] M. Elimelech, X. Zhu, A.E. Childress, S. Hong, Role of membrane surface morphology in colloidal fouling of cellulose acetate and composite aromatic polyamide reverse osmosis membranes, *J. Membr. Sci.* 127 (1997) 101–109.
- [41] E.J. Elzinga, D.L. Sparks, Phosphate adsorption onto hematite: An in situ ATR-FTIR investigation of the effects of pH and loading level on the mode of phosphate surface complexation, *J. Colloid Interface Sci.* 308 (2007) 53–70.
- [42] M. Asadi-Eydivand, M. Solati-Hashjin, A. Farzadi, N.A.A. Osman, Artificial neural network approach to estimate the composition of chemically synthesized biphasic calcium phosphate powders, *Ceram. Int.* 40 (2014) 12439–12448.
- [43] S.V. Dorozhkin, M. Epple, Biological and medical significance of calcium phosphates, *Angew. Chem. Int. Ed Engl.* 41 (2002) 3130–3146.
- [44] A.D. Shah, *Antibiotics in Water Treatment: The Role of Water Quality Conditions on Their Fate and Removal During Chlorination and Nanofiltration*, ProQuest, 2008.
- [45] M.Y. Kiriukhin, K.D. Collins, Dynamic hydration numbers for biologically important ions, *Biophys. Chem.* 99 (2002) 155–168.

- [46] Y. Marcus, A simple empirical model describing the thermodynamics of hydration of ions of widely varying charges, sizes, and shapes, *Biophys. Chem.* 51 (1994) 111-127.
- [47] A.H.M.A. Sadmani, R.C. Andrews, D.M. Bagley, Impact of natural water colloids and cations on the rejection of pharmaceutically active and endocrine disrupting compounds by nanofiltration, *J. Membr. Sci.* 450 (2014) 272–281.
- [48] W.R. Bowen, H. Mukhtar, Characterisation and prediction of separation performance of nanofiltration membranes, *J. Membr. Sci.* 112 (1996) 263–274.
- [49] D. Bhattacharyya, J.M. McCarthy, R.B. Grives, Charged membrane ultrafiltration of inorganic ions in single and multi-salt systems, *AIChE J.* 20 (1974) 1206–1212.
- [50] J.M.M. Peeters, J.P. Boom, M.H.V. Mulder, H. Strathmann, Retention measurements of nanofiltration membranes with electrolyte solutions, *J. Membr. Sci.* 145 (1998) 199–209.
- [51] I. Koyuncu, M. Yazgan, D. Topacik, H.Z. Sarikaya, Evaluation of the low pressure RO and NF membranes for an alternative treatment of Buyukcekmece Lake, in: K.J. Ives, D. Nozaic (Eds.), *Part. Remov. Reserv. Surf. Waters*, I W a Publishing, London, 2001: pp. 107–115.
- [52] S. Ding, Y. Yang, H. Huang, H. Liu, L. Hou, Effects of feed solution chemistry on low pressure reverse osmosis filtration of cesium and strontium, *J. Hazard. Mater.* 294 (2015) 27–34.
- [53] A.K. SenGupta, *Ion Exchange and Solvent Extraction: A Series of Advances*, CRC Press, 2007.
- [54] T. Fujioka, S.J. Khan, J.A. McDonald, R.K. Henderson, Y. Poussade, J.E. Drewes, et al., Effects of membrane fouling on N-nitrosamine rejection by nanofiltration and reverse osmosis membranes, *J. Membr. Sci.* 427 (2013) 311–319.
- [55] A. Azais, J. Mendret, S. Gassara, E. Petit, A. Deratani, S. Brosillon, Nanofiltration for wastewater reuse: Counteractive effects of fouling and matrice on the rejection of pharmaceutical active compounds, *Sep. Purif. Technol.* 133 (2014) 313–327.
- [56] Y. Kiso, Y. Sugiura, T. Kitao, K. Nishimura, Effects of hydrophobicity and molecular size on rejection of aromatic pesticides with nanofiltration membranes, *J. Membr. Sci.* 192 (2001) 1-10.
- [57] A.R.D. Verliefde, E.R. Cornelissen, S.G.J. Heijman, I. Petrinic, T. Luxbacher, G.L. Amy, et al., Influence of membrane fouling by (pretreated) surface water on rejection of pharmaceutically active compounds (PhACs) by nanofiltration membranes, *J. Membr. Sci.* 330 (2009) 90-103.
- [58] A.R.D. Verliefde, E.R. Cornelissen, S.G.J. Heijman, I. Petrinic, T. Luxbacher, G.L. Amy, et al., Influence of membrane fouling by (pretreated) surface water on rejection of pharmaceutically active compounds (PhACs) by nanofiltration membranes, *J. Membr. Sci.* 330 (2009) 90-103.
- [59] C. Bellona, J.E. Drewes, The role of membrane surface charge and solute physico-chemical properties in the rejection of organic acids by NF membranes, *J. Membr. Sci.* 249 (2005) 227-234.

- [60] A.E. Childress, M. Elimelech, Relating Nanofiltration Membrane Performance to Membrane Charge (Electrokinetic) Characteristics, *Environ. Sci. Technol.* 34 (2000) 3710-3716.
- [61] A.E. Childress, M. Elimelech, Effect of solution chemistry on the surface charge of polymeric reverse osmosis and nanofiltration membranes, *J. Membr. Sci.* 119 (1996) 253-268.
- [62] P. Xu, J.E. Drewes, T.-U. Kim, C. Bellona, G. Amy, Effect of membrane fouling on transport of organic contaminants in NF/RO membrane applications, *J. Membr. Sci.* 279 (2006) 165-175.

Chapter IV

Elimination of pharmaceuticals by electrochemical oxidation

Contents

IV.A Electrochemical oxidation in synthetic solution.....	143
IV.A.1 Study of ciprofloxacin as molecule model	143
IV.A.1.1 Electrochemical study of ciprofloxacin.....	143
IV.A.1.2 Galvanostatic electrolysis of CIP solution	145
IV.A.1.3 Conclusion.....	147
IV.A.2 Influence of the applied current on CIP mineralization.....	147
IV.A.2.1 Influence of applied current on CIP degradation rate	148
IV.A.2.2 Influence of applied current on COD decay.....	151
IV.A.2.3 Influence of applied current on TOC mineralization	154
IV.A.2.4 Influence of applied current on intermediates production and mineralization..	154
IV.A.2.5 Conclusion.....	157
IV.A.3 Removal of common organic waste and the other pharmaceuticals.....	157
IV.A.3.1 Removal of urea as a common organic waste	158
IV.A.3.1.1 Electrolysis of Urea solution	158
IV.A.3.1.2 Oxidation pathway of urea	160
IV.A.3.2 Mineralization of Salbutamol and sulfamethoxazole.....	162
IV.A.3.3 Conclusion.....	164
IV.A.4 Influence of the matrix on the pharmaceutical removal	165
IV.A.4.1 Influence of salts to electrolysis of pharmaceuticals.....	165
IV.A.4.1.1 Presence of sulfates	165
IV.A.4.1.2 Presence of chlorides.....	168
IV.A.4.1.3 Conclusion.....	176
IV.A.4.2 Removal of pharmaceuticals in presence of urea.....	176
IV.A.4.3 Competition and interaction between pharmaceuticals during electrochemical oxidation	180

IV.A.5 Modelling of anodic degradation for organic with BDD anode	183
IV.A.5.1 Model description.....	184
IV.A.5.2 Comparison of model and experimental values	188
IV.A.6 Conclusion:	196
IV.B Electrochemical oxidation of pharmaceuticals in wastewater.....	198
VI.B.1. Elimination of pharmaceuticals and AOX.....	198
VI.B.2 Conversion of ions (in particular Cl ⁻) during electrolysis	201
VI.B.3 Electrolysis of NF concentrate in acid condition	204
VI.B.4 Conclusion.....	205
IV. Conclusion.....	207
References.....	208

This chapter investigates the removal of pharmaceuticals by electrochemical oxidation. In this chapter, the impact of the composition of the solution (organic and inorganic components) is studied. For that, the interaction between pharmaceuticals, the chemical reactions between pharmaceuticals and electrogenerated oxidants or byproducts is studied.

This chapter has two parts: the section IV.A is devoted to the elimination of pharmaceuticals in synthetic solutions and in section IV.B. The study is performed in NF retentate.

IV.A Electrochemical oxidation in synthetic solution

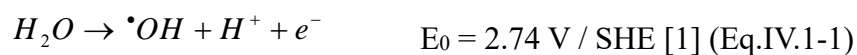
This section investigates the removal of pharmaceuticals containing in the synthetic solutions by electrochemistry. The influence of factors on electrooxidation are studied such as the applied current intensity, the presence of salts and common organic waste, the competition and interaction between pharmaceuticals on the degradation of pharmaceuticals. Finally, a numerical model for the degradation of pharmaceutical during electrolysis is also proposed in this chapter.

IV.A.1 Study of ciprofloxacin as molecule model

The first part of this study is devoted to the electrochemical study of the oxidation by cyclic voltammetry. Then galvanostatic electrolyses are performed. Ciprofloxacin (CIP) degradation and mineralization rate are followed.

IV.A.1.1 Electrochemical study of ciprofloxacin

The electrochemical behavior of CIP in sulfuric acid solution is studied by cyclic voltammetry. Fig.IV-1 presents the cyclic voltammograms obtained on BDD in the electrolyte (H₂SO₄ 0.1M) with and without CIP (0.068mM). The voltammogram of H₂SO₄ (0.1M) shows the oxidation of water at 1.25 V/SCE (corresponding to 0.95 mA cm⁻²). According to BDD's electrochemical properties, ·OH is expected to be produced from water discharge as Eq. IV.1-1.



In presence of CIP an oxidation peak was observed before the water discharge at 1V / SCE, the current intensity of the oxidation wave has a peak value of 2.27 mA cm^{-2} . This wave is an irreversible direct electrons transfer between CIP and BDD anode.

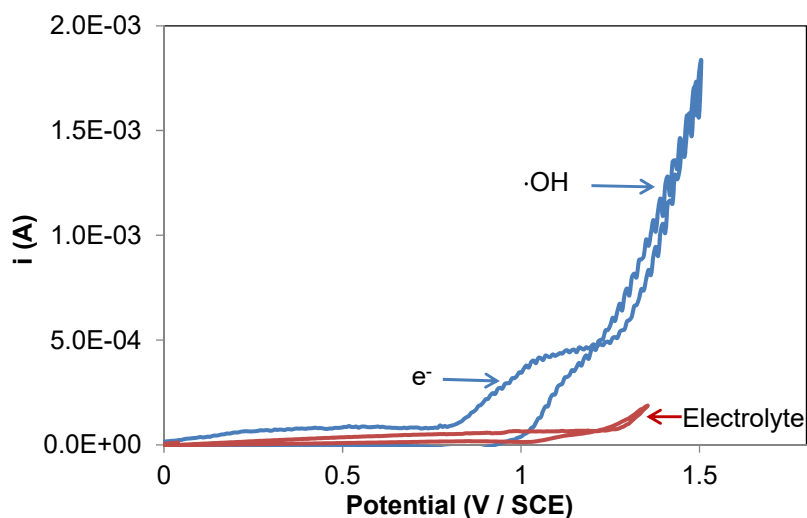


Fig.IV-1 Cyclic voltammetry of CIP 0.068 mM in 0.1M H_2SO_4 . Working electrode: BDD (0.196 cm^2), Counter electrode: Pt, Reference electrode: SCE. Scan rate: 100 mVs^{-1} , $\omega = 800 \text{ rpm}$.

Montes et al. [2] observed the similar behavior with BDD electrode in Britton-Robinson solution ($\text{pH} = 10$), the oxidation current of CIP started to increase at approximately $+0.85 \text{ V/ref}$ and reached a plateau value between $+0.95$ and $+1.10 \text{ V/ref}$. The mechanism of CIP oxidation involving two-electrons was proposed by Fotouhi and Alahyari with multi-wall carbon nanotubes film-modified glassy carbon electrode [3] (see Fig.IV-2).

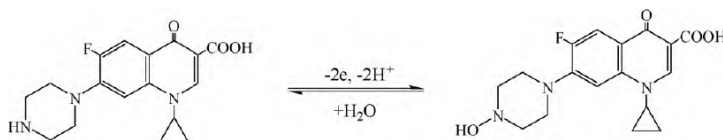


Fig.IV-2 electrochemical reaction of CIP

In parallel hydroxyl radical produced during water discharge. Hydroxyl radical, a strong oxidant, act as a for oxygen transfer.

Thus, CIP can be oxidized by BDD anode with two pathways: direct electron transfer and oxygen transfer via $\cdot\text{OH}$.

IV.A.1.2 Galvanostatic electrolysis of CIP solution

Galvanostatic electrolyses are performed in synthetic solutions containing CIP. Fig.IV-2 shows that the concentration of CIP decays with (a) EO time and (b) electrical charge. CIP degradation follows a pseudo-first order kinetic and the observed rate constant (k_{obs}) is determined as 0.0287 min^{-1} (inset panel). 97 % of CIP removal was reached after 120 min of electrolysis with a charge consumption of 0.2 Ah L^{-1} . The total removal of CIP was obtained after 180 min.

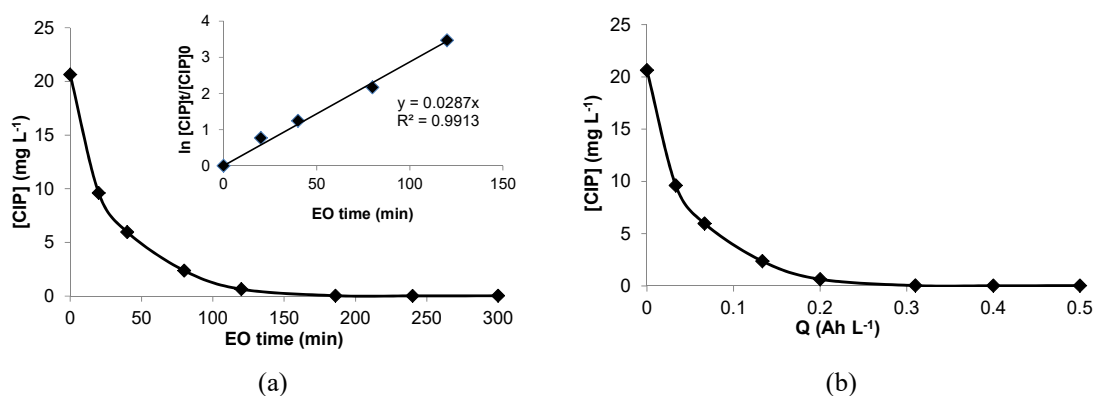


Fig.IV-2 CIP concentration decay with (a) EO time and (b) electrical charge during 300min electrolysis of 1L CIP solution in K_2SO_4 0.1 M at pH = 3.7. $[CIP]_0 = 20.64 \text{ mg L}^{-1}$ (0.0623 mM), $I = 0.1 \text{ A}$ ($i = 1.45 \text{ mA/cm}^2$, $i_{lim}^0 = 1.29 \text{ mA/cm}^2$), flow rate = 366 L h^{-1} , $T = 30 \text{ }^\circ\text{C}$. Inset panel: pseudo –first order kinetic analysis of CIP

The removal of TOC is shown in Fig.IV-3 (a) during electrolysis of CIP solution. 84% of TOC was removed after 300 min (0.5 Ah L^{-1}) of electrolysis.

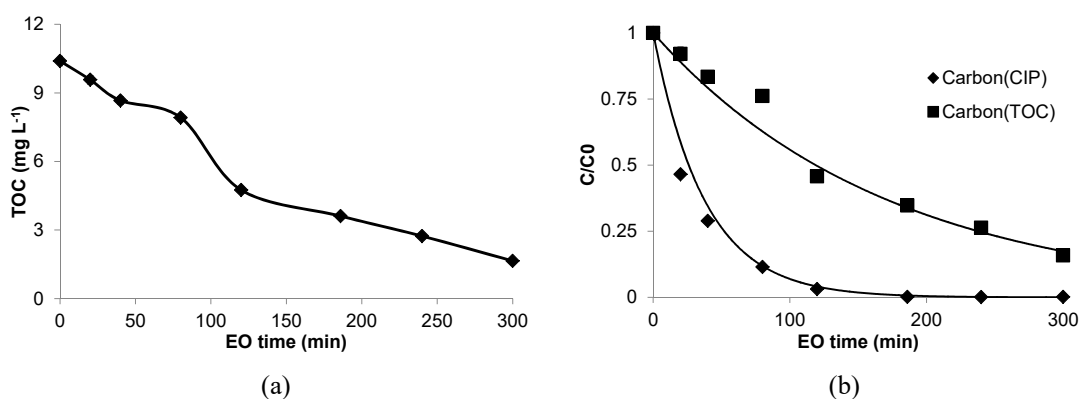


Fig.IV-3 (a) TOC degradation (b) Normalization of carbon of CIP and carbon of TOC during electrolysis of 1L CIP solution in K_2SO_4 0.1 M at pH = 3.7. $[CIP]_0 = 20.64 \text{ mg L}^{-1}$ (0.0623 mM), $I = 0.1 \text{ A}$ ($i = 1.45 \text{ mA/cm}^2$, $i_{lim}^0 = 1.29 \text{ mA/cm}^2$), flow rate = 366 L h^{-1} , $T = 30 \text{ }^\circ\text{C}$.

Fig.IV-3(b) presents a comparison between TOC and carbons calculated from the remaining CIP concentration (1 mol of CIP corresponds to 17 mol of carbons). The difference of the carbons of CIP and carbons of TOC represents the intermediates of CIP degradation. Fig.IV-3 (b) highlights that CIP was completely removed after 180 min, the remaining TOC is 46%, which corresponds to the intermediate compounds from CIP oxidation. The complete mineralization takes more time and energy due to the mass transfer limitation. Moreover, some generated carboxylic acids have low reaction rate with $\bullet\text{OH}$ compared with aromatics [4].

FigIV-4 plots the COD decay with time during electrolysis. The graph compares the experimental value and theoretical COD decay which can be calculated with Eq.I-24 (see chapter I) in the case of mass transfer controlled regime. A good agreement between experimental COD and theoretical values are observed. 100% of COD was removed after 300 min of electrolysis (0.5 Ah L^{-1}).

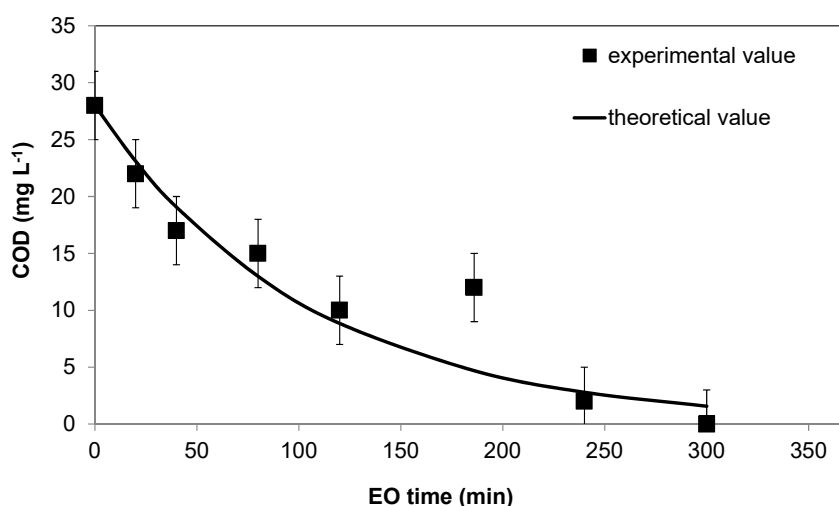


Fig.IV-4 COD decay with time during electrolysis of 1L CIP solution in K_2SO_4 0.1 M at $\text{pH} = 3.7$. $[\text{COD}]_0 = 28 \text{ mg L}^{-1}$, $I = 0.1\text{A}$ ($i = 1.45 \text{ mA cm}^{-2}$, $i_{\text{lim}}^0 = 1.29 \text{ mA cm}^{-2}$), flow rate = 366 L h^{-1} , $T = 30 \text{ }^\circ\text{C}$

The concentration of NO_3^- and NH_4^+ during electrolysis of CIP solution was present on Fig.IV-5. During degradation of CIP, NO_3^- and NH_4^+ appear after 10 min electrolysis corresponding to 20 % CIP degradation. After 300 min of electrolysis, removal of organic nitrogen reaches 62 %. The nitrogen in CIP structure is converted to NO_3^- and NH_4^+ with a ratio of 1:3.

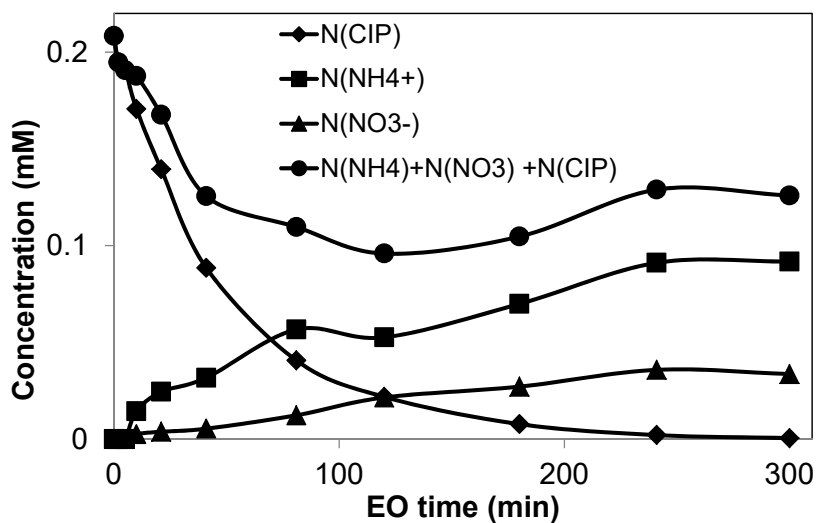


Fig.IV-5 Nitrogen concentration of CIP, and the concentration of NO_3^- and NH_4^+ during electrolysis 1L of synthetic CIP solution: $[\text{CIP}]_0 = 0.069 \text{ mM}$ in K_2SO_4 0.02 mM ; $I = 0.1 \text{ A}$ ($I_{\text{lim}} = 0.08 \text{ A}$), flow rate = 366 L h^{-1} , $T = 30 \text{ }^\circ\text{C}$.

IV.A.1.3 Conclusion

This section is devoted to the electrooxidation of CIP chosen as molecule model of pharmaceuticals. The oxidation has occurred by direct electron transfer and via $\cdot\text{OH}$ (oxygen transfer). Its degradation follows pseudo-first-order kinetics. COD decayed with a good agreement between experimental and theoretical value under mass transfer controlled. The mineralization degree of CIP solution ($\text{TOC}_{\text{final}}/\text{TOC}_0$) reached 84% after 300 min of electrolysis.

IV.A.2 Influence of the applied current on CIP mineralization

This section investigates the influence of the applied current on the rate of CIP degradation rate, TOC and COD removal. The galvanostatic electrolyses are conducted at various applied current intensities corresponding to different regimes: $I < I_{\text{lim}}^0$, $I > I_{\text{lim}}^0$, $I \gg I_{\text{lim}}^0$. The initial limiting current intensities are calculated with initial COD values, according to BDD's electrochemical properties (Eq.I-24). The operating conditions for each electrolysis are presented in table VI-1.

Table IV-1 Applied current and initial operating conditions for each electrolysis with BDD anode in K_2SO_4 0.1 M, $T = 30\text{ }^\circ\text{C}$, flow rate = 366 L h^{-1} , $[\text{COD}] \approx 35\text{ mg/L}$, $[\text{TOC}] \approx 10\text{-}11\text{ mg/L}$

	[CIP] ₀ (mM)	Current intensity I (A)	Current density i (mA cm ⁻²)	i_{lim}^0 (mA cm ⁻²)	I/I_{lim}^0
	0.0522	0.03	0.43	0.93	0.5
$I < I_{\text{lim}}^0$	0.0523	0.05	0.72	0.93	0.8
	0.0622	0.1	1.45	1.10	1.3
$I > I_{\text{lim}}^0$	0.0561	0.5	7.25	1.00	7.2
$I \gg I_{\text{lim}}^0$	0.0568	1.5	21.74	1.00	21.7

IV.A.2.1 Influence of applied current on CIP degradation rate

Figure IV-6 presents temporal profile of CIP concentration using different current intensities and the degradation rate of CIP. It was observed generally that CIP degrades fast with an increasing applied current. The influence of applied current density on CIP degradation rate differs from current regimes.

(i) $I < I_{\text{lim}}^0$

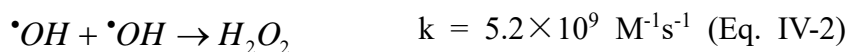
As expected, it can be observed that the higher current intensity is the faster the removal of CIP, when the applied current intensity is lower than the initial limiting current intensity.

(ii) $I > I_{\text{lim}}^0$

Fig.IV-6 (b) presents that for both current intensities ($I = 0.1\text{ A}$ and $I = 0.5\text{ A}$), CIP concentration decreases with the same rate and 100% of CIP was removed after 180 min of electrolysis. In this case, the applied current is higher than the initial limiting current intensity, and then the process is mass transfer controlled. The removal rate of CIP does not depend on the applied current.

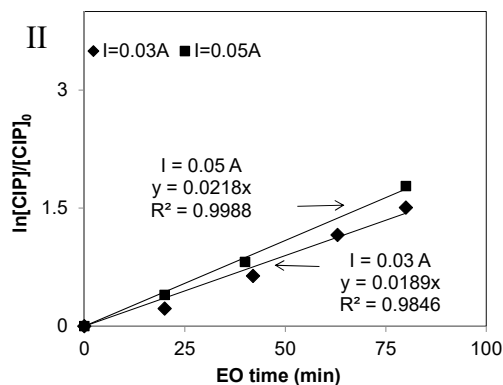
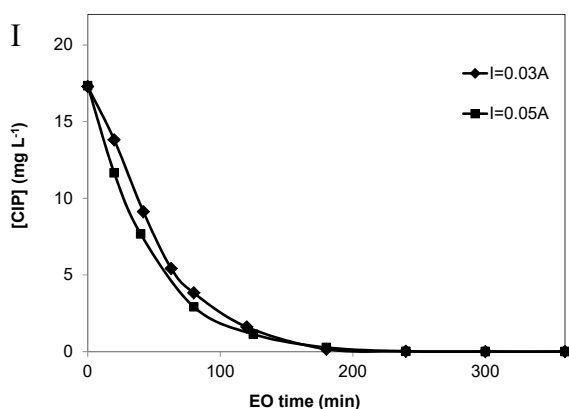
(iii) $I \gg I_{\text{lim}}^0$

The observed degradation rate of CIP at 1.5 A is much higher than the case $I = 0.1$ or 0.5A. CIP was degraded completely around 100 min. These results can be explained as follows: besides the oxidation of organics, the generation of oxygen happens at the same time as Eq. IV-2 to Eq. IV-4 [5].

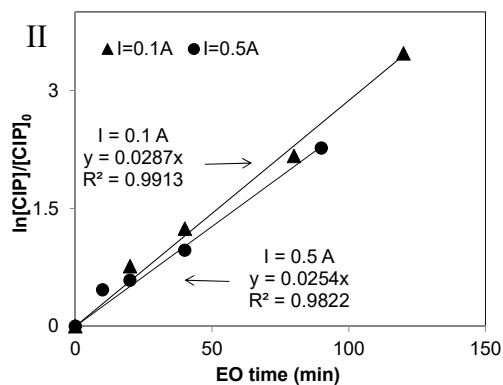
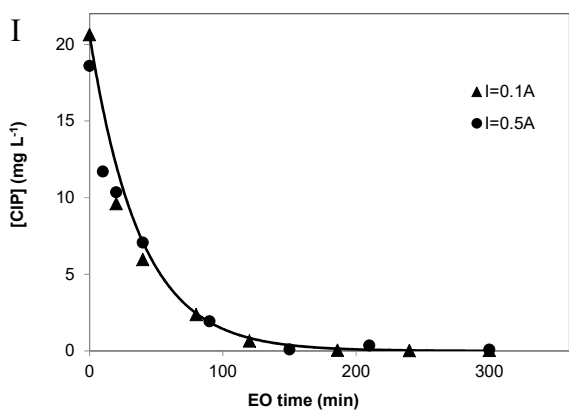


Herein, the applied current intensity is much higher than the limiting current intensity. The current used for oxygen generation ($I_{\text{applied}} - I_{\text{lim}}$) is more significant than the case $I = 0.1$ and 0.5A and more oxygen bubbles were generated close to the electrode. The formation of bubbles in the hydrodynamic system able to enhance mass coefficient was reported by Vogt [6]. Consequently, the mass transfer coefficient increases locally. In the case of mass transfer control, the increasing mass transfer coefficient can lead to the faster degradation rate. Flox et al. [5] reported that the electrogenerated oxygen bubbles can accelerated the degradation rate of phenol with BDD anode. To prove this hypothesis, the influence of the current on COD variation will be investigated on section IV.1.2.2.

(a) $I < I_{lim}^0$



(b) $I > I_{lim}^0$



(c) $I \gg I_{lim}^0$

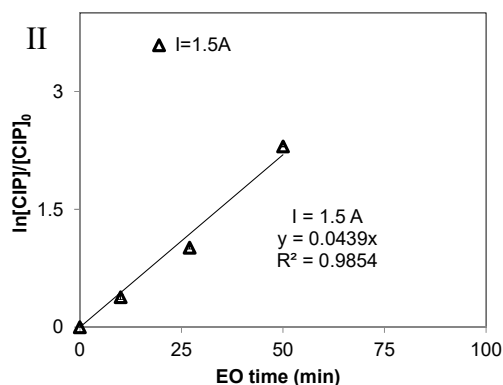
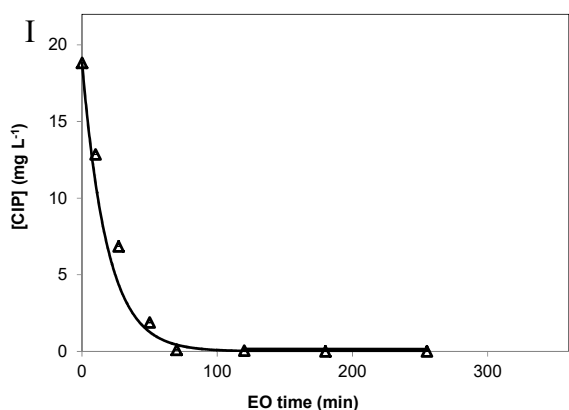


Fig.IV-6 The concentration of CIP decays with EO time (I) and the observed degradation rate (II) during electrolysis of 1L CIP solution in K_2SO_4 0.1 M at pH = 3.7 with various current (a, b, c). Flow rate = $366 L h^{-1}$, $T = 30 ^\circ C$. The ratio of I/I_{lim}^0 and initial concentration of CIP see table VI-1.

More obviously, Fig.IV-7 illustrates CIP degradation rate versus the applied current intensity. $I < I_{lim}^0$, the degradation of CIP depends on I , for $I > I_{lim}^0$, the influence of current

intensity becomes more important at very high values, when the production of dioxygen becomes majority.

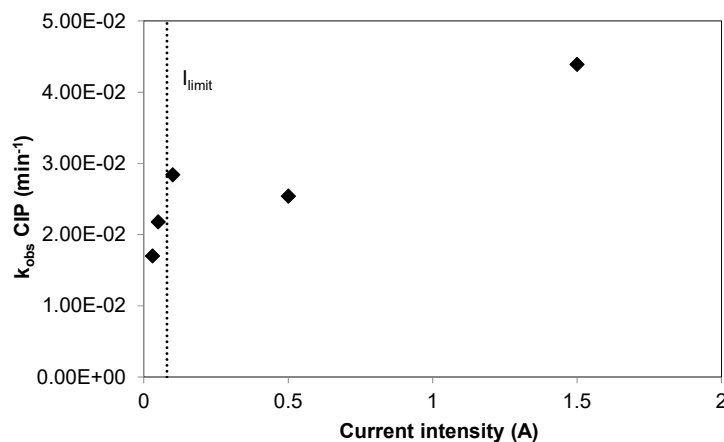


Fig.IV-7 CIP observed degradation rate versus applied current density. Operating conditions: see Fig.IV-5.

IV.A.2.2 Influence of applied current on COD decay

Figure IV-8 presents COD decay using various applied current intensities. In Fig IV-8(a), in the case of $I < I_{lim}^0$ according to BDD's electrochemical properties, the COD follows a linear relationship as function of electrooxidation time (Eq.I-20); then after critical time (Eq.I-22), the applied current is higher than the limiting current, the COD decreases exponentially (Eq.I-24) as shown on the Fig IV-8 (b) and (c). Fig.IV-8 (b) describes the case of the kinetic regime under diffusion limitation. A good agreement between theoretical and experimental values is observed in the graph (a and b).

When the applied current is much higher than the initial limiting current (graph c), the experimental COD values decrease faster than the theoretical ones during the first 50 min and then raises until the end of experiment.

(i) $t \leq 50 \text{ min}$

To explain these deviations, it can be taken account that during the electrolysis, the current exceeded than the limiting current ($I_{applied} - I_{lim}$) leads to the evolution of oxygen at the anode, as pointed out on section IV.1.2.1. Consequently, the rate of the gas evolution close to the electrode has a great effect on the mass transfer since a release of bubbles increase the mass transfer coefficient. Previous studies in our laboratory were performed to evaluate the mass transfer coefficient taking account the generation of bubbles [5,7]. Annex IV-1 presents all the calculations for the corrected COD decay which corresponds to the dashed line on FigIV-8 (c).

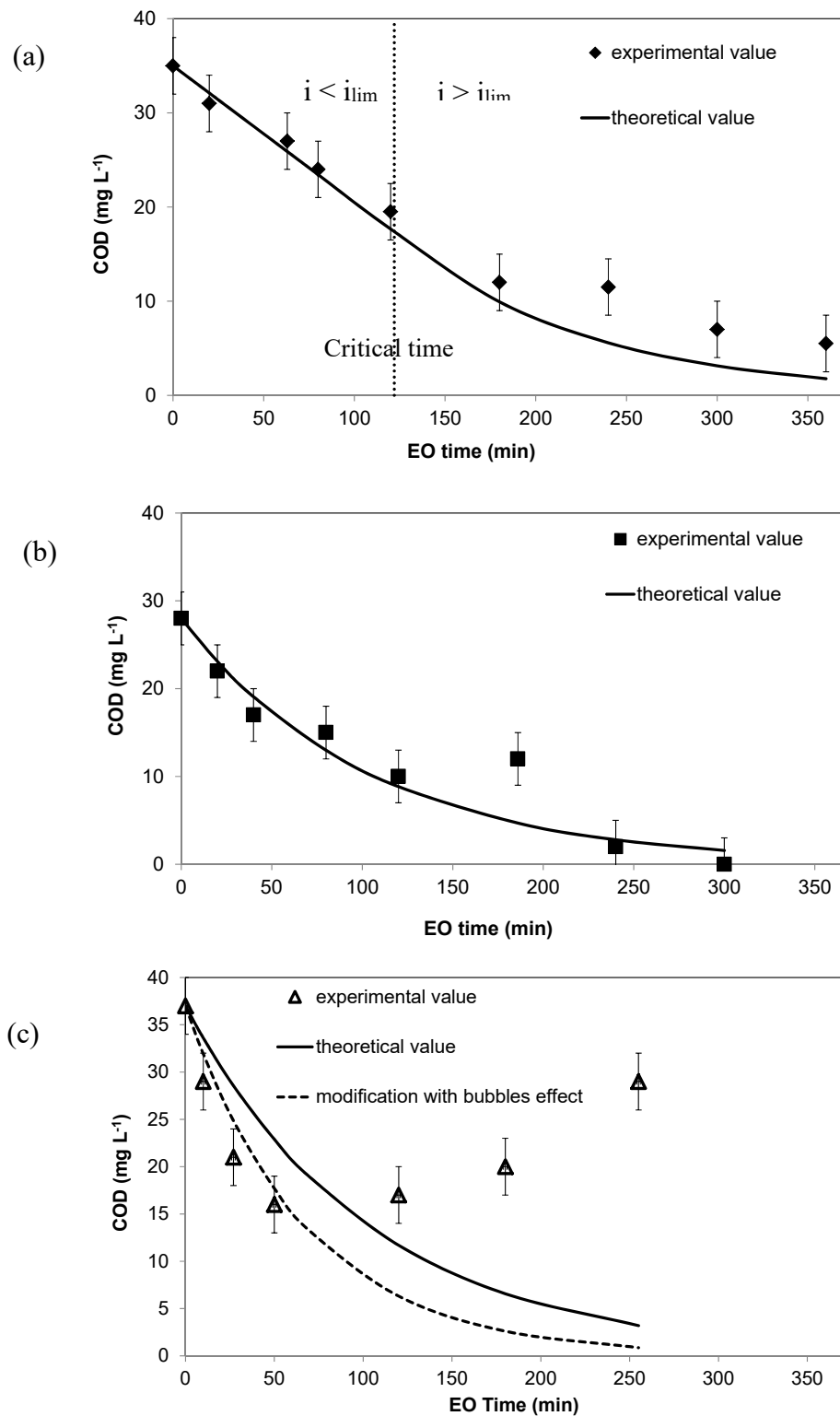


Fig.IV-8 COD decay with time during electrolysis of 1L CIP solution in K_2SO_4 0.1 M at pH = 3.7 with various current, flow rate = 366 L h⁻¹, T = 30 °C.

(a) $I < I_{lim}^0$, $[COD]_0 = 35$ mg L⁻¹, $I = 0.03$ A ($i = 0.064$ mA cm⁻², $i/i_{lim}^0 = 0.5$);

(b) $I > I_{lim}^0$, $[COD]_0 = 28$ mg L⁻¹, $I = 0.1$ A ($i = 1.45$ mA cm⁻², $i/i_{lim}^0 = 1.3$);

(c) $I \gg I_{lim}^0$, $[COD]_0 = 37$ mg L⁻¹, $I = 1.5$ A ($i = 1.45$ mA cm⁻², $i/i_{lim}^0 = 21.7$)

(ii) $t \geq 100$ min: the experimental COD values increase continuously.

In parallel the increase of COD, the analysis of sample shows the decrease of TOC after 100 min (see Fig.IV-9).

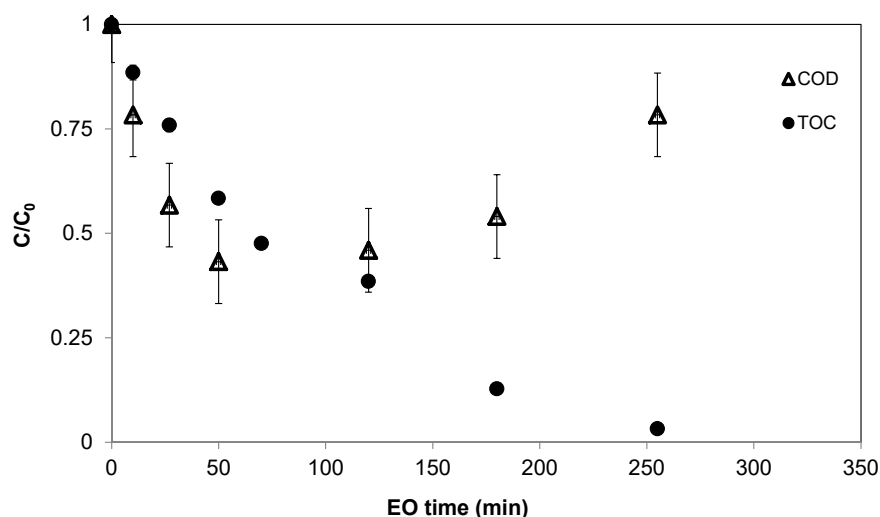
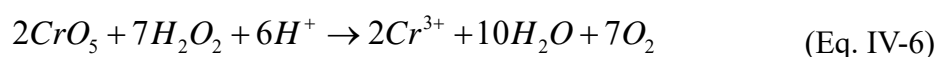
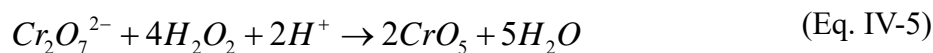


Fig.IV-9 COD and TOC variation with time during electrolysis of 1L CIP solution in K_2SO_4 0.1 M at pH = 3.7 with applied current $I = 1.5A$ ($I = 207 A m^{-2}$), flow rate = $366 L h^{-1}$, $T = 30 ^\circ C$

Thus, this unexpected increase of COD does not depend on the concentration of organics. The depletion of organic leads a higher surplus of hydroxyl radicals which are very reactive and form H_2O_2 [8] (Eq. IV-2). The hydrogen peroxide can be oxidized by dichromate in the COD test tube to produce Cr^{3+} . The reactions are presented on eq.IV.1-5 and IV.1-6 [9].



To verify this hypothesis, H_2O_2 solutions at various concentrations were prepared and measurements of COD were carried out. Fig.IV-10 shows the obtained results. A linear relationship was observed and the concentration of H_2O_2 can be evaluated from the COD value. Around 1.5 mM of H_2O_2 remained after at 255 min of electrolysis with an applied current intensity of 1.5A, considering that the COD related to 0.03 mM at 255 min is

negligible.

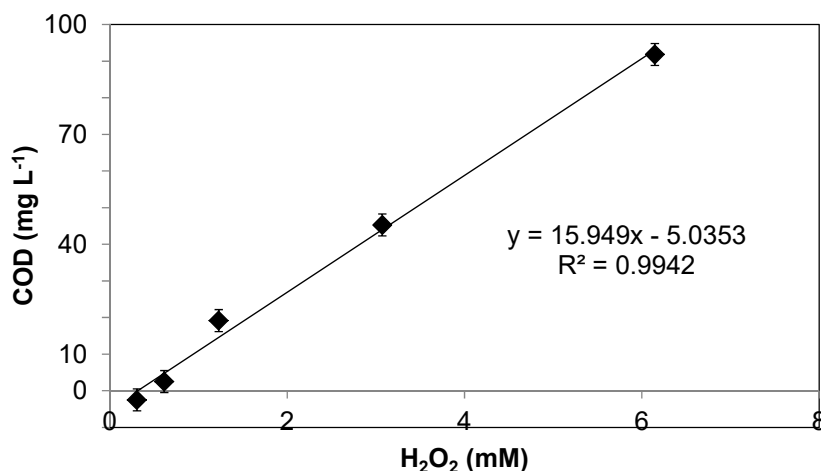


Fig.IV-10 Correlation of concentrations between H₂O₂ and COD

IV.A.2.3 Influence of applied current on TOC mineralization

Table IV-2 presents the TOC values at initial and 240 min using various current intensities. One can clearly distinguish three “groups” corresponding to 3 regimes: $I < I_{lim}^0$: $TOC_{t=240}/TOC_0 = 66\%$, $I > I_{lim}^0$: $TOC_{t=240}/TOC_0 = 75\%$, $I \gg I_{lim}^0$: $TOC_{t=240}/TOC_0 = 97\%$, respectively. The decay of TOC with electrolysis time for each electrolysis are shown in Annex IV-2.

Table IV-2 The TOC values at initial and 240 min during electrolysis of 1L CIP solution in K₂SO₄ 0.1 M at pH = 3.7 with various current, flow rate = 366 L h⁻¹, T = 30 °C

	$I < I_{lim}^0$		$I > I_{lim}^0$		$I \gg I_{lim}^0$
	$I = 0.03$ A	$I = 0.05$ A	$I = 0.1$ A	$I = 0.5$ A	$I = 1.5$ A
TOC ₀	10.5	9.4	10.4	10.0	11.0
TOC _{t=240}	3.3	3.2	2.7	2.2	0.35
TOC _{t=240} /TOC ₀	67%	66%	74%	78%	97%

IV.A.2.4 Influence of applied current on intermediates production and mineralization

The amounts of intermediates produced during CIP degradation can be estimated by the difference between carbons from CIP and TOC, Δ , in the solution (as defined previously in section IV.A.1.2). As shown on Fig.IV-11, the amounts of intermediates products increase from the beginning of electrolysis, then reached a maximum value and

began to decline after complete removal of CIP.

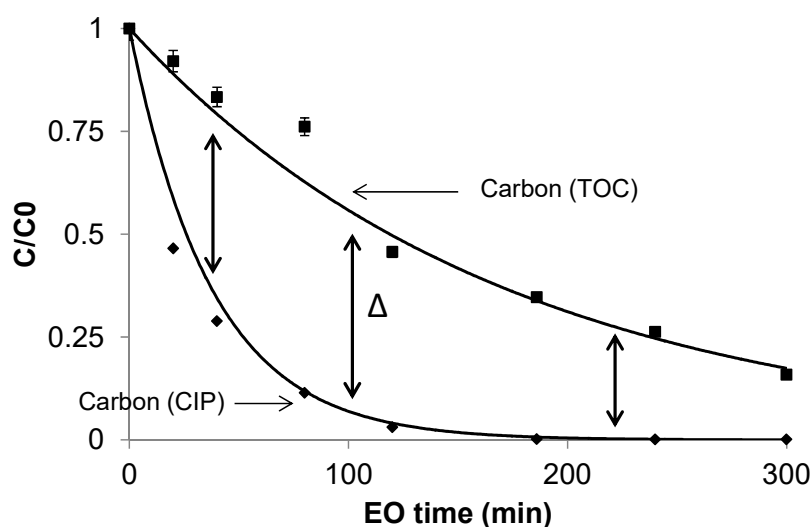


Fig.IV-11 Estimation of Δ and its variation during electrolysis of 1L CIP solution in K_2SO_4 0.1 M at pH = 3.7 at 0.1 A, flow rate = 366 L h^{-1} , $T = 30 \text{ }^\circ\text{C}$.

The carbons from CIP and total organic carbon are compared at various applied current in Annex IV-3, separately. At initial state, the total organic carbon corresponds to the initial carbons coming from CIP.

The variation of Δ with time is shown in Fig.IV-12. With each applied current the maximum amounts of intermediates is quite the same. The higher the current is, the shorter is the range of time where intermediates present.

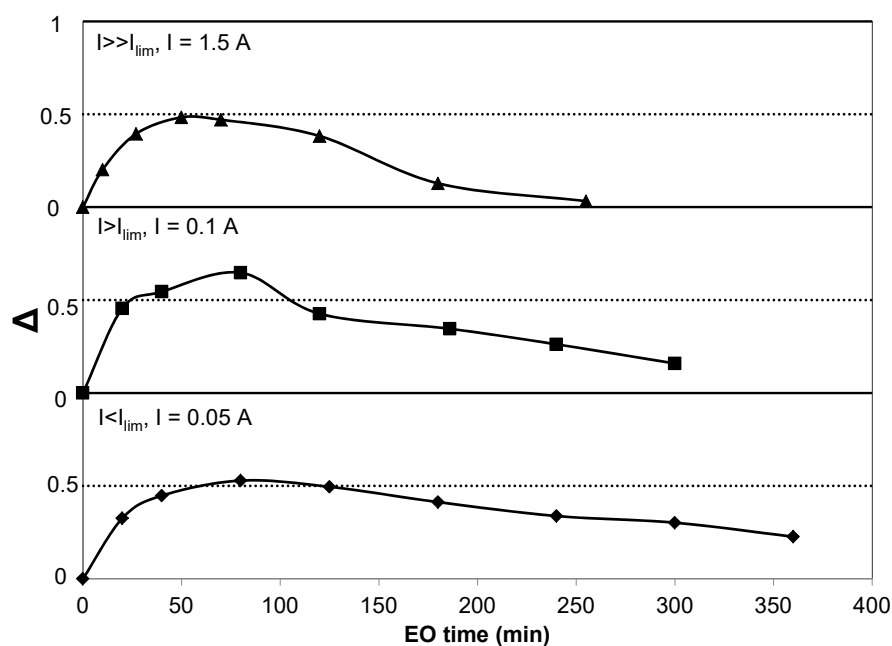


Fig.IV-12 The variation of Δ (the amounts of intermediates) during electrolysis of 1L CIP solution in K_2SO_4 0.1 M at pH = 3.7 at various applied current (0.05 - 0.1 A), flow rate = 366 L h^{-1} , $T = 30 \text{ }^\circ\text{C}$.

For a given operating condition, the total amounts of intermediates produced during the mineralization of CIP can be calculated as the differences between the carbons concentration of CIP and total organic carbons as the shadow part of Fig.IV-13.

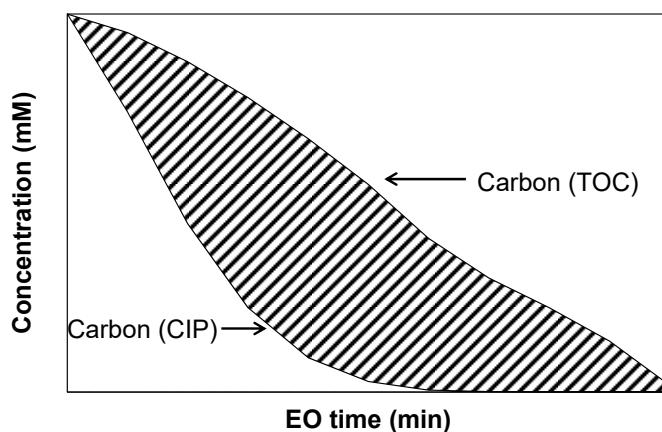


Fig.IV-13 Calculation of total amounts of intermediates during electrolysis

The total amounts of intermediates during electrolysis can be calculated with Eq.IV.1-7. The duration for the calculation was 300 minutes. The function of $Carbon_{TOC}(t)$ and $Carbon_{CIP}(t)$ was simulated with RSQ function (R^2) higher than 92%.

$$[\text{intermediates}] = \int_0^t Carbon_{TOC}(t)dt - \int_0^t Carbon_{CIP}(t)dt \quad (\text{Eq.IV.1-7})$$

To understand the effect of current to total amount of intermediates, the total amount of intermediates for each applied current were calculated according to Eq.IV.1-7, integrating from t (0, 300). The raw data of $Carbon_{TOC}(t)$ and $Carbon_{CIP}(t)$ is shown on Annex 3.

Fig.IV-14 plots the variation of total amounts of intermediates produced during mineralization of CIP at various applied current. $I < I_{lim}^0$, the amount of by-products decreases sharply with the increasing current; while in the case $I > I_{lim}^0$, the total amounts of by-products is the same for an increasing current intensity in the range of 0.1 - 0.5A and a slightly decrease is observed at 1.5A.

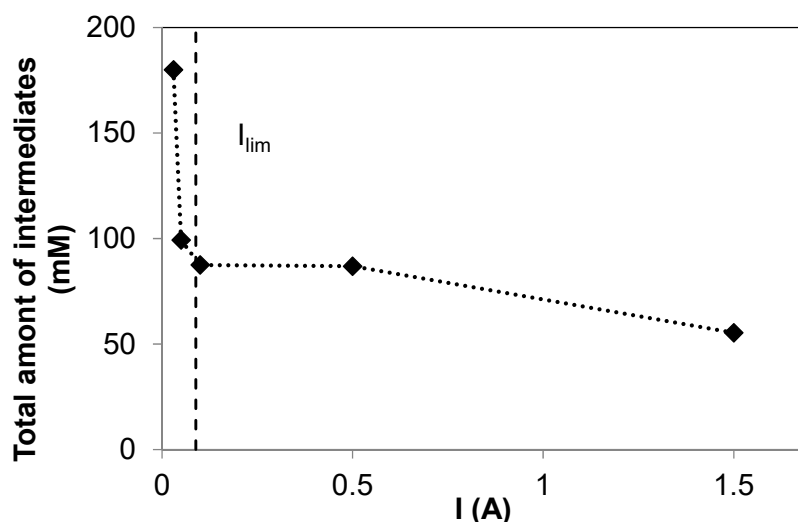


Fig.IV-14 The variation of total amounts of intermediates produced during electrolysis of 1L CIP solution with various applied current in K_2SO_4 0.1 M at pH = 3.7, flow rate = $366 L h^{-1}$, $T = 30 ^\circ C$.

An example of the calculation of energy consumption and mineralization rate in the synthetic solution is shown in Annex IV-4. The current intensity close to the limiting current can be the best compromise of less energy consumption and high mineralization rate.

IV.A.2.5 Conclusion

The increase of the current density accelerates CIP degradation, COD removal and TOC mineralization. Some effects have been evidenced like electrogeneration of oxygen bubbles and hydrogen peroxide which have a great impact on the COD removal.

The total amounts of intermediates are inversely proportional to applied currents: $I < I_{lim}^0$, it decreases sharply with an increasing current, while in the case of $I > I_{lim}^0$, it is stable or decreases slightly.

IV.A.3 Removal of common organic waste and the other pharmaceuticals

In hospital wastewater, micropollutants are corresponding to a few percentages of the organics. The common organic waste is present in higher concentration than the micropollutants in wastewater. Urea is the major organic in fresh human urine and can be reached a concentration close to $25g L^{-1}$ [10–12], while the concentration of

pharmaceuticals are in the range of 1 mg L^{-1} [13]. In this section, urea is studied as a common organic waste present in hospital wastewater at higher concentration than pharmaceuticals in wastewater. Salbutamol and sulfamethoxazole with high risk level to environment are selected for this study because both are usually present in hospital wastewater [14].

This section investigates the electrooxidation of urea and others pharmaceuticals: salbutamol (SALBU) and sulfamethoxazole (SMX) in single organic synthetic solution. The object is to understand their electrochemical oxidation behavior with BDD anode.

IV.A.3.1 Removal of urea as a common organic waste

The electrochemical behavior of urea was reported by Hernández et al. [15] with BDD anode. Figure IV-15 presents the cyclic voltammograms of electrolyte (NaClO_4 1M) contained 0, 0.1 and 1M of urea. In presence of urea no oxidation peak was observed before the water discharge, which indicated that no direct electron transfer occurs during the oxidation of urea. The increasing current density at 1.5V with urea concentration is observed in the region of water oxidation where the formation of hydroxyl radicals occurs. Thus, the oxidation of urea occurred via $\cdot\text{OH}$.

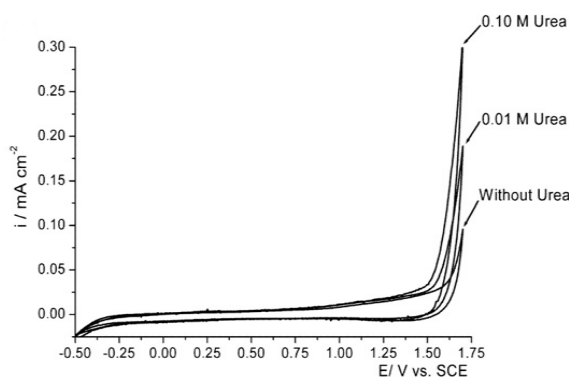


Fig.IV-15 Cyclic voltammetry in 1 M NaClO_4 with different urea concentrations, working electrode: BDD (50 cm^2), Reference electrode: SCE. Scan rate: 30 mv s^{-1} [13].

IV.A.3.1.1 Electrolysis of Urea solution

Galvanostatic electrolyses were performed at $30 \text{ }^\circ\text{C}$ on solutions containing urea (0.63 M) at 0.5 A . Samples were taken regularly for analysis by UV spectroscopy for urea concentration and TOC. In this study, COD cannot be measured accurately with the standard method. Indeed, in spite of its strong oxidizing power, some nitrogenous organic compounds cannot be completely oxidized by dichromate solution [16,17].

Figure IV-16 shows the concentration of urea and TOC with electrooxidation time. The

initial urea concentration was 0.63 mM and the applied current was 0.5 A. In this case, the process is limited by mass transfer ($I > I_{lim}^0$). It was observed that the concentration of urea and TOC decreased sharply with the electrooxidation time. The observed degradation rate of urea is 0.0152 min^{-1} , which is slower than CIP (0.0254 min^{-1}) at the same current intensity. After two hours, removal of urea and TOC reached 93% and 74%, respectively. Then TOC and urea concentration stabilized. This stabilization can be due to the low concentration of urea and the transfer limitation, in addition the kinetic of the reaction between hydroxyl radical and urea is low ($7.9 \times 10^5 \text{ M}^{-1} \text{ s}^{-1}$) [18]. It was also reported that urea is refractory to ozone treatment [19]. Nevertheless, urea is biodegradable and can be degraded into NH_3 and CO_2 through the hydrolysis process controlled by the enzyme ureases [20] which are found in numerous bacteria, fungi, algae, plants and some invertebrates, as well as in soils, as a soil enzyme [21].

The amounts of intermediates can be characterized by the difference between the TOC and carbons from urea. Herein, urea is a molecule containing one carbon, so the molar concentration of urea is the molar concentration of carbon. From Fig.IV-15, the temporal curves of TOC and urea are quite close, which indicate few intermediates are observed during the electrochemical oxidation of urea with BDD anode. It can be explained as following: for the degradation of urea, the first step is the $\cdot\text{OH}$ attack at $-\text{NH}_2$ moiety. This pathway is very slow and the determined-step for urea degradation [22]. It can be proposed that once the first step happens, urea degrade and the intermediates are mineralized in a short time.

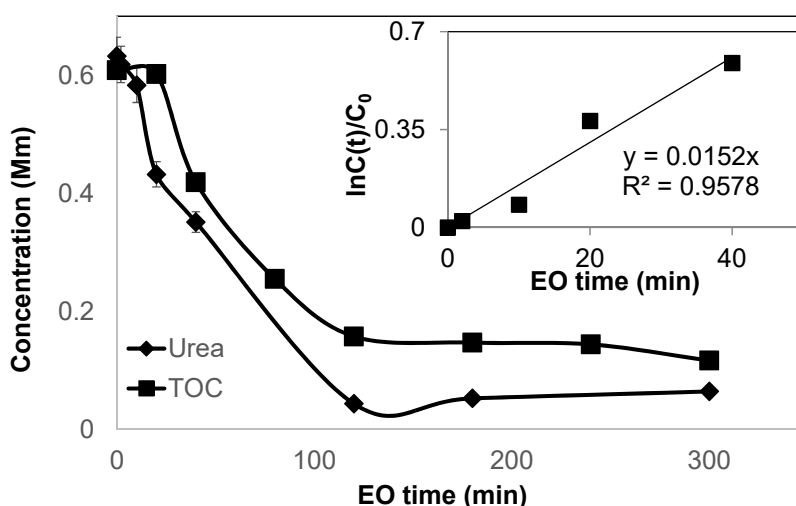


Fig.IV-16 Concentration of urea and TOC decayed with EO time and during electrolysis of 1L urea solution in K_2SO_4 0.1 M at $\text{pH} = 3.7$. $[\text{Urea}]_0 = 0.63 \text{ mM}$ (38.1 mg L^{-1}), $[\text{TOC}]_0 = 0.6 \text{ mM}$ (7.12 mg L^{-1}), $I = 0.5\text{A}$ ($I_{lim}^0 = 0.17\text{A}$), flow rate = 366 L h^{-1} , $T = 30^\circ\text{C}$. Insert panel: the observed degradation rate of urea.

IV.A.3.1.2 Oxidation pathway of urea

Figure IV-17 shows the variation of the concentration of NH_4^+ , NO_3^- , and urea. NH_4^+ and NO_3^- are the products by urea oxidation. NO_3^- is the main form of nitrogen product at the beginning of electrolysis. The concentration of it reached a maximum value as 0.94 mM at 120 min when the urea concentration reached a minimum value. NH_4^+ appeared after 20 min of electrolysis and then remained constant until the end (0.14 mM). The total of nitrogen from NH_4^+ , NO_3^- , and urea at 300 min reached 94 % of the initial nitrogen from urea.

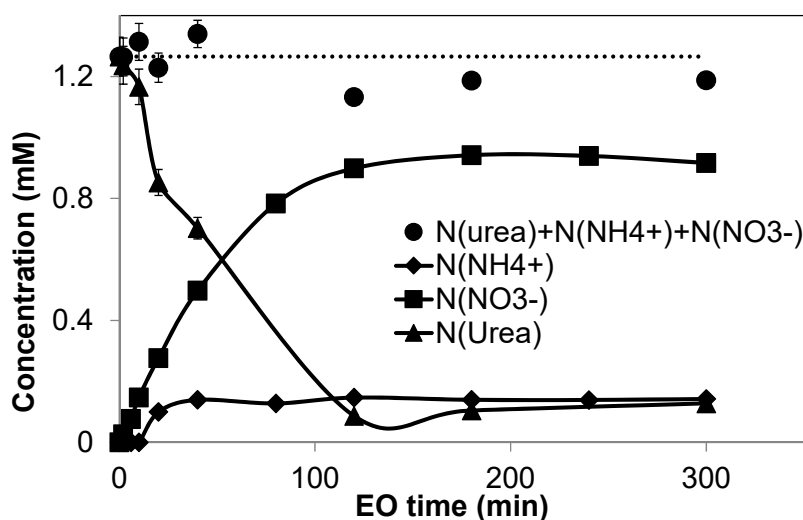


Fig.IV-17 Concentration of nitrogen in form of NH_4^+ , NO_3^- , urea and total nitrogen in the solution during electrolysis of 1L urea solution in K_2SO_4 0.1 M at pH = 3.7-7 (pH increase during electrolysis). The dashed line is the initial concentration of nitrogen in the solution (from urea). $[\text{Urea}]_0 = 0.63$ mM (38.1 mg L^{-1}), $I = 0.5\text{ A}$ ($I_{\text{lim}}^0 = 0.17\text{ A}$, oxidation product is nitrate), flow rate = 366 L h^{-1} , $T = 30\text{ }^\circ\text{C}$.

The mechanism of urea mineralization can be discussed, according to the final products: NH_4^+ and NO_3^- . The carbon atom in the urea structure has +4 oxidation states (and no extractable C-H bond is present), $\bullet\text{OH}$ attack is forced at the $-\text{NH}_2$ moiety. This first pathway is very slow and determines the slow rate of urea disappearance [22]. It leads, probably, to the transformation of an amino group into a nitrous group, followed by the detachment of nitrite ions, rapidly oxidized to nitrate [22–24,24,25]. Calza et al. suggested that the product of NH_4^+ (or $\text{NH}_3\cdot\text{H}_2\text{O}$ depending on the pH) was probably formed by the $\bullet\text{OH}$ attack on the carbon atom after the attack on the N atom. Then the production of carbamic acid allowed NH_3 discharged or in the form of $\text{NH}_3\cdot\text{H}_2\text{O}$ and NH_4^+

depending on the solution) (Fig.IV-18).

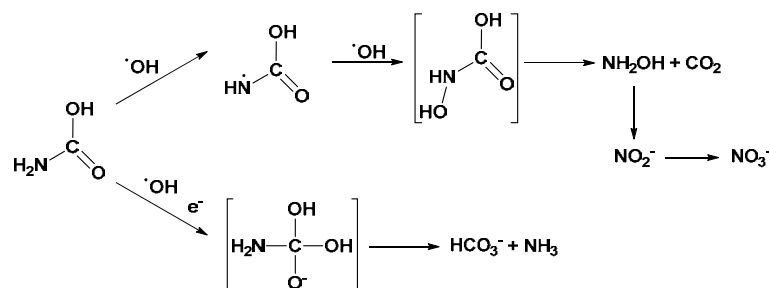


Fig.IV-18 Chemical reaction of carbamic acid with hydroxyl radicals [22]

In the present, the ratio $[\text{NH}_4^+] / [\text{NO}_3^-]$ is 1:7, from which it can be inferred that the $\bullet\text{OH}$ mainly attack the N atom rather than C atom. From table IV-3, noting that the first 2 min 0.014 mM urea in the solution is removed and 0.027 mM NO_3^- is produced, it seems to be that the entire nitrogen from urea is converted to NO_3^- at first. The basic pathway proposes that the two $-\text{NH}_2$ moiety were attacked by $\bullet\text{OH}$ and transformed into a nitrous group, followed by the detachment of nitrite ions, rapidly oxidized to nitrate, as discussed above. After 20 min of electrolysis, NH_4^+ is present which intimates that the pathway of $\bullet\text{OH}$ attack on the carbon atom after the attack on the N atom occurs. At this time, the N from urea reacts and the concentration of $\text{NO}_3^- + \text{NH}_4^+$ diverges, which indicates there is another reaction probably the formation of carbamic acid allowing producing NH_4^+ ..

Table IV-3 Concentration of urea, NO_3^- and NH_4^+ during electrolysis (Operating conditions: see Fig.IV-16)

EO time (min)	Urea reacted (mM)	N(Urea reacted) (mM)	NO_3^- produced (mM)	NH_4^+ produced (mM)	$\text{NO}_3^- + \text{NH}_4^+$ (mM)
2	0.014	0.028	0.027	0	0.027
20	0.207	0.413	0.277	0.100	0.376
120	0.589	1.179	0.899	0.147	1.046

Thus, the pathways proposed is shown in Fig.IV-19.

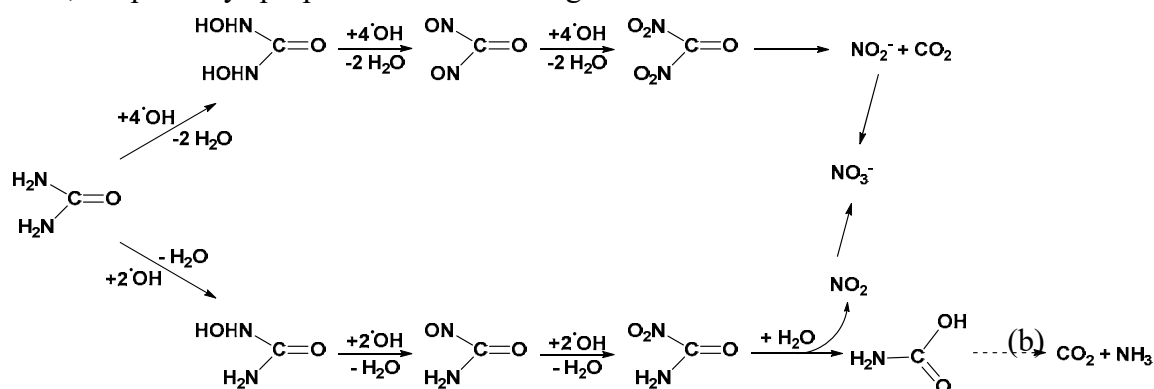


Fig.IV-19 Pathways proposed for urea oxidation, step (b) according to Fig.IV-18

From the pathway of urea electrooxidation, two -NH_2 moieties in urea molecule structure can be attacked by $\bullet\text{OH}$ and transformed into a nitrous group in one step leading a low production of intermediates. In the case of photocatalysis, the oxidation of organic nitrogen follows two step: attack on one -NH_2 moiety and production of nitrous group and carbamic acid which are oxidized to NH_3^+ and CO_2 in a second step[22,24].

IV.A.3.2 Mineralization of Salbutamol and sulfamethoxazole

The electrooxidation of two other pharmaceuticals salbutamol (SALBU) and sulfamethoxazole (SMX) is studied in this section. Electrolyzes were performed in single organic system and the results were compared with ciprofloxacin in the same operating conditions.

The electrochemical behavior of SALBU and SMX were studied by Karuwan et al. [26] and Boudreau et al. [27].

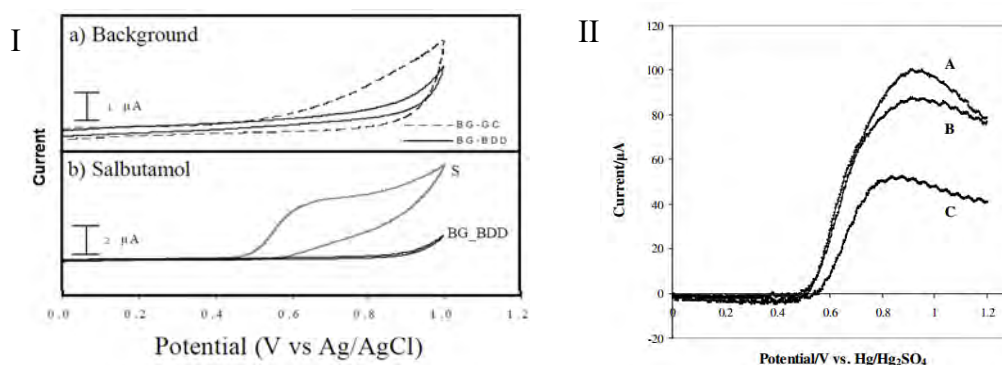


Fig.IV-20 (I) Background (BG) and signal (S) voltammograms obtained from 1 mM SALBU solution at pH 8.3, Working electrode: BDD, Reference electrode: SCE. Scan rate: 100 mv s^{-1} [26]. (II) Linear voltammetry of SMX in 0.05 M Na_2SO_4 Working electrode: Si/BDD (1 cm^2), Reference electrode: NHE. Scan rate: 50 mV s^{-1} . (A) 1 mM; (B) 0.5mM; (C) 0.25 mM [27].

From the cyclic voltammograms of SALBU (Fig.IV-20 (I)), an oxidation peak is observed before water discharge, an irreversible direct electron transfer has occurred. The authors also observed the electrode fouling on the BDD surface. It suggests to be due to the electrochemical oxidation of salbutamol which undergoes electron transfer gives phenolic radical which may combine and form a dimer [26,28,29]. The electrochemical reaction between SALBU and anode and the mechanism of fouling was proposed in Fig.IV-21.

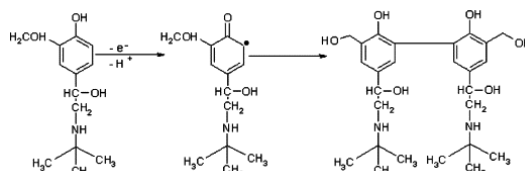


Fig.IV-21 The proposed electrochemical reaction of SALBU by electron transfer [26,28].

Fig.IV-20 (II) presents the cyclic voltammetry of SMX in 0.05 M Na₂SO₄ at different SMX concentrations [27]. The oxidation peak can be seen at +0.85 V and the current increases with the SMX concentration. The oxidation of SMX also has two pathways: direct electron exchange and reaction with hydroxyl radical. The author also observed the deposition of a polymeric film on the anode before the water discharge. Direct oxidation of SMX to the corresponding azo compound had previously been observed at carbon anodes, through a series of direct one electron oxidations [30].

The electrooxidation behavior of salbutamol and sulfamethoxazole during galvanostatic electrolyses of solution containing a single organic has been investigated.

Fig.IV-22 shows the degradation of salbutamol, sulfamethoxazole and ciprofloxacin during 300 min of electrolysis.

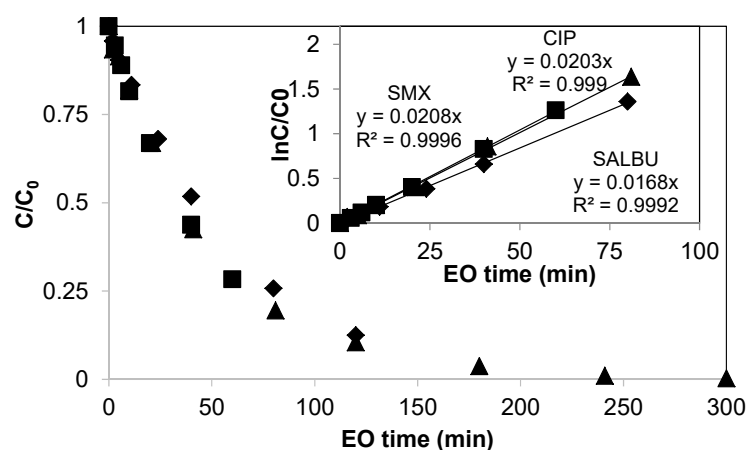


Fig.IV-22 Comparison of the degradation of \blacklozenge salbutamol, \blacksquare sulfamethoxazole, \blacktriangle ciprofloxacin decay with EO time. 1L synthetic solution in K₂SO₄ 0.02 M. [SALBU]₀ = 0.0671mM, [SMX]₀ = 0.0596 mM, [CIP]₀ = 0.0695 mM, I = 0.5A (I > I_{lim}), Flow rate = 366 L h⁻¹, T = 30 °C. Inset panel: the observed degradation rate of SALBU, SMX and CIP.

The removal of the three molecules follows a pseudo first order kinetic. It can be observed that CIP, SMX and SALBU degradation rate is almost the same (0.0203 min^{-1} , 0.0208 and 0.0168 min^{-1} , respectively) with a slightly difference with SALBU. The complete removal of them is observed at around 250 min (2.08 Ah L^{-1}).

Fig.IV-23 plots the normalized concentration of TOC of salbutamol, sulfamethoxazole and ciprofloxacin with EO time. TOC from SALBU decreases as the same rate as TOC from CIP, while TOC from SMX seems to decrease faster. The mineralization degree ($\text{TOC}_{\text{final}} / \text{TOC}_0$) was 80% after 300 min electrolysis. The difference can be due to the fact that SMX contains only 10 carbons in the molecular structure (in comparison with CIP (17)). The amount of intermediates produced during electrooxidation of SALBU and SMX is discussed in Annex IV-5. One can note that the amounts of intermediates depend on the carbon number of the organic molecule.

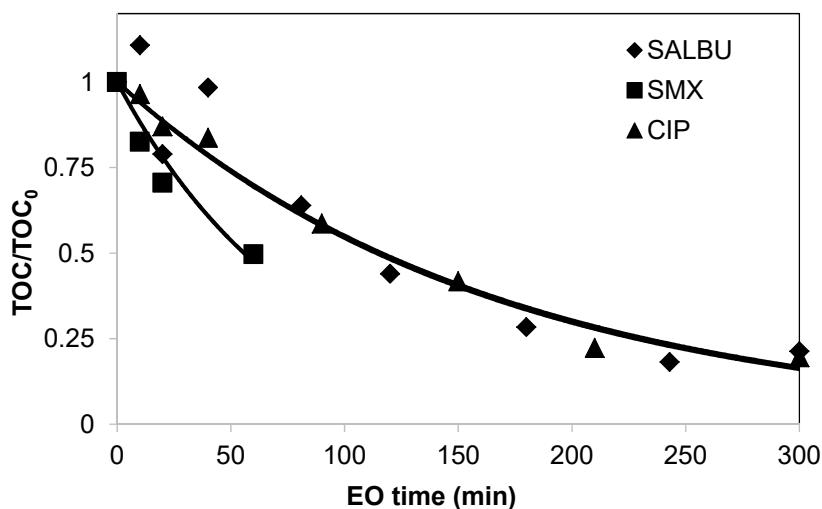


Fig.IV-23 Normalized concentration of TOC, salbutamol, sulfamethoxazole and ciprofloxacin with EO time. Operating conditions see Fig.IV-26. $[\text{TOC}(\text{SALBU})]_0 = 11.4 \text{ mg L}^{-1}$, $[\text{TOC}(\text{SMX})]_0 = 7.5 \text{ mg L}^{-1}$, $[\text{TOC}(\text{CIP})]_0 = 10.1 \text{ mg L}^{-1}$.

IV.A.3.3 Conclusion

Urea as the common waste organic was mineralized using BDD anode. 94% of urea was removed after 180 min electrochemical oxidation. The oxidation of both $-\text{NH}_2$ moieties of urea molecule can be attacked by $\bullet\text{OH}$ and transformed into a nitrous group in one step. Both of salbutamol and sulfamethoxazole can be oxidized through direct electron transfer with BDD anode and reaction with $\bullet\text{OH}$. The degradation of SMX, SALBU and CIP almost follows the same rate. In section IV.4.3, the competition between

these pharmaceuticals will be studied.

IV.A.4 Influence of the matrix on the pharmaceutical removal

The hospital wastewaters contain basic components like salts and common organic compounds such as urea and micropollutants (like pharmaceuticals and hormones) [31]. This part is devoted to the influence of these components on the performance of the electrochemical oxidation of pharmaceuticals. The electrolyses were carried out in synthetic solutions containing: salts and pharmaceutical; ciprofloxacin and urea or two pharmaceuticals.

The objective is to clarify the influence of components on the mineralization of pharmaceuticals in the wastewater and in view to the application of the process in real wastewater.

IV.A.4.1 Influence of salts to electrolysis of pharmaceuticals

The presence of salts in wastewater allows increasing the conductivity and acts as electrolyte. Moreover, some salts are electroactive and can generate mediators which can react with pharmaceuticals, Fig.IV-24 [32].

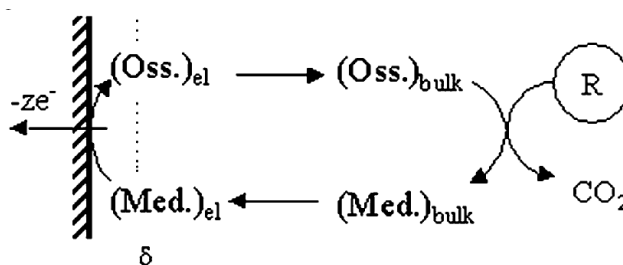


Fig.IV-24 Scheme of the electrochemical process for the removal of organic compounds by indirect oxidation [32]

Thanks to the electrochemical properties of BDD allowing the generation of $\cdot OH$ at the anode surface, strong oxidants such as peroxy and oxo compounds, metal ions, ozone, and chlorine species can be electrogenerated [33–35].

IV.A.4.1.1 Presence of sulfates

To show the role of sulfate species on the removal of pharmaceuticals, the electrochemical oxidations of CIP, SMX, SALBU were performed in K_2SO_4 0.02M (pH = 6.4) and K_2SO_4 0.1M (pH = 3.7 adjusted with H_2SO_4 0.1 M solution). The main form of

sulfate in K_2SO_4 solution is SO_4^{2-} . The concentration of undissociated H_2SO_4 is negligible and the concentration of HSO_4^- can be calculated with the dissociation constant (1×10^{-2}) of Eq.IV.1-8 [36].



The concentrations of HSO_4^- and SO_4^{2-} in both solutions are given in Table IV-4.

Table IV-4 Concentration of SO_4^{2-} , HSO_4^- and the pharmaceuticals in the synthetic solutions at initial time

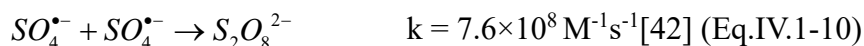
Concentration (mol L ⁻¹)	K_2SO_4 0.1M pH = 3.7	K_2SO_4 0.02M pH = 6.4 (initial)
$[SO_4^{2-}]$	9.8×10^{-2}	2×10^{-2}
$[HSO_4^-]$	1.9×10^{-3}	8×10^{-7}
[SALBU]	6.77×10^{-5}	6.71×10^{-5}
[SMX]	6.23×10^{-5}	6.95×10^{-5}
[CIP]	6.23×10^{-5}	6.95×10^{-5}

Fig.IV-25 presents the degradation of SALBU, SMX and CIP in K_2SO_4 0.1M and 0.02M during electrolysis. Fig.IV-25 (a) shows the same degradation rates are observed in both electrolytes. There is no influence of sulfate on the SALBU removal. Fig.IV-25 (b) shows that the degradation rate of SMX is slightly higher in K_2SO_4 0.1M. Fig.IV-25 (c) shows that CIP degradation is obviously faster in K_2SO_4 0.1 M solution: the total removal of CIP is obtained in 180 min (in comparison with 250 min in K_2SO_4 0.02 M solution, inset panel). The higher concentration of K_2SO_4 leads to faster CIP degradation.

Murugananthan et al. [37] observed that the effective mineralization of ketoprofen can only be achieved when the supporting electrolyte is Na_2SO_4 , comparing to $NaNO_3$, $NaCl$ and explained this phenomenon to the generation of $S_2O_8^{2-}$ and $SO_4^{\bullet-}$ from SO_4^{2-} with a BDD anode. $SO_4^{\bullet-}$ is a strong oxidant for wastewater treatment with high potential ($E_0 = 2.43V$ [38]) [39,40]. Only HSO_4^- and undissociated H_2SO_4 react with $\bullet OH$ radicals to form sulfate radical [41]. In the present experimental conditions, the generation of $SO_4^{\bullet-}$ and $S_2O_8^{2-}$ is shown on Eq.IV.1-9 and Eq.IV.1-10.



Radical $SO_4^{\bullet-}$ may product $S_2O_8^{2-}$ by recombination [42].



However, $S_2O_8^{2-}$ is a weaker oxidant than $\cdot OH$ and $SO_4\cdot^-$ [6]–[8]. Thus, the impact of sulfate to pharmaceutical oxidation is mainly due to the radical $SO_4\cdot^-$ formation.

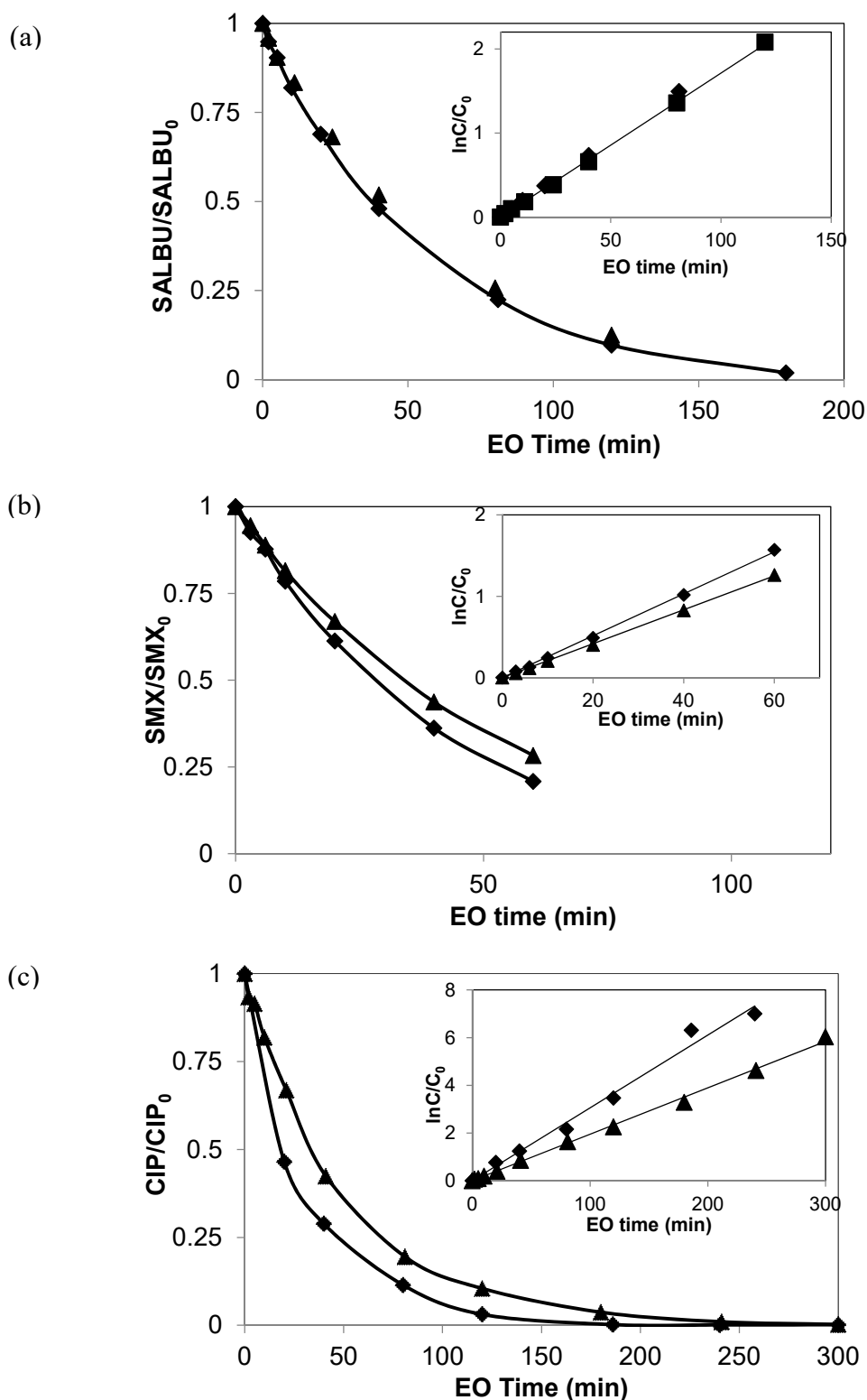


Fig.IV-25 The normalized concentration of pharmaceuticals during electrolyses: (a) SALBU, $I = 0.5A$ (b) SMX, $I = 0.5A$ (c) CIP, $I = 0.1A$ in \blacklozenge K_2SO_4 0.1M, $pH = 3.7$, \blacktriangle K_2SO_4 0.02M, $pH = 6.4$, flow rate = $366 L h^{-1}$, $T = 30 ^\circ C$. Inset: the observed degradation rate of pharmaceuticals.

Table IV-4 shows that in case of K_2SO_4 0.1M, $\text{pH} = 3.7$, the concentration of HSO_4^- is 2000 times higher than in K_2SO_4 0.02 M, $\text{pH} = 6.4$. Thus, the $\text{SO}_4^{\cdot -}$ was produced in K_2SO_4 0.1M solution, while in K_2SO_4 0.02M solution, the production of the $\text{SO}_4^{\cdot -}$ was negligible.

The different behaviors of the degradation SALBU, SMX and CIP in Fig.IV-25 highlights the selectivity of $\text{SO}_4^{\cdot -}$. It was reported that sulfate radical is more selective than $\cdot\text{OH}$ due the different radical reaction mechanisms [40,43,44]. Herein, SALBU degraded with the same rate in both in K_2SO_4 0.1M and K_2SO_4 0.02M solutions, indicating that SALBU is inert to react with $\text{SO}_4^{\cdot -}$. For SMX and CIP, the reaction between $\text{SO}_4^{\cdot -}$ and them occurs and the rate constants equals 1.61×10^{10} [45] and $1.2 \times 10^9 \text{ M}^{-1} \text{ s}^{-1}$ [46], respectively. Thus, the additional reaction between SMX, CIP and $\text{SO}_4^{\cdot -}$ (in the K_2SO_4 0.1 M) leads to a faster degradation of them.

Moreover, the removal of TOC and COD depends on the electrolyte. Fig.IV-26 (a) shows the TOC decrease which is faster after 80 min in K_2SO_4 0.1M. 84 % of TOC removal is reached after 300 min of electrolysis and only 71 % in K_2SO_4 0.02 M solution. The presence of $\text{SO}_4^{\cdot -}$ plays a role after 80 min which corresponds to 81% of CIP removal. These results indicates that $\text{SO}_4^{\cdot -}$ reacts with some intermediates which are produced during electrochemical oxidation of CIP. The similar behavior is observed for the removal of COD Fig.IV-26 (b).

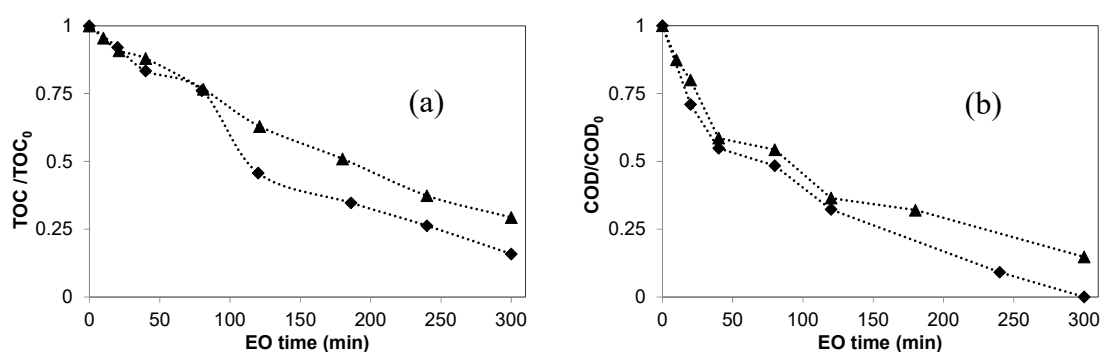


Fig.IV-26 The normalized variation of TOC (a) and COD (b) during electrolysis of 1L of CIP solution. ◆ K_2SO_4 0.1M, $\text{pH} = 3.7$, $[\text{TOC}]_0 = 10.40 \text{ mg L}^{-1}$ ▲ K_2SO_4 0.02M, $\text{pH} = 6.4$, $[\text{TOC}]_0 = 11.17 \text{ mg L}^{-1}$ $I = 0.1\text{A}$, flow rate = 366 L h^{-1} , $T = 30 \text{ }^\circ\text{C}$.

IV.A.4.1.2 Presence of chlorides

Chloride ion is a common salt in wastewater. Numerous studies highlight that the presence of chloride allows accelerating the removal of organic by means of the chemical

reaction via electrogenerated active chlorine which is able to degrade organic pollutants [47–49]. However, the undesired organochloride compounds can be formed. The objective of this section is to study the influence of the presence of chloride ions on the removal of pharmaceuticals.

Considering the production of hydroxyl radicals by water discharge on BDD, the reactions involving hydroxyl radical should be taken account besides the direct electron transfer reactions. Numerous reactions involving chlorine occur via electron transfer and chemical reaction with hydroxyl radical [50–56]. Fig.IV-27 exhibits the possible pathway during electrooxidation of Cl^- .

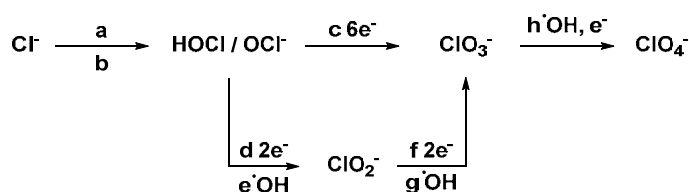


Fig.IV-27 Oxidation Pathways of Cl^-

In table IV-5, the corresponding reactions are listed. One can remark that the perchlorate can be formed during an ultimate step, which is undesired due to that perchlorate due to health risks[4,57].

Table IV-5 Reactions of chlorine species corresponding to Fig.IV-26 during electrolysis

Reaction		Ref.
a $2\text{Cl}^- \rightarrow \text{Cl}_2 + 2e^-$	$E^0 = 1.36\text{V}$	[50],
$\text{Cl}_2 + \text{H}_2\text{O} \rightarrow \text{HOCl} + \text{Cl}^- + \text{H}_2\text{O}$		[58]
b $\text{Cl}^- + \cdot\text{OH} \longleftrightarrow \text{ClOH}^{\cdot-}$	$k_{\text{For}} = 4.3 \times 10^9 \text{ M}^{-1} \text{ s}^{-1}$	[59]
c $6\text{HOCl} + 3\text{H}_2\text{O} \rightarrow 2\text{ClO}_3^- + 4\text{Cl}^- + 12\text{H}^+ + 3/2\text{O}_2 + 6e^-$		[50]
$6\text{OCl}^- + 3\text{H}_2\text{O} \rightarrow 2\text{ClO}_3^- + 4\text{Cl}^- + 6\text{H}^+ + 3/2\text{O}_2 + 6e^-$	$E^0 = 0.46\text{V}$	
d $\text{OCl}^- + 2\text{OH}^- \rightarrow \text{ClO}_2^- + \text{H}_2\text{O} + 2e^-$	(alkaline solution)	[52]
e $\cdot\text{OH} + \text{OCl}^- \rightarrow \cdot\text{ClO} + \text{OH}^-$	$k = 9 \times 10^9 \text{ M}^{-1} \text{ s}^{-1}$	[51]
$\cdot\text{OH} + \cdot\text{ClO} \rightarrow \text{ClO}_2^- + \text{H}^+$	$k > 1 \times 10^9 \text{ M}^{-1} \text{ s}^{-1}$	
f $\text{ClO}_2^- + 2\text{OH}^- \rightarrow \text{ClO}_3^- + \text{H}_2\text{O} + 2e^-$	(alkaline solution)	[52]
g $\cdot\text{OH} + \text{ClO}_2^- \rightarrow \cdot\text{ClO}_2 + \text{OH}^-$	$k = 6 \times 10^9 \text{ M}^{-1} \text{ s}^{-1}$	[51]
$\cdot\text{OH} + \cdot\text{ClO}_2 \rightarrow \text{ClO}_3^- + \text{H}^+$	$k = 4 \times 10^9 \text{ M}^{-1} \text{ s}^{-1}$	
h $\text{ClO}_3^- \rightarrow \cdot\text{ClO}_3 + e^-$		[56]
$\cdot\text{ClO}_3 + \cdot\text{OH} \rightarrow \text{HClO}_4$		

IV.A.4.1.2.1 Electrochemical oxidation of CIP solution in presence and absence of chloride

Electrolyses were carried out with CIP solutions with and without chloride ions in the regime of mass transfer control. The range of Cl^- concentration was chosen according to the concentration range in NF retentate (chapter V).

Fig.IV-28 shows the decay of COD in the presence and absence of Cl^- . The decay of COD follows the theoretical value (Eq. I-24) in both cases. The decay rate of COD does not change significantly in the presence of Cl^- .

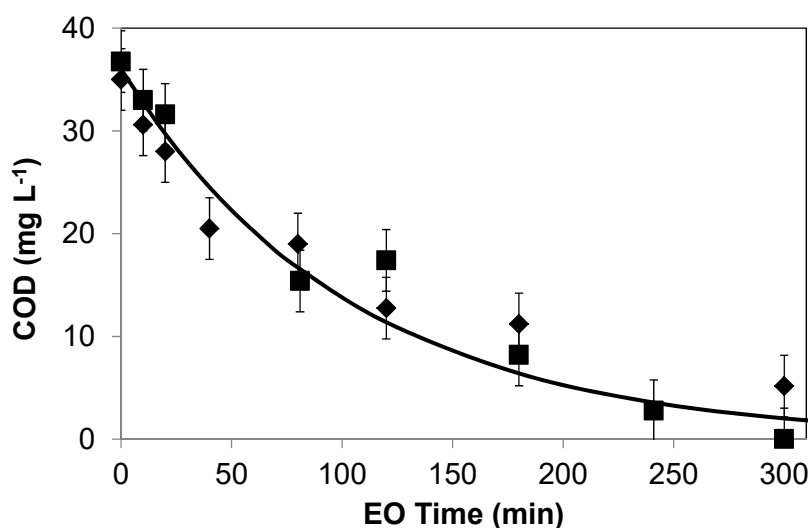


Fig.IV-28 COD decay in ◆ K_2SO_4 0.02M, ■ K_2SO_4 0.02M+2.25mM KCl during electrolysis of 1L CIP solution, $I = 0.1\text{A}$, (1.45 mA cm^{-2}). —: theoretical COD value. $[\text{COD}]_0 = 35 \text{ mg L}^{-1}$, flow rate = 366 L h^{-1} , $T = 30 \text{ }^\circ\text{C}$.

Figure IV-29 (a) shows the degradation of CIP in presence or absence of chlorides at 0.1A. The remarkable acceleration for CIP degradation is observed in presence of Cl^- : the complete removal of CIP is reached at 80 min in presence of Cl^- while 240 min in absence of Cl^- . Moreover, it can be observed in Fig.IV-29 (b) that the removal of TOC is faster in presence of Cl^- : after 300 min of electrolysis 90 % of TOC is removed, while in the absence of Cl^- , the removal is only 70 %. The faster degradation in presence of Cl^- can be attributed to the additional oxidation reaction with the electrogenerated active chlorine (eq. a, e in Table IV-5) which can react with CIP and intermediates. Malpass et al. [49] reported that the removal of atrazine with NaCl as supporting electrolyte is quite faster than with Na_2SO_4 and NaNO_3 using DSA electrodes. The same trend was obtained in the

work of degradation of 17 β - estradiol on BDD anode [60].

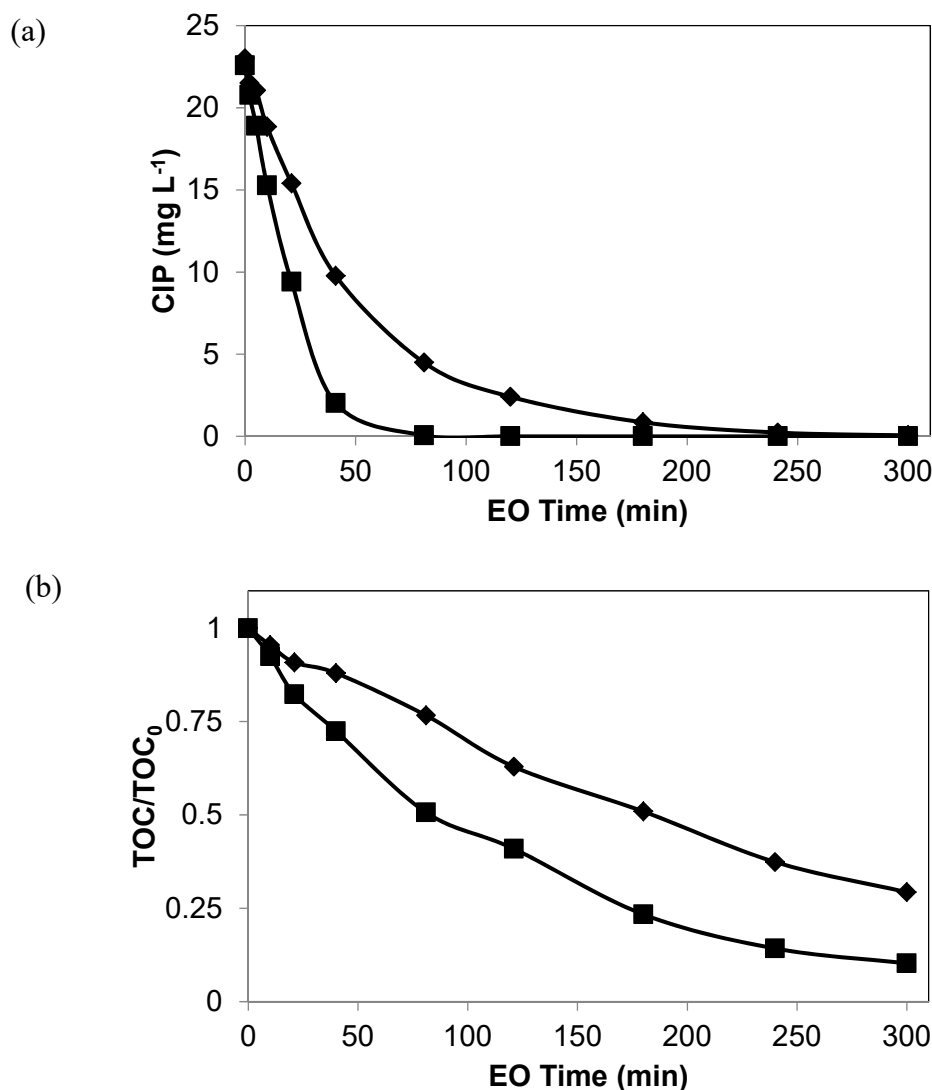
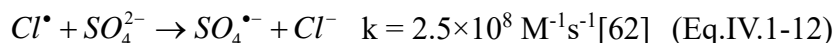


Fig.IV-29 Variation of CIP (a) and TOC (b) in ◆ K₂SO₄ 0.02M, ■ K₂SO₄ 0.02M + 2.25mM KCl, during electrolysis of 1L CIP solution, [CIP]₀ = 22.30 mg L⁻¹ (0.068 mM), [TOC₀] = 11.17 mg L⁻¹, I = 0.1A (1.45 mA cm⁻²), flow rate = 366 L h⁻¹, T = 30 °C

Moreover, it is possible to generate sulfate radicals (oxidants) via the electrogenerated chloride radical (Cl•). Ferro et al. [58] discussed on a mechanism pathway for the formation of Cl₂ from 2Cl• and Brito et al. also suggested a direct oxidation of chloride with BDD anode (probably Cl⁻ → Cl•) [61] as Eq.IV.1-11. On the anode surface, the reaction between Cl• and SO₄²⁻ which can form SO₄•⁻ are reported by Das et al. [62] as the Eq.IV.1-12.



Then the $\text{SO}_4^{\bullet-}$ generated in the presence of chloride and sulfate accelerates the degradation of CIP and some byproducts.

Fig.IV-30 shows the CIP degradation with the electrical charge in presence of chloride at 0.1A and 3A. It can be observed that at low current intensity (0.1A), the chloride concentration decrease when 90 % of CIP is removed.

Conversely, at higher current intensity (3A), chloride is oxidized from the beginning of the electrolysis. In addition, at 0.1 A, the complete removal of CIP occurs with a charge consumption of 0.13 Ah L^{-1} when 1.6 % of Cl^- is oxidized. At 3A, 100 % of CIP removal is reached for 0.25 Ah L^{-1} and 14 % Cl^- is oxidized. At high current intensity, more electrical charge is spent for oxidation of Cl^- during CIP removal.

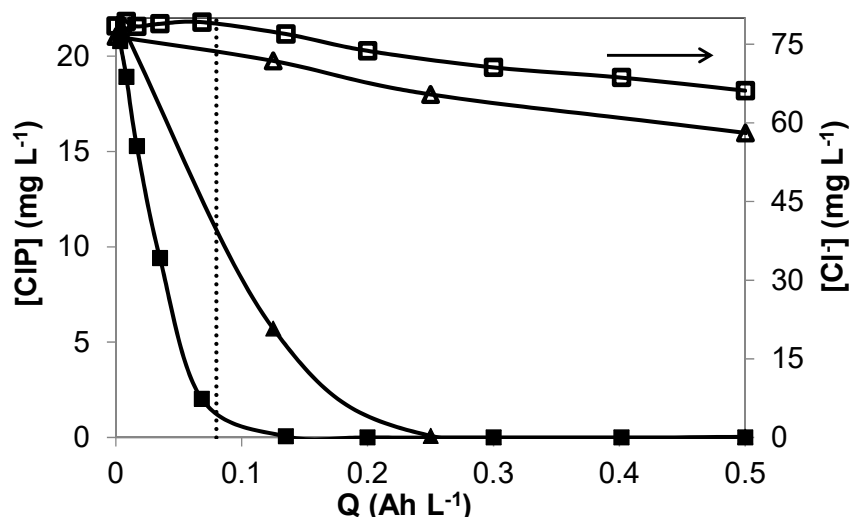


Fig.IV-30 CIP decay with electrical charge in K_2SO_4 0.02M + 2.25 mM KCl ■ I = 0.1A (1.45 mA cm^{-2}), ▲ I = 3 A (43.47 mA cm^{-2}) during electrolysis of 1L CIP solution, $[\text{CIP}]_0 = 22.3 \text{ mg L}^{-1}$, flow rate = 366 L h^{-1} , T = 30 °C. full symbols: ■ and ▲ represent [CIP]; empty symbols: □ and ▲ represent $[\text{Cl}^-]$.

The TOC measurement shows that only 41 % has been removed at 3A after 300 min whereas 90% reached at 0.1 A for the same duration (Annex IV-6). The incomplete TOC removal in the presence of chloride were also reported by Muruganathan et al. in the case of mineralization of bisphenol A, atenolol and ketoprofen with BDD anode [37,63,64]. In these studies the poor mineralization efficiency was observed in the presence of Cl^- , which may be attributed to the possible formation of chlorinated compounds in higher current intensity (3A).

In conclusion, the use of a very high current intensity ($\frac{I}{I_{lim}^o} > 30$) generates oxidation of Cl^- . The incomplete mineralization and formation of undesired organochlorine compounds may occur in these conditions. The next part is devoted to analyse the electrogenerated chlorine species.

IV.A.4.1.2.3 Chlorine species conversion and AOX

To understand the role of Cl^- and intermediate compounds, analysis of the species and ions during electrolysis were performed.

Figure IV-31 shows the chlorine species conversion during electrolysis of CIP (2.25mM) in presence of Cl^- at 0.1A and 3A.

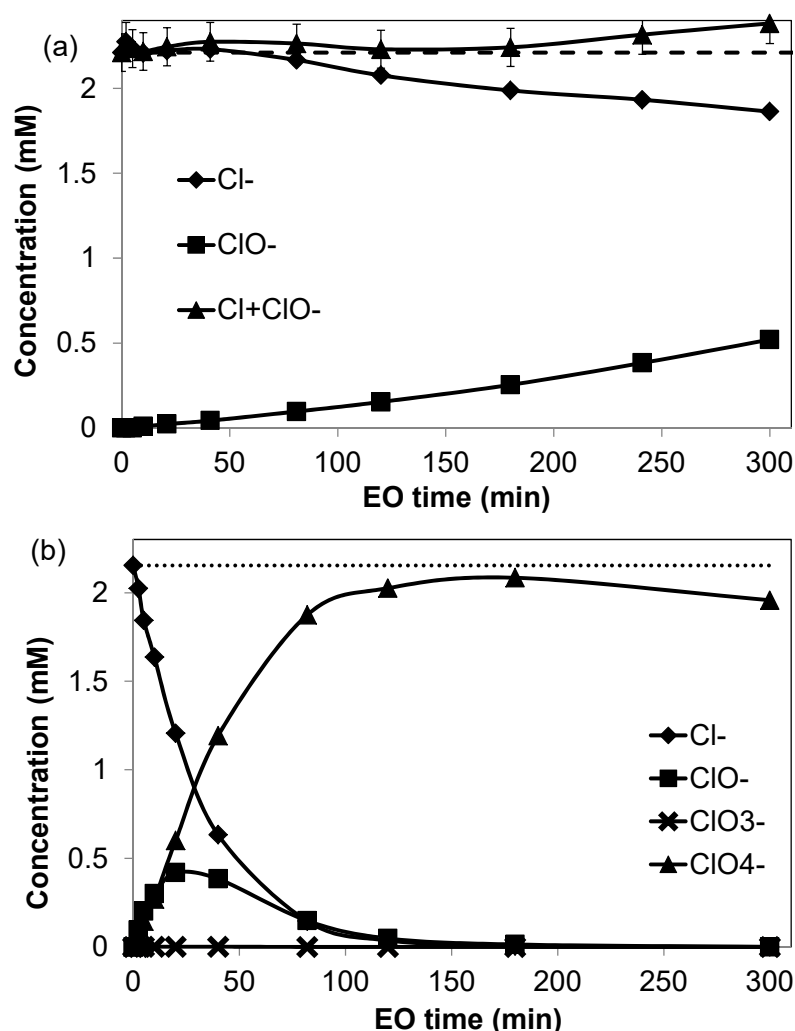
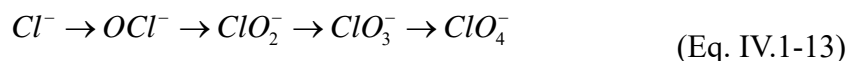


Fig.IV-31 Chlorine transformation in K_2SO_4 0.02M + 2.25mM KCl (a) $I = 0.1\text{A}$ (1.45 mA cm^{-2}), (b) $I = 3\text{A}$ (43.48 mA cm^{-2}) during electrolysis of 1L CIP solution, flow rate = 366 L h^{-1} , $T = 30 \text{ }^\circ\text{C}$. The dashed line is the total concentration of chlorine in the solution.

The formation of hypochlorite species (HClO and ClO⁻) occurs during electrolysis in both case at 0.1A and 3A. When the current intensity is 0.1A, Cl⁻ is oxidized in hypochlorite (the sum of the concentration of Cl⁻ and ClO⁻ equals the initial concentration of Cl⁻). In the case of higher current intensity (3A), ClO⁻ and ClO₄⁻ are formed from the beginning of electrolysis. The concentration of ClO⁻ reaches a maximum value of 0.42 mM at 20 min, then decreases to 0.05mM at 120 min and disappears at the end of electrolysis. The concentration of ClO₃⁻ presented during the electrolysis at 3A is lower than the detection limit of ionic chromatography (< 1ppm). After 300 min of electrolysis, 90% of chloride is converted into perchlorate which is the only ionic chlorine species in the solution at 3A.

From Fig.IV-27, it can be noted that electrogenerated oxygen species play an important role for the generation of ClO₄⁻ [53,54,65].



In the case of a high applied current intensity, large amounts of electrogenerated oxygen species (mainly •OH) are produced, which allows the reaction of the intermediate species with oxygen species and forming ClO₄⁻. Jung et al also found the electrogeneration rate of ClO₄⁻ depended on the concentration of oxygen species (•OH, H₂O₂, O₃). A faster generation rate of ClO₄⁻ was observed at higher concentration of oxygen species [53]. The non-observation of intermediates species ClO₂⁻ and ClO₃⁻ are owing to their short-live and instability in this operating condition, even the oxidation of ClO₃⁻ to ClO₄⁻ is slow and the rate-determining step [4,56]. Brito et al. has also observed that ClO₄⁻ formed with higher current intensity and ClO₂⁻ and ClO₃⁻ were present before the formation of ClO₄⁻[61].

Fig.IV-32 shows the formation of hypochlorite as a function of electrical charge during electrolysis at 0.1 and 3A. At the beginning, the ClO⁻ concentration varies with the electrical charge with the same rate in both cases (3A and 0.1A). After 0.25 Ah L⁻¹, the concentration of ClO⁻ continues to increase at 0.1 A, while it begins to decrease until zero at 3 A. The production of ClO⁻ at beginning does not depend on the current intensity. The disappearance of ClO⁻ for high current (3A) can be explained by its oxidation by oxygen transfer.

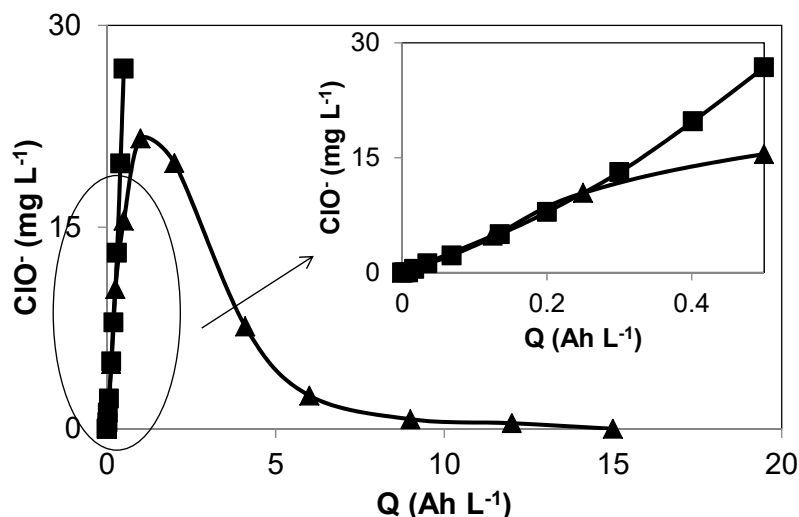
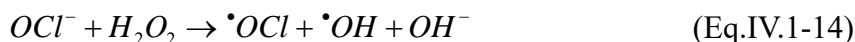


Fig.IV-32 Formation of hypochlorite versus the electrical charge in K_2SO_4 0.02M + 2.25mM KCl ■ $I = 0.1A$ (1.45 mA cm^{-2}), ▲ $I = 3A$ (43.48 mA cm^{-2}) during electrolysis of CIP solution (1L), flow rate = 366 L h^{-1} , $T = 30 \text{ }^\circ\text{C}$.

These reactions occur mainly on the electrode surface but also in the bulk. Castagna et al. [66] reported the reaction between ClO^- and H_2O_2 as Eq.IV.1-14



The risk to form organochloride product which are toxic for environment and human health seems to exist in particular at high current intensity. Adsorbable Organic Halogen (AOX, II.4.7) were analyzed in the samples after electrolysis. Results are summarized in Table IV-6

Table IV-6 Concentration of AOX at initial time and after 300 min of electrolysis of 1L of K_2SO_4 0.02M + 2.25mM KCl containing CIP at 0.1 and 3A, flow rate = 366 L h^{-1} , $T = 30 \text{ }^\circ\text{C}$.

Current intensity (A)	EO time (min)	Q (Ah L ⁻¹)	Initial Cl ⁻ concentration (mg L ⁻¹)	AOX (μM Cl)	TOC (mg L ⁻¹)
0	0	0	77.0	< LD	11.2
3	300	15	76.5	130	6.8
0.1	300	0.5	78.5	10	1.1

Table IV-6 highlights that at 3 A, the amount of AOX at the end of electrolysis is 13 times higher than at 0.1 A. The significant formation of AOX at 3A explains the low removal of TOC (39%) at the end of electrolysis. The formation of AOX is due to

reactions between organic compounds and electrogenerated active chlorine species (e.g., Cl_2 , OCl , HOCl) and chlorine radicals ($\text{Cl} \cdot$, $\text{ClO}_x \cdot$). At higher current intensity (3A) the amount of these electrogenerated compounds is very important. Consequently, increase the risk of the AOX formation.

In the case of the study on the treatment by other electrodes, Chaplin reported that BDD surface has surface radical sites (for example $\text{C-O} \cdot$ and $\text{C} \cdot$ radical sites), which can act as stabilized adsorption sites for $\text{ClO}_x \cdot$ radicals on BDD surface [4]. Bagastyo et al. [67] found that the production of haloacetic acids (HAAs) and halomethanes (THMs) are more important using BDD electrode than Ti/Pt-IrO₂ and Ti/SnO₂-Sb: for BDD, the formation of HAAs and THMs reached 62.4 and 9.1 μM , respectively at the end of the experiment ($Q = 5.6 \text{ Ah L}^{-1}$). In the case of Ti/SnO₂-Sb, 34.2 μM of HAAs and 8.9 μM , of THMs were formed after 5.6 Ah L^{-1} , while 27.4 μM of HAAs and 5.6 μM of THMs were measured for the Ti/Pt-IrO₂ anode.

In this study, the TOC value (Annex IV-6) which probably corresponds to the AOX keeps stable between 120 min (6 Ah L^{-1}) and 300 min (5 Ah L^{-1}). The decrease of TOC is not observed even for an enhancement of 15 Ah L^{-1} (300min). The AOX persist during electrooxidation, although Chaplin [4] suggest that halogenated organic compounds can be totally oxidized after elimination of halogen ions or compounds.

Thus, the choice of appropriate current intensity is important to limit the formation of refractory and toxicity AOX for application of electrochemical oxidation with BDD to treat the wastewater in presence of chlorine.

IV.A.4.1.3 Conclusion

The salts in the wastewater can acts as inorganic oxidants. The species and amount of these inorganic oxidants can be important. On one hand, such oxidants allow increasing the removal of organics (case of sulfate). On the other hand, the presence of chlorides can be the source of halogenated compounds in particular at high current density. This study highlighted that the choice of operating conditions determines the efficiency and viability of the process.

IV.A.4.2 Removal of pharmaceuticals in presence of urea

This section investigates the interaction and competition of pharmaceuticals during the electrolysis of a solution containing pharmaceuticals and a common organic. Urea was chosen as model of common organic. Electrolyzes were carried out in synthetic

solution containing CIP and urea with different concentrations under galvanostatic conditions. The applied current intensities were higher than the limiting current.

Fig.IV-33 shows the variation of urea and CIP concentrations with EO time in the case of mono component solutions (CIP or urea) and bi-component solutions (CIP and urea). The analysis of these data allows estimating the constant rate k_{obs} for each case, these values are reported in the Fig.IV-34. It can be observed that the degradation of CIP follows the same rate in a single solution and in the presence of urea when the ratio $[CIP]_0:[urea]_0 = 1:2$. Surprisingly, CIP degrades faster in presence of higher urea concentration. One can note that during the first 10 min the degradation of CIP follows the same rate, after that the rate is faster in the case of higher concentration of urea ($[CIP]_0:[urea]_0 = 1:11$). It can be assumed that by-products generated from the urea oxidation can react with CIP. Considering the degradation of urea, it appears the same rate in all solutions and the concentration is stabilized after 120 min.

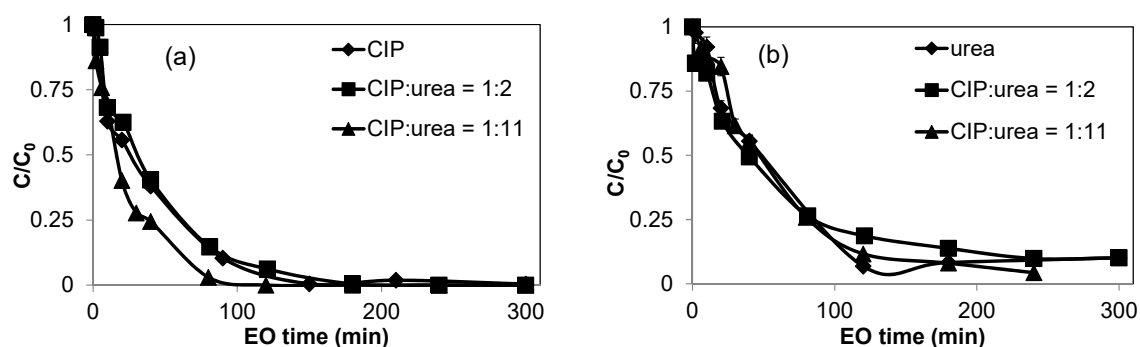


Fig.IV-33 CIP (a) and urea (b) concentration versus time during electrolyses: \blacklozenge CIP solution (a) $[CIP]_0 = 0.061\text{mM}$, urea solution (b) $[urea]_0 = 0.63\text{ mM}$; \blacksquare CIP and urea solution $[CIP]_0:[urea]_0 = 1:2$, $[CIP]_0 = 0.042\text{ mM}$, $[urea]_0 = 0.09\text{ mM}$; \blacktriangle CIP and urea solution $[CIP]_0:[urea]_0 = 1:11$, $[CIP]_0 = 0.053\text{ mM}$, $[urea]_0 = 0.61\text{ mM}$. $I = 0.5\text{A}$ ($I > I_{lim}^0$), flow rate = 366 L h^{-1} , electrolyte: $\text{K}_2\text{SO}_4\ 0.1\text{ M}$, $T = 30\text{ }^\circ\text{C}$.

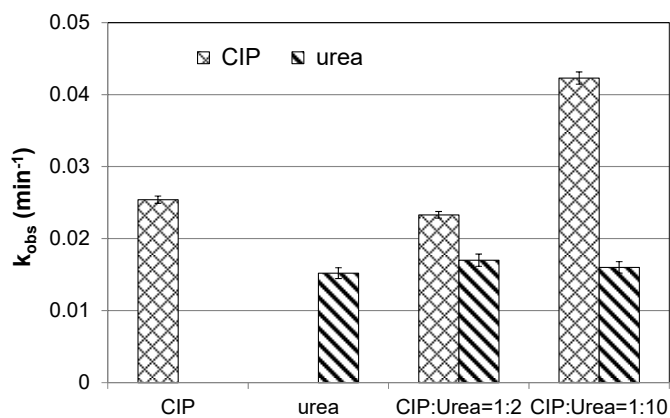


Fig.IV-34 The observed degradation constant rates, k_{obs} , of CIP and urea (obtained in 80 min) in 4 electrolyses: CIP solution and urea solution, CIP and urea solution $[CIP]_0:[urea]_0 = 1:2$; CIP and urea solution $[CIP]_0:[urea]_0 = 1:11$. Operating condition see Fig.IV-45.

Fig.IV-35 presents the TOC decay with time at different ratio of concentration: $[CIP]_0:[urea]_0 = 1:2$ and $[CIP]_0:[urea]_0 = 1:11$. Whatever the initial TOC value, the TOC value reaches 4 mg L^{-1} after 120 min. Then 95% of TOC is mineralized after 300 min, while in the case of $[CIP]_0:[urea]_0 = 1:2$, less removal of TOC is obtain as 90%. The TOC decay confirms the role of some productions from the oxidation of urea in CIP degradation. This value is stabilized because of the depletion of organic matter and then the limitation of mass transfer.

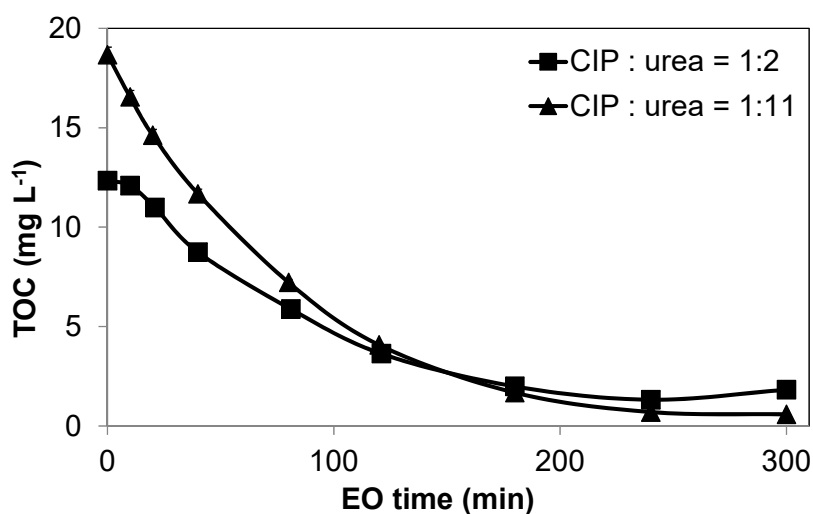


Fig.IV-35 The variation of TOC during 300 min electrolyzes of CIP and urea solutions in K_2SO_4 0.1M, pH = 3.7, I = 0.5A, flow rate = 366 L h^{-1} , T = $30 \text{ }^\circ\text{C}$.

The oxidation pathway of urea was discussed in section IV.1.3.1.2. The final products are NO_3^- and NH_4^+ . The presence of them does not impact on the degradation of pharmaceuticals (Annex IV-8, degradation of CIP in K_2SO_4 0.1M + 2.5mM NH_4^+ and degradation of SMX in K_2SO_4 0.1M + 2.5mM NO_3^-).

For a better understanding of the mechanism of interaction CIP/Urea, the concentration of nitrogen compounds has been followed. Fig.IV-36 presents nitrogen conversion during 300min of electrolysis of CIP and urea solution when the ratio of CIP and urea is $[CIP]_0:[urea]_0 = 1:2$ and 1:11. For both ratio, all the nitrogen are converted into NH_4^+ and NO_3^- at the end of electrolysis.

(a) For $[CIP]_0:[urea]_0 = 1:2$, the final ratio of $[NH_4^+]/[NO_3^-]$ is around 1:1. Considering the molecular structure, the nitrogen from CIP and urea is almost the same amount ($N(CIP):N(Urea) = 3:4 \approx 1:1$). As discussed on section IV.1.1.2 and IV.1.3.1.2, the nitrogen of urea is probably mainly converted into NO_3^- and the one of CIP into NH_4^+ . It

explains why the observed $[\text{NH}_4^+]/[\text{NO}_3^-]$ is around 1:1.

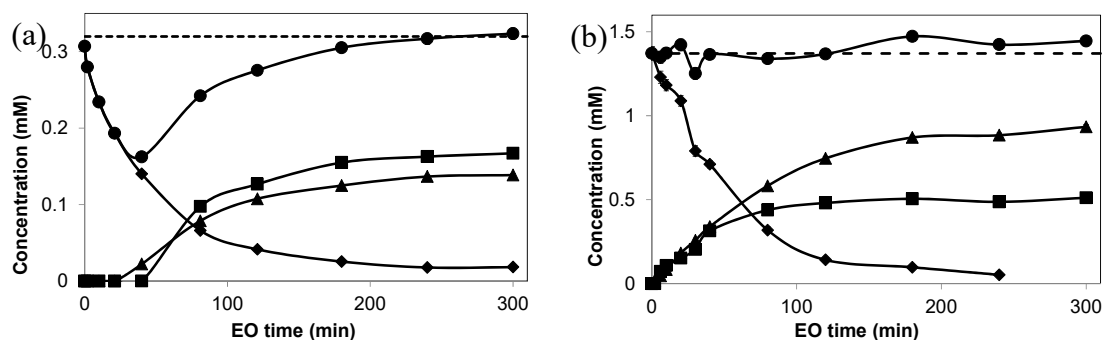


Fig.IV-36 Conversion of nitrogen during 300 min of electrolyses of 1L synthetic solutions containing CIP and urea with different ratio and K_2SO_4 0.1 M at $\text{pH} = 3.7$. $I = 0.5\text{A}$, flow rate = 366 Lh^{-1} , $T = 30 \text{ }^\circ\text{C}$. ◆ : concentration of N from CIP and urea, ■ : concentration of NO_3^- , ▲ : concentration of NH_4^+ ● : the sum of concentration of N from CIP, urea, NO_3^- and NH_4^+ .

(a) $[\text{CIP}]_0:[\text{urea}]_0 = 1:2$, $[\text{CIP}]_0 = 0.045 \text{ mM}$, $[\text{urea}]_0 = 0.094 \text{ mM}$;

(b) $[\text{CIP}]_0:[\text{urea}]_0 = 1:11$, $[\text{CIP}]_0 = 0.053 \text{ mM}$, $[\text{urea}]_0 = 0.606 \text{ mM}$.

(b) In the case of $[\text{CIP}]_0:[\text{urea}]_0 = 1:11$, considering the initial ratio of $\text{N}(\text{CIP}):\text{N}(\text{Urea}) = 3:22$ and 90% of nitrogen comes from urea. The NH_4^+ and NO_3^- produced from CIP are negligible in this case. The final ratio of $[\text{NH}_4^+]/[\text{NO}_3^-]$ is around 1:2. This value is different as the one obtained in the case of electrolysis of urea solution ($[\text{NH}_4^+]/[\text{NO}_3^-] = 1:7$). According to the oxidation pathway of urea (section IV.1.3.1.2), NH_4^+ is released from the carbamic acid (key intermediates from urea oxidation), which indicates that in the case of $[\text{CIP}]_0:[\text{urea}]_0 = 1:11$ more carbamic acid is produced. Nevertheless, to prove the influence of carbamic acid on the oxidation rate of CIP, further studies are needed.

Although the completely removal of urea is not efficient by electrochemical oxidation, the urea is nontoxic and has shown grade biodegradability [20]. The target of electrochemical oxidation here is to mineralize the bio-refractory pharmaceuticals and it seems the presence of urea in higher concentration ($[\text{CIP}]_0:[\text{urea}]_0 = 1:2$ or $[\text{CIP}]_0:[\text{urea}]_0 = 1:11$) does not prevent the degradation of CIP but render it faster. These results promote the feasibility and efficiency of electrooxidation of pharmaceuticals in wastewater on BDD.

IV.A.4.3 Competition and interaction between pharmaceuticals during electrochemical oxidation

This section investigates the competition and interaction of pharmaceuticals during the electrochemical oxidation process. Two interactions will be treated here: (i) ciprofloxacin (CIP) and sulfamethoxazole (SMX); (ii) CIP and salbutamol (SALBU). In each case, the applied current intensity is higher than the limiting current intensity under galvanostatic.

(i) Competition and interaction between CIP and SMX

The electrolysis was performed with the solution containing CIP and SMX. After 300 min (2.5 Ah L^{-1}) of electrolysis, an excellent removal of TOC (92%) is obtained (Annex-9). Fig.IV-37 shows the variation of CIP and SMX concentrations during electrolysis. The degradation of CIP and SMX follows a pseudo first order kinetic. It can be observed that both pharmaceuticals almost are degraded at quite the same rate; there is a slight difference at the beginning of electrolysis, probably due to the competition of them in the reaction with $\cdot\text{OH}$. The rate constants between CIP and $\cdot\text{OH}$, 2.15×10^{10} [68], is higher than the rate constant of SMX with $\cdot\text{OH}$, 7.02×10^9 [45]. This difference favors faster degradation rate of CIP.

A very good agreement between experimental and theoretical COD (Eq. IV-24) value is presented in the inset panel.

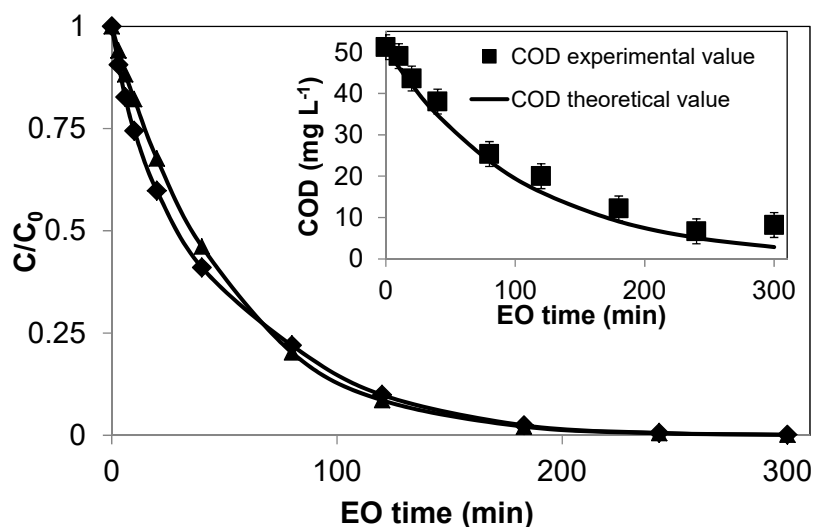


Fig.IV-37 CIP \blacklozenge and SMX \blacktriangle variation with EO time during 300 min electrolysis of 1L solution in K_2SO_4 0.02 M at pH = 3. $[\text{CIP}]_0 = 0.072 \text{ mM}$, $[\text{SMX}]_0 = 0.0572 \text{ mM}$. $I = 0.5 \text{ A}$ ($i = 7.25 \text{ mA cm}^{-2}$, $i > i_{\text{lim}}^{\circ}$), flow rate = 366 L h^{-1} , $T = 30 \text{ }^{\circ}\text{C}$. Inset panel: theoretical and experimental decay of COD.

(ii) Competition and interaction between CIP and SALBU

Fig.IV-38 presents the degradation of CIP and SALBU during electrolysis of solution containing both pharmaceuticals.

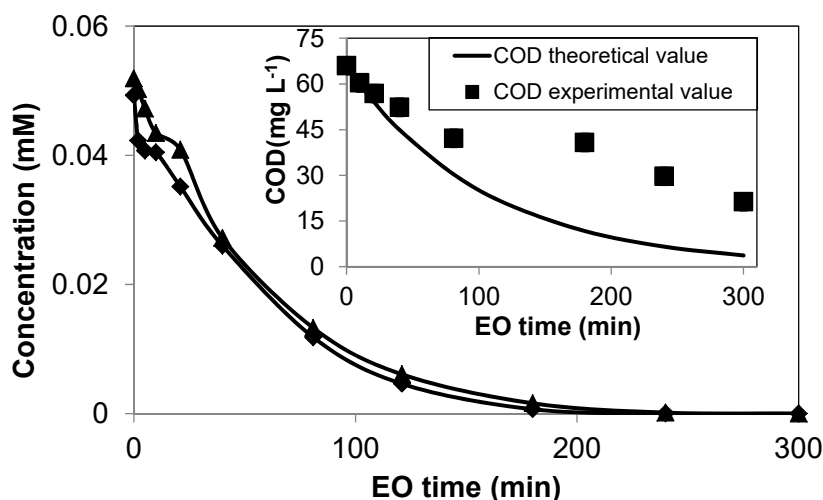


Fig.IV-38 CIP \blacklozenge and SALBU \blacktriangle removal with EO time during 300 min electrolysis of 1L solution in K_2SO_4 0.1 M at pH = 3. $[CIP]_0 = 0.052$ mM, $[SALBU]_0 = 0.049$ mM. $I = 0.5A$ ($I > I_{lim}^0$), flow rate = 366 L h^{-1} , $T = 30$ °C. Inset panel: theoretical and experimental decay of COD.

It can be observed that during the first 50 min, CIP seems to decrease slightly faster than SALBU and then both degrade at the same rate. Complete removal is obtained in around 200 min for both. In addition, 90% of TOC are mineralized after 300 min (2.5 Ah L^{-1}) (Annex IV-9). The inset panel shows the corresponding COD decay during 300 min of electrolysis. After 100 min, the experimental COD becomes slower than the theoretical ones.

Fig.IV-39 plots the removal of CIP and SALBU with EO time in the case of mono component solutions (CIP or SALBU) and bi-component solutions ($[CIP]_0 : [SALBU]_0 = 1:1$).

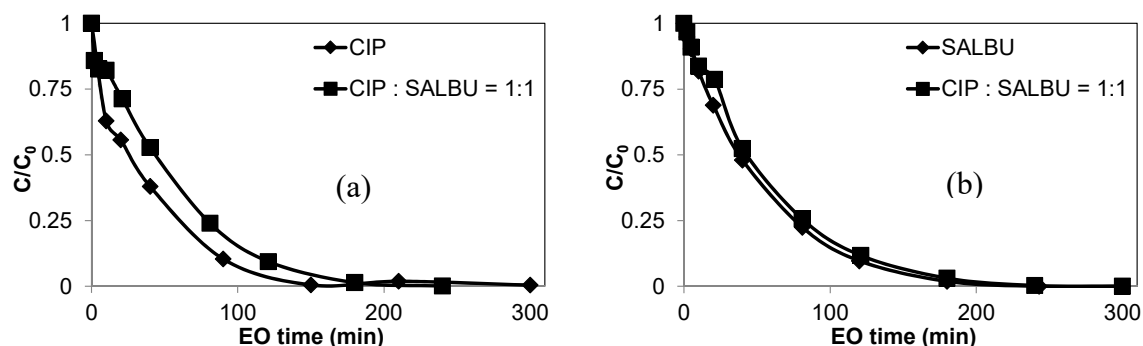


Fig.IV-39 Degradation of CIP (a) and SALBU (b) with time during 3 electrolyzes: \blacklozenge CIP solution (a) $[CIP]_0 = 0.061$ mM, SALBU solution (b) $[SALBU]_0 = 0.067$ mM; \blacksquare CIP and SALBU mixture solution $[CIP]_0 : [SALBU]_0 = 1:1$, $[CIP]_0 = 0.049$ mM, $[SALBU]_0 = 0.052$ mM $I = 0.5A$ ($I > I_{lim}^0$), flow rate = 366 L h^{-1} , electrolyte: K_2SO_4 0.1 M, $T = 30$ °C.

It can be observed clearly (Fig.IV-39 (a)) that during the first 10 min, CIP degrades with the same rate with or without SALBU and then the degradation of CIP in the multi-component solution is slower. In the case of SALBU there is no difference (Fig.IV-39 (b)).

Fig.IV-40 presents the constant rates of CIP, SALBU and SMX removal in mono component and mixture solutions. In SALBU and CIP mixture solution, it can be noticed clearly that the degradation rate of CIP in mixture solutions is lower; it seems that the presence of SALBU hinders the degradation of CIP. However, in SMX and CIP mixture solution, this phenomenon is not observed.

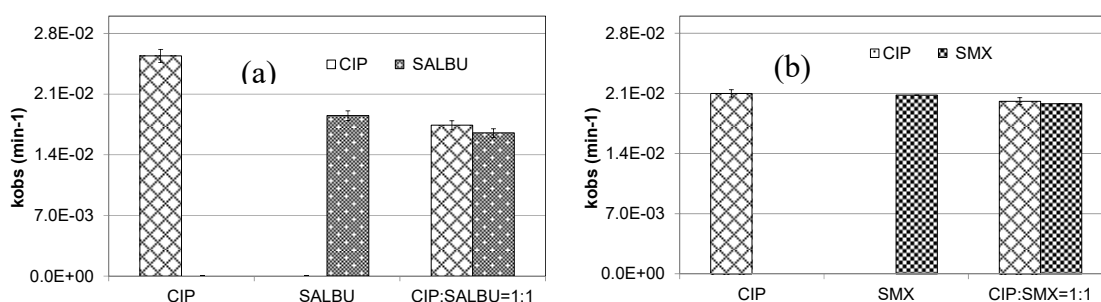


Fig.IV-40 (a) observed degradation rates of CIP and SALBU for 3 electrolyzes: CIP solution ($[CIP]_0 = 0.059$ mM) SALBU solution ($[SALBU]_0 = 0.066$ mM), CIP and SALBU mixture solution in K_2SO_4 0.1 M, $I = 0.5A$ ($I > I_{lim}^0$). Operating conditions: see Fig.IV-37 (b) Observed degradation rates of CIP and SMX for 3 electrolyses: CIP solution ($[CIP]_0 = 0.0561$ mM) , SMX solution ($[SMX]_0 = 0.057$ mM), CIP and SMX mixture solution in K_2SO_4 0.02 M, $I = 0.5A$ ($I > I_{lim}^0$). Operating conditions: see Fig.IV-36.

Thus, during electrochemical oxidation of pharmaceuticals in multicomponent solutions (CIP and SMX; CIP and SALBU), the interaction and the competition can induce different impacts on the degradation of pharmaceuticals, depending on the pharmaceuticals' properties. In the case of electrolysis of CIP and SMX solution, CIP decreases slightly faster than SMX; it is probably due to the higher kinetic constant of CIP with $\cdot OH$. The degradation of CIP and SMX occurs almost at the same rate in mono component and mixture solutions. The experimental values of COD vary with a good agreement with theoretical value, which confirmed the applicability of this model for multiple pharmaceuticals systems.

Conversely, the presence of SALBU slows down the CIP oxidation. Different hypothesis can be formulated: SALBU or intermediates can compete for the reaction with hydroxyl radical. Another hypothesis is that. a part of SALBU can be oxidized by direct

electron exchange on BDD, which undergoes the formation of a dimer [26,28,29], as discussed in section IV.1.3.2. This formation on the electrode surface can hinder the oxidation of CIP.

IV.A.5 Modelling of anodic degradation for organic with BDD anode

Fig.IV-41 shows a general scheme of the possible pathway during electrooxidation of electroactive organic with BDD anode. The oxidation can occur at the anode surface by direct electron transfer (1) or by oxygen transfer (3) (reaction with $\cdot\text{OH}$ generated by water discharge (2)). Because of the weak interaction between BDD surface and hydroxyl radical, $\cdot\text{OH}$ can be considered as quasi free on the surface [69]. If the amount of available $\cdot\text{OH}$ is enough, complete mineralization can be reached (7). Otherwise, it is possible to generate organic radicals (5) with chain reactions [70].

The oxidation via direct electron exchange occurs only on the anode surface, and the reaction with $\cdot\text{OH}$ happens in a narrow zone adjacent to the electrode surface ($< 1.0 \mu\text{m}$), while the chain reaction between organic radical and oxygen can occur from the anode surface to the bulk depending on the duration life of the species.

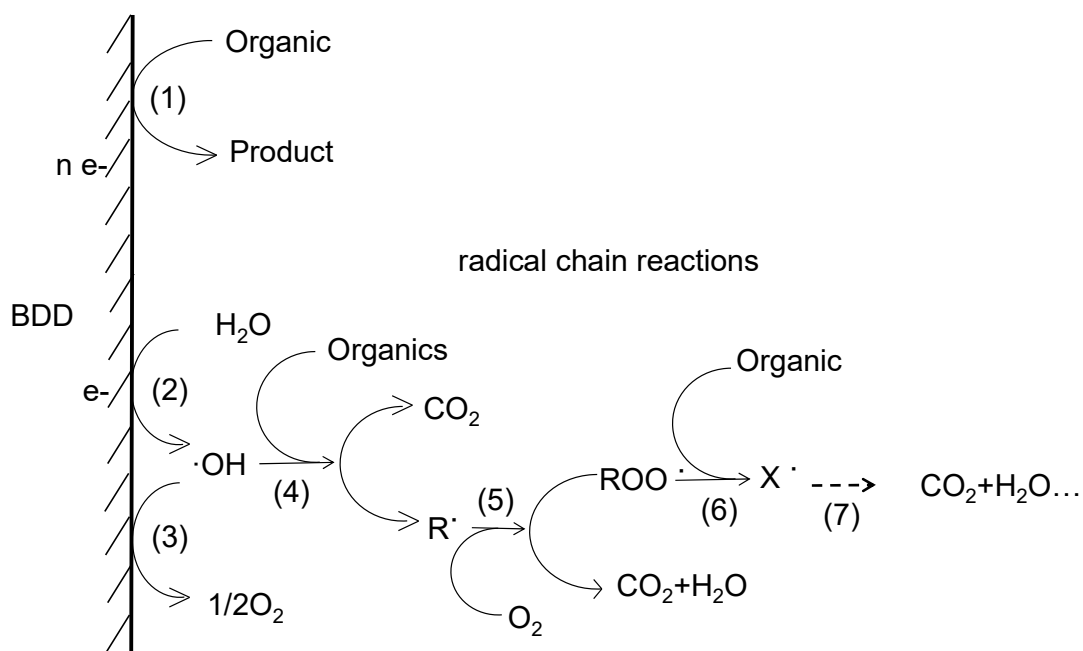


Fig.IV-41 Oxidation pathway of organic in BDD system: (1) direct electron exchange, (2) electrogeneration of $\cdot\text{OH}$, (3) generation of oxygen (4) formation of organic radicals via reaction between organics and hydroxyl radicals, (5) reaction between O_2 and organic radical, (6) reaction between peroxy radicals and organics in the solution, (7) complete mineralization

IV.A.5.1 Model description

The direct electrooxidation can be written as



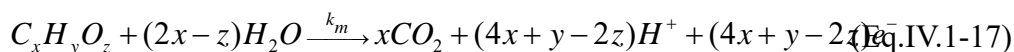
The corresponding initial limiting current density depends on the mass transfer coefficient k_d (m s^{-1}):

$$i_{lim,ne}^0 = nFk_d[C]_0 \quad (\text{Eq.IV.1-16})$$

Where $i_{lim,ne}^0$ is initial limiting current density of directly electron transfer (A m^{-2}), n is the number of electrons exchanged, F is Faraday constant as (96485 C mol^{-1}) and $[C]_0$ is the initial concentration of electroactive species in the solution (mol m^{-3}).

When the current density is lower than the $i_{lim,ne}$ the oxidation process is controlled by electron transfer.

When the applied current density is higher than $i_{lim,ne}$, the oxidation of water occurs and reactive oxygen species can be generated. Free hydroxyl radicals allow mineralizing organic compound. The equivalent number of exchanged electrons can be calculated with Eq.IV.1-17:



k_m is the constant rate of mineralization.

The equivalent number of exchanged electrons γ can be written as:

$$\gamma = 4x + y - 2z \quad (\text{Eq.IV.1-18})$$

The limiting current density corresponding to the total mineralization of the organics ($i_{lim,\bullet OH}^0$, A m^{-2}) is a function of γ , k_d and $[C]_0$.

$$i_{lim,\bullet OH}^0 = (4x + y - 2z)Fk_d[C]_0 \quad (\text{Eq.IV.1-19})$$

Depending on the value of the initial concentration of organics and the applied current intensity, three different regimes can be considered.

- (a) $i \leq i_{\text{lim,ne}}^0$
 (b) $i_{\text{lim,ne}}^0 < i < i_{\text{lim},\cdot\text{OH}}^0$,
 (c) $i > i_{\text{lim},\cdot\text{OH}}^0$

This model is based on the mass balance (Section I.3.3) by which molecule disappearance can be expressed as

$$V \frac{d[C]_t}{dt} = -\Gamma A \quad (\text{Eq.IV.1-20})$$

V is the reservoir volume (volume of the solution), A is the electrode surface (m^2), Γ is the reaction rate of organic on the electrode.

- (a) $i \leq i_{\text{lim,ne}}^0$

In this regime, only direct electron exchange occurs, the reaction rate of organic is the direct electrochemical reaction rate by electrons transfer (Γ_{e^-}) which depends on the applied current density i :

$$\Gamma = \Gamma_{e^-} = \frac{i}{nF} \quad (\text{Eq.IV.1-16})$$

Then Eq.IV.1-22 can be written as:

$$V \frac{d[C]_t}{dt} = -\Gamma_{e^-} A \quad (\text{Eq.IV.1-22})$$

The integration of Eq.IV.1-22 gives the expression of the temporal concentration,

$$C(t) = C_0 - \frac{iA}{nFV} t \quad (\text{Eq.IV.1-23})$$

To calculate Γ_{e^-} , for a constant current density equals to the limiting current density $i_{\text{lim,ne}}$ corresponding to the part of the current density used to oxidized organic molecule.

$$\Gamma_{e^-} = \frac{i_{\text{lim,ne}}}{nF} = k_d C(t) \quad (\text{Eq.IV.1-24})$$

In this case, the concentration profile of the organic specie becomes:

$$C(t) = C_0 \exp\left(-\frac{Ak_d}{V}t\right) \quad (\text{Eq.IV.1-25})$$

(b) $i_{\text{lim},ne^-} < i < i_{\text{lim},\cdot\text{OH}^0}$

For a current density higher than the limiting current density, the oxidation of water occurs. Then the rate of oxidation of organic is expressed as the sum of the rate of electron transfer and the rate of reaction with $\cdot\text{OH}$ ($\Gamma_{\cdot R}$)

$$\Gamma = \Gamma_{e^-} + \Gamma_{\cdot R} \quad (\text{Eq.IV.1-26})$$

The oxidation of organic can be expressed as

$$V \frac{d[C]}{dt} = -(\Gamma_{e^-} + \Gamma_{\cdot R})A \quad (\text{Eq.IV.1-27})$$

Here, the $i_{\cdot\text{OH}}$ (part of current density used to generate $\cdot\text{OH}$) is calculated with the difference between the applied current density and i_{lim,ne^-} :

$$i_{\cdot\text{OH}} = i - i_{\text{lim},ne^-} \quad (\text{Eq.IV.1-28})$$

The $\cdot\text{OH}$ chain reaction rate depends on the generation rate of hydroxyl radicals. As shown on Eq.IV.1-17, mineralization of one mol $\text{C}_x\text{H}_y\text{O}_z$ consumes γ mol of $\cdot\text{OH}$. The reaction rate of organic with $\cdot\text{OH}$ radical chain reactions ($\Gamma_{\cdot R}$) can be written as Eq.IV.1-29.

$$\Gamma_{\cdot R} = \frac{i_{\cdot\text{OH}}}{\gamma F} \quad (\text{Eq.IV.1-29})$$

Combining Eq.IV.1-27 and Eq.IV.1-29, it can be obtained:

$$V \frac{dC(t)}{dt} = -k_d AC(t) - \frac{i_{\cdot\text{OH}}}{\gamma F} A \quad (\text{Eq.IV.1-30})$$

In the case of $n \ll \gamma$, it can be considered that the main part of the applied current density is used to produce $\cdot\text{OH}$, $i = i_{\cdot\text{OH}}$.

Integration of Eq.IV.1-27, $t = 0$, $C_{t=0} = C_0$, the temporal variation of C in the range

($i_{lim,ne}^0 < i < i_{lim,\cdot OH}^0$):

$$C(t) = -\frac{i_{\cdot OH}}{\gamma F k_d} + K \exp\left(-\frac{A k_d}{V} t\right) \quad (\text{Eq.IV.1-31})$$

where K depends on the initial organic concentration, electrons number for mineralization of organics ($i_{\cdot OH} = i_{applied}$).

$$K = C_0 + \frac{i_{\cdot OH}}{\gamma F k_d} \quad (\text{Eq.IV.1-32})$$

This behavior persists until a critical time (t_{cr}), at which the applied current density (i) equals the limiting current density for mineralization.

A characteristic parameter α is defined as

$$\alpha = \frac{i}{i_{lim,\cdot OH}^0} \quad (\text{Eq.IV.1-33})$$

The concentration of organic on critical time is $[C]_{cr}$ defined by Eq. IV.1-34

$$[C]_{cr} = \alpha [C]_0 \quad (\text{Eq.IV.1-34})$$

Substituting Eq.IV.1-34 to Eq.IV.1-31, the critical time can be calculated as

$$t_{cr} = -\frac{V}{A k_d} \ln\left(\frac{2\alpha\gamma - \alpha n}{\gamma + \alpha\gamma - n}\right) \quad (\text{Eq.IV.1-35})$$

As the electrons number of direct exchange is far less than the electrons number of mineralization ($n \ll \gamma$), the function can be simplified:

$$t_{cr} = -\frac{V}{A k_d} \ln\left(\frac{2\alpha}{1+\alpha}\right) \quad (\text{Eq.IV.1-36})$$

(c) $i > i_{lim,\cdot OH}^0$

In the case of applied current density higher than the limiting current density for the complete mineralization $i > i_{lim,\cdot OH}^0$. The reaction with radicals is described by

pseudo-first-order kinetics. The reaction of organic for \bullet OH radical chain reactions is written as

$$\Gamma_{R^{\bullet}} = -k_m C(t) \quad (\text{Eq.IV.1-37})$$

k_m is constant rate of mineralization in s^{-1} (see Eq.IV.1-16).

Combining Eq.IV.1-24, and Eq.IV.1-37, then Eq.IV.1-27 is written as Eq.IV.1-36:

$$\frac{dC(t)}{dt} = -\frac{A}{V} k_d C(t) - k_m C(t) \quad (\text{Eq.IV.1-38})$$

In the case of $i > i_{lim}^0$, the variation of organic concentration with time can be calculated with Eq.IV.1-39,

$$C(t) = C^0 \exp \left[-\left(\frac{A k_d}{V} + k_m \right) t \right] \quad (\text{Eq.IV.1-39})$$

IV.A.5.2 Comparison of model and experimental values

When $i > i_{lim}$, \bullet OH, \bullet OH which is quasi free on the electrode surface can react massively on organics. In this case, the oxidation is not selective and k_m does not depend on the nature of organic, the rate of oxidation depends on the hydrodynamic conditions. To determine k_m , experimental data from the electrolysis of urea is used, because urea don't have the direct electron transfer with BDD. In that case $\frac{i}{i_{lim,OH}} = 2.9$, then concentration of urea follows an exponential relation as Eq.IV.1-40

$$C(t) = C_0 \exp(-k_m t) \quad (\text{Eq.IV.1-40})$$

k_m can be evaluated by the liner relationship between $-\ln C(t)/C_0 \sim t$ (Fig.IV-42)

$$-\ln \frac{C(t)}{C_0} = k_m \cdot t \quad (\text{Eq.IV.1-41})$$

The linear relationship allows to estimate $k_m = 2.54 \times 10^{-4} \text{ s}^{-1}$

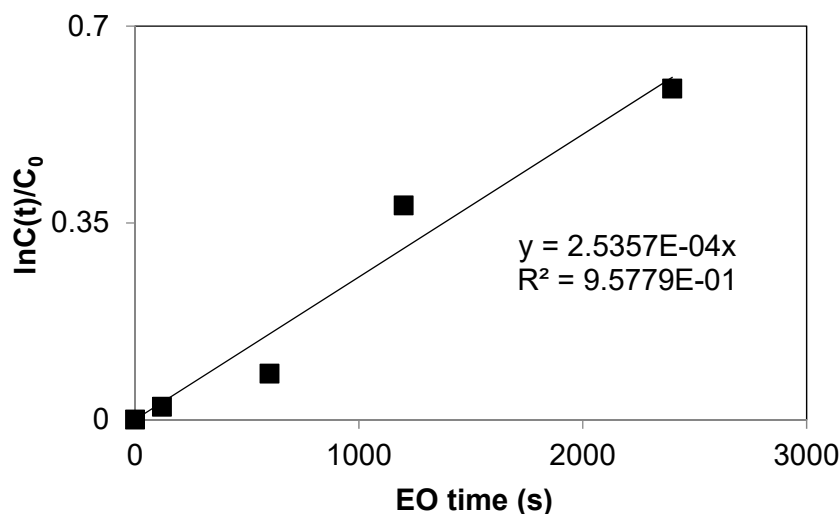


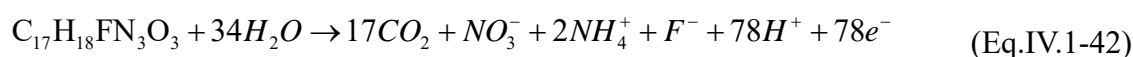
Fig.IV-42 Variation of $-\ln C(t)/C_0$ with electrooxidation time during electrolysis of 1L of urea solution in K_2SO_4 0.1 M at pH = 3.7. $[\text{Urea}]_0 = 0.63 \text{ mM}$ (38.1 mg L^{-1} , $i = 7.24 \text{ mA cm}^{-1}$ ($i_{\text{lim}}, \cdot \text{OH} = 2.46 \text{ mA cm}^{-1}$), flow rate = 366 L h^{-1} , $T = 30 \text{ }^\circ\text{C}$.

Three pharmaceuticals: CIP, SMX and SALBU are selected to test the model. Cyclic voltammograms have shown that these three pharmaceuticals can be degraded by both direct electrons exchange with electrode and chemical reaction with $\cdot \text{OH}$. Table IV-7 gives the number of exchanged e^- and the equivalent e^- for complete mineralization.

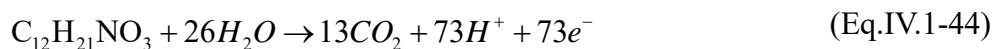
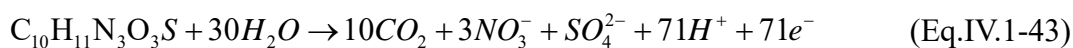
Table IV-7 Electrons numbers of CIP, SMX, SALBU for direct oxidation, n and for mineralization, γ

Pharmaceuticals	CIP	SMX	SALBU
n	2	1	1
γ	78	71	73

The mineralization of CIP by radical chain reactions is presented in Eq.IV.1-42. The nitrogen is calculated as that one-third into NO_3^- and two-third into NH_4^+ , according the experimental nitrogen conversion of CIP (section IV.1.1.2). The value of γ is 78.



For SMX and SALBU, the nitrogen is considered to be converted into NO_3^- (in ionic chromatograph, just NO_3^- is observed); the corresponding reaction of mineralization is shown in Eq.IV.1-43 and Eq.IV.1-44. The values of γ are presented on table IV-6.



Then the initial limiting current for mineralization ($i_{\text{lim}, \cdot\text{OH}}^0$) by electron exchange and $\cdot\text{OH}$ radical chain reactions is calculated with Eq.IV.1-35.

(a) Simulation at $i_{\text{lim}, \text{ne}}^0 < i < i_{\text{lim}, \cdot\text{OH}}^0$

Table IV-8 summarizes the operating conditions during electrolyses of CIP solution and the calculated limiting current densities ($i_{\text{lim}, \text{ne}}^0$, $i_{\text{lim}, \cdot\text{OH}}^0$), the critical time considering to $i = i_{\text{lim}, \cdot\text{OH}}^0$ (Eq.IV.1-33)

Table IV-8 Applied current density, initial limiting current and the calculated critical time for the electrolyses on the range $i_{\text{lim}, \text{ne}}^0 < i < i_{\text{lim}, \cdot\text{OH}}^0$

Applied current density (mA cm ⁻²)	[CIP] ₀ (mM)	$i_{\text{lim}, \text{ne}}^0$ (mA cm ⁻²)	$i_{\text{lim}, \cdot\text{OH}}^0$ (mA cm ⁻²)	α	t_{cr} (min)
0.43	0.052	0.023	0.90	0.47	45
0.72	0.052	0.023	0.90	0.8	34

Fig.IV-43 presents the experimental values obtained during electrolysis in the case of $i_{lim,ne^-}^0 < i < i_{lim,OH}^0$ at 0.43 mA cm^{-2} and simulated values according to Eq.IV.1-31 and Eq.IV.1-39 (separated by critical time). A good agreement between experimental and model is observed. Fig.IV-44 shows the simulation using another current density 0.72 mA cm^{-2} ($t_{cr} = 34 \text{ min}$). Also, a good accordance is observed.

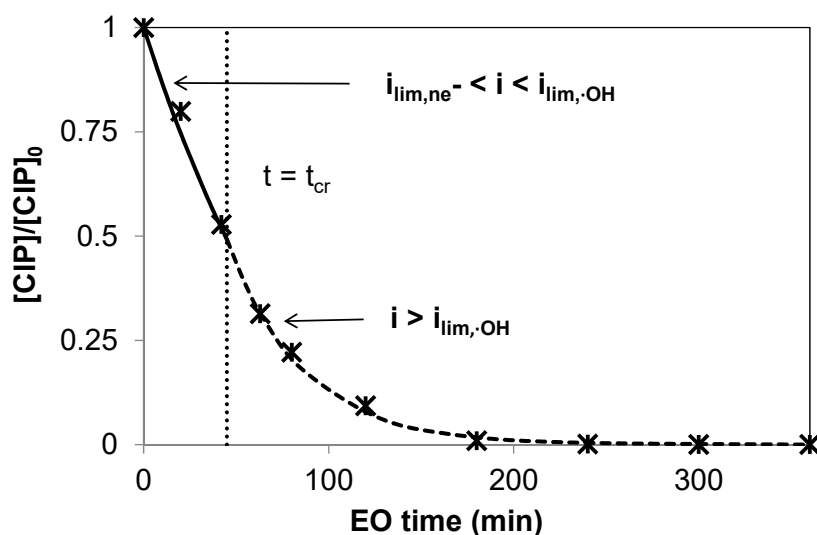


Fig.IV-43 Normalized CIP concentration with electrooxidation time (symbol: experimental) comparing with the model: — continuous line : $i_{lim,ne^-} < i < i_{lim,OH}^0$ (calculated by Eq.IV.1-31) and --- dashed line : $i > i_{lim,OH}^0$ (calculated by Eq.IV.1-39). The applied current density is 0.43 mA cm^{-2} in K_2SO_4 0.1 M at $\text{pH} = 3.7$. $[\text{CIP}]_0 = 0.052 \text{ mM}$, flow rate = 366 L h^{-1} , $T = 30 \text{ }^\circ\text{C}$.

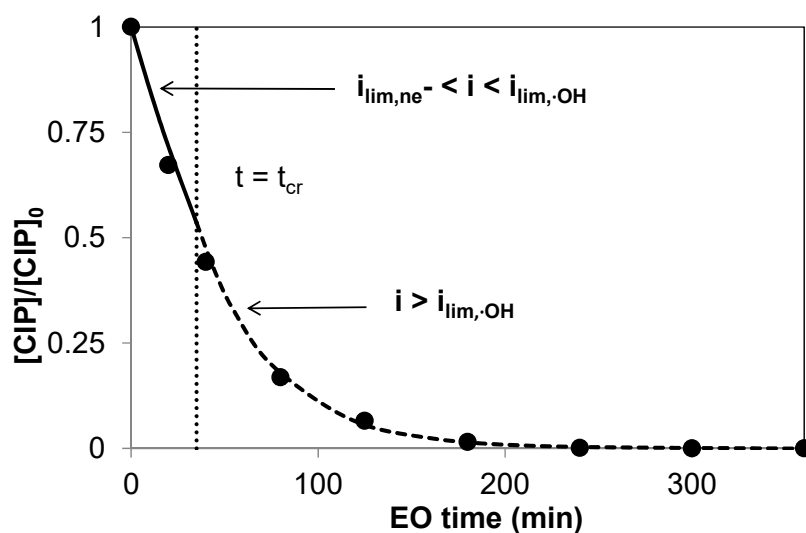


Fig.IV-44 Normalized CIP concentration with electrooxidation time (symbol: experimental) with electrooxidation time comparing with the model: $i_{lim,ne^-} < i < i_{lim,OH}^0$ (calculated by Eq.IV.1-31), continuous line —; $i > i_{lim,OH}^0$ (calculated by Eq.IV.1-39), dashed line ---. The applied current density is 0.72 mA cm^{-2} in K_2SO_4 0.1 M at $\text{pH} = 3.7$. $[\text{CIP}]_0 = 0.052 \text{ mM}$, flow rate = 366 L h^{-1} , $T = 30 \text{ }^\circ\text{C}$.

(b) Simulation at $i = 7.24 \text{ mA cm}^{-2}$ in the region $i > i_{\text{lim},\text{OH}}^0$

In the case of $i > i_{\text{lim},\text{OH}}^0$, electrolyses were carried out with two pharmaceuticals CIP and SMX at 7.24 mA cm^{-2} which corresponds to the range of $i > i_{\text{lim},\text{OH}}^0$. Table IV-9 shows the limiting current densities and applied current densities for each electrolysis.

Table IV-9 Limiting current densities and applied current densities in electrolyses of Fig. IV-44 ($i > i_{\text{lim},\text{OH}}^0$)

Molecule	Initial concentration (mM)	$I_{\text{lim},\text{ne}}^0$ (mA cm^{-2})	$I_{\text{lim},\text{OH}}^0$ (mA cm^{-2})	Applied current density i (mA cm^{-2})
CIP	0.059	0.026	1.02	7.24
SMX	0.053	0.012	0.95	7.24

For each electrolysis, Fig.IV-45 compares the experimental value and model calculated from Eq.IV.1-39 at $i > i_{\text{lim},\text{OH}}^0$. Once again, an excellent accordance is obtained for both CIP and SMX in the case of $i > i_{\text{lim},\text{OH}}^0$.

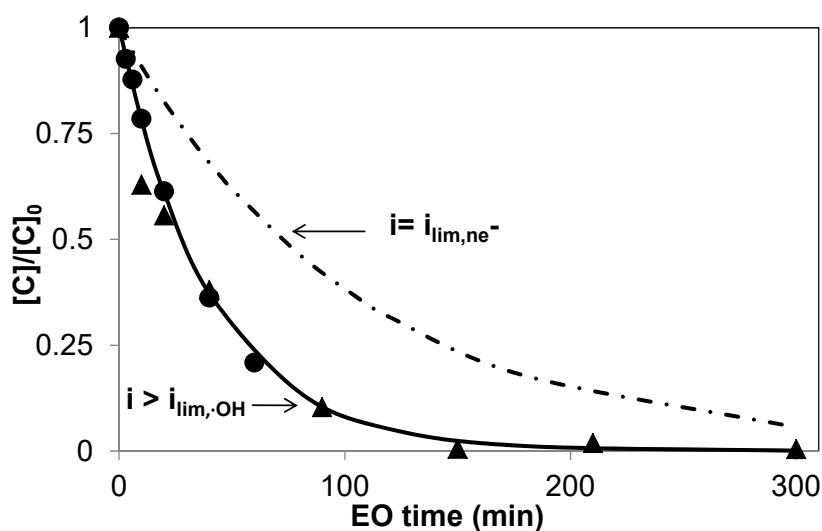


Fig.IV-45 Comparison of normalized experimental concentration of CIP ▲ and SMX ● during electrolysis and model: continuous line — $i > i_{\text{lim},\text{OH}}^0$ (calculated by Eq.IV.1-39); dashed line --- $i = i_{\text{lim},\text{ne}}^0$ (Eq.IV.1-24). The applied current density is 7.24 mA cm^{-2} in K_2SO_4 0.1 M at $\text{pH} = 3.7$. $[\text{CIP}]_0 = 0.059 \text{ mM}$, $[\text{SMX}]_0 = 0.053 \text{ Mm}$, flow rate = 366 L h^{-1} , $T = 30 \text{ }^\circ\text{C}$.

(c) Effect of presence of SO_4^{2-} on the removal of organics

Previously (section IV.A.4.1.1), the role of electrolyte, in particular the sulfate anions which can form $\text{SO}_4 \cdot^-$ via chemical reaction with $\cdot\text{OH}$, was evidenced for the

removal of organics.

k_m , which is evaluated by the urea degradation from Eq.IV.1-41, was observed from electrolysis performed in K_2SO_4 0.1M. In this case, k_m can be presented as the sum of $k_{\bullet OH}$ and $k_{SO_4 \bullet^-}$:

$$k_m = k_{OH\bullet} + k_{SO_4\bullet^-} \quad (\text{Eq.IV.1-44})$$

where, k_m is the constant rate of mineralization involving the reaction $\bullet OH$ and $SO_4 \bullet^-$ radicals; $k_{\bullet OH}$, the reaction rate with $\bullet OH$; $k_{SO_4 \bullet^-}$ is the reaction rate with $SO_4 \bullet^-$.

As discussed on section IV.A.4.1.1 (Table IV-4), the amounts of $SO_4 \bullet^-$ can be 5 times lower in K_2SO_4 0.02 M solution, than in K_2SO_4 0.1M (pH = 3). One can consider that the reaction of $SO_4 \bullet^-$ is not significant in the case of K_2SO_4 0.02 M. The value of $k_{SO_4 \bullet^-}$ can be evaluated by comparing the degradation of SMX in K_2SO_4 0.1M, pH = 3 and K_2SO_4 0.02 M.

This value of $k_{\bullet OH}$ and $k_{SO_4 \bullet^-}$ can be evaluated by comparing the degradation of SMX in K_2SO_4 0.1M, pH = 3 and K_2SO_4 0.02 M.

In K_2SO_4 , pH = 3, the degradation of SMX can be written as Eq.IV.1-45

$$-\ln \frac{C(t)}{C_0} = \left(\frac{Ak_d}{V} + k_m \right) t \quad (\text{Eq.IV.1-45})$$

In K_2SO_4 0.02 M, the degradation of SMX can be written as Eq.IV.1-46

$$-\ln \frac{C(t)}{C_0} = \left(\frac{Ak_d}{V} + k_{OH\bullet} \right) t \quad (\text{Eq.IV.1-46})$$

From the different linear relationship of $-\ln C(t)/C_0 \sim t$, the $k_{SO_4 \bullet^-}$ are evaluated.

Fig.IV-46 shows linear relationship of $-\ln C(t)/C_0 \sim t$ with different slop values during electroxidation of SMX in K_2SO_4 0.1M and K_2SO_4 0.02 M.

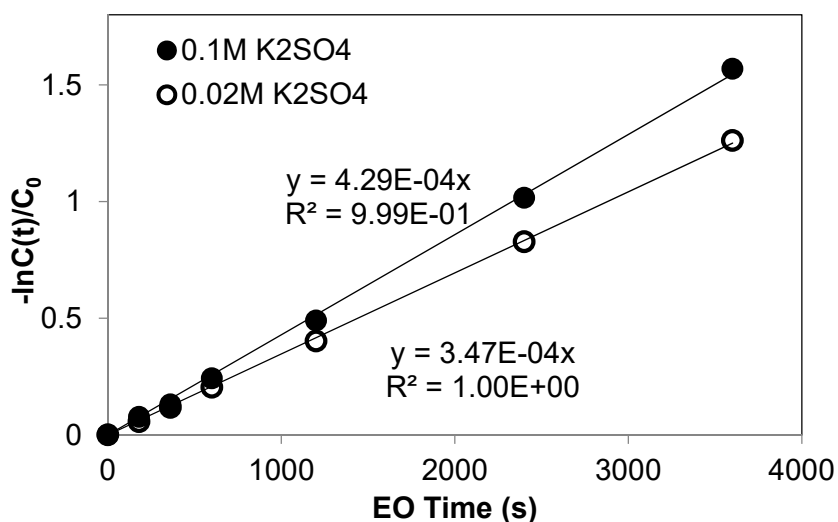


Fig.IV-46 Variation of $-\ln C(t)/C_0$ with electrooxidation time during electrolysis of 1L of SMX solution in K_2SO_4 0.1 M at pH = 3.7 ($[SMX]_0 = 0.053$ mM) and K_2SO_4 0.02 M solution ($[SMX]_0 = 0.059$ mM). $i = 7.24$ mA cm^{-1} ($i_{lim,OH} \approx 1$ mA cm^{-1}), flow rate = 366 L h^{-1} , $T = 30$ °C.

The calculated value of k_{OH} and $k_{SO_4 \cdot^-}$ are presented in table IV-10

Table IV-10 Values of k_{OH} and $k_{SO_4 \cdot^-}$ (Fig.IV-45)

	Slope (s^{-1})	k_{OH} (s^{-1})	$k_{SO_4 \cdot^-}$ (s^{-1})
K_2SO_4 0.02 M	3.47×10^{-4}	3.47×10^{-4}	0
K_2SO_4 0.1M	4.29×10^{-4}	3.47×10^{-4}	8.2×10^{-5}

The electrolyses were carried out with solution of CIP or SALBU. The degradation of SALBU is not impacted by the presence of $SO_4 \cdot^-$ (section IV.1.4.1). The experimental conditions of electrolyses of different pharmaceuticals in K_2SO_4 0.1 and 0.02 M are presented on Table IV-11.

Table IV-11 The limiting current densities and applied current densities during electrolyses ($i > i_{lim,OH^0}$)

	C_0 (mM)	i_{lim,OH^0} (mA cm^{-2})	i (mA cm^{-2})	k_{OH} (S^{-1})	Electrolyte
CIP	0.069	1.19	1.45	1.72×10^{-4}	K_2SO_4 0.02 M
SMX	0.059	1.08	7.24	1.72×10^{-4}	K_2SO_4 0.02 M
SALBU	0.068	1.23	7.24	1.72×10^{-4}	K_2SO_4 0.02 M
SALBU	0.067	1.22	7.24	1.72×10^{-4}	K_2SO_4 0.1 M

Fig.IV-46 shows experimental data and the model using $k_m = k_{OH^{\cdot-}}$ and $k_m = k_{OH^{\cdot-}} + k_{SO_4^{\cdot-}}$ (Eq.IV.1-37) with $k_{OH} = 3.47 \times 10^{-4} s^{-1}$ and $k_{SO_4 \cdot^-} = 8.2 \times 10^{-5} s^{-1}$ for

electrolysis at $i_{lim,OH}$. This figure evidences that in the case of electrolysis carried out in K_2SO_4 (0.02 M), a good agreement with the model obtained with k_{OH} . This model seems to confirm that SALBU doesn't react with sulfate radical and the role of SO_4^{2-} during electrolysis.

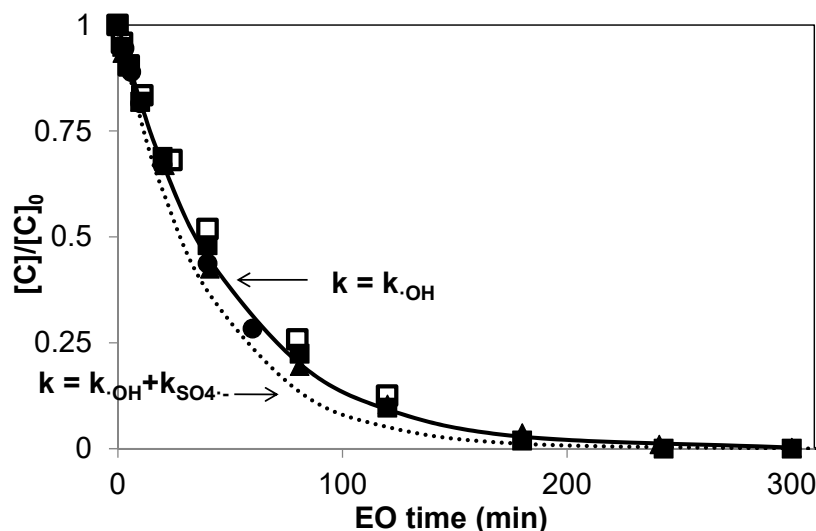


Fig.IV-46 Experimental and numerical data obtained for electrolysis of: CIP ▲, SMX ● and SALBU ■ in K_2SO_4 0.02M and SALBU □ in K_2SO_4 0.1M at $i > i_{lim,OH}^0$: continuous line — (Eq.IV.1-39 with $k_m = k_{OH} = 2.54 \times 10^{-4}$), dashed line --- (Eq.IV.1-39 with $k_m = k_{OH} + k_{SO_4^{2-}}$), flow rate = 366 L h^{-1} , $T = 30 \text{ }^\circ\text{C}$.

(d) Effect of oxygen bubbles

When the $i \gg i_{lim,OH}^0$, electrogenerated oxygen bubbles can be considered to enhance the mass transfer coefficient and then accelerate the degradation of organics as discussed in IV.1.2.2. The electrolysis of CIP solution at high current density ($i \gg i_{lim,OH}^0$) was performed. The applied current density and mass transfer coefficients: hydrodynamic (k_d^h) and global (k_d including the hydrodynamic and bubble effects) are presented on table IV-12 (the calculation follows Annex IV-1).

Table IV-12 the parameter for the electrolysis of CIP with high current density

[CIP] (mg L^{-1})	i_{applied} (A m^{-2})	i_{lim} (A m^{-2})	i_{O_2} (A m^{-2})	k_d^h (m s^{-1})	k_d (m s^{-1})	k_m (s^{-1})
20.4	217	10	207	2.31×10^{-5}	4.33×10^{-5}	2.54×10^{-4}

Fig IV-48 shows the good agreement between experimental and model using a global mass transfer coefficient including the effect of electrogenerated bubbles.

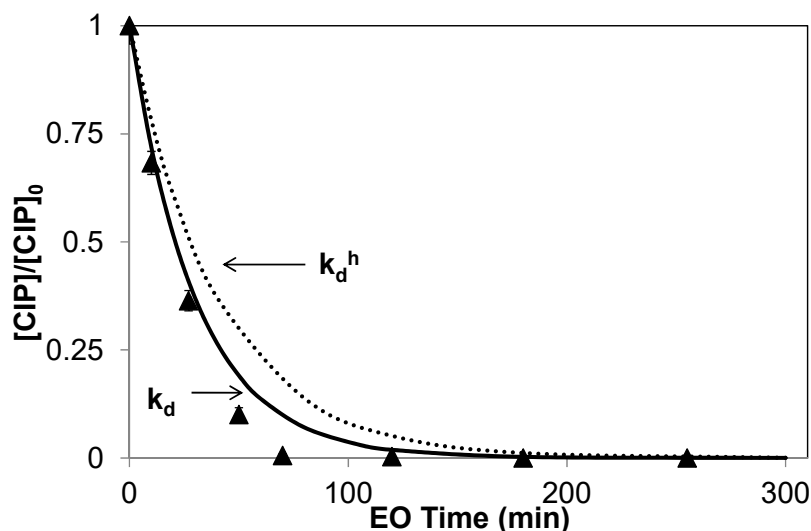


Fig.IV-48 Experimental and numerical data obtained for electrolysis of CIP in K_2SO_4 0.1M, $i = 21.7 \text{ mA cm}^{-2}$ $i \gg i_{lim, \cdot OH}^0$: continuous line — (Eq.IV.1-37 with $k_d = 4.33 \times 10^{-5} \text{ m s}^{-1}$), dashed line --- (Eq.IV.1-37 with $k_d^h = 2.31 \times 10^{-5} \text{ m s}^{-1}$), flow rate = 366 L h^{-1} , $T = 30 \text{ }^\circ\text{C}$.

Thus, the experimental validation of the model at several conditions with one or three pharmaceuticals shows excellent agreement in the investigated cases.

IV.A.6 Conclusion:

A complete study was performed on the treatment of solutions containing ciprofloxacin by electrooxidation using BDD anode. The complete mineralization can be reached and the experimental COD values are in accordance with the COD model. At low current density ($I < I_{lim}^0$), the amount of intermediates decreases sharply with the increasing current density; while in the case of $I > I_{lim}^0$, the total amount of intermediates doesn't change significantly..

The salts present in the wastewater can play a significant role in the process. Since, strong oxidants ($SO_4^{\cdot-}$, ClO^- and $ClO\cdot$) can be generated at the anode and react chemically with the organic matter. On the other hand, some undesired products can be generated by reaction with hydroxyl radicals such ClO_4^- and AOX in presence of Cl^- . The study on the operating conditions evidenced that the current density must be chosen carefully..

Rather than a hindering effect, the presence of urea even at higher concentration can accelerate the degradation of pharmaceuticals.

In the case of synthetic solutions which contain two pharmaceuticals, the interaction and the competition can induce different impacts on the degradation of pharmaceuticals. . A model allowing predicting the variation of organic concentration is developed. The effects of electrolyte and the electrogenerated oxygen bubbles are also taken into account. The numerical model was validated by experimental data obtained with electrolysis of 3 pharmaceuticals at different operating conditions. In all investigated cases, the comparison of model with experimental dates shows a good agreement.

IV.B Electrochemical oxidation of pharmaceuticals in wastewater

This chapter investigates the elimination of pharmaceuticals in the NF retentate which is the concentrated solution of MBR effluents from hospital wastewater. The objective is to identify the feasibility and the impact of the real media (hospital wastewater) on the electrochemical process. Table VI-13 presents physico-chemical characteristics and composition of this wastewater matrix. Around 50 pharmaceuticals are analysed in the MBR permeate from hospital and concentrated in NF retentate [71].

Table VI-13 Physico-chemical characteristics and composition of the wastewater matrix (NF retentate of MBR effluents)

Property	Value	Ions	Concentration
pH	7.84	Na ⁺ (mg L ⁻¹)	161
COD (mg L ⁻¹)	86	K ⁺ (mg L ⁻¹)	34
BOD ₅ (mg L ⁻¹)	0	Mg ²⁺ (mg L ⁻¹)	9
TOC (mg L ⁻¹)	40	Ca ²⁺ (mg L ⁻¹)	70
UV ₂₅₄	1.13	Cl ⁻ (mg L ⁻¹)	70
HCO ₃ ⁻ (mg L ⁻¹)	63	NO ₃ ⁻ (mg L ⁻¹)	152
Conductivity (mS cm ⁻¹)	1.17	SO ₄ ²⁻ (mg L ⁻¹)	110
		PO ₄ ³⁻ * (mg L ⁻¹)	13
Concentration of target pharmaceuticals (µg L ⁻¹)			
Ciprofloxacin		81	
Cyclophosphamide		22	
Ifosfamide		4	

*Due to the analysis method, all phosphate species H₃PO₄, H₂PO₄⁻, HPO₄²⁻ and PO₄³⁻ in the solution were measured in the form of PO₄³⁻.

VI.B.1. Elimination of pharmaceuticals and AOX

Fig.IV-49 shows the decay of COD with EO time during electrolysis of NF retentate. It appears that a very good agreement is obtained between experimental and theoretical values (I-24). Moreover, COD decay after 120 min of electrolysis is slightly faster than the theoretical ones. It can be suggested that an additional phenomenon occurs during the electrochemical oxidation. In wastewater, there are a large amount of salts, as shown on

table IV-13, which can not only act as electrolyte support but also react with $\cdot\text{OH}$ to generate strong oxidants. The results shown in paragraph IV.A.4.1 evidenced that $\text{SO}_4 \cdot^-$ and ClO^- can be electrogenerated from sulphate and chloride, respectively. These oxidants react chemically with organics. For electrochemical treatment of landfill leachate using a BDD anode, Anglada et al. [72] reported that the evolution of COD follows the theoretical value at the current densities of 300 and 400 A m^{-2} , while at higher current densities (600, 900 and 1200 A m^{-2}), the oxidation rate of COD is higher than the theoretical one. These authors owe these phenomena to the strong influence of the indirect electrochemical oxidation due to electrogenerated oxidants from salts present in the electrolyte support.

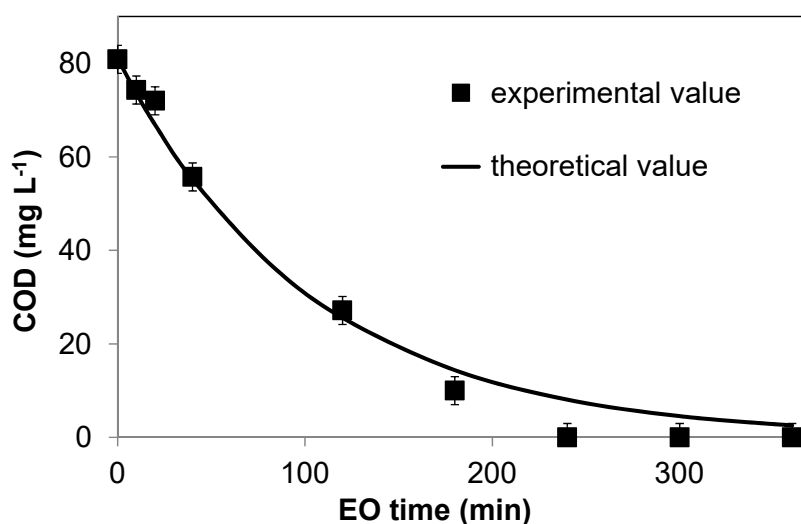


Fig.IV-49 The decay of experimental and theoretical COD with EO time during 360 min electrolysis of 1L NF retentate. $[\text{COD}]_0 = 81 \text{ mg L}^{-1}$, $I = 0.3\text{A}$ ($i = 4.34 \text{ mA cm}^{-2}$, $i_{\text{lim}} = 2.25 \text{ mA cm}^{-2}$), $\text{pH} = 7.8$, flow rate = 366 L h^{-1} , $T = 30 \text{ }^\circ\text{C}$

Fig. IV-50 presents the degradation of CIP with EO time during 360 min electrolysis of 1L NF retentate. The complete removal of CIP is obtained after 80 min (0.4 Ah L^{-1}). It can be observed that during the first 15 min CIP decreases faster with a higher degradation rate, then the degradation rate decreases. The change of degradation rate is possibly induced by the production of several kinds of intermediates which can compete with CIP for the oxidation and slow down the observed CIP degradation rate in the complex matrix. Nevertheless, the degradation rate of CIP in the NF retentate matrix (0.091 min^{-1} for the first 15 min and then 0.034 min^{-1}) is higher than the case of in synthetic solution in the same current density range: 0.028 min^{-1} at 0.5A (section

IV.A.2.1). The faster degradation of CIP in the NF retentate can be attributed to the influence of electrogenerated inorganic oxidants and some intermediates from organics oxidation. As discussed on section IV.A.4.1, the oxidants ($\text{SO}_4^{\cdot-}$ and hypochlorite) electrogenerated from sulphate and chloride can accelerate the degradation of CIP; the presence of urea was also observed to lead to a faster degradation of CIP.

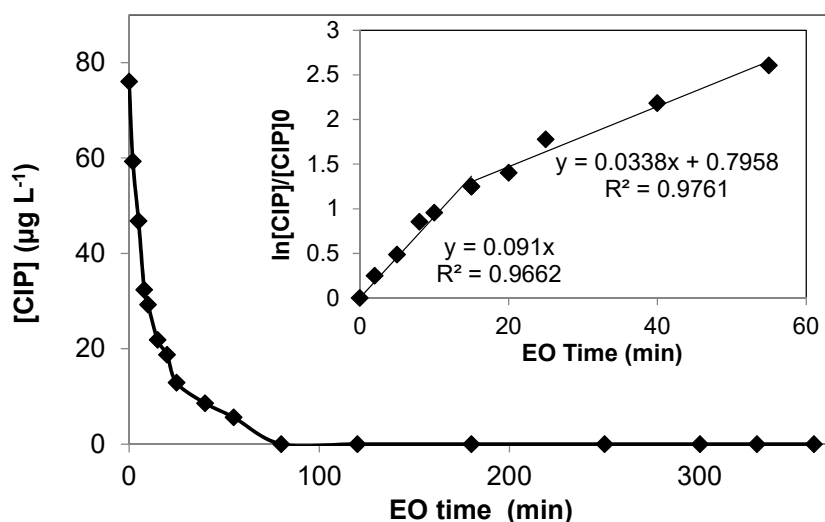


Fig.IV-50 Decay of CIP with EO time during 360 min electrolysis of 1L NF retentate. $[\text{CIP}]_0 = 76 \mu\text{g L}^{-1}$ ($0.23 \mu\text{M}$), $I = 0.3\text{A}$ ($i = 4.34 \text{ mA cm}^{-2}$, $i_{\text{lim}} = 2.25 \text{ mA cm}^{-2}$), $\text{pH} = 7.8$, flow rate = 366 L h^{-1} , $T = 30 \text{ }^\circ\text{C}$. Inset: The observed degradation rate of CIP.

Table IV-14 shows the concentration of target pharmaceuticals, TOC and AOX at initial time and after 360 minutes of electrolysis of 1 L NF retentate. Target pharmaceuticals: ciprofloxacin, cyclophosphamide and ifosfamide are totally removed after electrolysis. Final TOC reaches 3 mg L^{-1} and AOX also decreases from $2300 \mu\text{g Cl L}^{-1}$ to $450 \mu\text{g Cl L}^{-1}$.

Table VI-14 Concentrations of selected pharmaceuticals, TOC and AOX at initial time and after 360 minutes of electrolysis of 1 L NF retentate, operating conditions: see Fig.IV-49

	Ciprofloxacin ($\mu\text{g L}^{-1}$)	Cyclophosphamide ($\mu\text{g L}^{-1}$)	ifosfamide ($\mu\text{g L}^{-1}$)	TOC (mg L^{-1})	AOX ($\mu\text{g Cl L}^{-1}$)
$[\text{C}]_{\text{NF concentrate}}$	81	22	4	40	2300
$[\text{C}]_{t=360\text{min}}$	0	0	0	3	450
% Removal	100%	100%	100%	92.5%	80%

VI.B.2 Conversion of ions (in particular Cl⁻) during electrolysis

The presence of Cl⁻ in the process has to be studied carefully in particular because of the possible formation of toxic by-product such as ClO₄⁻. Fig.IV-51 presents the conversion of chlorine species during 360 min electrolysis of 1L NF retentate. It appears that the concentration of Cl⁻ declines with time and ClO⁻, ClO₃⁻ and ClO₄⁻ are formed (concentration of ClO₃⁻ is lower than the quantification limits <1 mg L⁻¹). As we can see, the sum of ionic chlorine species (Cl⁻ + ClO⁻ + ClO₄⁻) is higher than the initial concentration of ionic chlorine (only Cl⁻).

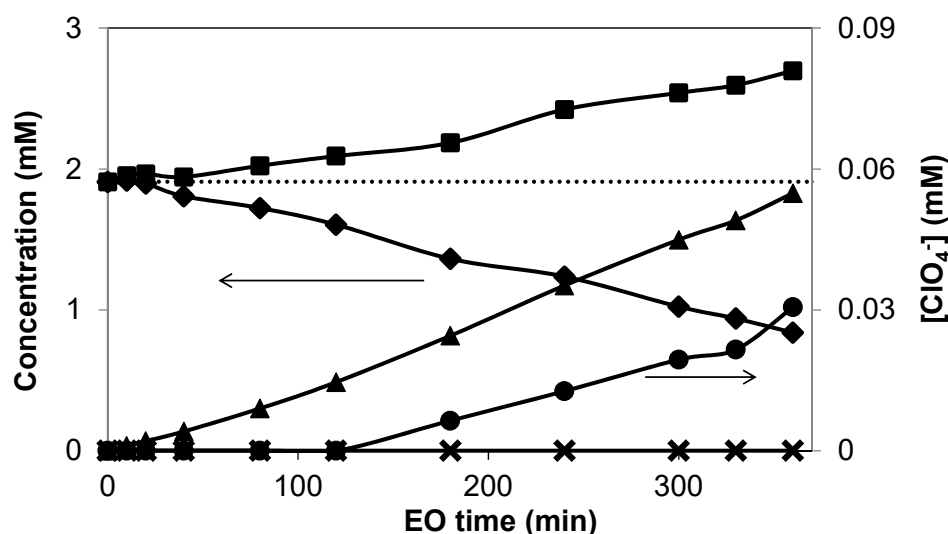


Fig.IV-51 Variation of concentrations of chlorine species: (a) Cl⁻ (◆); Cl⁻ + ClO⁻ + ClO₄⁻ (■); (b) ClO⁻ (▲), ClO₃⁻ (✕) ClO₄⁻ (●) with EO time during 360 min electrolysis of 1L NF retentate with different pH: pH 7.8, The dashed lineis the initial chloride concentration. [Cl⁻]₀ = 67 mg L⁻¹, operating conditions: see Fig.IV-49

Table IV-15 presents the concentration of chlorine species at initial time and after electrolysis. The part exceeding the initial value is probably due to the release of chlorine during the oxidation of organics which contain chlorine atoms.

Table VI-15 Concentrations of chlorine species at initial time and after 360 minutes of electrolysis of 1 L NF retentate. Operating conditions: see Fig.IV-50

Concentration (mM)	[Cl ⁻]	[ClO ⁻]	[ClO ₄ ⁻]	[Cl ⁻]+[ClO ⁻]+[ClO ₄ ⁻]
[C] _{NF concentrate}	1.9	0	0	1.9
[C] _{t= 360min}	0.8	1.8	0.03	2.7

The generation of undesired perchlorate ClO_4^- , it appears after 180 min. After 360 min of electrolysis, the concentration of ClO_4^- is 3 mg L^{-1} . Based on these findings, tests of ecotoxicity and AOX measurements have been implemented for the study on the coupling of nanofiltration and electrooxidation in chapter V.

In order to investigate the conversion of organic nitrogen, sulphate and phosphate from the pharmaceuticals and organic waste and evolution of the other ions, the ionic concentrations were analysed. Fig.IV-52 shows the variation of ionic concentrations with time during 360 min electrolysis of 1L NF retentate. Two kinds of tendencies are observed.

It appears that the concentration of NO_3^- and SO_4^{2-} slightly increase during the process and stabilizes at around 180 min. (The increasing amount of NO_3^- and SO_4^{2-} are 17 mg L^{-1} and 9 mg L^{-1} , respectively). This increasing concentrations can be explained by the degradation of organics which contains S or/and N. This fact has been already observed during oxidation of urea and salbutamol (N in the molecular structures) and sulfamethoxazole (S and N in molecular structure) in synthetic solution.

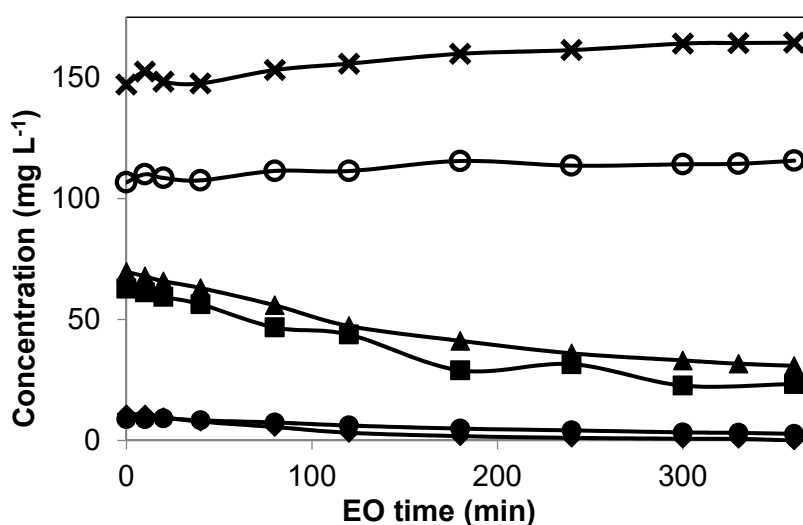


Fig.IV-52 Evolution of the concentration of $\times \text{NO}_3^-$, $\circ \text{SO}_4^{2-}$, $\blacktriangle \text{Ca}^{2+}$, $\bullet \text{Mg}^{2+}$, $\blacklozenge \text{PO}_4^{3-}$ and $\blacksquare \text{HCO}_3^-$ with EO time during 360 min electrolysis of 1L NF retentate, $\text{pH} = 7.8$. $[\text{NO}_3^-]_0 = 147.2 \text{ mg L}^{-1}$, $[\text{SO}_4^{2-}]_0 = 106.7 \text{ mg L}^{-1}$, $[\text{Ca}^{2+}]_0 = 69.8 \text{ mg L}^{-1}$, $[\text{Mg}^{2+}]_0 = 8.8 \text{ mg L}^{-1}$, $[\text{PO}_4^{3-}]_0 = 10.8 \text{ mg L}^{-1}$, $[\text{IC}]_0 = 62.8 \text{ mg L}^{-1}$, operating conditions: see Fig.IV-49.

For the variation of the concentrations of Mg^{2+} , PO_4^{3-} , Ca^{2+} and HCO_3^- , one can observe the decrease of them with electrooxidation time. The decline of the concentrations of Ca^{2+} and inorganic carbon (mainly HCO_3^-) is significant from 69.8 mg

L⁻¹ to 30.8 mg L⁻¹ and from 62.8 mg L⁻¹ to 23.3 mg L⁻¹. Then the concentrations of Mg²⁺, PO₄³⁻ decrease from 8.8 mg L⁻¹ to 2.7 mg L⁻¹ and from 10.8 mg L⁻¹ to 0 mg L⁻¹, respectively. The disappearance of them is probably due to the scaling which occurs on the electrolysis cell.

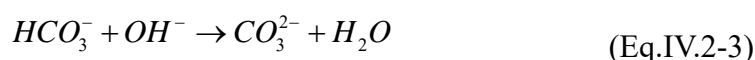
Van Hege [73] also observed the decrease of concentrations of Mg²⁺ and Ca²⁺ in the solution during electrooxidation of reverse osmosis membrane concentrates with BDD anode.

The principle of the electrochemical scaling is the following:

During water electrolysis, dissolved oxygen is reduced on the cathode in a large potential range:



The generation of hydroxyl ions (Eq.IV.2-1 and Eq.IV.2-2) disturbs the calco-carbonic equilibrium of the solution with an increasing pH at the cathode surface. Hydrocarbonate ions (HCO₃⁻) are converted to carbonate ions:



Carbonate ions may react with calcium ion to form calcium carbonate on the cathode surface.



The scaling of calcium carbonate was observed during electrochemical water softening [74,75].

In the same way, the precipitation of Mg(OH)₂ happens at the cathodes [76].



To verify this hypothesis, the electrochemical cell was washed with pure water and

then with 0.7 L of H₂SO₄ 0.1M solution. The acidic solution was recirculated in the system for 1 h and the concentration of ions in the solution was measured before and after washing. It appears that the concentrations of Mg²⁺, PO₄³⁻, Ca²⁺ increased in the solution after recirculation. Table VI-16 summarizes the different masses of Mg²⁺, PO₄³⁻, Ca²⁺ and inorganic carbon, the mass loss during 360 min of electrolysis and the mass recovered after 1 hour of recirculation of acidic solution.. It can be observed that there is a good correlation between the increasing mass of Mg²⁺, PO₄³⁻, Ca²⁺ in H₂SO₄ 0.1 M after recirculation and the disappearance of these ions during the electrolysis of NF retentate, except inorganic carbon evolving as CO₂ in acidic solution.

Table VI-16 The different mass of Mg²⁺, PO₄³⁻, Ca²⁺ and inorganic carbon from the beginning and after 360 minutes of electrolysis and the mass of them in the H₂SO₄ 0.1 M solution after 1 h recirculation. Operating conditions: see Fig.IV-66

Mass (mg)	Mass _{t=0}	Mass _{t=360}	(mass) _{t=0} – (mass) _{t=360}	mass washed out
PO ₄ ³⁻	10.8	0	10.8	8.3
Mg ²⁺	8.8	2.7	6.1	7.3
Ca ²⁺	69.8	30.8	39	31.4
Inorganic carbon	62.8	23.3	39.5	-

Even the scaling occurred during the electrolysis, the increasing of cell potential was not observed during the electrolysis. The deposit should be porous and doesn't hinder the electron transfer. However, the long-term effect should be taken care considering the life of electrodes. This phenomenon is well known in the case of water treatment. The good correlation between the disappearance mass of Mg²⁺, PO₄³⁻, Ca²⁺ indicates that recirculation with acidic solution can be an effective method to deal with the scaling on the cell. The regularly recirculation with acidic solution in the electrolysis system can be the proposal strategy to protect the electrode which works in the NF retentate matrix. Another treatment consists to apply regularly a reverse polarity at electrodes to dissolve the scaling deposit.

VI.B.3 Electrolysis of NF concentrate in acid condition

Then the electrolysis was performed in NF retentate after adjusting pH to 3.7 (with H₂SO₄ 0.1M). The COD decay is slightly faster at acidic pH (Annex IV-10). Moreover, it seems that the oxidation of Cl⁻ and formation of ClO⁻ and ClO₄⁻ are more significant in

acid conditions (Annex IV-10). The risk of formation of toxic compounds increases at pH 3, besides ClO_4^- . Considering this point, the conversion of chlorine species during electrolysis of NF retentate in acidic condition should be studied.

The concentration of HCO_3^- in acidic NF retentate (14.0 mg L^{-1} , $\text{pH} = 3.7$) is less important than in the NF retentate (62.8 mg L^{-1} , $\text{pH} = 7.8$) at the beginning of electrolysis, because of the formation of CO_2 from HCO_3^- at lower pH. After electrolysis, only the concentration of HCO_3^- and Mg^{2+} decreases slightly from 14 mg L^{-1} to 0.3 mg L^{-1} and from 10.6 mg L^{-1} to 3.4 mg L^{-1} , respectively. The concentrations of Ca^{2+} and PO_4^{3-} are stable. These results confirm that at $\text{pH} = 3.7$ the problem of scaling for the process is less important.

Table IV-17 Concentrations of Ca^{2+} , Mg^{2+} , PO_4^{3-} and inorganic carbon before and after 360 min electrolysis of 1L NF retentate. $I = 0.3\text{A}$ ($i = 4.34 \text{ mA cm}^{-2}$, $i_{\text{lim}} = 2.25 \text{ mA cm}^{-2}$), $\text{pH} = 3.7$ (with $0.5 \text{ mmol H}_2\text{SO}_4$ addition), flow rate = 366 L h^{-1} , $T = 30 \text{ }^\circ\text{C}$

Concentration (mg L^{-1})	Concentration t = 0	Concentration t = 360 min
Ca^{2+}	71.4	72.1
Mg^{2+}	10.6	3.4
PO_4^{3-}	11.0	11.3
HCO_3^-	14.0	0.3

VI.B.4 Conclusion

The electrooxidation of NF retentate from MBR effluent of hospital wastewater was studied. At the end of electrolysis, the experimental COD decay is faster than the theoretical one, probably due to additional chemical oxidation with electrogenerated oxidants. The targeted pharmaceuticals: ciprofloxacin, cyclophosphamide and ifosfamide are completely removed after electrolysis. The degradation rate of CIP is higher than in the synthetic solution, which are also owing to the additional chemical oxidation by the electrogeneration oxidants. A good removal of TOC and AOX are also observed.

The scaling (in the electrolysis cell) which containing Ca^{2+} , Mg^{2+} , PO_4^{3-} and inorganic carbon is due to the locational increase of pH at cathode. The cell potential did not increase during electrolysis, while considering the lifetime of electrode and long-time effect, the regularly recirculation with acidic solution in the electrolysis system can be the proposal strategy to remove scaling in the electrolysis cell. The electrolysis in acidic

solution shows slightly higher decay rate of COD and the mainly part of scaling can be avoided. However, that more Cl^- is oxidized in the acidic condition and more production of undesired ClO_4^- is the disadvantage factor to carry out electrolysis in acidic condition.

IV. Conclusion

A complete study was performed on the treatment of solutions containing ciprofloxacin by electrooxidation using BDD anode. The influence of operating conditions and the competition between components oxidation in the reactor are studied. Rather than a hindering effect, the presence of ions and common organics in the concentrate can accelerate the degradation of pharmaceuticals. In particular, the formation of organohalogenes due to the presence of chloride can be controlled thanks to the choice of appropriate operating conditions. A model giving the temporal variation of pharmaceuticals concentration is established. One objective is to access to the best compromise between mineralization of pharmaceuticals and energy consumption.

Based on the study in synthetic solution, the electrochemical oxidation shows an excellent elimination of pharmaceuticals and AOX in the NF retentate. The targeted pharmaceuticals: ciprofloxacin, cyclophosphamide and ifosfamide are completely removed after electrolysis. The degradation rate of CIP is higher than in the synthetic solution, due to additional chemical oxidation with electrogenerated oxidants. In the presence of Ca^{2+} , Mg^{2+} , PO_4^{3-} and inorganic carbon, the scaling can be avoid at low pH. . By contrast, at low pH the production of undesired ClO_4^- is more important.

In conclusion, this work has evidenced promising results on the removal of pharmaceuticals by electrochemical process using a BDD anode both in synthetic solutions or real wastewater. The next chapter is devoted to its implementation in the coupling with the nanofiltration.

References

- [1] R. Tenne, K. Patel, K. Hashimoto, A. Fujishima, *An International Journal Devoted to all Aspects of Electrode Kinetics, Interfacial Structure, Properties of Electrolytes, Colloid and Biological Electrochemistry* Efficient electrochemical reduction of nitrate to ammonia using conductive diamond film electrodes, *J. Electroanal. Chem.* 347 (1993) 409–415.
- [2] R.H.O. Montes, M.C. Marra, M.M. Rodrigues, E.M. Richter, R.A.A. Muñoz, *Fast Determination of Ciprofloxacin by Batch Injection Analysis with Amperometric Detection and Capillary Electrophoresis with Capacitively Coupled Contactless Conductivity Detection*, *Electroanalysis*. 26 (2014) 432–438.
- [3] L. Fotouhi, M. Alahyari, *Electrochemical behavior and analytical application of ciprofloxacin using a multi-walled nanotube composite film-glassy carbon electrode*, *Colloids Surf. B Biointerfaces*. 81 (2010) 110–114.
- [4] B.P. Chaplin, *Critical review of electrochemical advanced oxidation processes for*
- [5] C. Flox, E. Brillas, A. Savall, K. Groenen-Serrano, *Kinetic Study of the Electrochemical Mineralization of m-Cresol on a Boron-Doped Diamond Anode*, *Curr. Org. Chem.* 16 (2012) 1960–1966.
- [6] H. Vogt, *Mass-Transfer at Gas Evolving Electrodes with Superposition of Hydrodynamic Flow*, *Electrochimica Acta*. 23 (1978) 203–205.
- [7] E. Weiss, *Etude cinétique de la dégradation électrochimique de composés organiques sur l'anode de diamant dope au bore: application à la dépollution d'effluents aqueux*, *Doctoral thesis, Université Paul Sabatier-Toulouse III, 2006*.
- [8] B. Marselli, *ELECTROCHEMICAL OXYGEN TRANSFER REACTION ON SYNTHETIC BORON-DOPED DIAMOND THIN FILM ELECTRODE*, *Doctoral thesis, Université de Genève, 2004*.
- [9] A.F. Holleman, E. Wiberg, N. Wiberg, *Lehrbuch der anorganischen Chemie*, de Gruyter, 1985.
- [10] D. Griffith, D. Musher, C. Itin, *Urease - Primary Cause of Infection-Induced Urinary Stones*, *Invest. Urol.* 13 (1976) 346–350.
- [11] J.A. Wilsenach, C.A.H. Schuurbijs, M.C.M. van Loosdrecht, *Phosphate and potassium recovery from source separated urine through struvite precipitation*, *Water Res.* 41 (2007) 458–466.
- [12] K.A. Landry, T.H. Boyer, *Diclofenac removal in urine using strong-base anion exchange polymer resins*, *Water Res.* 47 (2013) 6432–6444.
- [13] M. Winker, F. Tettenborn, D. Faika, H. Gulyas, R. Otterpohl, *Comparison of analytical and theoretical pharmaceutical concentrations in human urine in Germany*, *Water Res.* 42 (2008) 3633–3640.

- [14] P. Verlicchi, M. Al Aukidy, A. Galletti, M. Petrovic, D. Barceló, Hospital effluent: Investigation of the concentrations and distribution of pharmaceuticals and environmental risk assessment, *Sci. Total Environ.* 430 (2012) 109–118.
- [15] M. Cataldo Hernández, N. Russo, M. Panizza, P. Spinelli, D. Fino, Electrochemical oxidation of urea in aqueous solutions using a boron-doped thin-film diamond electrode, *Diam. Relat. Mater.* 44 (2014) 109–116.
- [16] J. Chudoba, J. Dalešický, Chemical oxygen demand of some nitrogenous heterocyclic compounds, *Water Res.* 7 (1973) 663–668.
- [17] L. Li, S. Zhang, G. Li, H. Zhao, Determination of chemical oxygen demand of nitrogenous organic compounds in wastewater using synergetic photoelectrocatalytic oxidation effect at TiO₂ nanostructured electrode, *Anal. Chim. Acta.* 754 (2012) 47–53.
- [18] G.V. Buxton, C.L. Greenstock, W.P. Helman, A.B. Ross, Critical Review of rate constants for reactions of hydrated electrons, hydrogen atoms and hydroxyl radicals ($\cdot\text{OH}/\cdot\text{O}^-$ in Aqueous Solution, *J. Phys. Chem. Ref. Data.* 17 (1988) 513–886.
- [19] R.G. Rice, M.E. Browning, R.S.K.E.R. Laboratory, J.E. Group, A.C. Corporation, I.O. Association, Ozone for industrial water and wastewater treatment: a literature survey, Robert S. Kerr Environmental Research Laboratory, Office of Research and Development, U.S. Environmental Protection Agency, 1980.
- [20] M. Winker, B. Vinnerås, A. Muskolus, U. Arnold, J. Clemens, Fertiliser products from new sanitation systems: Their potential values and risks, *Bioresour. Technol.* 100 (2009) 4090–4096.
- [21] B. Krajewska, R. van Eldik, M. Brindell, Temperature- and pressure-dependent stopped-flow kinetic studies of jack bean urease. Implications for the catalytic mechanism, *JBIC J. Biol. Inorg. Chem.* 17 (2012) 1123–1134.
- [22] P. Calza, E. Pelizzetti, C. Minero, The fate of organic nitrogen in photocatalysis: an overview, *J. Appl. Electrochem.* 35 (2005) 665–673.
- [23] V. Maurino, C. Minero, E. Pelizzetti, P. Piccinini, N. Serpone, H. Hidaka, The fate of organic nitrogen under photocatalytic conditions: degradation of nitrophenols and aminophenols on irradiated TiO₂, *J. Photochem. Photobiol. Chem.* 109 (1997) 171–176.
- [24] E. Pelizzetti, P. Calza, G. Mariella, V. Maurino, C. Minero, H. Hidaka, Different photocatalytic fate of amido nitrogen in formamide and urea, *Chem. Commun.* (2004) 1504–1505.
- [25] P. Piccinini, C. Minero, M. Vincenti, E. Pelizzetti, Photocatalytic mineralization of nitrogen-containing benzene derivatives, *Catal. Today.* 39 (1997) 187–195.
- [26] C. Karuwan, T. Mantim, P. Chaisuwan, P. Wilairat, K. Grudpan, P. Jittangprasert, et al., Pulsed Amperometry for Anti-fouling of Boron-doped Diamond in Electroanalysis of β -Agonists: Application to Flow Injection for Pharmaceutical Analysis, *Sensors.* 6 (2006) 1837–1850.

- [27] J. Boudreau, D. Bejan, S. Li, N.J. Bunce, Competition between Electrochemical Advanced Oxidation and Electrochemical Hypochlorination of Sulfamethoxazole at a Boron-Doped Diamond Anode, *Ind. Eng. Chem. Res.* 49 (2010) 2537–2542.
- [28] S. Griese, D.K. Kampouris, R.O. Kadara, C.E. Banks, The underlying electrode causes the reported “electro-catalysis” observed at C60-modified glassy carbon electrodes in the case of N-(4-hydroxyphenyl)ethanamide and salbutamol, *Electrochimica Acta.* 53 (2008) 5885–5890.
- [29] J.-F. Zhi, H.-B. Wang, T. Nakashima, T.N. Rao, A. Fujishima, Electrochemical Incineration of Organic Pollutants on Boron-Doped Diamond Electrode. Evidence for Direct Electrochemical Oxidation Pathway, *J. Phys. Chem. B.* 107 (2003) 13389–13395.
- [30] R. Goyal, A. Srivastava, Electrochemical Oxidation of Sulfamethoxazole at Pyrolytic-Graphite Electrode - an Example of Free-Radical Dimerization, *Indian J. Chem. Sect. -Inorg. Bio-Inorg. Phys. Theor. Anal. Chem.* 29 (1990) 635–638.
- [31] R.G. Rice, M.E. Browning, R.S.K.E.R. Laboratory, J.E. Group, A.C. Corporation, I.O. Association, Ozone for industrial water and wastewater treatment: a literature survey, Robert S. Kerr Environmental Research Laboratory, Office of Research and Development, U.S. Environmental Protection Agency, 1980.
- [32] C. Comninellis, G. Chen, eds., *Electrochemistry for the Environment*, Springer New York, New York, NY, 2010.
- [33] M. Panizza, G. Cerisola, Direct And Mediated Anodic Oxidation of Organic Pollutants, *Chem. Rev.* 109 (2009) 6541–6569.
- [34] M. Panizza, G. Cerisola, Application of diamond electrodes to electrochemical processes, *Electrochimica Acta.* 51 (2005) 191–199.
- [35] K.G. Serrano, Wastewater Treatment by Electrogeneration of Strong Oxidants Using Borondoped Diamond (BDD), in: G. Kreysa, K. Ota, R.F. Savinell (Eds.), *Encycl. Appl. Electrochem.*, Springer New York, 2014: pp. 2126–2132.
- [36] Ionization Constants of Inorganic Monoprotic Acids, Chemistry.msu.edu.
- [37] M. Murugananthan, S.S. Latha, G. Bhaskar Raju, S. Yoshihara, Anodic oxidation of ketoprofen—An anti-inflammatory drug using boron doped diamond and platinum electrodes, *J. Hazard. Mater.* 180 (2010) 753–758.
- [38] P. Wardman, Reduction Potentials of One-Electron Couples Involving Free Radicals in Aqueous Solution, *J. Phys. Chem. Ref. Data.* 18 (1989) 1637–1755.
- [39] R.L. Siegrist, M. Crimi, T.J. Simpkin, *In Situ Chemical Oxidation for Groundwater Remediation*, Springer Science & Business Media, 2011.
- [40] H. Lutze, *Sulfate radical based oxidation in water treatment*, Universität Duisburg-Essen, 2013.
- [41] K. Serrano, P.A. Michaud, C. Comninellis, A. Savall, Electrochemical preparation of peroxodisulfuric acid using boron doped diamond thin film electrodes, *Electrochimica Acta.* 48 (2002) 431–436.

- [42] I.M. Kolthoff, I.K. Miller, The Chemistry of Persulfate. I. The Kinetics and Mechanism of the Decomposition of the Persulfate Ion in Aqueous Medium, *J. Am. Chem. Soc.* 73 (1951) 3055–3059.
- [43] M.M. Ahmed, S. Barbati, P. Doumenq, S. Chiron, Sulfate radical anion oxidation of diclofenac and sulfamethoxazole for water decontamination, *Chem. Eng. J.* 197 (2012) 440–447.
- [44] P. Neta, V. Madhavan, H. Zemel, R.W. Fessenden, Rate constants and mechanism of reaction of sulfate radical anion with aromatic compounds, *J. Am. Chem. Soc.* 99 (1977) 163–164.
- [45] R. Zhang, P. Sun, T.H. Boyer, L. Zhao, C.-H. Huang, Degradation of Pharmaceuticals and Metabolite in Synthetic Human Urine by UV, UV/H₂O₂, and UV/PDS, *Environ. Sci. Technol.* (2015).
- [46] M. Mahdi-Ahmed, S. Chiron, Ciprofloxacin oxidation by UV-C activated peroxymonosulfate in wastewater, *J. Hazard. Mater.* 265 (2014) 41–46.
- [47] C. Comninellis, A. Nerini, Anodic oxidation of phenol in the presence of NaCl for wastewater treatment, *J. Appl. Electrochem.* 25 (1995) 23–28.
- [48] M. Murugananthan, G. Bhaskar Raju, S. Prabhakar, Removal of tannins and polyhydroxy phenols by electro-chemical techniques, *J. Chem. Technol. Biotechnol.* 80 (2005) 1188–1197.
- [49] G.R.P. Malpass, D.W. Miwa, S.A.S. Machado, P. Olivi, A.J. Motheo, Oxidation of the pesticide atrazine at DSA® electrodes, *J. Hazard. Mater.* 137 (2006) 565–572.
- [50] K. Viswanathan, B.V. Tilak, Chemical, Electrochemical, and Technological Aspects of Sodium Chlorate Manufacture, *J. Electrochem. Soc.* 131 (1984) 1551–1559.
- [51] M.S. Siddiqui, Chlorine-ozone interactions: Formation of chlorate, *Water Res.* 30 (1996) 2160–2170.
- [52] L.R. Czarnetzki, L.J.J. Janssen, Formation of hypochlorite, chlorate and oxygen during NaCl electrolysis from alkaline solutions at an RuO₂/TiO₂ anode, *J. Appl. Electrochem.* 22 (1992) 315–324.
- [53] Y.J. Jung, K.W. Baek, B.S. Oh, J.-W. Kang, An investigation of the formation of chlorate and perchlorate during electrolysis using Pt/Ti electrodes: The effects of pH and reactive oxygen species and the results of kinetic studies, *Water Res.* 44 (2010) 5345–5355.
- [54] A.M. Polcaro, A. Vacca, M. Mascia, S. Palmas, J.R. Ruiz, Electrochemical treatment of waters with BDD anodes: kinetics of the reactions involving chlorides, *J. Appl. Electrochem.* 39 (2009) 2083–2092.
- [55] M.E.H. Bergmann, J. Rollin, Product and by-product formation in laboratory studies on disinfection electrolysis of water using boron-doped diamond anodes, *Catal. Today.* 124 (2007) 198–203.
- [56] O. Azizi, D. Hubler, G. Schrader, J. Farrell, B.P. Chaplin, Mechanism of Perchlorate Formation on Boron-Doped Diamond Film Anodes, *Environ. Sci. Technol.* 45 (2011) 10582–10590.

- [57] E.T. Urbansky, M.R. Schock, Issues in managing the risks associated with perchlorate in drinking water, *J. Environ. Manage.* 56 (1999) 79–95.
- [58] S. Ferro, A.D. Battisti, I. Duo, C. Comninellis, W. Haenni, A. Perret, Chlorine Evolution at Highly Boron-Doped Diamond Electrodes, *J. Electrochem. Soc.* 147 (2000) 2614–2619.
- [59] Y. Yang, J.J. Pignatello, J. Ma, W.A. Mitch, Comparison of Halide Impacts on the Efficiency of Contaminant Degradation by Sulfate and Hydroxyl Radical-Based Advanced Oxidation Processes (AOPs), *Environ. Sci. Technol.* 48 (2014) 2344–2351.
- [60] M. Murugananthan, S. Yoshihara, T. Rakuma, N. Uehara, T. Shirakashi, Electrochemical degradation of 17 β -estradiol (E2) at boron-doped diamond (Si/BDD) thin film electrode, *Electrochimica Acta.* 52 (2007) 3242–3249.
- [61] C. do N. Brito, D.M. de Araújo, C.A. Martínez-Huitle, M.A. Rodrigo, Understanding active chlorine species production using boron doped diamond films with lower and higher sp³/sp² ratio, *Electrochem. Commun.* 55 (2015) 34–38.
- [62] T.N. Das, Reactivity and Role of SO₅^{•-} Radical in Aqueous Medium Chain Oxidation of Sulfite to Sulfate and Atmospheric Sulfuric Acid Generation, *J. Phys. Chem. A.* 105 (2001) 9142–9155.
- [63] M. Murugananthan, S. Yoshihara, T. Rakuma, T. Shirakashi, Mineralization of bisphenol A (BPA) by anodic oxidation with boron-doped diamond (BDD) electrode, *J. Hazard. Mater.* 154 (2008) 213–220.
- [64] M. Murugananthan, S.S. Latha, G. Bhaskar Raju, S. Yoshihara, Role of electrolyte on anodic mineralization of atenolol at boron doped diamond and Pt electrodes, *Sep. Purif. Technol.* 79 (2011) 56–62.
- [65] H. Li, J. Ni, Electrogenation of disinfection byproducts at a boron-doped diamond anode with resorcinol as a model substance, *Electrochimica Acta.* 69 (2012) 268–274.
- [66] R. Castagna, J.P. Eiserich, M.S. Budamagunta, P. Stipa, C.E. Cross, E. Proietti, et al., Hydroxyl radical from the reaction between hypochlorite and hydrogen peroxide, *Atmos. Environ.* 42 (2008) 6551–6554.
- [67] A.Y. Bagastyo, D.J. Batstone, K. Rabaey, J. Radjenovic, Electrochemical oxidation of electro dialysed reverse osmosis concentrate on Ti/Pt–IrO₂, Ti/SnO₂–Sb and boron-doped diamond electrodes, *Water Res.* 47 (2013) 242–250.
- [68] T. An, H. Yang, G. Li, W. Song, W.J. Cooper, X. Nie, Kinetics and mechanism of advanced oxidation processes (AOPs) in degradation of ciprofloxacin in water, *Appl. Catal. B Environ.* 94 (2010) 288–294.
- [69] A. Kapałka, G. Fóti, C. Comninellis, Kinetic modelling of the electrochemical mineralization of organic pollutants for wastewater treatment, *J. Appl. Electrochem.* 38 (2007) 7–16.
- [70] G. Scholes, J. Weiss, Oxygen Effects and Formation of Peroxides in Aqueous Solutions, *Radiat. Res. Suppl.* 1 (1959) 177–189.
- [71] I. Quesada, Y. Gonzalez, S. Schetrite, H. Budzinski, K. Le Menach, O. Lorain, et al., PANACÉE : évaluation du fonctionnement d'un bioréacteur à membranes immergées traitant des effluents hospitaliers d'oncologie, *Rev. Sci. Eau.* 28 (2015) 1.

- [72] A. Anglada, A. Urtiaga, I. Ortiz, Pilot Scale Performance of the Electro-Oxidation of Landfill Leachate at Boron-Doped Diamond Anodes, *Environ. Sci. Technol.* 43 (2009) 2035–2040.
- [73] K. Van Hege, M. Verhaege, W. Verstraete, Electro-oxidative abatement of low-salinity reverse osmosis membrane concentrates, *Water Res.* 38 (2004) 1550-1558.
- [74] A. Bannoud, The electrochemical way of removing the hardness of water, *Desalination.* 93 (1993) 545–555.
- [75] C. Gabrielli, G. Maurin, H. Francy-Chausson, P. Thery, T.T.M. Tran, M. Tlili, Electrochemical water softening: principle and application, *Desalination.* 201 (2006) 150–163.
- [76] A. Kraft, M. Stadelmann, M. Blaschke, D. Kreysig, B. Sandt, F. Schröder, et al., Electrochemical water disinfection Part I: Hypochlorite production from very dilute chloride solutions, *J. Appl. Electrochem.* 29 (1999) 859–866.

Chapter V

**Treatment efficiency and toxicity removal
of combining EO and NF process**

Contents

V.1 Working diagram	215
V.2 Removal of toxicity by combining process	217
V.3 Energy consumptions	221
V.4 Discussion and conclusion	222
References.....	224

This chapter is devoted to the performances and efficiency of the coupling NF and EO process. The process efficiency will be assessed in terms of removal of targeted pharmaceuticals, final toxicity and energy consumption. The operating conditions for each process are chosen on the basis of the studies carried out in Chapters III and IV.

V.1 Working diagram

Hospital wastewater after MBR treatment is firstly treated by NF and the obtained concentrate corresponding to a volume reduction factor of 5 is treated by electrochemical oxidation. The permeate analysis allows to qualify the selectivity of the process when the productivity is evaluated through the permeate flux.

Regarding the productivity, a working diagram can be established from the results obtained in chapter III.B. This diagram represented in Fig V-1 plots permeate fluxes vs applied pressures. Different zones are defined which give the productivity of the process and the related fouling types depending on the operating conditions of the filtration.

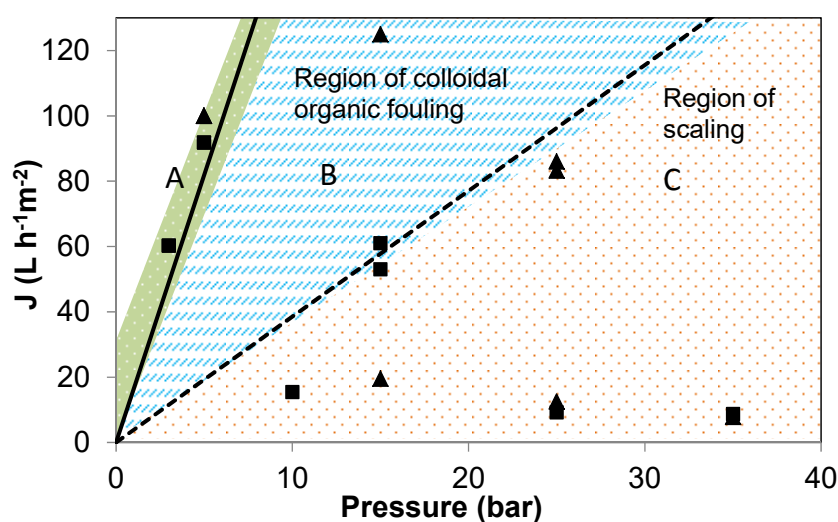


Fig.V-1 NF working diagram between applied pressures and permeate fluxes. Full line is the average pure water permeability; dashed line is the threshold permeability.

In Region A the applied pressure is lower than the critical one, thus an increasing applied pressure results in higher productivity.

For pressures higher than the critical value, the flux is controlled by fouling mechanism: Region B: colloidal silica and organics fouling or Region C combination of organics fouling and scaling. The study in Chapter III.B demonstrates that the occurrence of scaling is highly related to the pH of the MBR effluent matrix, associated to the effect of salts concentration. When the pH of filtrated solution is higher than 7.2, fouling involves a scaling phenomenon. Unfortunately, the pH of MBR effluents in most cases is alkaline as

this corresponds to optimal conditions for bacterial viability and oxidation efficiency [1]. Consequently, without adjusting pH, the working diagram of nanofiltration is limited to regions A and C.

The impact of fouling types and water matrix are discussed in chapter III.C. Fig.V-2 summarizes the rejection of targeted pharmaceuticals in working each region of NF. The complete removal (in the range of 94 % to 99 %) is reached in region C; while in region A, lower rejection is observed. Certainly, considering the variability of MBR effluent composition, there are some intermediate cases with an inhomogeneous scaling. These intermediate cases lead to an intermediate rejection rate (lower than in the case of homogenous scaling and higher than in unfouled conditions).

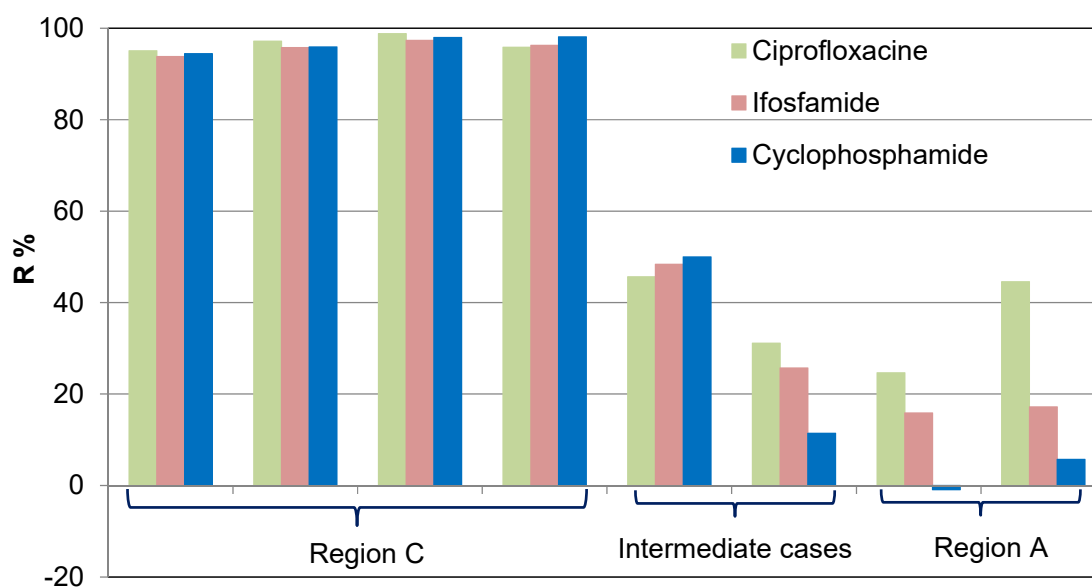


Fig.V-2 Rejection rate of 3 targeted pharmaceuticals, R, in different working regions of NF

Thus, salts, organics and pharmaceuticals concentrations in NF retentate depends on the initial MBR effluent composition and the NF working regions. This concentrate composition can impact the performances of the electrochemical oxidation. Two extreme cases will be studied for the coupling: regions A and C with a special focus on region C.

In the case of the maximum of selectivity, electrolysis was carried out on NF retentate coming from region C. The results shown in chapter IV.B highlighted a complete disappearance of CIP in 80 minutes (operating conditions: BDD anode, area 69 cm², I = 0.3 A, I_{lim} = 0.18 A). Duration of 6 h is needed to obtain an EO effluent free from targeted pharmaceuticals with a nearly total disappearance of TOC (92.5 %).

A specific study including ecotoxicity measurements is developed in the next paragraph to qualify the performances of the coupling process.

V.2 Removal of toxicity by combining process

The toxicity in terms of androgenic, estrogenic and pregnane X receptor (PXR)-like (xenobiotic response) activity was measured at the inlet and outlet of each process (NF retentate and permeate were collected after a volume reduction factor of 5).

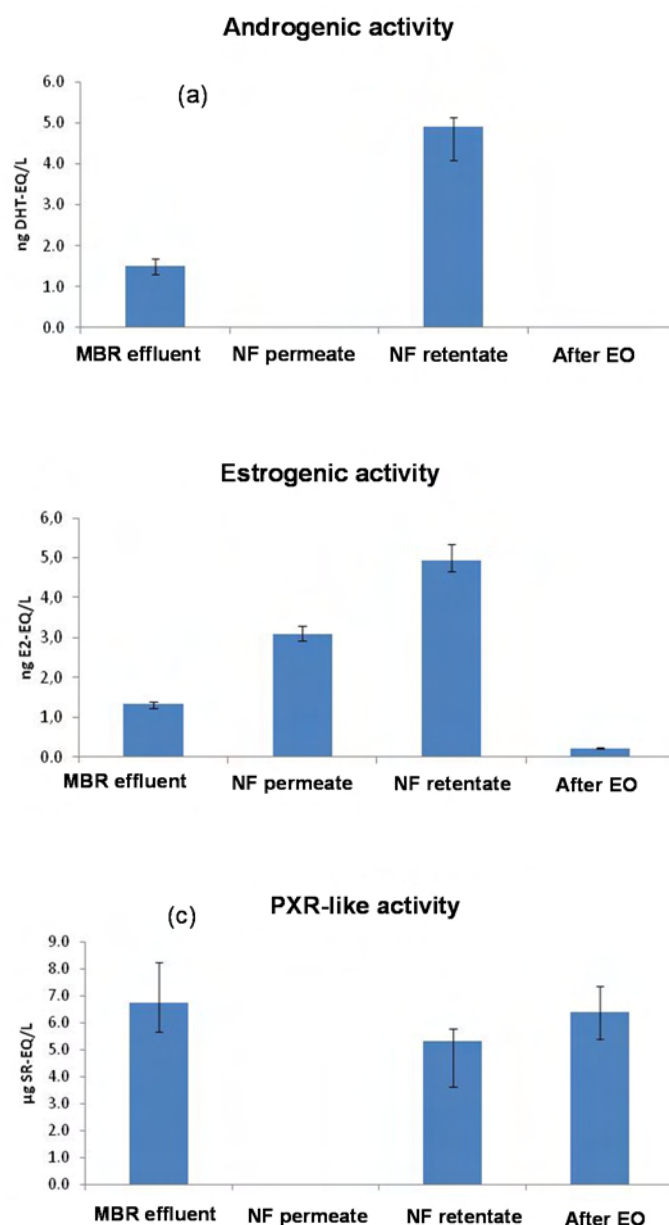


Fig.V-3 Biological toxic equivalents in terms of androgenic (a) estrogenic (b) and PXR-like activity (c) of MBR effluent, NF permeate, NF retentate and after EO.

Regarding the results on androgenic activity, the combining process shows an excellent efficiency; the effluents from both NF and EO are free of toxicity in spite of an important biological toxic equivalent in the NF retentate.

Regarding the results on estrogenic activity, the removal by NF process of toxic

compounds is not efficient. Nevertheless, EO exhibits a good performance to eliminate this kind of toxicity. Considering that the NF permeate could still pose the threats to the environment, in this case the choice of the membrane should be considered to reach a better rejection of compounds responsible for this toxicity.

In the case of PXR-like activity, NF permeate doesn't exhibit any toxicity, while the electrochemical oxidation increases the toxicity of the NF retentate. This case needs a special attention: in section IV.A.4.1.2, the possible formation of ClO_4^- and AOX during electrochemical oxidation has been evidenced. AOX compounds enhance the biological toxic equivalents in terms of PXR-like activity [1-2]. In the study of Chapter IV it was evidenced and underlined that at high current intensity the amount of the electro generated halogen organic compounds can be very important. To check this result, the PXR-like activity was measured after EO at lower current intensity ($I=0.2\text{ A}$ instead of 0.3 A) with various duration of treatment.

In parallel, regarding to the possible impacts of water matrix, the electrooxidation of NF concentrate obtained after filtration in Region A is studied. Results are shown in Fig.V-4.

Regarding the results obtained with NF retentate of region C, in comparison with 0.3 A , the decrease of toxicity in PXR-like activity is observed at 0.2 A . It seems that at an appropriate applied current density (close to the limiting current), the electrochemical oxidation shows a good performance for the removal of this kind of toxic compounds.

In working Region A, the NF process shows weakness in the selectivity, a non-negligible toxicity in terms of PXR-like activity is evidenced in the permeate. Nevertheless, the PXR-like activity in NF retentate decreases significantly after EO, even at higher current intensity (0.3 A).

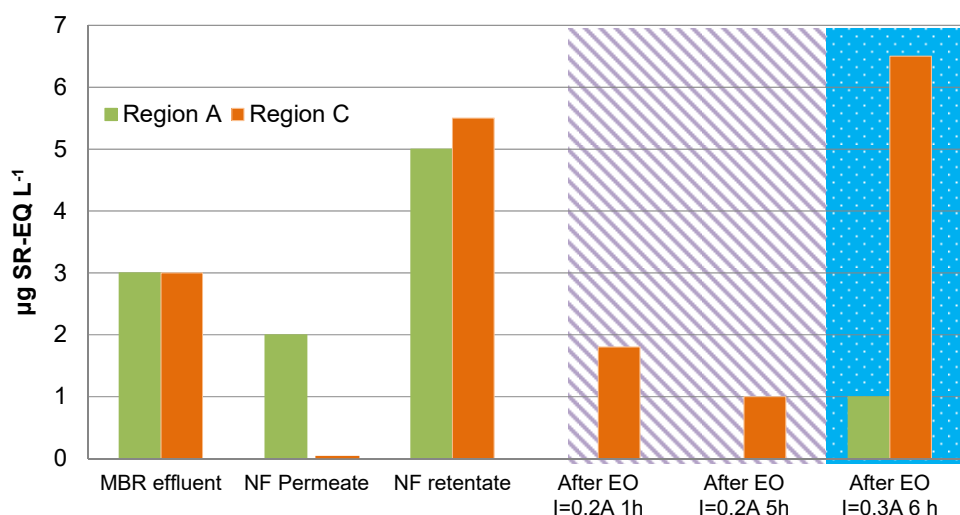


Fig.V-4 Biological toxic equivalents in terms of PXR-like activity of MBR effluent, NF permeate, NF retentate and after EO for two NF working conditions: regions A and C.

The comparison of results from EO treatment of NF retentate of regions A and C at

0.3 A evidences a great difference. This difference can be attributed to the composition of the concentrate. Table V-1 presents the concentrations of Cl^- and ClO_4^- in NF retentate and EO effluent. The formation of ClO_4^- is likely independent on the chloride concentration in this range, but is highly related to the applied current intensity as it was shown previously. Moreover, the concentration of ClO_4^- is the same in the EO effluents after 6 h of EO at 0.3 A for both NF retentate. Because the concentration of perchlorate is the same and the PXR-like activity is 6 times higher in the region C, one can conclude that in this range of concentration there is no correlation between the presence of ClO_4^- and the response in PXR-like activity.

Table V-1 Concentration of Cl^- in the NF retentate and concentration of ClO_4^- after EO

Concentration (mg L^{-1})	$[\text{Cl}^-]$ in NF retentate	$[\text{ClO}_4^-]$ T = 1 h	$[\text{ClO}_4^-]$ T = 5 h	$[\text{ClO}_4^-]$ T = 6 h
Region A, I = 0.3 A	47.2 ± 0.7	<LD	2.6 ± 1	3.8 ± 1
Region C, I = 0.2 A	67.8 ± 1	<LD	<LD	
Region C, I = 0.3 A	68.3 ± 1	<LD	2.2 ± 1	3.4 ± 1

Fig.V-5 presents the measurements of AOX in NF concentrate and after EO treatment at various current intensities and durations. The concentration of AOX present in the retentate decreases after EO in all conditions. Concentration of AOX after 6 h of EO at 0.3 A is higher when the electrooxidation is performed with the NF retentate from region C than from region A, which is in accordance with the tendency shown with the measurements of PXR-like activity.

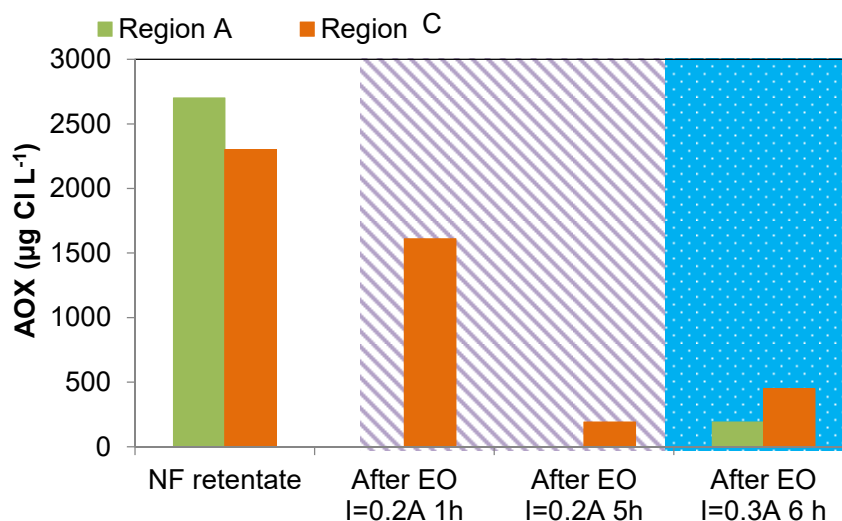


Fig.V-5 Concentration of AOX in various NF concentrate and EO effluent

To explain that the PXR-like activity after EO at 0.3A is very high although the concentration of AOX is lower in the EO effluent than the NF retentate, one can make the following assumption: it is possible that the toxicity depends on the AOX forms, some compounds which are more toxic are produced at this current density range.

Lower toxicity and AOX concentration after 6 h of EO at 0.3 A is obtained when the Cl⁻ concentration is lower (retentate from region A).

The production of AOX depends on the applied current intensity during the electrochemical treatment of NF retentate from region C, higher removal efficiency is obtained at lower applied current intensity (0.2 A) after 5 hours of EO. As discussed above, it is possible to form some toxic by-products in the case of electrolysis at higher applied current intensity (0.3A) during 6 hours of electrolysis. Pérez et al. [2] observed that more trihalomethanes were formed at higher current and that the concentration of them increase during electrooxidation of reverse osmosis concentrates generated in tertiary water treatment using BDD anode (surface area of 70 cm²). More precisely 200, 80, 50 µg L⁻¹ of trihalomethanes were formed at current densities of 200,100 and 50 A m⁻² after 6 hours of electrooxidation, respectively.

Table V-2 shows almost the same removal of target pharmaceuticals, TOC and COD using two applied current intensities, both higher than the limiting current density (calculated from COD, Eq.I-12). This result evidences that the lower current intensity close to I_{lim} can be the best choice to remove the targeted pharmaceuticals, TOC and COD. Moreover it reduces the risk of formation of ClO₄⁻ and toxic by-products.

Table V-2 Removal of CIP, TOC, COD and electrical charge at two current intensities for electrooxidation of NF concentrate in Region C

Applied current I (A)	EO time (min)	I_{lim} (A)	Electrical charge (Ah L ⁻¹)	CIP (mg L ⁻¹)	COD (mg L ⁻¹)	TOC (mg L ⁻¹)
0.2	300	0.18	1	100%	100%	91.0 %
0.3	300	0.18	1.8	100%	100%	91.5%

The low concentration of Cl⁻ in the NF retentate obtained in Region A allows avoiding the formation of toxic by-products during the electrochemical process. Even if the retentate from Region C contains more chlorides ions than on Region A, it is possible by controlling and using the appropriate current intensity to reduce the formation of toxic by-products.

As a conclusion, the coupling NF and EO process shows excellent elimination of toxicity in terms of androgenic and PXR-like activity in appropriate operating conditions. Regarding the androgenic activity, results suggest that the selected membrane is not adapted to remove it, another NF membrane type could be considered to improve the efficiency of the process.

V.3 Energy consumptions

Fig.IV-6 presents the energy consumption for the removal of the targeted pharmaceutical (CIP), COD and AOX during electrolysis of NF concentrate in working region A and C. In all cases the targeted pharmaceutical (CIP) has totally disappeared. It can be observed that the lowest efficiency of CIP removal is obtained during electrooxidation of NF retentate obtained in region A: removal of 48 μg of CIP in 1L solution needs 2.8 Watts. In contrast, the same energy consumption used for the electrochemical treatment of NF retentate from region C can remove around 70 μg of CIP in 1L.

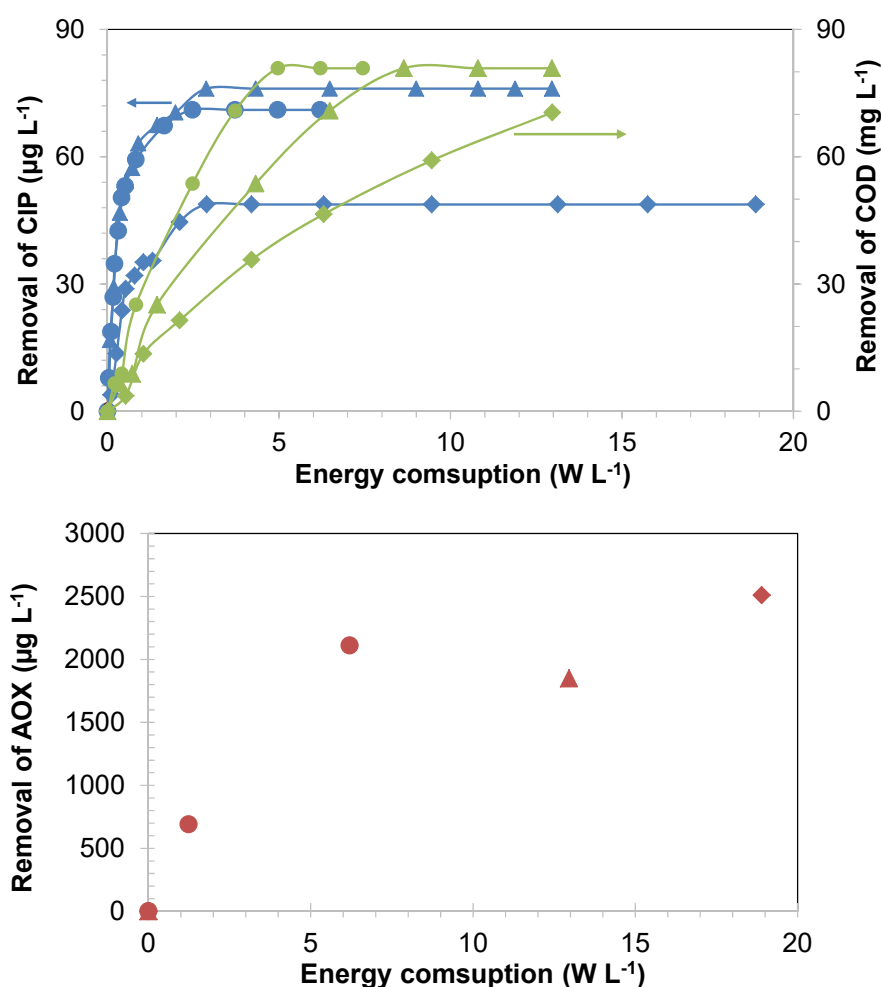


Fig.V-6 Removal of CIP (blue), COD (green) and AOX (red) in the NF retentate obtained in \blacklozenge Region A at $I = 0.3 \text{ A}$, \blacktriangle Region C, at $I = 0.3 \text{ A}$ and \bullet Region C at 0.2 A vs. energy consumption.

Due to the low salt rejection in region A, the conductivity of NF retentate is lower, which increases the cell voltage. Moreover, the low rejection of pharmaceuticals in Region A leads to high concentration of pharmaceuticals in permeate.

Thanks to the higher conductivity of NF retentate in region C, the AOX and COD removal

consumes less energy during electrooxidation. Expectedly, the one with lower applied current can reach best removal with lower energy consumption. In this case, 80 mg of COD can be removed with 4.4 W in 1 L solution.

V.4 Discussion and conclusion

According to the working diagram of NF, in the working region A, it is possible to reach the high NF productivity of $100 \text{ L h}^{-1} \text{ m}^{-2}$ with a low concentration of Cl^- in the retentate for avoiding the formation of organochlorides during the EO process. However, in these conditions the quality of the permeate is unsatisfactory in terms of toxicity and pose threats for the environment. In addition, because the conductivity of retentate is low, it results in a low energy efficiency in the following EO step. Thus, for these reasons, the region A doesn't correspond to the best operating conditions for the coupling process. The working region C can then be the best compromise.

The study carried out on chapter IV evidences that the applied current intensity is the key factor. When the applied current is close to the limiting current intensity, the efficiency is high and the concentration of organochlorides which can be formed during the electrooxidation of organics in presence of chloride ions is negligible. Nevertheless, during EO process the depletion of organics concentration leads to increase of $\frac{I}{I_{lim}}$. One solution is to adapt the value of the applied current intensity during the process. Previous study in chapter IV has shown that in all the cases the experimental values were in a good agreement with the COD model.

Another possibility is to adapt the geometry of electrochemical cell (by increasing the ratio electrode surface/reactor volume) to insert it in a continuous mode combined with feed-and-bleed continuous NF process and to control the range of COD concentration at the inlet of the electrochemical reactor.

To summarize, the best compromise for the NF operating conditions without adjusting pH, taking into account the toxicity criteria and energy consumption of the EO step, is situated in the working region C. In the case of wastewater containing chlorides, it will be necessary and safe to use an appropriate current intensity for EO.

After optimization, MBR effluent (7 L) which contents $8\text{-}36 \mu\text{g L}^{-1}$ of target pharmaceuticals and $3 \mu\text{g SR-EQ L}^{-1}$ of xenobiotic response was treated by coupling process. NF retentate was conducted in region C and the EO was performed at 0.2 A for 300 min. The flow diagram is shown in Fig.V-7. The coupling of NF and EO shows excellent efficiency for removal of target pharmaceuticals and toxicity. Xenobiotic response was completely removed by NF and the removal rate of pharmaceuticals was superior to 88 %. Xenobiotic response concentration of target pharmaceuticals which were concentrated in NF retentate were eliminated by EO. The final solution of EO was without pharmaceuticals and the toxicity decreased drastically. It can be believed that after

treatment, high quality water obtained by NF permeate and EO effluent can be discharged without detrimental effect on environment.

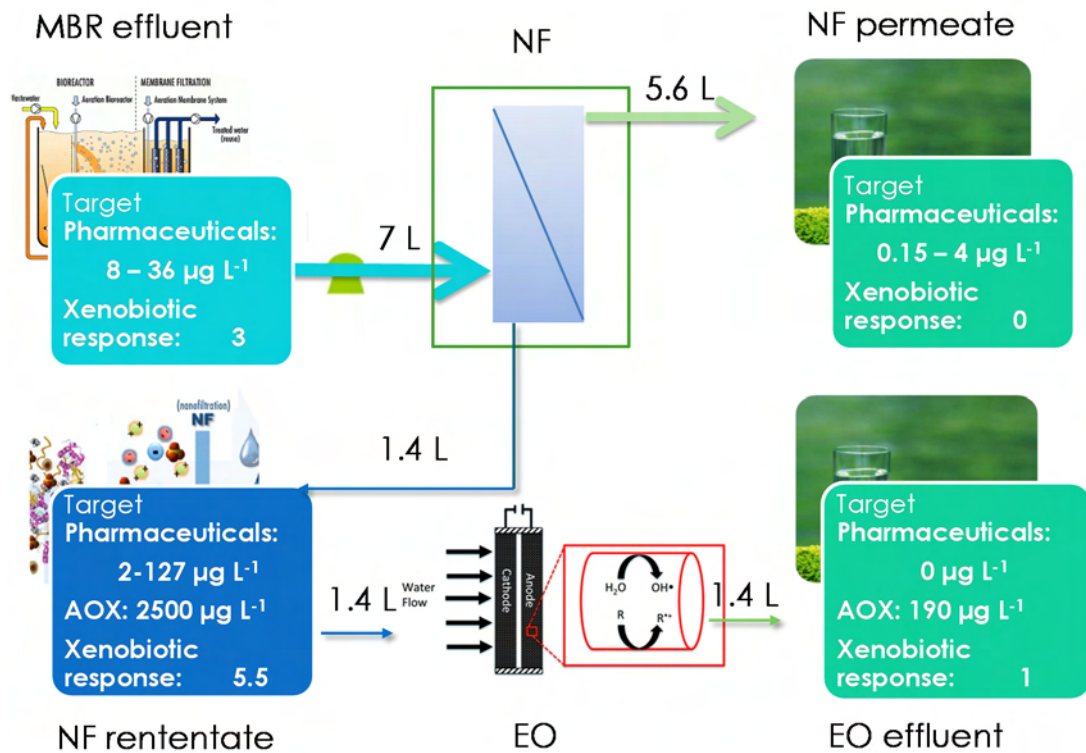


Fig.V-7 Example of tertiary treatment combining nanofiltration and electrochemical oxidation for elimination of pharmaceuticals and toxicity from MBR effluent, NF in region C, EO duration 300 min, $I = 0.2 \text{ A}$ ($I_{\text{lim}} = 1.8 \text{ A}$), $T = 30 \text{ }^\circ\text{C}$, flow rate = 366 L h^{-1} .

The comparison of the quality of effluent after treatment by the coupling process (NF permeate and after EO) with the irrigation water standards confirms the possibility of reuse of the treated water (See Annex V -1). Other reuse types can also be considered.

References

- [1] S. Judd, The status of membrane bioreactor technology, *Trends Biotechnol.* 26 (2008) 109-116.
- [2] G. Pérez, A.R. Fernández-Alba, A.M. Urtiaga, I. Ortiz, Electro-oxidation of reverse osmosis concentrates generated in tertiary water treatment, *Water Res.* 44 (2010) 2763-2772.

Conclusions

Conclusions

Numerous studies have demonstrated the occurrence of pharmaceuticals in the aquatic environment. The reason is these molecules are incompletely eliminated in wastewater treatment plants even if a membrane bioreactor (MBR) process is used. Considering their potential long-term toxicity towards exposed organisms, tertiary treatments are required to prevent the release of pharmaceuticals in aquatic ecosystems. Nanofiltration and electrochemical oxidation were proved to be promising processes for the separation and elimination of micropollutants. A tertiary treatment combining these two processes is proposed in this Thesis for the elimination of pharmaceuticals in hospital wastewaters after MBR.

The objective of this thesis was to investigate main parameters which influence the productivity and selectivity during NF in one hand, and the efficiency and safety of EO in the other hand, in order to be able to propose appropriate operating conditions to enhance the coupling efficiency in an economically viable and environmentally sustainable way.

NF and EO process were first studied separately in order to determine the effect of operating conditions and matrix on both processes.

In the first part, the critical flux and limiting flux which relate to the NF productivity were studied. The square wave filtration method, developed in previous studies to determine the critical flux during the filtration of a synthetic solution, has been implemented in the present work to estimate the critical flux during NF of MBR effluent matrix. The ideal productivity could be obtained with an initial flux lower than the critical flux to avoid irreversible fouling. For fluxes beyond this critical value, two limiting fluxes were observed. One of them was around the estimated critical flux while the other was well below due to the presence of scaling. Due to the low productivity when scaling occurs, a method predicting scaling by estimation of a threshold permeability before scaling was investigated.

A working diagram reporting the permeate flux versus applied pressure has been established and divided in three regions: un-fouling region, region of colloidal silica and organics fouling and region of scaling. This working diagram allows identifying the fouling type according to flux behaviors versus the pressure. Thanks to a set of independent filtrations using real water matrix with variabilities, effects of the matrix on the fouling mechanisms were studied. The appearance of either limiting flux values mentioned before was demonstrated to be dependent of water matrix characteristics, mainly organics and salts concentrations and pH. Maintaining the pH of filtrated solution at 6 is proposed and verified to be a solution to avoid the scaling.

In a second step, rejections of salts and pharmaceuticals were studied to determine the

influence of the water matrix and fouling types on the selectivity, beside other significant factors such as membrane material and structure and pharmaceuticals properties. With the unfouled membrane or in presence of a moderate organics fouling, rejection of ions and pharmaceuticals is predominantly governed by electrostatic repulsions and hydrophobic interactions respectively. With membrane fouled by scaling, the rejection of both ions and pharmaceuticals is governed by size exclusion leading to the excellent rate of removal.

In the second part, the electrochemical oxidation of pharmaceuticals was studied in synthetic solutions and NF retentate. The first aim was to determine how operating conditions and simultaneous presence of organics and inorganics affect the mineralization efficiency of pharmaceuticals with a specific focus on the formation of by-products in the presence of chloride ions. The strategy proposed was to, first, study the process using a synthetic solution to simplify the number of parameters, and then after that, study the process under real matrix condition (NF retentate).

Thus, a complete study was performed on the treatment of synthetic solutions containing ciprofloxacin by electrochemical oxidation using BDD anode. At low current density ($I < I_{lim}^0$), the amount of intermediates decreases sharply with increasing the current density; while in the case of $I > I_{lim}^0$, the total amount of intermediates doesn't change significantly. Using a current intensity slightly higher than limiting current can be the best compromise between the mineralization rate and energy consumption.

Salts present in the wastewater can play a significant role in the process. Since, strong oxidants ($SO_4^{\bullet-}$, ClO^- and ClO^{\bullet}) can be generated at the anode and react chemically with the organic matter. On the other hand, some undesired products can be generated by reaction with hydroxyl radicals such as ClO_4^- and AOX in the presence of Cl^- . The generation of ClO_4^- and AOX is facilitated at very high current density. The study on the influence of operating conditions evidenced that the current density must be chosen carefully.

Rather than a hindering effect, the presence of urea even at higher concentration can accelerate the degradation of pharmaceuticals. In the case of synthetic solutions which contain two pharmaceuticals, the interaction and competition can induce different impacts on the degradation of pharmaceuticals.

A model allowing predicting the variation of organic concentrations was developed and effects of salts and electrogenerated oxygen bubbles are also taken into account.

Considering the electrochemical oxidation of NF retentate in MBR effluent matrix, targeted pharmaceuticals were completely removed after electrolysis. The degradation rate of CIP was higher than in the synthetic solution, probably due to additional chemical oxidation with electrogeneration oxidants. A good removal of TOC, COD and AOX were also observed. The scaling (in the electrolysis cell) was observed due to the increase of the local

pH at cathode. The cell potential did not increase during electrolysis, while considering the lifetime of electrode and long-time effect, the regularly recirculation with acidic solution in the electrolysis system can be the proposal strategy to remove scaling.

In a last step, the efficiency of the coupling process was studied through the global elimination of pharmaceuticals from the influent and the removal of the related toxicity which can be more appropriate in term of evaluation of the efficiency of the process with environmental perspective.

Based on the working diagram of NF, filtration conditions corresponding to the un-fouling region insure higher productivity while low rejections in that case can lead to higher pharmaceuticals and toxic compounds concentrations in the permeate. In this case, NF permeate continues to pose threats on the environment, in addition to the production of a lower concentrated NF retentate which results in a lower energy efficiency for the removal of pharmaceuticals in the following EO step.

Operating EO in a current intensity higher while close to the limiting current is the best operating condition to obtain higher efficiency and avoid the production of toxic by-products. Considering the removal of toxicity, EO is confirmed to be an efficient and safe method if an appropriate operating current density is selected.

After optimization of operating conditions, the efficiency of the coupling process for the total removal of target pharmaceuticals has been demonstrated through the elimination of androgenic activators and PXR-like activators. It was still observed some estrogenic activators attributed to the fact that corresponding compounds were certainly not totally rejected by the membrane.

As further developments of this thesis, several possibilities are proposed. Concerning the NF, there is still an open question: how to obtain great productivity and high selectivity at the same time. The first track to be investigated is the technical and economic feasibility of a regulation of the feed pH, according to its impact factor on fouling and pharmaceuticals rejection. It can be conclude from the present study that filtration operated at a flux lower than the critical flux with adjusting pH to 6 could lead to (i) high productivity due to the absence of irreversible fouling especially scaling; (ii) acceptable rejection of pharmaceuticals due to the control of the enlargement of pore size attributed in alkaline water matrix to electrostatic repulsions within the membrane pores.

Expectedly, the adjustment of the pH during NF could be accompanied by higher cost and difficulty of application. This must be balanced with the lower productivity and cost of fouling removal without adjusting the pH.

To manage the EO process in an environmental and economic sustainable way, the

present work has evidenced that the choice of the applied current is the key factor. The objective is to control the formation of halogenated organics besides operating current. It already determined that the current density closed to the limiting current density can be the best operating condition to obtain the great process efficiency and avoid formation of AOX. However, I_{lim} depends on the COD which changes during EO experiments. The next step of this study will be the design of the coupling process. Some tracks of reflexion have been proposed such as:

- (i) Adapt the applied current during the EO time; this study has evidenced that the implementation is possible thanks to the excellent adequacy between COD model and experiments.
- (ii) Adapt the geometry of the electrochemical cell to maintain the COD concentration at the inlet of the electrochemical cell in a continuous mode. For that a study is required to develop a new reactor with a high conversion rate per pass.
- (iii) Another way is to design the EO to only increase the biodegradability of effluents (without mineralization) with a recirculation in the MBR. In this case, the material of anode doesn't need the same oxygen overpotential as the one of BDD. The potential of the cell would be lower. The use of a carbon felt which gives a high active surface can be used. In this way refractory compounds are modified by electrooxidation into more biodegradable compounds.

At the end of this manuscript, it could be affirmed that this Thesis, providing a better understanding on the effects of the complex MBR effluent matrix on the behaviors of both NF and EO, paves the way for the application of NF and EO coupling process for the elimination of pharmaceuticals. From this knowledge, appropriate operating conditions can be achieved. Thus, the study can be used as a reference for industrial applications of this tertiary treatment process and for further developments in coupling treatment process.

Annex

Annex IV-1: Electrogenerated bubbles enhance the mass transfer coefficient

Breck [6] showed that the mass transfer coefficient the global mass transfer coefficient (k_d) is the sum of two contributions, the flow rate of reaction system (k_d^h) and the convection due to bubbles (k_d^b).

$$k_d = k_d^h + k_d^b \quad (\text{Eq.IV.1-5})$$

Nevertheless, Vogt [4] tested and proposed a more precise correlation given by Eq.IV.1-6, which takes into account the influence of the flow rate on the bubble radius before dropping out :

$$k_d = k_d^b \left[1 + \left(\frac{k_d^h}{k_d^b} \right)^2 \right]^{0.5} \quad (\text{Eq.IV.1-6})$$

Where k_d is the global mass transfer coefficient, k_d^h and k_d^b is mass transfer coefficient contributed by flow rate of reaction system and the part from bubbles, respectively.

k_d^b depends on the gas flow production [4]:

$$k_d^b = B \left(\frac{\dot{V}_G}{S} \right)^m D^{0.5} \quad (\text{Eq.IV.1-7})$$

In this equation, B is a constant related to the bubbles (shape, diameter, surface tension); its value is estimated with experimental data, D is the gas diffusion coefficient in liquid phase, \dot{V}_G ($\text{m}^2 \text{s}^{-1}$) is the volumetric rate of gas evolution and S (m^2) area of the flow cross section. The constant value m is function of the gas nature. The average value for dioxygen in acid media is $m = 0.5$ [6], [7].

The gas flow production, $\left(\frac{\dot{V}_G}{S} \right)$ is a function of applied current density which produces oxygen, i_{O_2} (A m^{-2}), and the molar volume of oxygen, V_{mol} in $\text{m}^3 \text{mol}^{-1}$

$$\frac{\dot{V}_G}{S} = \frac{i_{O_2}}{nF} V_{mol} \quad (\text{Eq.IV.1-8})$$

Previous studies carried out in the LGC have been determined the constant B in the same system and operating conditions [3], [8]; $B \cdot D^{0.5}$ was tested as 4.3×10^{-3} , $i_{O_2} = 207 \text{ A m}^{-2}$. Then, k_d^b can be calculated as $2.4 \times 10^{-3} \text{ m s}^{-1}$ and the mass transfer coefficient in this case k_d was $3.5 \times 10^{-3} \text{ m s}^{-1}$.

In fact, the impact of current to mass transfer coefficient was merely observed at high applied current. Weiss [5] calculated the relationship of applied current and mass transfer coefficient (Fig.IV-9).

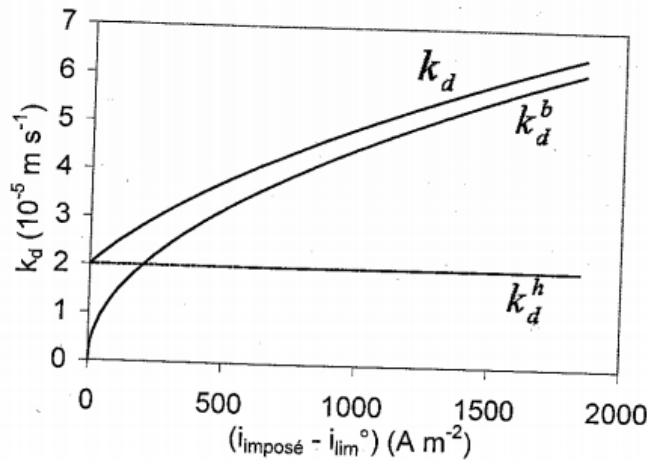


Fig.1 the relationship of applied current and mass transfer coefficient [5]

That is the reason why the CIP degradation rate was quit the same with current 0.1 and 0.5 A ($I_0 > I_{\text{lim}}^0$, $I/I_{\text{lim}}^0 = 7.2$), but raised significant when the current increasing to 1.5A ($I \gg I_{\text{lim}}^0$, $I/I_{\text{lim}}^0 = 21.7$) on the section IV.1.2.1: at 0.5 the current consumed to produce oxygen ($i_{\text{applied}} - i_{\text{lim}}^0$) is 62 A m^{-2} and the mass transfer coefficient was negligible; at 1.5A this value can be 207 A m^{-2} and the contribution of oxygen bubbles to mass transfer coefficient was significant from the Fig.IV-9.

Annex IV-2: TOC decayed with time during electrolysis of 1L CIP solution with various applied current density

Fig. 2 presents the evolution of TOC with EO time as various applied current intensity. It was observed that the removal of TOC became faster at a higher applied current. Value decreased slightly and was even stable at the first 10 min in the case $I < I_{lim}^0$. As we discussion on section IV.1.2.1.1, CIP can be oxidized by BDD anode with two pathways: directly electrons transfer and oxygen transfer via $\cdot OH$. That directly electrons transfer between CIP and anode just can degrade CIP molecule instead of releasing carbon dioxide to reduce organic carbon in the solution. TOC mineralization merely could happen in the case oxidation via $\cdot OH$. On the other hand, the reaction between CIP and anode, CIP and $\cdot OH$ happened and the competed at the same time. When the applied current lower than the limiting current (charge controlled), the oxidation is not completely. The slow decline of TOC at the beginning of electrolysis was due to that the main reaction was directly electrons transfer between CIP and anode. Until the part of current which produce $\cdot OH$ increased and took the dominant role in the electrolysis, TOC mineralize can be in a faster rate.

TOC decayed with almost the same rate, when the applied current increased from 0.1A to 0.5A, whereas a faster TOC mineralization was obtained when the current became to 21 times of limiting current ($I \gg I_{lim}^0$). This phenomenon was owing to that the effect of electrogeneration bubble on mass transfer coefficient was more significant at a very high applied current as discussion above.

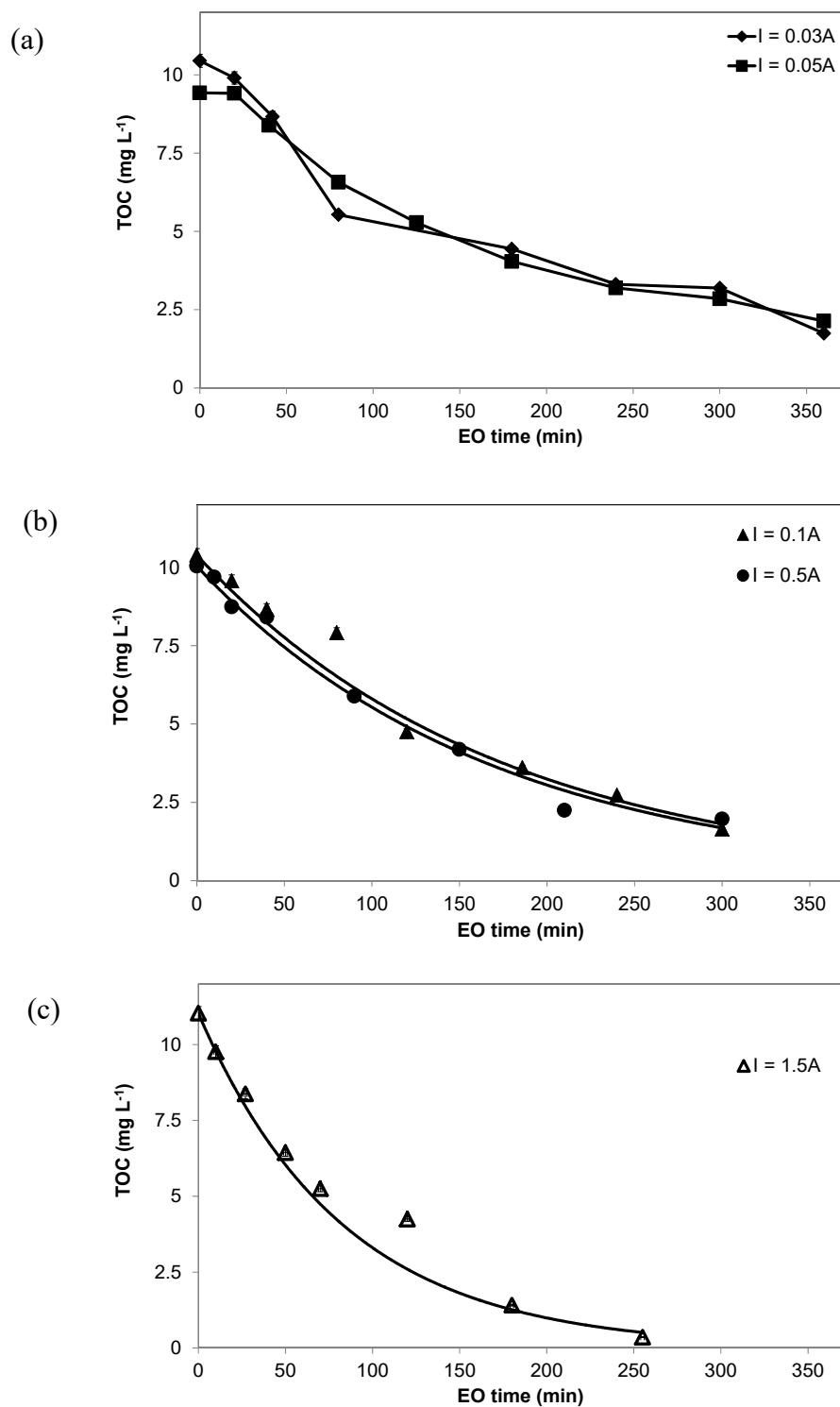


Fig.2 TOC decayed with time during electrolysis of 1L CIP solution in K_2SO_4 0.1 M at pH = 3.7 with various current, flow rate = $366 L h^{-1}$, $T = 30 ^\circ C$. $[TOC]_0$ shown on table IV-2, $I_{lim} \approx 0.08A$

(a) $I < I_{lim}^0$, $I = 0.03A$ and $I = 0.05A$

(b) $I > I_{lim}^0$, $I = 0.1A$ and $I = 0.5 A$

(c) $I \gg I_{lim}^0$, $I = 1.5 A$

Annex IV-3: the carbons from CIP and total organic carbon are compared at various applied current

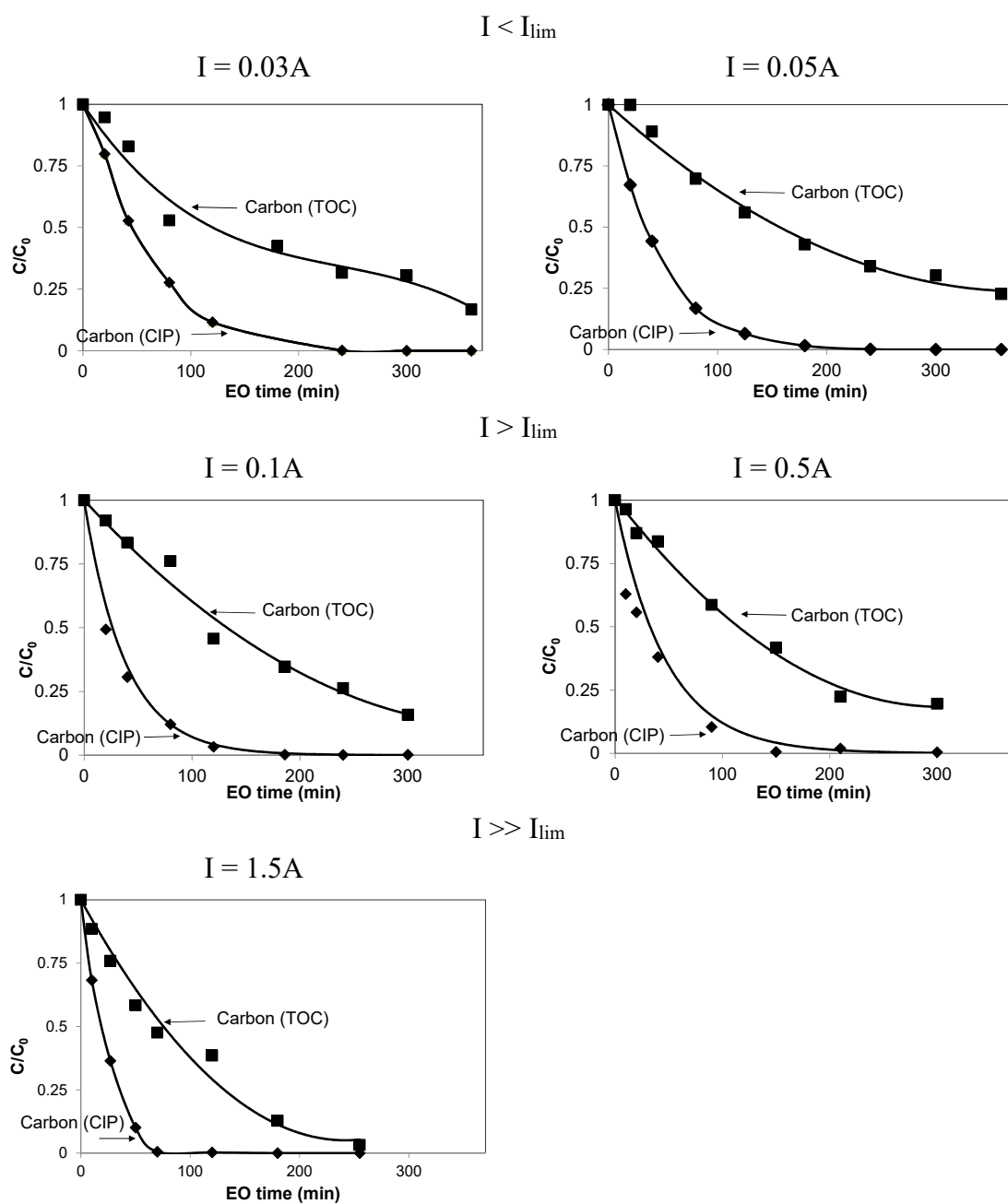


Fig. 3 Comparing the comparing of carbons from CIP and total organic carbons during electrolysis of 1L CIP solution in K_2SO_4 0.1 M at pH = 3.7 at various applied current, flow rate = $366 L h^{-1}$, T = 30 °C.

Annex IV-4: An example of the calculation of energy consumption and mineralization rate in the synthetic solution

Fig.4 presents the time and corresponding energy for complete CIP and 80% of TOC removal with various applied currents. From the figure, the time for 80 % TOC removal shorten 30 % from 400 to 280 min decreased with the applied current 0.03, 0.05 and 0.1 A, and then the decline became slower when the applied current exceeded limiting current. The removal time was 270 min and 130 min when the applied current increases to 0.5 and 1.5 A, respectively. The removal time of CIP was observed as similar phenomenon. When the applied current rose from 0.03 A to 0.1A the removal time decreased from 190 min to 150 min, whereas the removal time keep stable at 140 min with the current increasing from 0.1A to 0.5A. Then a slight decline was occurred to 85 min when the applied current was 1.5 A.

Considering energy consumption, energy consumption for 70 % TOC removal at applied current of 0.03, 0.05, 0.1, 0.5 and 1.5 A were 0.2, 1.2, 1.8, 9.5 and 19.3 Wh L⁻¹, respectively. Comparing the applied current 0.03 and 0.1A, the energy consumption rose from 0.18 to 1.43 Wh L⁻¹ and TOC removal time shortened 37%. On the other hand, in the range of 0.1 A to 1.5 A, a large amount energy consumption earned a slightly removal time decline.

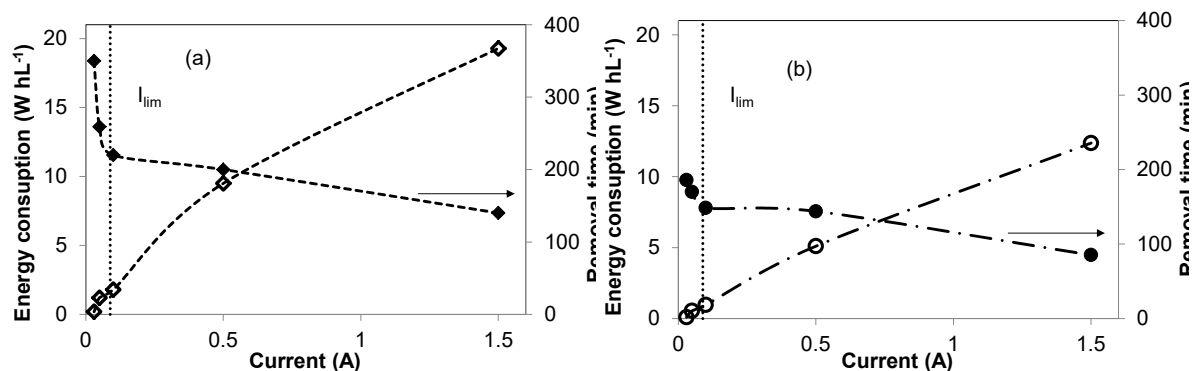


Fig.IV-4 Time (solid points) and corresponding energy consumption (hollow points) for 100% CIP (a), 80% TOC removal (b) during electrolysis of 1L CIP solution with various applied current in K₂SO₄ 0.1 M at pH = 3.7, flow rate = 366 L h⁻¹, T = 30 °C

One can be abstracted from Fig.4 that the limiting current intensity could be a “critical current intensity”: when the current intensity lower than the limiting current intensity, increasing current shortens the removal time and the energy consumption slightly increases; when the current intensity exceeds limiting current intensity, the

increasing current leads to higher energy consumption with insignificant removal time shortened for both CIP and TOC. Table.1 presents the values of removal time shorten, energy consumption increased and also energy consumption for shortening every minutes for the 80 % TOC and completely CIP removal in two current range: 0.03 to 0.1 A ($I \leq I_{lim}^0$), 0.1 to 1.5 A ($I > I_{lim}^0$). It can be noticed that the special energy consumption for shorten 1 min for TOC removal was 0.013 WhL⁻¹ in the range of 0.03 to 0.18A, and the almost 10 times energy consumption was required at current range 0.1 to 1.5 A ($I > I_{lim}^0$). It is the same tendency in the case of completely CIP removal.

Table.1 Comparison of the shorten of time and corresponding energy consumption in two current range for 80 % TOC and completely CIP removal

Current range	TOC		CIP	
	0.03 to 0.1 A	0.1 to 1.5A	0.03 to 0.1 A	0.1 to 1.5A
Time shortened min	120	144	37	63
Energy consumption increased WhL ⁻¹	1.6	17.5	0.9	11.4
Energy consumption for every min (WhL ⁻¹) min ⁻¹	0.013	0.12	0.024	0.18

Thus, the current intensity which value close to the limiting current can be the best compromise of less energy consumption and better mineralization rate.

Annex IV-5: The discussion of the amounts of intermediaries produced during electrooxidation of SALBU and SMX in comparing with CIP

To discussion the amounts of intermediaries produced during electrooxidation of SALBU and SMX, we also introduce the concept of Δ as the different of carbons of TOC and carbons of molecule (SALBU or SMX or CIP, identified on section IV.1.2.4). Comparing with CIP, it can be observed from the Fig.IV-28 that Δ of SALBU and CIP reach a peak value at the same time around 80 min of electrolysis and the maximum Δ of CIP is higher than SALBU. The total amount of intermediates produced during electrolysis can be characterized by the intermediates surface ($\int_0^t \Delta dt$). From the figure it can be observed that the amount of intermediaries of CIP produced during electrolysis is more than SALBU and SMX, which can be expected due to CIP is a more complex molecule and containing more carbons than the others. The amounts of intermediaries of SALBU and SMX are almost the same at the first 1 h. It can be infer that probably, the amounts of intermediaries produced during electrolysis of pharmaceuticals depend on the carbons number of molecule in the same operating condition.

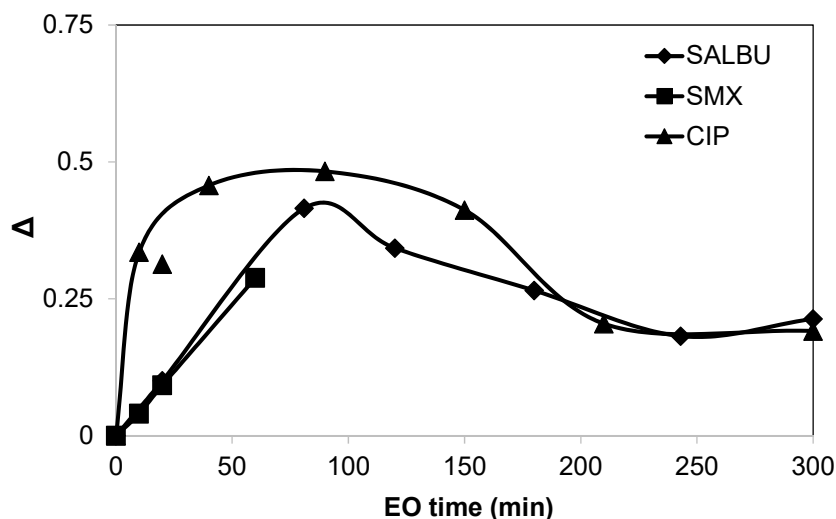


Fig. 5 The variation of Δ of SALBU, SMX and CIP with EO time during 300 min electrolysis. Operating condition see Fig.IV-26.

Annex IV-6: TOC decay in presence of Cl^- with current intensities as 0.1A and 3A

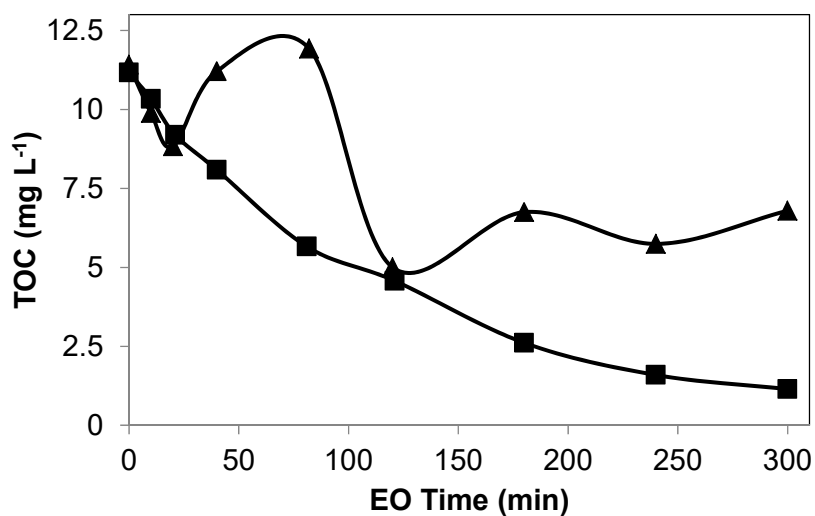


Fig.6 TOC decayed in K_2SO_4 0.02M+2.25mM KCl, \blacklozenge $I = 0.1\text{A}$ (1.45 mA cm^{-2}), \blacktriangle $I = 3 \text{ A}$ (43.47 mA cm^{-2}). $[\text{TOC}]_0 = 11 \text{ mg L}^{-1}$, during electrolysis of 1L CIP solution, flow rate = 366 L h^{-1} , $T = 30 \text{ }^\circ\text{C}$.

Annex IV-7

Fig.7 shows the degradations of CIP and urea with EO time in synthetic solutions containing both molecules with different ratios: $[CIP]_0:[urea]_0 = 1:2$ and $[CIP]_0:[urea]_0 = 1:11$. For the ration of $[CIP]_0:[urea]_0 = 1:2$ (Figure IV-44 (a)), it can be observed that the completely removal of CIP is reached after 180 min of electrolysis, while the concentration of urea seems to be stabilized at 0.009 mM. This stabilization was already observed during electrolysis of urea solution. For the ration of $[CIP]_0:[urea]_0 = 1:11$ (Fig.8 (a)), the degradation of CIP is surprisingly rapider than the case the concentration of urea as double of CIP as shown on Fig. 8 (b): the completely removal of CIP is obtained only after 100 min of electrolysis.

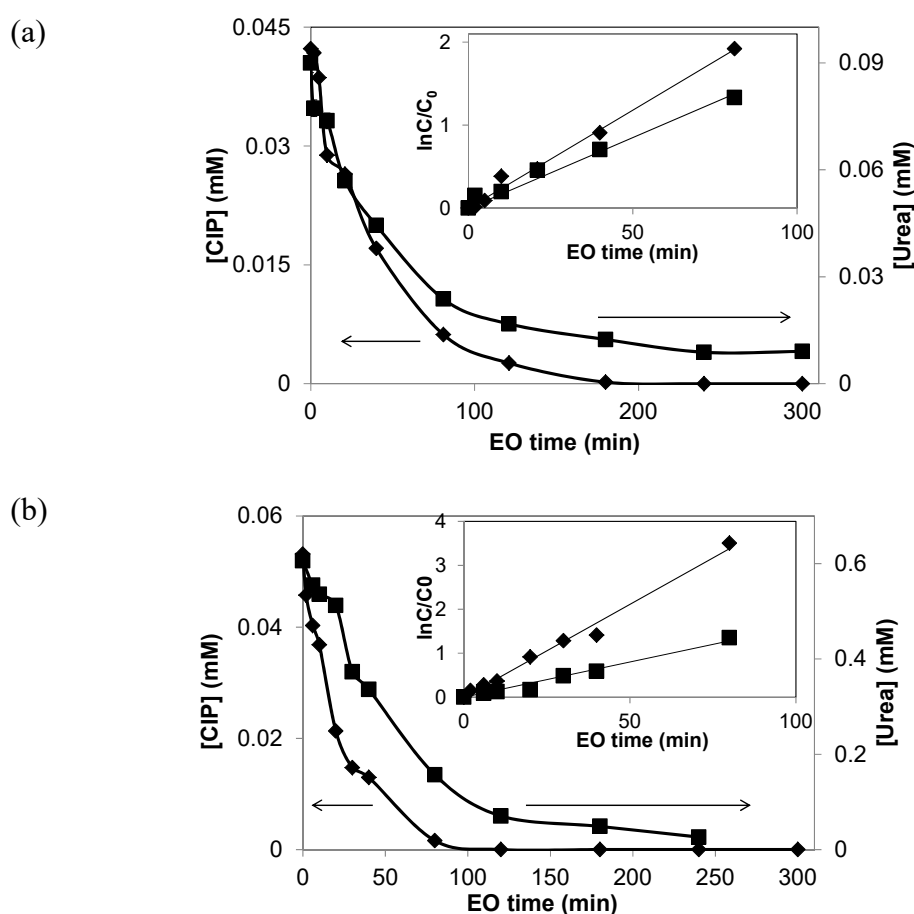


Fig. 7: The evolution of the concentrations of CIP and urea during 300 min electrolyses of 1L in synthetic solutions containing CIP and urea with different ratio and K_2SO_4 0.1 M at pH = 3.7. $I = 0.5A$, flow rate = $366 L h^{-1}$, $T = 30 ^\circ C$. Inset: the kinetics analysis of CIP and urea.

(a) $[CIP]_0:[urea]_0 = 1:2$, $[CIP]_0 = 0.045$ mM, $[urea]_0 = 0.094$ mM;

(b) $[CIP]_0:[urea]_0 = 1:11$, $[CIP]_0 = 0.053$ mM, $[urea]_0 = 0.606$ mM.

Annex IV-8 Degradation of pharmaceutical in presence of NH_4^+ and NO_3^-

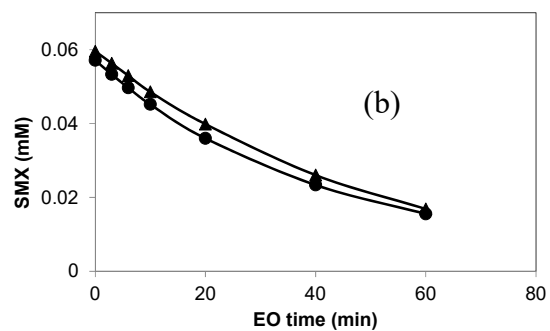
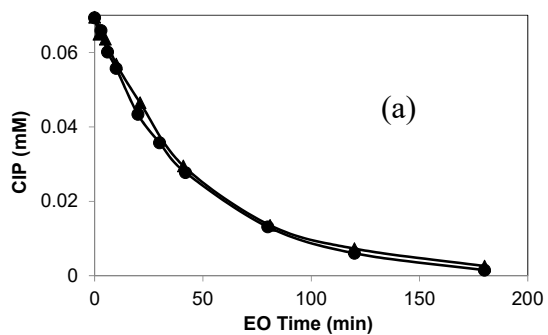


Fig.8 (a) CIP degraded with $I = 0.1$ A in ▲ K_2SO_4 0.02M, ● $I = 0.5$ A in K_2SO_4 0.1M + 2.5mM NH_4^+ during electrolysis of 1L CIP solution, $[\text{CIP}]_0 = 0.069$ mM, flow rate = 366 L h^{-1} , $T = 30$ °C.

Fig.8 (b) SMX degraded with $I = 0.5$ A in ▲ K_2SO_4 0.02M, ● KNO_3 0.02M during electrolysis of 1L SMX solution, $[\text{SMX}]_0 = 0.060$ mM, flow rate = 366 L h^{-1} , $T = 30$ °C

Annex IV-9: Decay of TOC during electrooxidation of CIP and SALBU

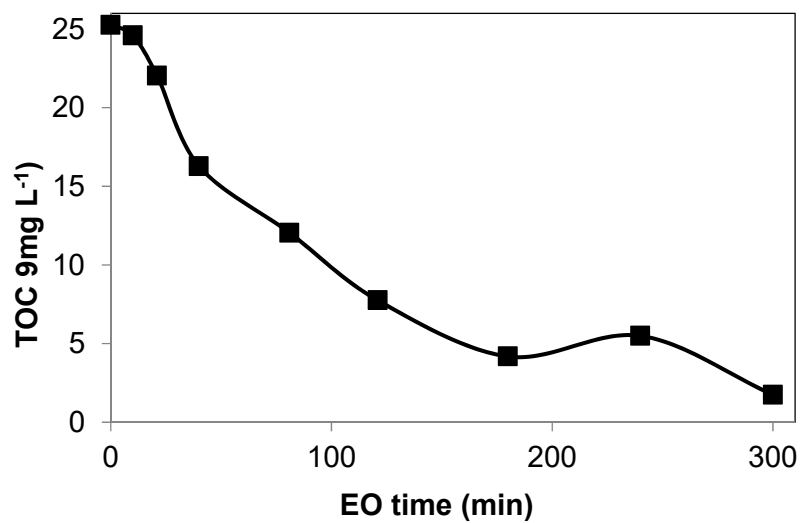


Fig.9 Decay of TOC in CIP and SALBU solution $I = 0.5A$ ($I > I_{lim}^0$), $[TOC]_0 = 25.4 \text{ mg L}^{-1}$, flow rate = 366 L h^{-1} , electrolyte: K_2SO_4 0.1 M , $T = 30 \text{ }^\circ\text{C}$.

Annex IV-10: Influence pH on the decay of COD and conversation of Cl^- during electrooxidation of NF concentrate

Influence pH on the decay of COD

The influence of pH on the decay of COD was also studied. Fig.IV-10 shows the decay of COD with time in the cases of $\text{pH} = 3.7$ and $\text{pH} = 7.8$ during 360 min electrolysis of 1L NF concentrate. It can be observed that the decay of COD in $\text{pH} = 3.7$ is faster than the case of $\text{pH} = 7.8$ and simulation value. This phenomenon is probably due to that the additional electrogenerated oxidants besides $\cdot\text{OH}$ is easier to be generated or stabilized in acidic solution and then the additional chemical oxidation is more significant. For example, as we discussed, the $\text{SO}_4 \cdot^-$ is easier to be generated in acidic solution due to higher concentration of HSO_4^- in acidic solution.

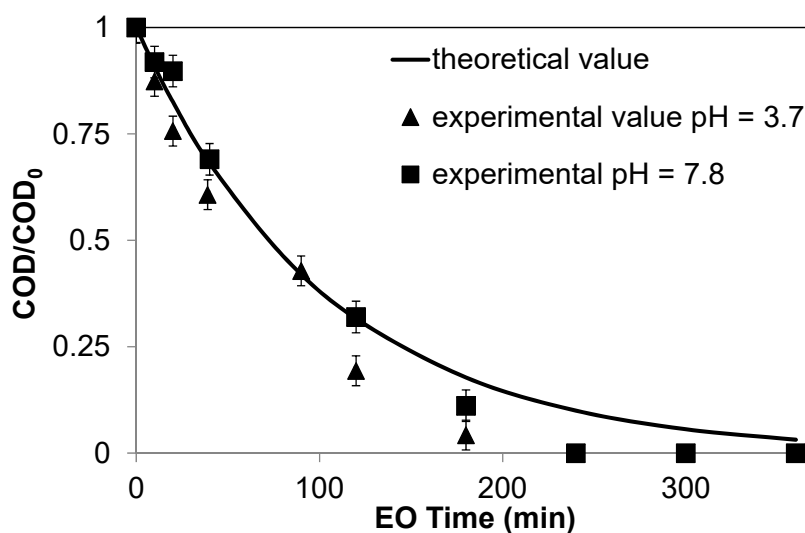


Fig.IV-10 The decay of COD with time in different pH: ■ pH =3.7, ◆ pH = 7.8 and — simulated value during 360 min electrolysis of 1L NF concentrate. $[\text{COD}]_0 \approx 81 \text{ mg L}^{-1}$, $I = 0.3\text{A}$ ($i = 4.34 \text{ mA cm}^{-2}$, $i_{\text{lim}} = 2.25 \text{ mA cm}^{-2}$), flow rate = 366 L h^{-1} , $T = 30 \text{ }^\circ\text{C}$

The influence pH on the conversation of chlorine species

The conversation of chlorine species are studied with different pH by measurement of the concentration of ionic chlorine species.

Fig.IV-11 presents the conversation of chlorine species during 360 min electrolysis of 1L NF retentate. It appears that the concentration of Cl^- declines with the electrooxidation time and ClO^- and ClO_4^- are formed. As we can see from Fig. IV-11 (a), the sum of ionic chlorine species ($\text{Cl}^- + \text{ClO}^- + \text{ClO}_4^-$) is higher than the initial

concentration of ionic chlorine (only Cl^-). The exceed part is proposed to be the oxidation productions of organics which contain chlorine. The amounts of them are the same in both cases of $\text{pH} = 7.8$ and 3.7 . The decrease of concentration of Cl^- is related to the pH of solution: in the case of $\text{pH} = 3$, the concentration of Cl^- decreases faster than the other.

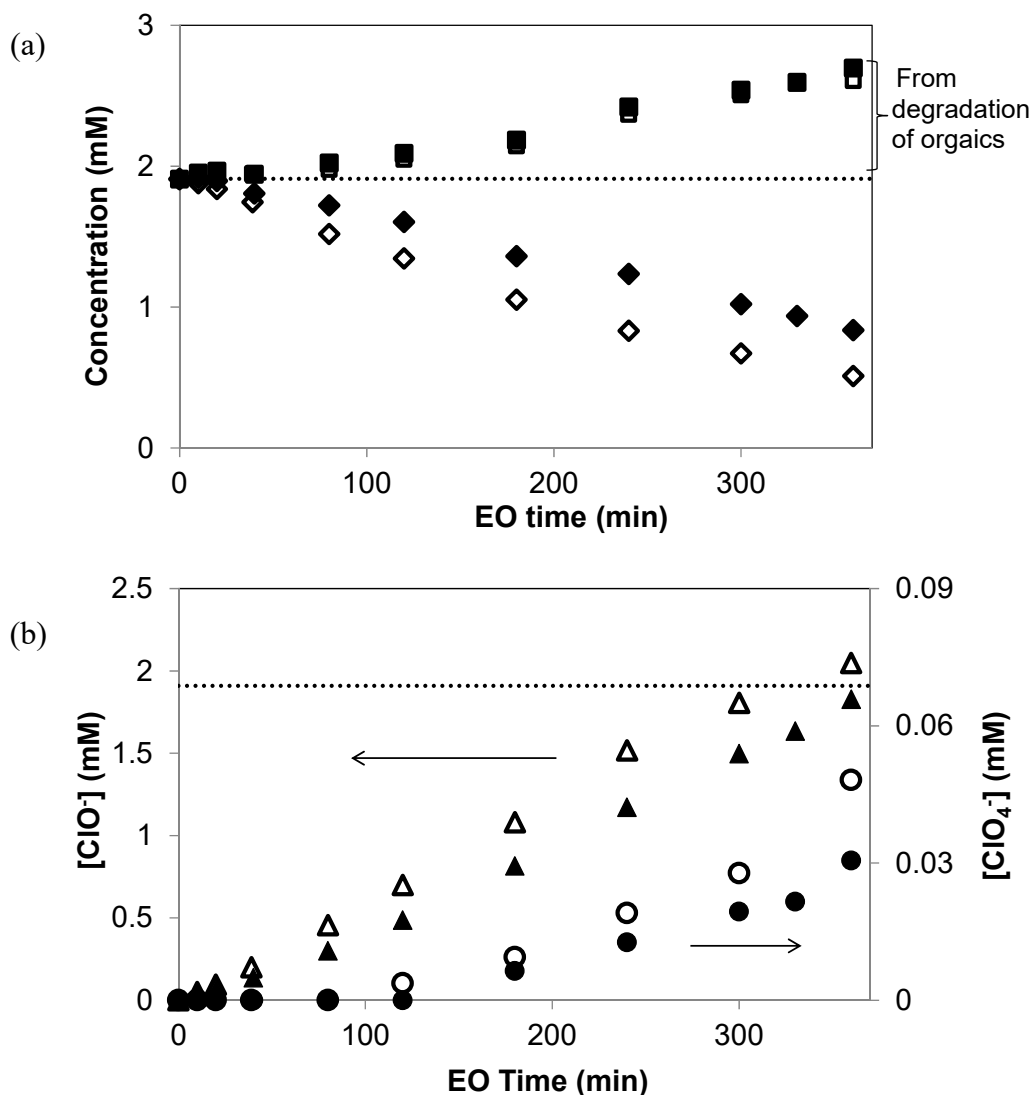


Fig.IV-11 The evolution of the concentration of chlorine species: (a) Cl^- ($\blacklozenge, \blacklozenge$); $\text{Cl}^- + \text{ClO}^- + \text{ClO}_4^-$ ($\blacksquare, \blacksquare$); (b) ClO^- ($\blacktriangle, \blacktriangle$), ClO_4^- (\bullet, \circ) with EO time during 360 min electrolysis of 1L NF retentate with different pH : $\text{pH} = 7.8$, blank symbols; $\text{pH} = 3$ (with $0.5 \text{ mmol H}_2\text{SO}_4$ addition), hollow symbols. The dashed line is the initial chloride concentration. $[\text{Cl}^-]_0 = 67 \text{ mg L}^{-1}$, $I = 0.3\text{A}$ ($i = 4.34 \text{ mA cm}^{-2}$, $i_{\text{lim}} = 2.25 \text{ mA cm}^{-2}$), flow rate = 366 L h^{-1} , $T = 30 \text{ }^\circ\text{C}$.

Fig.IV-11 (b) compares the formation of ClO^- and ClO_4^- in two pH. It can be observed that the formation of ClO^- is also faster at $\text{pH} = 3.7$. To the generation of undesired ClO_4^- , it begin to release in the solution at 120 min in the case of $\text{pH} = 3$, while it appears latter at 180 min at $\text{pH} = 7.8$ during electrolysis. Considering the amount of formation, more ClO_4^- is formed at the same electro oxidation time (also the same charge consumption) in acidic case. After 360 min of electrolysis, the concentration of ClO_4^- is 4.8 mg L^{-1} in acidic condition, while the concentration is 3 mg L^{-1} at $\text{pH} = 7.8$.

Annex V-1: Water quality of effluence from coupling process

Table V-1 Quality of the effluent treated by the coupling process (NF permeate and after EO) Comparison with Irrigation water standards

	Feed	NF permeate		EO effluent			Irrigation water standard
		Region A	Region B	Region A	Region B		
					I = 0.3A	I = 0.2 A	
Conductivity ($\mu\text{S cm}^{-1}$)	-	-	-	504	1061		0-3000
pH	-	-	-	7.38	7.33	7.35	6.00-8.50
Na^+ (mg L^{-1})	68.6	67.3	67.3	75.3	162.4	145.5	0-920
K^+ (mg L^{-1})	21.5	16.6	16.6	19.17	35.3	33.2	0-2.0
Mg^{2+} (mg L^{-1})	3.8	1.71	4.2	1.5	2.7	3.23	0-400
Ca^{2+} (mg L^{-1})	32.7	17.4	37	28.3	30.9	33.6	0-60.00
$\text{NH}_4^+\text{-N}$ (mgL^{-1})	-	-	-	-	-	-	0-5.00
Cl^- (mg L^{-1})	46.5	37.6	52.6	15.45	29.8	50.7	0-1065
ClO^- (mg L^{-1})	-	-	-	67.4	94.5	34.5	ND ^a
ClO_4^- (mg L^{-1})	-	-	-			-	ND ^a
NO_3^- (mg L^{-1})	1.0	0.56	1.2	25.4	164.5	155.0	0-10.0
SO_4^{2-} (mg L^{-1})	30.0	5.30	12.8	56.2	9.0	81.7	0-960
PO_4^{3-} (mg L^{-1})	9.0	2.7	4.7	0.49	< LD*	< LD*	0-2.00
HCO_3^- (mg L^{-1})	63.2	65.4	48.1	23.5	23.3	21	0-610
COD (mg L^{-1})	30	4	9	0	0	0	ND ^a
TOC (mg L^{-1})	10.23	0.97	5.49	1.7	2.9	3.6	ND ^a
AOX($\mu\text{g Cl L}^{-1}$)	380	NDA ^b	NDA ^b	1610	450	190	ND ^a

< LD*: due to the entrapped phosphate into the scaling in the electrolysis cell.

ND^a: No standard;

NDA^b: No data;

Reference

- [1] T.R. Beck, A Contribution to the Theory of Electrolytic Chlorate Formation, *J. Electrochem. Soc.* 116 (1969) 1038–1041.
- [2] H. Vogt, Mass-Transfer at Gas Evolving Electrodes with Superposition of Hydrodynamic Flow, *Electrochimica Acta.* 23 (1978) 203–205.
- [3] L.J.J. Janssen, J.G. Hoogland, The effect of electrolytically evolved gas bubbles on the thickness of the diffusion layer, *Electrochimica Acta.* 15 (1970) 1013–1023.
- [4] C. Flox, E. Brillas, A. Savall, K. Groenen-Serrano, Kinetic Study of the Electrochemical Mineralization of m-Cresol on a Boron-Doped Diamond Anode, *Curr. Org. Chem.* 16 (2012) 1960–1966.
- [5] C. Rcaud, A. Savall, P. Rondet, N. Bertrand, K. Groenen Serrano, New electrodes for silver(II) electrogeneration: Comparison between Ti/Pt, Nb/Pt, and Nb/BDD, *Chem. Eng. J.* 211–212 (2012) 53–59.
- [6] E. Weiss, Etude cinétique de la dégradation électrochimique de composés organiques sur l'anode de diamant dope au bore: application à la dépollution d'effluents aqueux, Doctoral thesis, Université Paul Sabatier-Toulouse III, 2006.

Tertiary treatment combining nanofiltration and electrochemical oxidation for the elimination of pharmaceuticals in wastewater

The coupling of nanofiltration and electrochemical oxidation is studied for the tertiary treatment of hospital wastewater after membrane bioreactor treatment. The effectiveness of nanofiltration is greatly affected by membrane fouling. In order to ensure sustainable flux and high performances during nanofiltration step, fouling mechanisms are investigated. The critical flux and the limiting flux are determined and associated with the combined effect of the organic colloidal fouling and the scaling. Impact of the fouling layer and of the presence of organic matters in the matrix on pharmaceuticals rejection is also investigated. NF retentate is then treated by electrochemical oxidation on BDD anode. The influence of operating conditions and the competition between components oxidation in the reactor are studied. Rather than a hindering effect, the presence of ions and common organics in the concentrate can accelerate the degradation of pharmaceuticals. In particular, the formation of organohalogenes due to the presence of chloride can be controlled thanks to the choice of appropriate operating conditions. A model for the degradation of pharmaceuticals over electrooxidation time is established. One objective is to access to the best compromise between mineralization of pharmaceuticals and energy consumption. After optimization of the operating conditions of both processes, their coupling is confirmed to be efficient for the elimination of pharmaceuticals and the reduction of the toxicity of the effluent, allowing to consider its release into the environment or its reuse.

Keywords: Pharmaceutical Elimination, Nanofiltration, Electrochemical Oxidation, Critical Flux, Fouling Mechanism, Toxicity Removal

Traitement tertiaire couplant nanofiltration et oxydation électrochimique pour l'Élimination des produits pharmaceutiques présents dans les eaux usées

Le couplage de la nanofiltration et de l'oxydation électrochimique est étudié pour le traitement tertiaire des eaux usées de l'hôpital après leur traitement par bioréacteur à membrane. L'efficacité de la nanofiltration est fortement influencée par le colmatage. Afin d'assurer des flux durables et des performances élevées lors de l'étape de nanofiltration, les mécanismes de colmatage sont étudiés. Les flux critique et limite sont déterminés et liés à l'effet combiné du colmatage colloïdal organique et du dépôt inorganique. L'impact de la couche de colmatage et de la présence de matières organiques dans la matrice sur la rétention des produits pharmaceutiques est également évalué. Le rétentat de la nanofiltration est ensuite traité par oxydation électrochimique sur une anode BDD. L'influence des conditions opératoires et la compétition lors de l'oxydation des constituants au sein du réacteur sont évaluées. Au lieu d'être rédhibitoire au bon fonctionnement du procédé, la présence des ions et des composés organiques dans le concentrat peut accélérer la dégradation des produits pharmaceutiques. En particulier, la formation de composés organohalogénés due à la présence de chlorure peut être contrôlée par le choix de conditions opératoires appropriées. Un modèle décrivant la dégradation des produits pharmaceutiques en fonction du temps d'électrooxydation est établi. Un des objectifs est d'accéder au meilleur compromis entre la minéralisation des produits pharmaceutiques et la consommation d'énergie. Après optimisation des conditions opératoires des 2 procédés, il est démontré que leur couplage est efficace pour l'élimination de produits pharmaceutiques et la diminution de la toxicité de l'effluent, permettant d'envisager son rejet dans l'environnement ou sa réutilisation.

Mots-clés : Élimination de produits pharmaceutiques, Nanofiltration, oxydation électrochimique, Flux critique, mécanismes colmatage, élimination toxicité